Structural defects in II-VI epitaxial Layers

Brown, Paul D.

How to cite:

Brown, Paul D. (1988) *Structural defects in II-VI epitaxial Layers*, Durham theses, Durham University. Available at Durham E-Theses Online: http://etheses.dur.ac.uk/6589/

Structural Defects in II-VI Epitaxial Layers

by

Paul D. Brown, A.L.C.M., B.Sc.

A thesis submitted for the
degree of Doctor of Philosophy
in the University of Durham

December, 1988

Abstract

This study has principally been concerned with the structural assessment of a range of II-VI epitaxial layers using the combined techniques of cross-sectional transmission electron microscopy and microdiffraction. Iodine reactive ion sputtering has been used for the final stage of sample preparation, and this has been shown to produce electron transparent foils with a greatly reduced artefactual defect content, as compared with samples prepared by argon ion milling.

The two conflicting conventions for the polarity determination of CdTe, as proposed by Warekois (1962) and Fewster (1983), have led to considerable confusion in the recent international literature. This issue has been resolved using the microdiffraction technique to identify the best $\{111\}$ *CdTe polar face for the epitaxial growth of (Hg,Cd)Te. This proved to be the* $\{\bar{1}\bar{1}\bar{1}\}$ *Te surface, and this result is in agreement with the Fewster convention for CdTe crystal polarity.*

The study of wide band-gap II-VI compounds has been mainly concerned with heterostructures of ZnSe/ZnS grown by MOVPE on (001) *oriented GaAs. Observations along orthogonal* $< 110 >$ *directions demonstrated the strong anisotropy in the defect distribution of these epitaxial layers. Microtwins were found exclusively in the* $[1\bar{1}0]$ *epilayer projection lying on advancing* $\{111\}A$ *planes. A model has been proposed, based on the differential motion of* α *and* β *dislocations in the sphalerite structure, to explain the defect anisotropy. It is considered that the large difference in the ionic radii of* Zn^{2+} *and* S^{2-}*, and material doping are primarily responsible for this phenomenon.*

The study of narrow band-gap II-VI compounds has been mainly concerned with the structural assessment of hybrid substrates for the epitaxial growth of (Hg,Cd)Te. Lamella twins lying parallel to the interfacial plane characterised $\{111\}$ *CdTe epitaxial layers grown by MOVPE on* $\{100\}$ *and* $\{\bar{1}\bar{1}\bar{1}\}B$ *GaAs, and on* $\{\bar{1}\bar{1}\bar{1}\}B$ *CdTe substrates, while the* $\{100\}$*CdTe/*$\{100\}$*GaAs system exhibited a network of misfit dislocations. MOVPE grown layers of (Hg,Cd)Te on both* $\{\bar{1}\bar{1}\bar{1}\}B$ *CdTe and CdTe/*$\{\bar{1}\bar{1}\bar{1}\}B$ *GaAs hybrid substrates have also been investigated. This study is complemented by an assessment of the anisotropic defect distribution in MBE grown (Cd,Zn)Te/CdTe strained layer superlattices, which have potential application as high quality lattice matched substrates for (Hg,Cd)Te. Finally a provisional study of the intermediate band-gap ZnTe and ZnTe/CdTe multilayer system is presented.*

Dr G. J. Russell, 1944-1988

Graham was more than just a supervisor. He was both a Boss and a close friend. Sadly, he is no longer around to receive my thanks.

He had a habit of suggesting that certain jobs couldn't be done and so, with due deference I took great delight in proving him wrong. This rivalry was the basis of a strong student/supervisor relationship which was truly appreciated. There are two memories of the Boss which will stay with me. The first is of his fierce determination never to turn down a challenge. He was always on the go and created a buzz around the place which made things happen. The second is of a man who always made time for other people. His loss was a sad day for us all.

This thesis is dedicated to
The Boss

Acknowledgements

I would like to take this opportunity to thank my co-supervisor John Woods for preserving the identity of the Applied Physics Group in Durham, and Andy Boy for reading this script at short notice while well hassled. My thanks also go to Ken Durose and Janet Hails for their help and encouragement, and to the many people who created the friendly atmosphere around the Department. Especially Uncle Norman, who has an amazing knowledge when it comes to finding bits of kit stashed away, but a memory like a sieve when it comes to doing odd jobs! And Heider, if only for impromptu lessons in Arabic. And there's Frank, with his instant repartee, quaint turn of phrase and philosophical outlook on life which somehow made the days seem a bit brighter! The folk down the workshop, it must be said, are brilliant. Thanks to Brian, Harry, Roger and Glen, and Davy Boy for cutting the crystals, and Peter for keeping the 'scopes going, and Julie and Kay, and the secretaries Pauline and Jane. They do an excellent job and this is the place to say it.

Finally, my thanks and love go to us mam, dad 'n' Taff, and to Frances for keeping my feet on the ground.

Contents

1. Introduction

'II-VI Compounds,' in the broadest sense, refers to the family of materials formed from elements of group II and group VI of the periodic table. Interest in these materials, however, has generally been confined to the sulfides, selenides and tellurides of zinc, cadmium and mercury (see figure 1.1). These compounds can be used to form a variety of optoelectronic devices which are capable of operating in the far infra-red through to the near ultra-violet regions of the electromagnetic spectrum.[1,2]

The chalcogenides of zinc and cadmium are termed 'wide band-gap' materials (see Table 1.1), and much of the early work on these II-VI compounds concerned deep centre photoluminescence in ZnS and photoconductivity in CdS.[1] II-VI cathodoluminescent and electroluminescent phosphors have subsequently found many commercial applications in cathode ray tubes, lamps and displays. The luminescent properties of doped ZnS and ZnSe can be tailored by altering the dopant species. Mn doped ZnS, for example, emits a characteristic yellow/orange colour and this compound is presently being developed as both an a.c. and a d.c. electroluminescent display.[2] [3] At present there is also considerable interest in the luminescent properties of ZnSe and Zn(S,Se) mixed crystals because of the commercial demand for light emitting diode structures and electroluminescent cells which operate in the blue region of the spectrum.[2] [4] In comparison, CdS is found to be a relatively poor phosphor at room temperature, but does exhibit a very strong photoconductive effect. The main problem associated with the crystal growth of many II-VI compounds is that of reliably obtaining p-type material because of auto-compensation effects.

CdTe and ZnSe[4] are presently the only II-VI compounds which can be made in both low resistivity n- and p-type form. CdTe may be used to form photoconductive and photovoltaic device structures,[5] and has additional applications in electro-optic modulators, and x-ray and γ-ray detectors.[6] Also, CdTe and ZnSe may be used to form a variety of optical elements such as lenses, Brewster windows, partially reflecting mirrors and anti-reflection coatings,[6] and CdTe is favoured as a substrate for the epitaxial growth of (Hg,Cd)Te.[6]

The Hg chalcogenides are either 'narrow band-gap' semiconductors or semi-metals and ternary alloys based on these compounds have been extensively developed in more recent years for their ability to detect in the infra-red. In particular, considerable

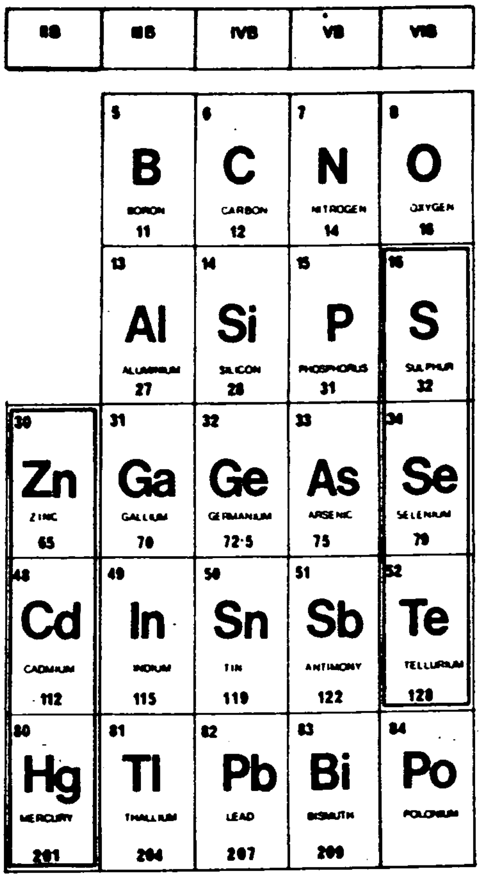

Figure 1.1 'II-VI' Compounds.

II-VI Compound (cubic)	Lattice Parameter (a_o)A	Room Temperature Band-Gap (eV)
ZnS	5.4093	3.54
ZnSe	5.6676	2.58
ZnTe	6.101	2.26
$CdS_{(hex)}$	4.1348	2.42
$CdSe_{(hex)}$	4.299	1.74
CdTe	6.477	1.44
HgSe	6.084	semi-metal
HgTe	6.429	

Table 1.1 'II-VI' lattice parameters and room temperature band-gaps.

attention has been given to $Hg_{1-x}Cd_xTe$ (MCT), the semiconducting nature of which was first ascertained by Lawson et al in 1959.[7] Variation of the alloy composition allows the compound band-gap to be varied between that of the semi-metal HgTe, which has a negative band-gap of -0.3eV ($x = 0$), and that of the semiconductor CdTe, which has a direct band-gap of 1.44eV ($x = 1$). Notably, the alloy of composition $Hg_{0.795}Cd_{0.205}Te$ has a band-gap of 0.10eV at 77K (liquid nitrogen) and is sensitive to radiation of wavelength 12.4μm.[8] This coincides with an atmospheric window to the infra-red which lies between 8 and 14μm. The motivation for the development of this alloy came from the need to replace the existing pyroelectric triglycene sulphate thermal imagers which lacked speed and sensitivity, and the Hg doped Ge photoconductive infra-red detectors which were also troubled by low sensitivity and required cooling to liquid helium temperatures for their successful operation.[9] MCT is favoured for the present generation of infra-red detectors because it has a good native passivating oxide and can be hybridised with silicon. Unlike lead tin telluride, for example, which is also sensitive to long wavelength radiation, but has the major disadvantage of a large expansion coefficient.[9] MCT is further favoured because the alloy of composition $Hg_{0.69}Cd_{0.31}Te$ is sensitive to 4.3μm radiation which corresponds to the 3 to 5μm infra-red atmospheric window, while alloy compositions in the range $0.65 < x < 0.8$ are sensitive to radiation between 1.0 and 1.7μm and have potential applications in fibre optic communication systems.

The high electron mobility ($\approx 10^5 cm^2V^{-1}sec^{-1}$) of MCT and the high electron to hole mobility ratio (≈ 400) coupled with a modest dielectric constant facilitates the formation of a variety of photoconductive and photovoltaic (or photodiode) devices, and transistor structures.[10] The present generation of MCT photoconductive (SPRITE) detectors[9] [10] are intrinsic charge transfer devices which provide time delay and integration processing within the focal plane. In order to ensure that their performance is only limited by background radiation, the rate of optical excitation of the carriers must exceed the thermal excitation rate, and the generation and recombination noise must be greater than the Johnson noise. This defines a number of physical parameters for the active MCT alloy. It is required that the minority carrier lifetimes are long ($\gtrsim 3\mu s$) to ensure adequate charge integration, and that the minority carrier concentrations are low to ensure low majority carrier concentrations ($\approx 10^{14} cm^3$) and so to reduce the effects of Johnson noise. Material with good optical absorption and high quantum efficiency is also required so that the generation thickness is low. These detectors, however, require complex mechanical scanning over a two-dimensional array, and are further limited by the need for long integration times at long (12μm) wavelengths. In addition, the only infra-red detection devices suitable for mass production at this time are the pyroelectric platinum silicide Schottky barrier detectors integrated with a silicon CCD addressing system.[9] These devices also require excessive cooling for their operation in the 8 to 12μm region. Consequently, there is considerable interest in the production of 'staring arrays' formed from MCT photodiodes. Such devices offer the possibility of increased sensitivity, lower power dissipation and greater complex signal processing within the array itself, and thereby provide a comparatively simple, cheap alternative to the existing MCT technology. In order to achieve high sensitivity and long minority carrier lifetimes in these photodiodes, it is necessary to produce large areas ($> 1cm^2$) of high quality, single crystal material. Bulk grown MCT, however, suffers from low compositional uniformity and contains an unacceptably high defect concentration. In addition, operation at long wavelengths (and low temperatures) necessitates the use of a charge-coupled device system to address the active elements, rather than cheaper field effect transistors.[10] These factors combined have contributed to the rapid development of thin film processing techniques in a joint attempt to produce device quality MCT, along with an integrated detection and processing circuit fabricated on a common single crystal substrate.

In addition to the photoconductive and photovoltaic detector, MCT also has potential application as a highly efficient, low cost solar cell. Device efficiencies in excess of 10% have been reported for electrodeposited Cd rich polycrystalline MCT,[11] and this simple processing technique could easily be scaled up to the commercial environment. There are also reports of MCT light emitting devices which operate in the 2 to 4μm wavelength range,[12] along with MCT/CdTe/MCT quantum barrier heterostructures which are found to exhibit a negative differential resistance and so have applications in high frequency devices such as microwave oscillators, amplifiers and mixers.[13] MCT is also found to exhibit various non-linear optical effects which arise from a large third order susceptibility and consequently, this alloy also has application in devices based on phenomena such as resonant four photon mixing and optical phase conjugation, and MCT may also be used as a spin-flip Raman laser.[14] In view of the large number of applications of this alloy, in terms of investment, MCT is the third most widely researched semiconductor after Si and GaAs.[15]

In general, II-VI compounds prepared using traditional bulk growth techniques contain an unacceptably high concentration of defects and hence, do not satisfy the quality requirements of modern device structures. However, the attraction of fabricating arrays of active II-VI optoelectronic devices hybridised with an established signal processing technology on a common single crystal substrate has provided the driving force for the detailed investigation of the epitaxial growth of many of these II-VI compounds over the last few years.[16–18]

The first step in the development of any particular epitaxial growth technology is to establish the feasability of depositing a particular compound in thin film form and then to optimise the conditions for epitaxial growth. The assessment of the structural properties of the deposited thin films is an essential part of this development process. The emphasis of this study is given to the structural assessment of a range of II-VI epitaxial layers, grown by Metal Organic Vapour Phase Epitaxy (MOVPE), using a variety of electron microscopy based techniques. Particular emphasis is given to the technique of cross-sectional transmission electron microscopy which uniquely provides for the direct observation of the epilayer microstructure.

There are several epitaxial growth techniques which are presently being used for the production of II-VI compounds and the principles of Molecular Beam Epitaxy (MBE), Liquid Phase Epitaxy (LPE) and MOVPE are briefly introduced and compared in the next chapter. The last few years has seen a great increase in interest in the use of MOVPE[17] [19] because this process offers the best compromise between material quality and scalability to the commercial production environment. The structural defects commonly found in sphalerite are then described, and illustration is made by reference to bulk grown CdTe and to a comparative study of the techniques of argon ion milling and iodine reactive ion sputtering for TEM sample preparation.

In Chapter 3, the determination of non-centrosymmetric crystal polarity is considered, and the confusion in the international literature regarding the polarity determination of CdTe is resolved.

Chapter 4 presents the results of a study of the defect microstructure of a number of wide band-gap II-VI epitaxial layers. The main part of this study is given to the assessment of epilayers of ZnSe and ZnS, and heterostructures of ZnSe/ZnS grown onto {100} oriented GaAs substrates. This chapter is then concluded by a brief description of sputter deposited ZnS films.

Chapter 5 is concerned with the assessment of narrow band-gap materials. In particular, emphasis is given to hybrid substrates which consist of buffer layers of CdTe deposited onto GaAs. A comparison is then made of the structural properties of epitaxial layers of MCT deposited onto bulk CdTe and hybrid CdTe/GaAs substrates. This study is complemented by an investigation of two MBE grown CdTe/(Cd,Zn)Te strained layer superlattice systems which have potential application as high quality lattice matched substrates for MCT epitaxial growth. This chapter is concluded by a preliminary investigation of MOVPE grown ZnTe, and an assessment of the first CdTe/ZnTe superlattice grown in Durham.

REFERENCES

1. The Physics and Chemistry of II-VI Compounds, ed. M. Aven and J.S. Prener, pub. North-Holland, 1967
2. H. Hartmann, R. Mach and B. Selle, *Wide-Gap II-VI Compounds as Electronic Materials* in 'Current Topics in Materials Science,' Vol. 9, ed. E. Kaldis, pub. North Holland, 1982
3. A.P.C. Jones, *Electroluminescence in Epitaxial Thin Films of ZnS and ZnSe*, Ph.D thesis, Dunelm, 1987
4. T. Yasuda, I. Mitsuishi and H. Kukimoto, *Appl. Phys. Lett.* **52** (1988) 57
5. C. Cohen-Solal, M. Barbe, H. Afifi and G. Neu, *J. Crystal Growth* **72** (1985) 512
6. K. Zanio, Chapter 4, '*Applications*' in Semiconductor and Semimetals, Vol. 13, Cadmium Telluride, ed. R.K. Willardson and A.C. Beer, Academic Press, New York, 1978
7. W.D. Lawson, S. Nielson, E.H. Putley and A.S. Young, *J. Phys. Chem. Solids* **9** (1959) 325
8. M.W. Scott, *J. Appl. Phys.* **40** (1969) 4077
9. D.E. Charlton, *J. Crystal Growth* **59** (1982) 98
10. C.T. Elliott, *J. Crystal Growth* **72** (1985) 453
11. B.M. Basol and E.S. Tseng, *Appl. Phys. Lett.* **48** (1986) 946
12. R. Zucca, J. Bajaj and E.R. Blazejewski, *J. Vacuum Sci. Technol.* **A6** (1988) 2728
13. D.H. Chow and T.C. McGill, *Appl. Phys. Lett.* **48** (1986) 1485
14. P.W. Kruse and J.F. Ready, *Nonlinear Optical Effects in* $Hg_{1-x}Cd_xTe$, in Semiconductor and Semimetals, Vol. 16, Defects, (Hg,Cd)Se, (Hg,Cd)Te, ed. R.K. Willardson and A.C. Beer, Academic Press, New York, 1981
15. P.W. Kruse, *The Emergence of* $(Hg_{1-x}Cd_x)Te$ *as a Modern Infrared Sensitive Material*, in ' Semiconductors and Semimetals' Vol. 18, Mercury Cadmium Telluride, ed. R.K. Willardson and A.C. Beer, Academic Press, New York, 1981
16. J.B. Mullin, S.J.C. Irvine and J. Tunnicliffe, *J. Crystal Growth* **68** (1984) 214

17. J.B. Mullin, S.J.C. Irvine, J. Giess and A. Royle, *J. Crystal Growth* **72** (1985) 1

18. B. Cockayne and P.J. Wright, *J. Crystal Growth* **68** (1984) 223

19. J.L. Schmit, *J. Vacuum Sci. Technol.* **A3** (1985) 89

2. Growth and Structural Assessment Techniques

2.1 Introduction

This chapter is divided into two main sections, the first of which is concerned with the techniques of crystal growth. Particular attention is given to the bulk growth of CdTe from the vapour phase, and to the epitaxial growth of MCT. The second section deals with the preparation of samples in cross-section for the observation of the epilayer microstructure in the electron microscope. A description of the iodine reactive ion sputtering process which is used for the final stage of sample preparation is given and this is compared with the more commonly used argon ion beam milling procedure. Artefacts of both sample preparation processes are illustrated and this work is complemented by a study of the structural defects found in bulk grown CdTe.

2.2 Bulk Crystal Growth

Single crystals of many II-VI compounds can be obtained by growth either from the melt or from the vapour phase.[1] Directional freezing from a congruent melt, as used in the Bridgman technique, allows the production of large single crystals in a few days. However, the high growth temperatures (*e.g.* 1092°C for CdTe) associated with this technique enhance compound contamination effects from the quartz crucible. Alternatively, the use of Te-rich solutions promotes crystal growth at lower temperatures, but this growth process is limited due to the small sizes of crystals which can be formed. Consequently, bulk crystal growth from the vapour phase is advantageous for binary II-VI compounds because it allows the production of large single crystals of material at growth temperatures well below the compound melting point.

The Durham Technique

Single crystals of ZnSe, ZnS, CdSe, CdS and CdTe have been grown using the vapour phase technique developed in Durham.[2] As shown in figure 2.1, charge material is stored in a sealed evacuated capsule and transport to the conical growth tip, following sublimation, is promoted by a temperature gradient. A reservoir containing one of the elemental species, located in a separate fixed temperature zone, is connected to the silica ampoule via a capiliary tube. Control of the reservoir temperature allows the partial pressure of the tail species to be maintained over the charge material. This in turn facilitates the control of the partial pressures of the constituent elements and allows the total partial pressure close to the minimum value (P_{min}) to be defined. This condition, which corresponds to the case of maximum transport, is recognised as being the optimum condition for stoichiometric growth.[3,4]

For the case of CdTe, growth proceeds at a temperature of 940°C as the capsule is drawn through the temperature profile at a rate of 1 to 2mmhr^{-1} over a period of 4 to 5 days, as illustrated in figure 2.1. In practice a slight excess of Te ($\approx$ 1%) is added since this has been found to prevent the growing crystal sticking to the silica capsule.[5] Cooling down to room temperature takes a further 3 days.

The bulk growth of MCT

Early attempts to produce single crystals of MCT using bulk crystal growth techniques were made using cast-recrystallisation.[6] Melt of the required composition is rapidly frozen to produce fine grained polycrystalline material, and this is then recrystallised during a prolonged annealing process. The two main problems with this technique are that impurities become frozen into the alloy and that the minority carrier lifetimes are too low for device requirements. Similarly, the Bridgman -Stockbarger technique is regarded as being inappropriate for use with MCT. Even though this process has the advantage of strong impurity segregation effects, CdTe and HgTe segregation is also promoted and this leads to variations in alloy composition. The problems associated with the production of bulk single crystals of MCT by controlled solidification have stimulated the development of a number of epitaxial thin film growth techniques, principal among which are Liquid Phase Epitaxy, Vapour Phase Epitaxy and Molecular Beam Epitaxy for the production of this alloy. The attraction of these growth techniques is that they provide for lower growth temperatures, shorter growth times and produce material with a better compositional uniformity compared to bulk grown material.

2.3 Epitaxial Growth

Epitaxial growth is the phase-transition deposition of a thin film of material (epitaxial layer) onto a crystal substrate. The thermodynamics of the growth system determines the equilibrium composition of the constituent phases, and the introduction of a non-equilibrium situation acts to promote the process of solidification and hence, epitaxy.

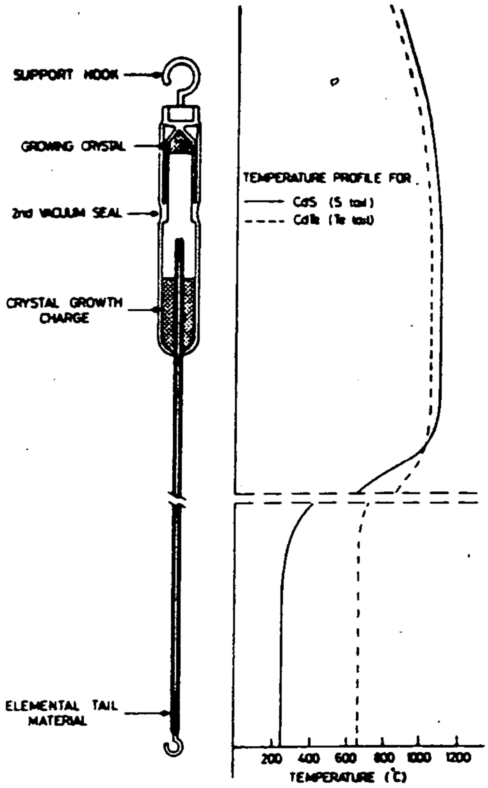

Figure 2.1 Bulk crystal growth: The 'Durham technique', [2].

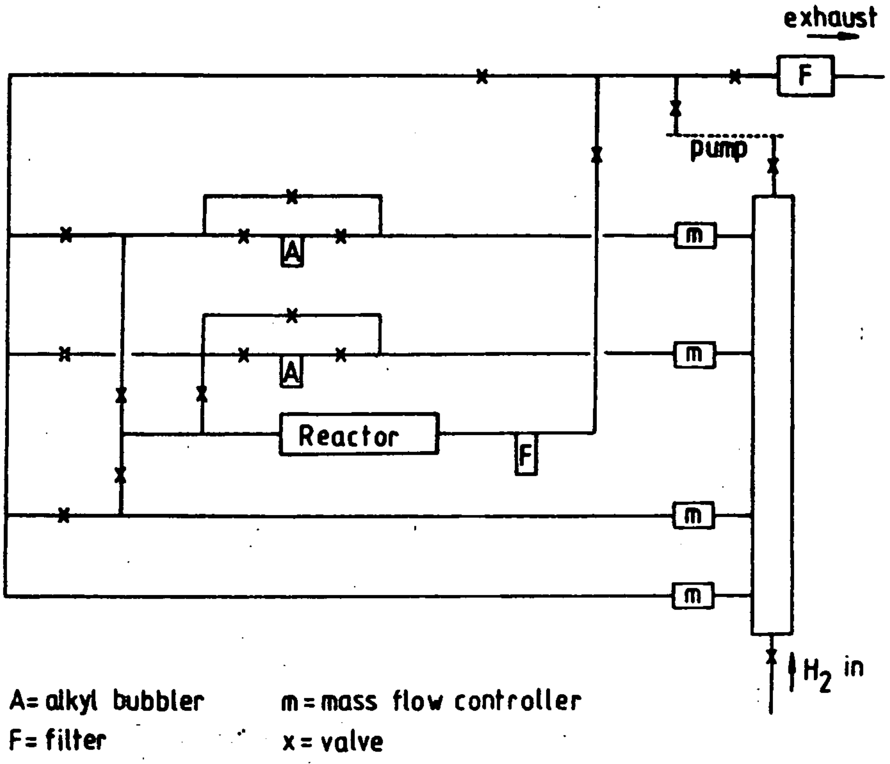

Figure 2.2 Schematic diagram of the Durham MOVPE system, [8].

Mass transport to the growth surface coupled with surface effects such as migration and sticking coefficients are crucial limiting parameters for this process.

Vapour phase epitaxy concerns two distinct processes. During Physical Vapour Deposition a polycrystalline or amorphous charge is raised to a high temperature, and material transported down a temperature gradient is deposited onto a substrate surface without any change in chemical composition. In contrast, Chemical Vapour Deposition requires a transport agent, and a chemical reaction to form the growth compound is promoted above the substrate material. Such a chemical process is limited by the system thermodynamics, and the availability of sufficiently pure reactants which must be compatable with the substrate material and growth apparatus. Consequently, the apparatus design and the determination of the optimum conditions for epitaxial growth is a complex problem.

Metal Organic Vapour Phase Epitaxy ⋆

Manasevit and Simpson first reported the deposition of II-VI compounds using the thermal Metal Organic Vapour Phase Epitaxy (MOVPE) technique in 1971.[7] Combinations of di-ethylzinc (Et_2Zn), di-methylcadmium (Me_2Cd), hydrogen sulphide, hydrogen selenide and di-methyltellurium (Me_2Te) were used to grow Zn and Cd chalcogenides on a variety of insulating substrates. A computer controlled MOVPE system has similarly been designed and built in Durham (figure 2.2).[8] The apparatus adopts the open tube gas flow system and employs a Pd diffused hydrogen gas stream to transport the alkyl precursors through the reaction chamber and by-pass lines. Gas flows and alkyl ratios are varied using Brook 5850TR mass flow controllers. Heating of the reactor wall is accommodated by four 750W quartz halogen lamps in preference to the more commonly used r.f. method of heating. Substrate crystals are placed on a graphite susceptor heated by a Mo wire and the lamp and susceptor temperatures are controlled by Eurotherm 810 three term controllers. The exhaust gases are filtered and scrubbed with activated graphite to remove Hg vapour and unreacted alkyls.

The Durham reactor has primarily been used for the deposition of CdTe, HgTe and MCT epitaxial layers on either CdTe or GaAs substrates. All of these systems examined during the course of this study were grown by Dr. Janet Hails† using the alkyls Me_2Cd

---

⋆ Otherwise known as Metal Organic Chemical Vapour Deposition

† Now at R.S.R.E., Malvern.

and di-ethyltellurium (Et_2Te), and elemental Hg. The CdTe substrates were prepared from bulk crystals grown using the Durham technique by Norman Thompson. The MOVPE system has recently been modified by the inclusion of additional lines for the use of Zn and Mn alkyls as part of a research program to investigate the (Hg,Cd,Zn,Mn)Te family of materials. The provisional study of epitaxial layers of ZnTe and ZnTe/CdTe superlattices reported in Chapter 5 uses material grown in Durham by Paul Clifton. The ZnS and ZnSe wide band-gap samples used for the study reported in Chapter 4 were grown by Dr. Patrick Jones* using a MOVPE reactor at R.S.R.E., Malvern.

The MCT epitaxial layers were grown using the Interdiffused Multilayer Process (IMP),[9,10] as opposed to the technique of direct alloy growth. During the IMP process alternate thin layers of CdTe and HgTe are sequentially deposited onto the substrate (see figure 2.3). Alloy formation occurs by the interdiffusion of the metallic species during epitaxy and the subsequent short anneal period. The alloy composition can be tailored by variation of the relative layer thicknesses.

The conditions used for the growth of the II-VI epitaxial layers investigated during the course of this study are summarised in Table 2.1.

The principles of MOVPE

Due to the complex nature of transport and thermal decomposition phenomena,[11] it is very difficult to predict the optimum conditions for the epitaxial growth of a ternary alloy such as MCT. While the ultra-high vacuum conditions associated with MBE, for example, allow the routine assessment of the epilayer surfaces during growth using Reflection High Energy Electron Diffraction (RHEED), the nature of the MOVPE growth technique precludes the use of any such investigative process. However, by assuming steady state growth conditions, consideration of the components adjacent to the growth interface can give an indication of the controlling parameters which determine alloy composition and growth rate.[12] In addition to the design of the reactor, the main factors to be considered are the alkyl partial pressures and ratios as determined by the carrier gas flow rates, and the susceptor and wall temperatures.

The pyrolysis of the reactant alkyls is a kinematic process and this rate factor is controlled by the supply of alkyls to the growth interface. Similarly, the incorporation of the metal species into the layer is also determined by the concentration of elements

---

* Now at B.T. and D., Ipswich

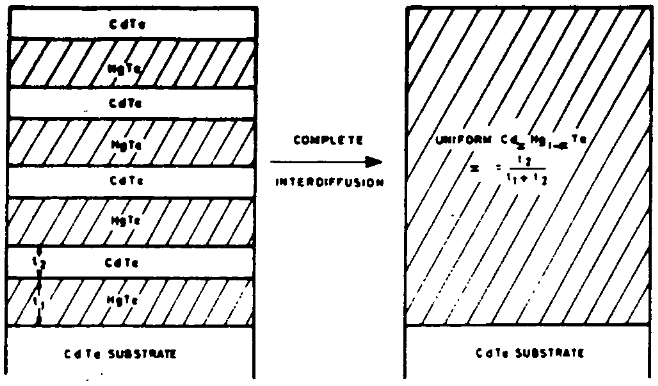

Figure 2.3 The Interdiffused Multilayer Process,[9].

Table 2.1 MOVPE Growth Conditions.

Growth Parameter		CdTe	HgTe	MCT[£]	ZnTe	CdTe/ZnTe[$]	ZnS	ZnSe
Susceptor Temp.(°C)		395	400	400	410	410	275[X]	275
Furnace Temp.(°C)		-	205[*]	205[*]	-	-	-	-
Flow Rates ($cm^3.min^{-1}$)	H_2 dil	4500[&]	500[w] or 0	4500	4500	4500	4500	4500
	Me_2Cd[y]	60 or 250	-	250	-	250	-	-
	Et_2Te[y]	250 or 1000	500 or 1000	1000	500	1000	-	-
	Me_2Zn[z]	-	-	-	90	90	5	5
	H_2S	-	-	-	-	-	80	-
	H_2Se	-	-	-	-	-	-	40
No. IMPS				70-80		40		
Growth Time (sec.)	Hg			35				
	Me_2Cd			5		2		
	Me_2Zn					30		
Layer Thickness	(um)			18	2	2	0.2 to 1	3 to 4
Growth Rate($A.sec^{-1}$)		120	50	4 to 8[x]			10	10

£ $Hg_{1-x}Cd_xTe$, x=0.2.

$ Growth cycle includes a 15sec. purge between each layer.

X 400°C when incorporating Mn.

* Hg temp. approx. 265°C.

& > $5000cm^3.min^{-1}$ over susceptor.

w Approx. $1000cm^3.min^{-1}$ over Hg and susceptor.

x For growth on {100} GaAs and {$\overline{111}$}B CdTe substrates respectively.

y Bubbler temperature maintained at room temperature

z Bubbler temperature maintained at -10°C present at the interface and by the thermodynamic properties of the various chemical species. In addition, there is a diffusion component present arising from the boundary layer which forms over the growth surface due to the laminar flow of the carrier gas. In the event of the arrival rate of the constituents exceeding the nucleation rate (*i.e.* the ability of the crystal lattice to incorporate the incoming species), then epilayers with a poor crystal structure, or even polycrystalline layers will be formed.

Epilayer composition is expected to be a function of the substrate temperature. This parameter is related to the different temperatures necessary for the effective decomposition of the reactant alkyls. For example, Me_2Cd decomposes more rapidly than Et_2Te, with 100% decomposition occurring at temperatures of 377°C and 450°C respectively.[13] Also, for equivalent alkyl flow rates, mercury only reacts with the tellurium alkyl at temperatures greater than 400°C.[13] This therefore sets a lower temperature limit of around 410°C for the epitaxial growth of MCT.[11] Reduction in the growth temperature acts to decrease the effective pyrolysis of the tellurium alkyl and so favours the formation of high x material.[14]

Epitaxial growth ideally should occur under conditions of low gas phase supersaturation, so that the partial pressures of the reactants do not deviate excessively from equilibrium conditions. This parameter can be controlled by the flow of the carrier gas through the alkyl bubblers. For example, during the IMP growth of MCT, flow ratios of about 4:1 between the Te and Cd alkyls are used to establish a 1:1 alkyl ratio, each with a partial pressure of around 1.5×10^{-3}torr. Epilayer growth then proceeds by variation of the main dilution hydrogen gas flow rate while maintaining a fixed susceptor temperature. The vapour pressure of elemental Hg, located in a bath placed upstream of the susceptor, is controlled by the temperature of the reactor wall which is heated by the quartz halogen lamps. A wall temperature of 200°C and a susceptor temperature of about 400°C combine to heat the Hg bath to around 265°C.[15] Growth of successive layers of HgTe and CdTe occur under alternating slow and fast gas flow conditions.[10] For the growth of HgTe, the Cd alkyl is initially diverted into the by-pass lines (see figure 2.2). Slow flow rates are then established to ensure there is adequate turbulence for 'Hg pick up' to create a supersaturated gas phase. Conversely, fast flow rates, as used for the deposition of CdTe, are found to be ineffective at 'Hg pick up'. Also, this growth condition helps to eliminate the problem of particulate deposition of CdTe, and thereby favours more uniform growth. In general, high flow velocities or low partial pressures tend to reduce epilayer growth rates. In contrast to the IMP process where the composition is controlled by epilayer thickness, the process of direct alloy growth varies the carrier gas flow rates through the bubblers to alter the alkyl ratio and so control alloy composition.

Adequate control of the initial stages of epilayer growth is known to be a critical process step as evidenced by the formation of {100} or {111} CdTe epitaxial layers on a {100} oriented GaAs substrate (see Chapter 5).[12] Since the surface reaction kinetics are important to the deposition mechanism, it is therefore reasonable to expect that the deposition rate is also dependent on substrate orientation because of polar effects.

Thermal catalysis of the reactant alkyls is advantageous because it introduces recirculation currents which promote homogenous gas phase reactions and hence, more uniform growth. Unfortunately, this process also leads to significant deposition onto the reactor walls. In addition, it is widely regarded that MCT epilayer growth is preferable at lower temperatures. Consequently, this has instigated the investigation of the use of alternative alkyls,[16] such as methylallyltelluride (MATe), di-isopropyltelluride (DIPT), and di-methylmercury (Me_2Hg), the latter as an alternative to elemental Hg. The IMP growth of MCT has been reported at a temperature of 350°C using DIPT, Me_2Cd and Hg,[17] while epitaxial HgTe has been deposited at 325°C by use of Et_2Te and Me_2Hg.[18] The MOVPE growth of HgTe has also been reported at 200°C by precracking Me_2Hg and Et_2Te.[19]

An alternative approach to low temperature epitaxial growth of MCT is by photo-MOVPE.[20,21] Alkyl photolytic decomposition by broadband[20] or laser[22,23] ultra-violet radiation has been shown to reduce CdTe and HgTe growth temperatures below 200°C, which is comparable to the deposition temperatures used by MBE.

In contrast, recent developments have seen an increase in the MOVPE growth temperatures used for the deposition of wide band-gap II-VI compounds.[24] The main problem with the epitaxial growth of ZnS and ZnSe is that of H_2S and H_2Se premature reaction.[25] Consequently, there has been recent interest either in the use of more stable heterocyclic compounds, such as thiophene (C_4H_4S) and selenothene (C_4H_4Se) and the alkyl Me_2Se,[26] all of which act to increase the growth temperature to around 450°C, or in the use of low pressure CVD.[24]

Molecular Beam Epitaxy

The general principle of Molecular Beam Epitaxy (MBE)[27] is very simple and belies the vast expense associated with this technique of crystal growth. Molecular or atomic beams are fired at a substrate held at an elevated temperature in ultra-high vacuum. The source material is held in an array of Knudsen effusion cells and their accurate temperature control determines the atomic beam fluxes. MBE growth temperatures are generally lower than those provided by MOVPE and LPE, and this favours the growth of highly uniform single crystals. The action of mechanical shutters over the effusion sources allow the incorporation of abrupt changes in the epilayer composition and formation of smooth atomistic surfaces. Like MOVPE, MBE also facilitates the introduction of dopants into the epilayer during the process of crystal growth. The epilayer composition can be determined by a combination of the substrate and the effusion cell temperatures, while variation of the shutter switching times allows the grading of material composition or doping concentration. The MBE technique and more recently laser assisted MBE[28] have been developed for the epitaxial growth of CdTe,[29] HgTe[30] and MCT.[31] The main attraction of MBE is that it allows the growth of a range of high quality, novel device structures. But in turn, MBE is limited by very slow growth times, of the order of $1\mu m$ hr^{-1}. Also, the high value of the Hg equilibrium vapour pressure necessitates the use of very high fluxes (10^{17} - 10^{18}cm^{-2}) of elemental Hg.[32]

Liquid Phase Epitaxy

The process of bringing a supersaturated solution into contact with a substrate crystal defines a non-equilibrium thermodynamic state which promotes epilayer growth. This is the basic principle of Liquid Phase Epitaxy (LPE). The growth of MCT is determined by the liquid solution composition, the mechanism for bringing the melt into contact with the substrate, and the mode of crystal growth.[13]

The most common method of growth is from a Te rich solution. This leads to the production of high quality uniform p-type ($\gtrsim 10^{17} cm^{-3}$) material which requires annealing over 1 to 2 days in a Hg rich environment to achieve type conversion. For comparison, LPE growth under Hg rich conditions produces material with the best surface morphology, but with low compositional uniformity. While growth from HgTe rich conditions produces graded layers due to an increase in Hg diffusion at elevated temperatures.[13]

The technique of tipping the melt onto a substrate is unsuitable for production purposes, but it does enable its use under vacuum conditions, thereby limiting Hg loss and allows accurate control over epilayer composition.[33] The process of dipping the substrate into the melt is most appropriate for use in a production environment.[34] The layer homogeneity is improved by the use of large melts, to limit depletion effects, coupled with melt rotation and agitation. However, the process suffers from the disadvantage of being performed under high pressure argon or hydrogen ambients. The alternative approach is to slide the melt on and off the substrate. While this process produces highly uniform layers, it requires long cycle times and results in the formation of a broad interdiffusion zone of around 3μm and again is less suitable for commercial production.

The main attraction of the LPE technique is that it is cheap compared with the other two epitaxial growth techniques, and that it allows the production of large areas of MCT. The main disadvantage is that high growth temperatures (typically 500^oC) make it difficult to produce the highly uniform, high quality material required by the next generation of infra-red devices. The difficulty of producing uniformally flat layers hinders device fabrication, and there are also problems with the reproducible growth of films with low carrier concentrations.[13]

Alternative epitaxial growth techniques

Briefly, there are a number of different approaches to the thin film deposition process as mentioned above. Many of these are either designed for the production of simple devices structures where the material quality is not a significant factor, or are no longer in favour, having been superseded by a more appropriate technology. For example, the use of HgI_2 for the growth of MCT by Chemical Vapour Transport[35] is no longer being investigated because of the problem of iodine incorporation into the epilayer.

There are several techniques which can be used for the simple, cheap deposition of CdTe for solar cell applications. These include closed-space vapour transport and closed-space sublimation, hot wall vacuum evaporation, electrodeposition and screen printing.[36] While these techniques are adequate for certain applications, the films are invariably polycrystalline in nature and unsuited for use as substrates for the epitaxial growth of MCT.

2.4 Sample Preparation

The preparation of bulk grown semiconducting compounds for observation in an electron microscope usually requires a sequential chemical polishing process[37] until the foil is sufficiently thin for the transmission of electrons (typically 1000Å). Such chemical techniques, however, are not particularly suited for the preparation of cross-sections of thin epitaxial layers.[38] The substrate is usually polished at a different rate to the epilayer and this precludes the preparation of uniform regions of material across the epilayer/substrate interface. Chemical techniques can, however, be used to prepare plan-view samples. Specimens may be thinned from the substrate side only, so that the surface layer becomes revealed following sample perforation. A slight modification to this technique is that of angle lapping,[39] in which the epilayer surface is initially polished at a low angle ($\approx 1^o$) to the plane of the interface such that subsequent preparation of the sample in plan view produces regions of electron transparent material which provide a depth profile of the transition from the epilayer to the substrate.

The preparation of epitaxial thin films in 90^o cross-section provides for the direct observation of the epilayer/substrate interfacial microstructure. This procedure, first used by Pettit and Booker in 1971 for the investigation of homoepitaxial silicon,[40] is now used for the majority of TEM investigations, as evidenced by articles in the Microscopy of Semiconducting Materials[41] conference series, for example.

The procedure used by the author for the preparation of epilayer cross-sections throughout this work was very similar to that developed by Chew and Cullis.[42,43] As-grown samples were cleaved to produce two thin strips of material and these were then glued face to face using epoxy resin (*i.e.* such that the epilayer material was in contact) as shown in figure 2.4. The wafer was then glued and sandwiched between two blocks of polycrystalline silicon (typically of dimensions $10 \times 2 \times 2mm$), which acted as a mechanical support for the sample during the subsequent mechanical polishing procedures. When the glue had set, the sandwich structure was attached to a glass microscope slide (scribed into about $\frac{1}{3}$ of its length) using melted wax. The first stage of mechanical polishing employed a simple perspex jig holding sheets of 600 grit SiC paper over which a slow trickle of water was allowed to flow. Samples were mechanically polished along the direction of the sandwich glue line until roughly half of the specimen bulk had been removed. An intermediate polishing stage used 12μm alumina powder mixed with water on a glass plate. Finally a buffing polishing process was used. This employed a motor driven turntable onto which was fixed a polishing pad, covered with a layer of water soluble 3μm diamond paste. These latter two process were designed to minimise the depth of the surface damage layer which is inevitably formed during mechanical polishing.[44] Buffing of the samples over a period of 10min produced a shiny surface. The sample was turned over, refixed to the glass slide with wax and the process repeated. As the sandwich structure became thinner, it was found necessary to remove any excess wax from the surrounding glass slide using a razor blade. This reduced the possibility of any wax becoming incorporated into the polishing pad surface and so inhibiting the polishing action. This sequential mechanical polishing procedure is capable of producing sandwich structures of around 50 to 70μm in thickness. Great care is needed, however, to ensure that the glass slide remains flat to the polishing surface otherwise a wedge shaped structure is produced which could cause problems during the later stages of sample preparation. As the sample became thinner, it was noted that the polycrystalline silicon block became rounded at the edges and began to flake away. As soon as this started to occur, the sample was transfered to the 12μm polishing stage and then buffed to a shiny surface using the 3μm polishing process. Extreme care was found to be needed during the final polishing stages since fracture of samples, grown on CdTe substrates in particular, tended to occur very easily. Slotted copper grids (3mm diameter) were then glued to the sample using epoxy resin so that the slot exposed the epilayer glueline. Careful sample preparation usually allowed two samples to be obtained from each sandwich structure. It was essential that these regions contained no cracks because such defects would undergo preferential attack during the subsequent ion beam milling process. The 3mm discs were then cut out using an ultrasonic drill, and floated off the glass slide by heating the wax before finally degreasing in boiling 1:1:1 trichloroethane.

Samples were then thinned to electron transparency by iodine reactive ion sputtering (at room temperature) in preference to the more commonly used procedure of argon ion beam milling.[42] A modified Ion Tech argon ion beam milling machine[45] was used for this process (see Figure 2.5a). The natural vapour pressure of elemental iodine, held in an evacuated ampoule located outside the milling chamber, is sufficient to supply the ion guns.[42] Focussed beams of iodine ions were fired at low angle ($\approx 15^o$) to the specimen until perforation occurred in a region known to contain the epilayer/substrate interface. The ion guns were modified such that a cathode was located on both front and rear faces. The forward ion beam was directed at the sample, while the reverse ion beam was directed at a metal stainless steel target suspended behind the gun by a glass rod which in turn was connected to the body of the gun by a metal collar (see figure 2.5b). A wire was taken from the target to an ammeter which gave a direct reading of the beam current. This experimental arrangement was incorporated to replace the existing Ion Tech enclosed cathode detection system, which has been shown to give a reading which is roughly an order of magnitude too high when compared with the free mounted detector.[46] Typically, the supply voltage and current used were 5kV and 1mA respectively which produced beam currents of around 20μA, while the chamber was held at a pressure of around 10^{-5} torr. Following, or close to the point of perforation, the milling conditions were reduced to 2-3kV, 1mA which gave beam currents of around 10μA. A few minutes of sputtering under these less severe conditions acted to produce foils with a lower defect content, as compared with the previous sputtering conditions (see section 2.5). Specimens of MCT on CdTe substrates were milled entirely at the lower milling conditions (see chapter 5). These generalised procedures using iodine were found to be applicable for use with a large number of II-VI compounds on either CdTe or GaAs substrates, and were similarly used with sputtered layers of ZnS on glass substrates. Gun lifetimes of the order of 500h are currently being achieved using the milling conditions described here. This figure is an order of magnitude greater than previously reported lifetimes.[42]

The technology for sputter thinning was originally developed for the preparation of inorganic solids for TEM.[47] Such procedures are now used extensively for the dry etching of compounds during device fabrication.[48] The use of ion beam milling for the preparation of cross-sections of semiconducting compounds allows a good deal of control when compared with chemical techniques. However, there is a tendancy for argon ion beam milling to leave an amorphous surface on sample foils of most materials,[49] including GaAs and Si, while a large number of defect loops are formed a short distance below the foil surface. The preparation of foils of InP by argon milling is also hindered by the preferential vaporization of phosphorus leaving globules of indium of the sample foil which act to mask the underlying defect structure.[50] The use of argon with II-VI compounds in particular results in the generation of extreme damage.[42] Of the alternative ion beam sources available for the preparation of TEM samples of semiconducting compounds, iodine, which removes material by a combination of bombardment and chemical attack, was found to be the most effective.[42]

Ion beam milled specimens usually contained electron transparent regions of the epilayer and epilayer/substrate interface. All samples were observed in a JEOL 100CX electron microscope operated at 100kV. There are several standard texts which deal with the operation of an electron microscope and the principles of electron microscopy,[51–54] so it is not proposed to describe them here. The next section introduces some of the defects commonly found in the sphalerite structure. Examples of these defects are provided with reference to a study on the structural defects in bulk CdTe grown from the vapour phase. A comparison of samples produced by argon and iodine milling is made and the artefacts which are generated during the process of ion beam milling are illustrated.

2.5 Structural defects in sphalerite

Crystallographic defects may be catagorised according to the number of dimensions they occupy. The nature of one-dimensional or point defects, such as atomic vacancies and impurity species located at either lattice or interstitial sites, cannot be ascertained using conventional electron microscopy techniques. However, the importance of such features in connection with the electrical characteristics of a semiconductor and their interaction with larger scale crystallographic defects is increasingly becoming a topic of debate.

The most commonly encountered two-dimensional or linear microstructural defect is the dislocation, which is characterised by $\underline{\mathbf{l}}$, the dislocation line, and the Burgers vector $\underline{\mathbf{b}}$, which is the atomic displacement necessary to generate the dislocation from the perfect lattice. For the fcc structure this defect may be regarded as being due to the insertion of an incomplete plane of atoms, or double atomic plane for the case of the sphalerite (figure 2.6a), into the crystal lattice which in turn is distorted in order to accommodate the defect. When imaged under conventional two-beam bright field conditions, dark contrast delineates the dislocation position because the Bragg condition is only satisfied by the uniform crystal lattice which surrounds the defect. A 60^o-dislocation is characterised by its Burgers vector which makes an angle of 60^o with the line of the dislocation. Alternatively, two 60^o-dislocations may interact to form a dislocation which is pure edge in character, for which the Burgers vector is perpendicular to the line of the dislocation. The type and arrangement of dislocations introduced during

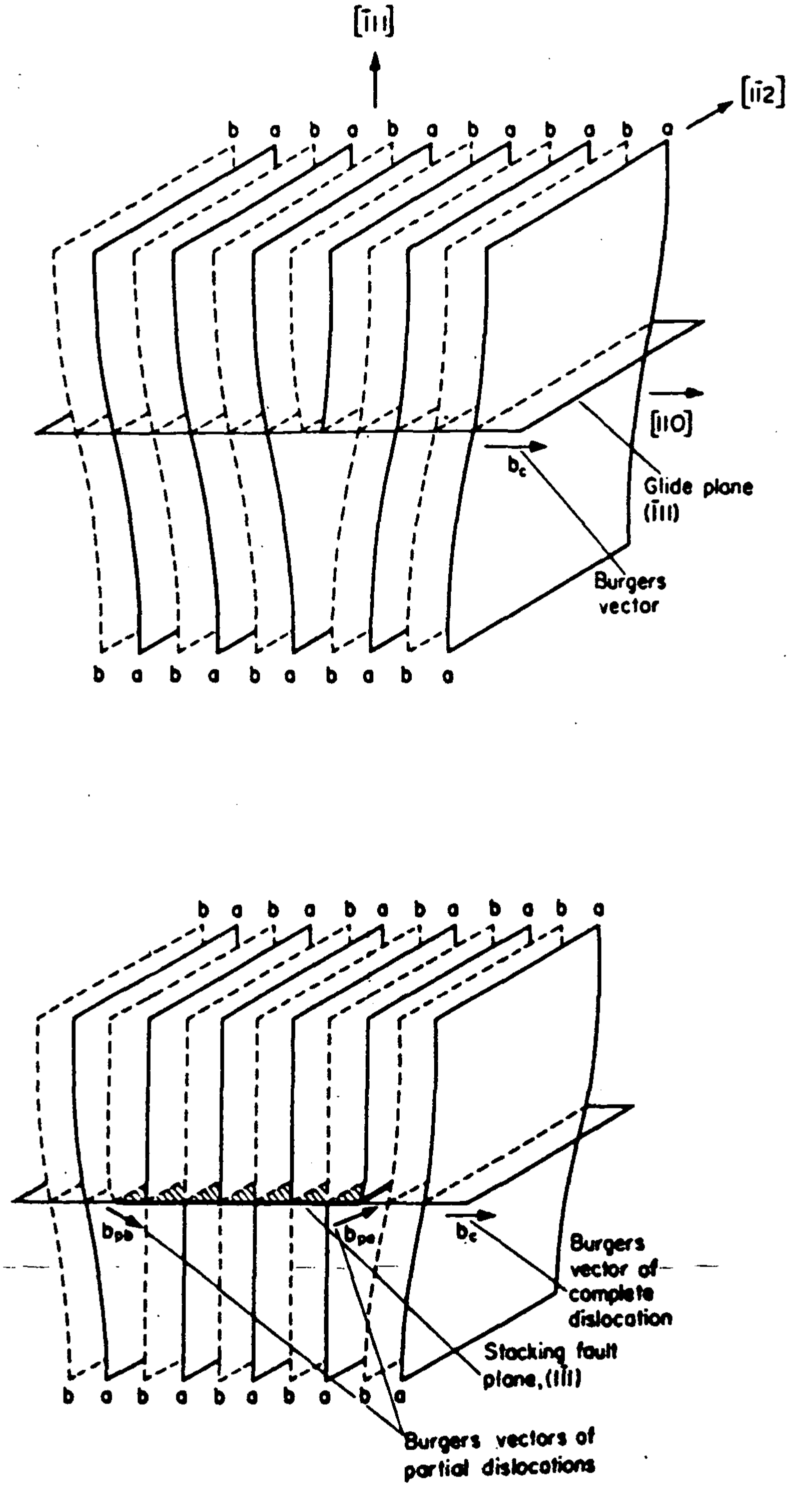

Figure 2.6 a) an un-dissociated and b) a dissociated dislocation in the sphalerite structure.

epilayer growth can severely influence epilayer quality and the performance of devices made from such layers. The electrical characteristics of a dislocation depend on the dislocation core, *i.e.* the atomic species at which the inserted plane of atoms terminates. For the sphalerite structure, dislocations may be either of the type α or β[55] as shown in figure 2.6c.

Dislocations in sphalerite II-VI compounds generally dissociate into two partial dislocations.[56] This leads to the formation of a stacking fault, as shown in figure 2.6b. The stacking disorder is bounded by two 60° dislocations,[57] and is either intrinsic or extrinsic[58] according to whether the fault arises from the presence or absence of an extra atomic plane respectively.

Large scale two-dimensional defects include the crystallographic boundaries, which range from the generalised grain boundary, through the low angle tilt boundary (or sub grain boundary) to the twin boundary for which there is a precise crystallographic relationship (relative rotation) between the twin and matrix material.

Three-dimensional imperfections cover features such as large scale inclusions, precipitates and voids.

In the following section, examples of many of these defects are illustrated with reference to the artefactual damage produced by ion beam milling and to the inherent defects found in bulk CdTe grown from the vapour phase using the Durham technique.

Artefacts of the sample preparation process

Early attempts to establish a reliable procedure using the ion beam milling machine entailed the use of very severe milling conditions upon CdTe using both argon and iodine. Typically, the milling conditions used, for an angle of around 20°, were 5kV and 3mA which produced beam currents of approximately 300μA as determined by the old fashioned Ion Tech enclosed detector.

Figure 2.7 shows a plan view micrograph of a CdTe sample milled using argon ions. The heavy speckle effect is due to the presence of a large number of small dislocation loops[59,60] which are believed to arise from condensing interstitial defects. The absence of these defects in similiar samples prepared by chemical thinning using $Br_2/MeOH$[5] clearly indicates that they are artefacts of the ion beam milling process. Under such extreme conditions these defects interact to form a number of much larger crystallo-

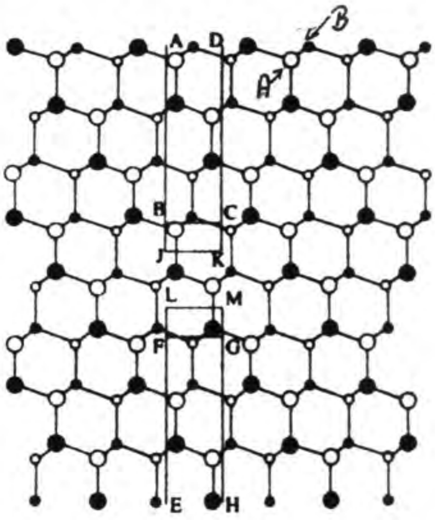

Figure 2.6c Definition of an α and β dislocation. Open and black circles represent the anion and cation respectively. α dislocations of the glide and shuffle type are created by the removal of sections ABCD and AJKD. Similarly, β dislocations of the glide and shuffle type are created by removal of sections EFGH and ELMH. Chapter 3, ref [17].

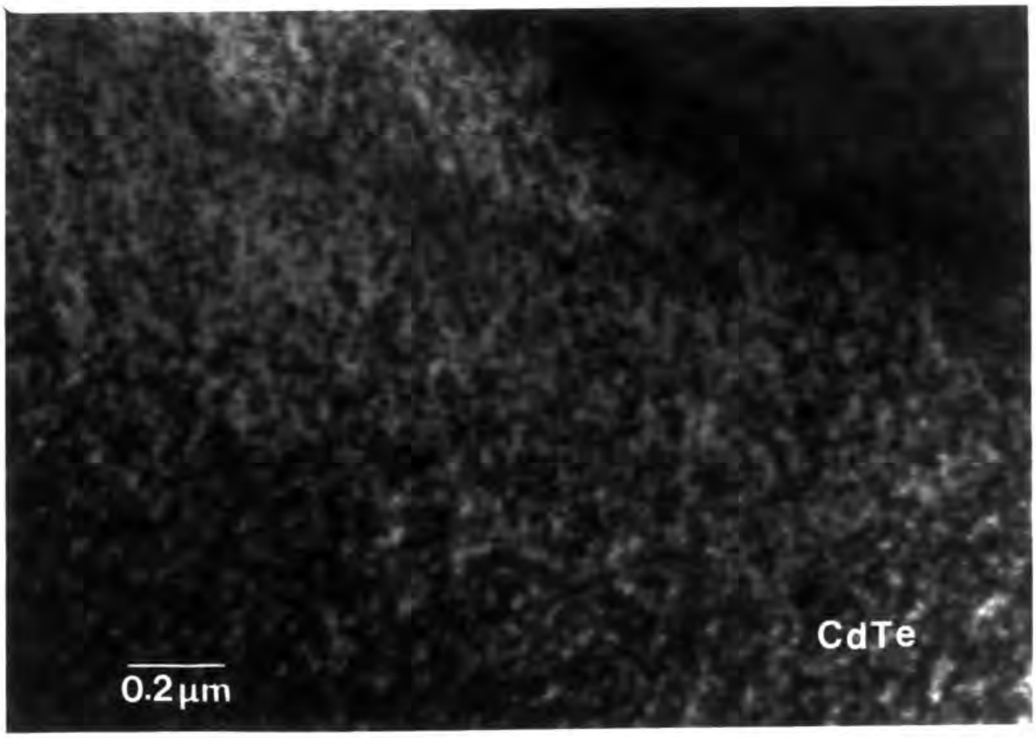

* g ↑ 220

Figure 2.7 Speckle damage in argon milled CdTe.

---

* The g-vectors assigned to many of the micrographs presented here refer to 'planes of a type', unless otherwise designated within ( ). This generalisation is made because knowledge of absolute crystal polarity (see Chapter 3) is needed for precise g-vector assignment.

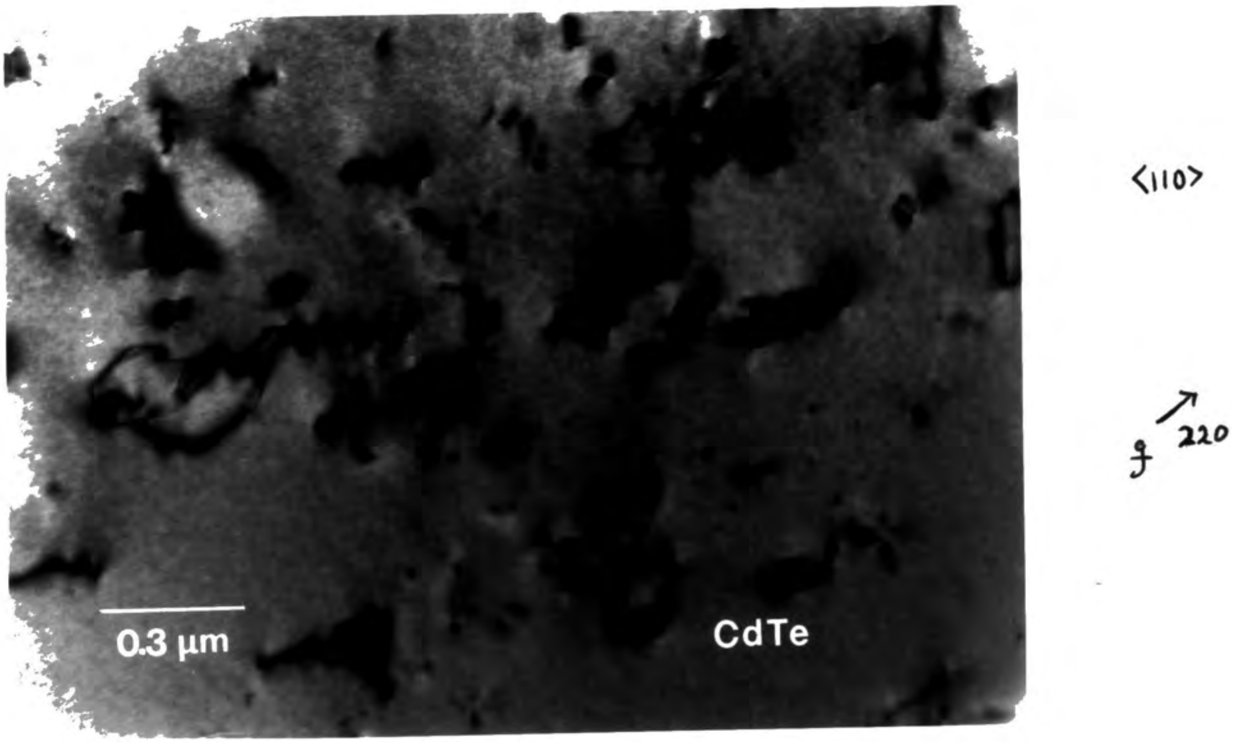

<u>Figure 2.8</u> a) Dislocations and dislocation loops and b) stacking faults in argon milled CdTe.

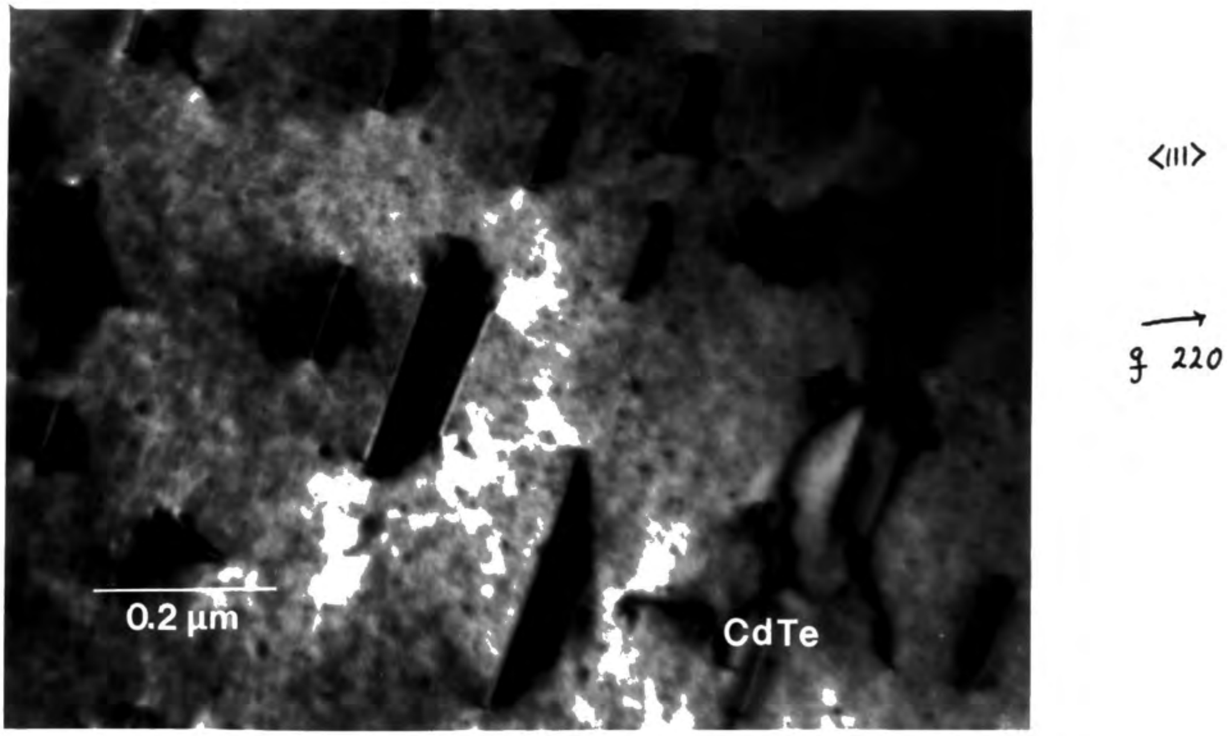

graphic defects (see figures 2.8a and 2.8b), such as dislocations, dislocation loops and stacking faults.

Using conventional $\underline{\mathbf{g}}.\underline{\mathbf{b}}$ defect analysis, where $\underline{\mathbf{b}}$ is the Burgers vector of the defect and $\underline{\mathbf{g}}$ is the operating reflection, the dislocations were found to be of the $\frac{1}{2} < 110 >$ type, which is the most commonly found dislocation in the sphalerite structure. Similarly, the orientation and nature of the stacking faults were determined by consideration of the value of $\underline{\mathbf{g}}.\underline{\mathbf{R}}_f$, where $\underline{\mathbf{R}}_f$ is the displacement vector of the crystal below the planar defect with respect to the top of the crystal. The outer fringes of the bright field images of these defects define the value of $\underline{\mathbf{g}}.\underline{\mathbf{R}}_f$ and the change in contrast of the corresponding dark field images gives the sense of slope of the defect in the foil.[52] The stacking faults, which lie on $\{111\}$ planes, were found to be intrinsic in nature.

Observations of the larger dislocation loops were made under conditions of $\pm\underline{\mathbf{g}}$. For positive values of $\underline{\mathbf{g}}.\underline{\mathbf{b}}$ it can be shown that the image lies outside the actual position of the loop and for negative values the image is formed inside the real position of the loop.[52] The sense of image shift obtained by reversing the sense of $\underline{\mathbf{g}}$ for a known value of $\underline{\mathbf{b}}$ allows the nature of the loop to be determined. The simple face-on loops were shown to lie on $\{111\}$ planes and were found to be interstitial in nature.

From considerations of the extinction contours at the edge of the sample foil, Lunn and Dobson[60] have shown that these small dislocation loops occupy a very narrow band of material approximately 50nm below the surface of the foil. This is consistent with the observation that there is no appreciable change in the defect density as the foil thickness increases. This depth is about an order of magnitude greater than the penetration distance of argon ions in this material,[61] which indicates that some diffusion related processes are operative. A similar density and distribution of interstitial dislocation loops have been found in electron irradiated II-VI compounds[62,63] as well as in ion implanted MCT.[64] In the latter case, however, a small distribution of vacancy loops was also found. Samples prepared under similar extreme conditions using iodine reactive ion sputtering were found to contain a similar distribution of speckle damage as the argon milled sample shown in figure 2.7, except that the defects were generally smaller.

Considerable improvement in the quality of the sample foils was achieved by adopting more moderate milling conditions. As shown in Figure 5.11b, it is possible to carefully prepare MCT/CdTe sample foils in which the artefactual dislocation loops are almost eliminated. The presence of this speckle damage is, however, a common feature in many of the sample foils prepared throughout this study. It is recognised as being a common problem with the II-VI compounds, and is thought to be a consequence of the low stacking fault energy associated with many of these materials.[56] Indeed, Chew and Cullis[42] have demonstrated that it is not possible to completely eliminate these defects from ZnS and ZnSe, even for specimens supported on a liquid nitrogen cooled sample stage while using very low beam currents. It is, however, immediately apparent that considerable improvement in the sample preparation process is achieved by use of iodine reactive ion sputtering as compared with argon ion beam milling, and valuable information concerning the native defect content of II-VI heteroepitaxial layers can be obtained, which otherwise would be masked by artefactual damage.

Mention should also be made of the limitations of iodine for use with MCT. The preferential etching of dislocations producing holes in the sample foil is a phenomenon which is often encountered when preparing cross-sections of MCT/CdTe (see figure 2.9a). It is noted that this effect is more likely to occur at nodes in the dislocation network. It is also noted that there is a slight change in the background speckle contrast across the interface of an MCT/CdTe sample, with the greater density of defects being present in the CdTe substrate. In view of the instability of the Hg-Te bond,[65] it is to be expected that MCT would suffer a similar or greater amount of damage as CdTe when thinned using iodine. Even though this is apparently not the case, it is argued that the lower background defect content of MCT (figure 2.9b) is due to the greater recovery of the alloy, which in turn is promoted by the elevated temperatures associated with ion beam milling.[59]

Structural defects in CdTe

The most commonly found large scale crystallographic defect in bulk grown CdTe is the twin boundary. There are numerous references to twin boundaries in many standard texts,[51] but briefly, a twin is characterised by its boundaries across which the atoms in twin and matrix are in mirror image positions. A simple first order twin boundary in fcc may be obtained by a rotation of the matrix by 70°32' about a $< 110 >$ zone axis.[5] In the fcc system the twin plane may be any of the four $\{111\}$ type planes. The microstructure of the twin boundary shown in figure 2.10a consists of an array of dislocations. The diffraction pattern taken from a twin along a $< 110 >$ zone axis (figure 2.10b), is a composite pattern arising from the two crystallographically related

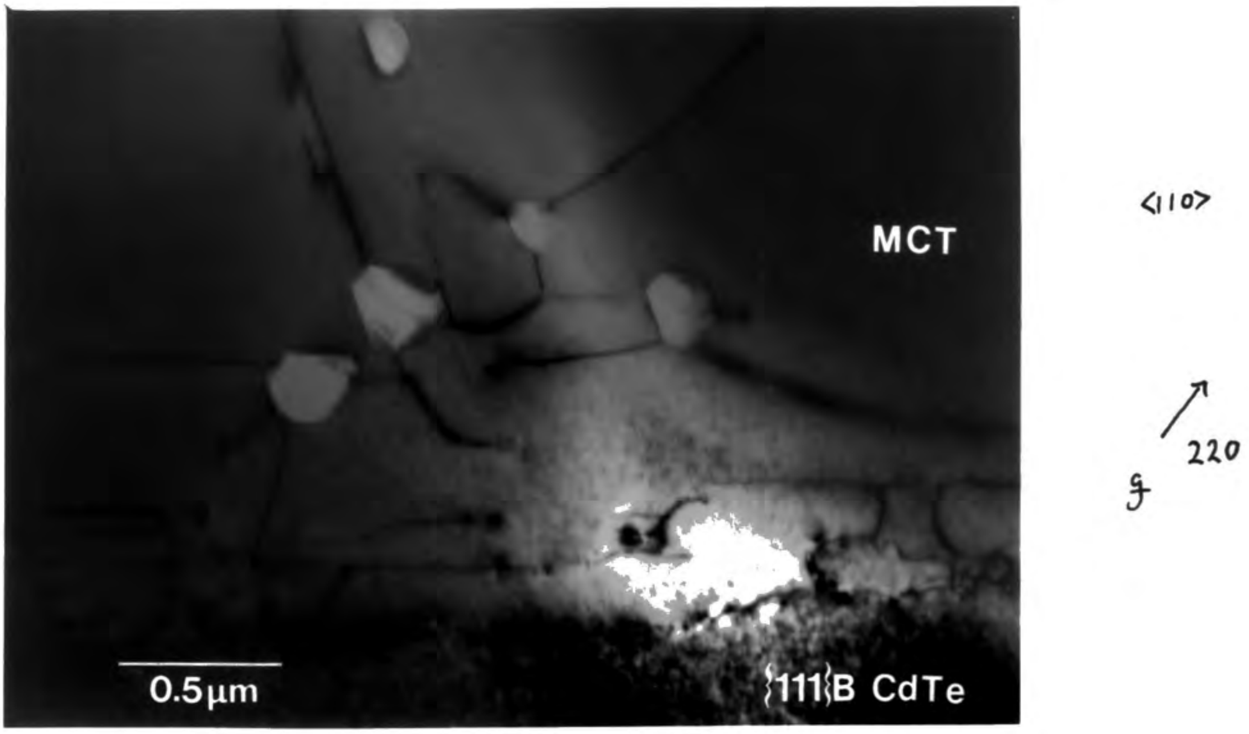

Figure 2.9a Preferential attack of dislocation nodes in iodine milled MCT.

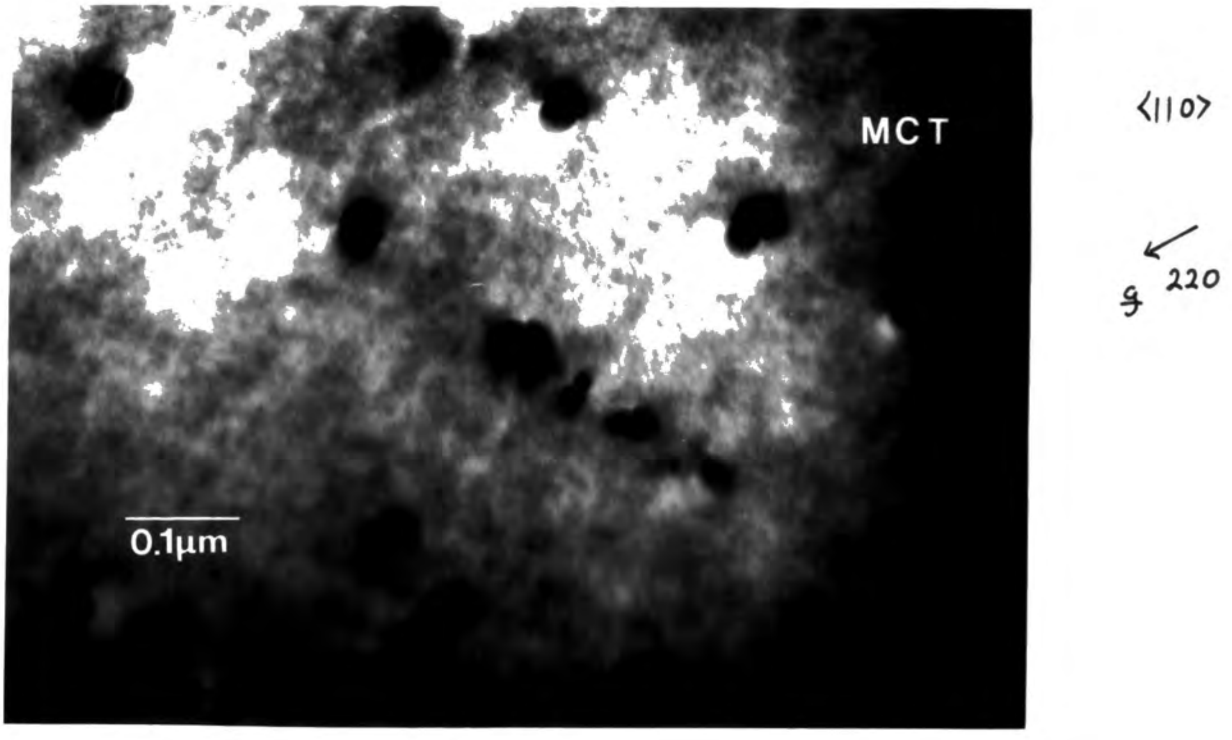

Figure 2.9b Dislocation loops in iodine milled MCT.

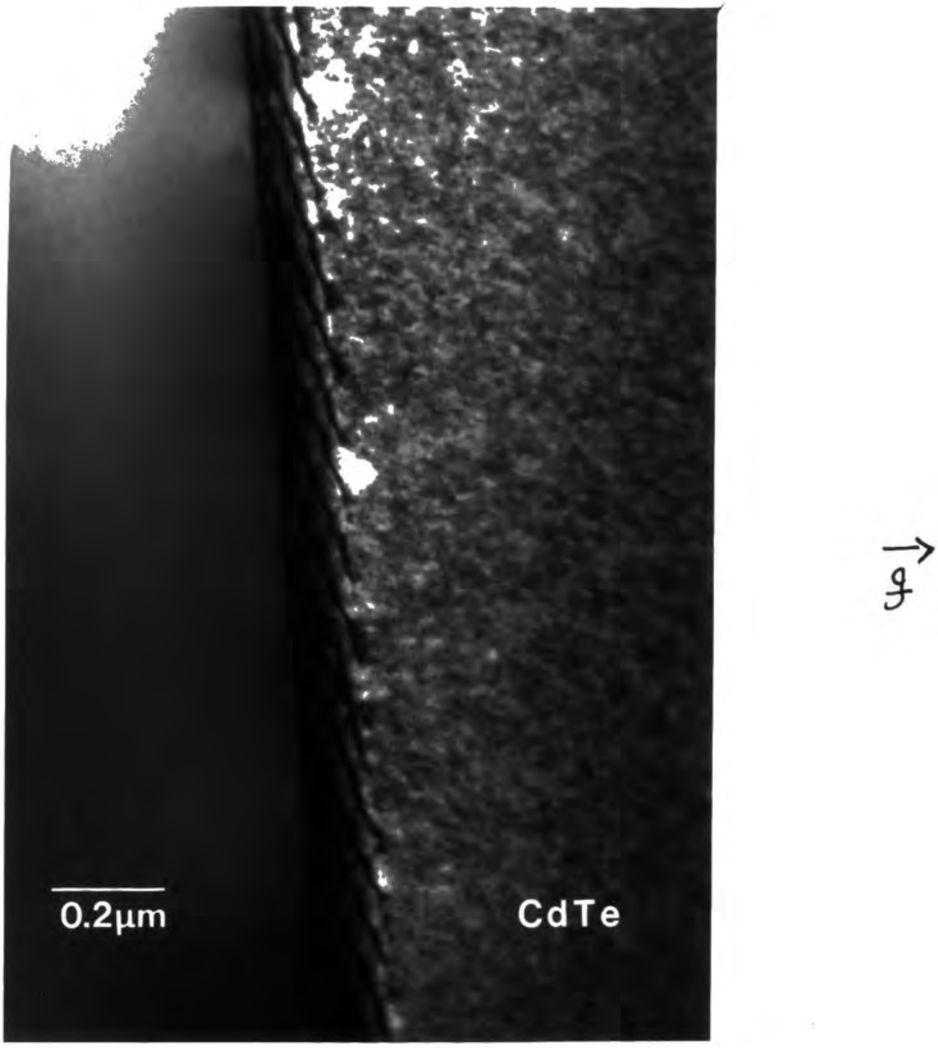

<u>Figure 2.10a</u> Twin boundary in CdTe.

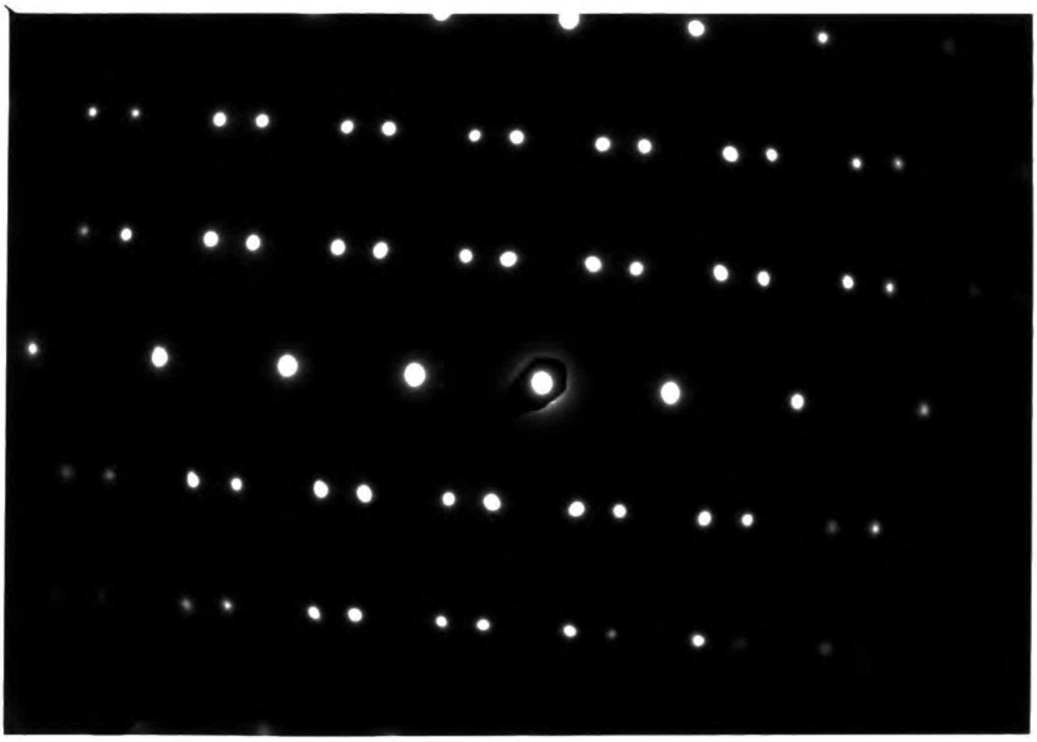

<u>Figure 2.10b</u> SAD pattern taken along <110> showing twin spots.

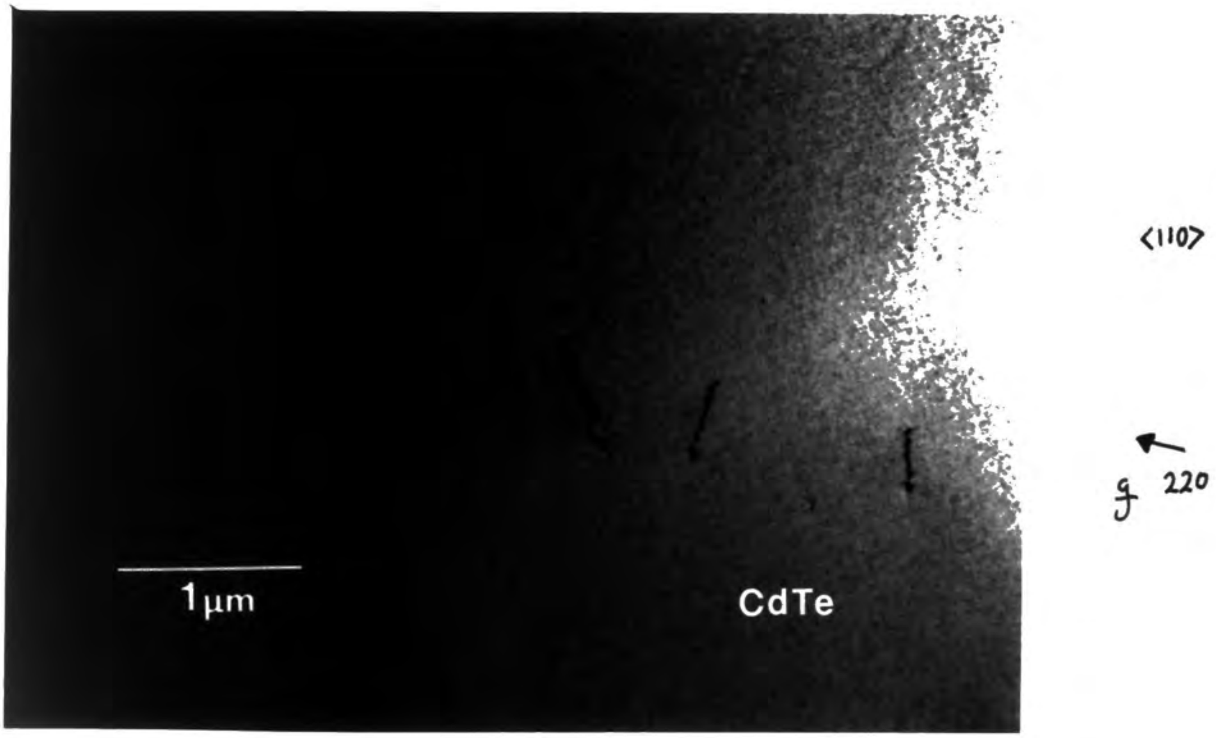

Figure 2.11 Low angle tilt boundary in iodine milled CdTe.

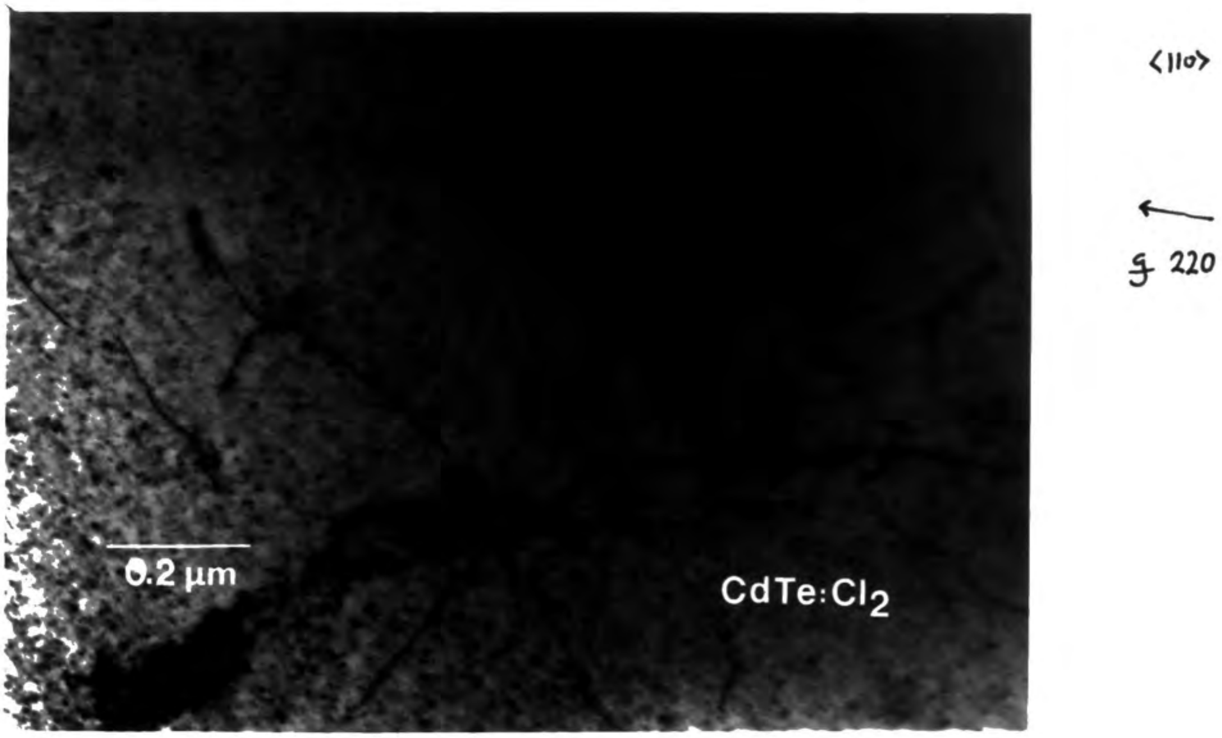

Figure 2.12 Sub-grain boundary and dislocations in CdTe:Cl_2.

orientations. For the beam incident along a $< 110 >$ direction, it can be shown that the twin reciprocal lattice points either coincide with existing matrix reciprocal lattice points or are displaced by vectors of $\pm\frac{1}{3} < 111 >$.[66] The presence of just one twinning axis in figure 2.10b indicates that twinning occurs on just one $\{111\}$ plane.

In addition to the occasional dislocation found in bulk grown CdTe, there was also the occasional observation of a sub-grain boundary as shown in figure 2.11. This defect is comprised of a loose disloction array which separates two regions of crystal which are mis-oriented by a very low angle ($< 1^o$). No precipitates were encountered in any of the systems examined during the course of this study.

For comparison the defect structure of a chlorine doped CdTe sample was also investigated. As shown in figure 2.12 the sample was characterised by a heavy dislocation content and many complex sub-grain boundaries were also observed. This defect microstructure is similar to that found in Zn doped CdTe.[5]

2.6 Summary

Descriptions of the bulk growth of CdTe from the vapour phase, and the epitaxial growth of MCT by MOVPE, MBE and LPE have been given. The technique used to prepare epitaxial layers for observation in cross-section in the electron microscope has also been described. Argon ion milling of II-VI compounds acts to produce extreme amounts of damage, and in particular large numbers of dislocation loops. Under severe milling conditions these defects interact to form dislocations, interstitial dislocation loops and intrinsic stacking faults. Considerable improvement to the sample preparation process has been achieved by the use of iodine reactive ion sputtering. The adoption of moderate milling conditions allows the preparation of sample foils with a greatly reduced artefactual defect content. The preferential attack of dislocations in MCT, which is either due to the associated strain field around such defects, or due to the attack of small precipitates located on the defects, is still a problem when using iodine sputtering at room temperature. It is likely that the use of a liquid nitrogen cooled sample stage would act to reduce or even eliminate these artefacts. Finally, the microstructural defect content of CdTe grown from the vapour phase has been shown to consist mainly of dislocations, sub-grain boundaries and twins.

REFERENCES

1. K. Zanio, Chapter 1, section 2, ' Crystal Growth' in *Semiconductor and Semimetals, Vol. 13*, Cadmium Telluride, ed. R.K. Willardson and A.C. Beer, Academic Press, New York, 1978
2. G.J. Russell, N.F. Thompson and J. Woods, *J. Crystal Growth* **71** (1985) 621
3. J.R. Cutter and J. Woods, *J. Crystal Growth* **47** (1979) 405
4. H. Hartmann, R. Mach and B. Selle, Section 4.2.1.2.1, Dissociative Sublimation, in *Current Topics in Materials Science, Vol. 9*, ed. E. Kaldis, pub. North Holland, 1982
5. K. Durose, *Structural Defects in CdTe*, Ph.D. thesis, Dunelm, 1986
6. D.E. Charlton, *J. Crystal Growth* **59** (1982) 98
7. H.M. Manasevit and W.I. Simpson, *J. Electrochem. Soc.* **118** (1971) 644
8. J.E. Hails and A.W. Brinkman, Proceedings of the U.K. II-VI Interaction Meeting - III, R.S.R.E., Malvern, Jan. 1986
9. J. Tunnicliffe, S.J.C. Irvine, O.D. Dosser and J.B. Mullin, *J. Crystal Growth* **68** (1984) 245
10. S.J.C. Irvine, J. Tunnicliffe and J.B. Mullin, *Materials Letters* **2** (1984) 305
11. S.J.C. Irvine, J. Tunnicliffe and J.B. Mullin, *J. Crystal Growth* **65** (1983) 479
12. P.L. Anderson, *J. Vacuum Sci. Technol* **A4** (1986) 2162
13. M.A. Herman and M. Pessa, *J. Appl. Phys.* **57** (1985) 2671
14. I.-R. Liaw, K.-S. Chou and M.-S. Lin, *J. Crystal Growth* **87** (1988) 529
15. P. Clifton, private communication
16. D.V. Shenai-Khatkhate, P. Webb and D.J. Cole-Hamilton, Proceedings of the U.K. II-VI Interaction Meeting - V, Southampton University, Sept. 1987
17. J. Thompson, P. Mackett, L.M. Smith, D.J. Cole-Hamilton and D.V. Shenai-Khatkhate, *J. Crystal Growth* **86** (1988) 233
18. J.D. Parsons and L.S. Lichtmann, *J. Crystal Growth* **86** (1988) 222
19. C.-H. Wang, P.-Y. Lu and L.M. Williams, *Appl. Phys. Lett.* **48** (1986) 1085

20. S.J.C. Irvine, J.B. Mullin and J. Tunnicliffe, *J. Crystal Growth* **68** (1984) 188

21. S.J.C. Irvine, J.B. Mullin, H. Hill, G.T. Brown and S.J. Barnett, *J. Crystal Growth* **86** (1988) 188

22. B.J. Morris, *Appl. Phys. Lett.* **48** (1986) 867

23. J.E. Jenson, P.D. Brewer, G.L. Olson, L.W. Tutt and J.J. Zinck, *J. Vacuum Sci. Technol.* **A6** (1988) 2808

24. J.B. Mullin, S.J.C. Irvine, J. Giess and A. Royle, *J. Crystal Growth* **72** (1985) 1

25. P.J. Wright, R.J.M. Griffiths and B. Cockayne, *J. Crystal Growth* **66** (1984) 26

26. H. Mitsuhashi, I. Mitsuishi, M. Mizuta and H. Kukimoto, *Japan J. Appl. Phys.* **24** (1985) L578

27. A.Y. Cho and J.R. Arthur, *Progress in Solid-State Chemistry* **10** (1975) 157

28. J.T. Cheung, G. Niizawa, J. Moyle, N.P. Ong, B.M. Paine and T. Vreeland, Jr., *J. Vacuum Sci. Technol.* **A4** (1986) 2086

29. S. Hwang, R.L. Harper, K.A. Harris, N.C. Giles, R.N. Bicknell, J.W. Cook, Jr. and J.F. Schetzina, *J. Vacuum Sci. Technol.* **A6** (1988) 2821

30. R.D. Feldman, S. Nakahara, R.F. Austin, T. Boone, R.L. Opila and A.S. Wynn, *Appl. Phys. Lett.* **51** (1987) 1239

31. K.A. Harris, S. Hwang, D.K. Blanks, J.W. Cook, Jr., J.F. Schetzina and N. Otsuka, *J. Vacuum Sci. Technol.* **A4** (1986) 2061

32. J.P. Faurie, A. Million, R. Boch and J.L. Tissot, *J. Vacuum Sci. Technol.* **A1** (1983) 1593

33. J.A. Mroczkowski and H.R. Vydyanath, *J. Electrochem. Soc.* **128** (1981) 655

34. C.C. Wang, S.H. Shin, M. Chu, M. Lanir and A.H.B. Vanderwyck, *J. Electrochem. Soc.* **127** (1980) 175

35. E.A. Irene, E. Tierney, H. Wiedemeier and D. Chandra, *Appl. Phys. Lett.* **42** (1983) 710

36. C. Cohen-Solal, M. Barbe, H. Afifi and G. Neu, *J. Crystal Growth* **72** (1985) 512

37. D.B. Holt, R. Porter and B.A. Unvala, *J. Sci. Instrum.* **43** (1966) 371

38. J.L. Hutchison, *Inst. Phys. Conf. Ser.* **No.87** (1987) 1

39. J. Fletcher, J.M. Titchmarsh and G.R. Booker, *Inst. Phys. Conf. Ser.* **No.52** (1980) 153

40. H.R. Pettit and G.R. Booker, *Proceedings of the 25th Anniversary Meeting of EMAG, Inst. Phys. Conf. Ser.* **10** (1971) 290

41. The bi-annual Microscopy of Semiconducting Materials Conference (1981, 83, 85 and 87), held in Oxford, and Published in the Institute of Physics Conference Series (Nos. 60, 67, 76 and 87 respectively)

42. N.G. Chew and A.G. Cullis, *Ultramicroscopy* **23** (1987) 175

43. A.G. Cullis, N.G. Chew and J.L. Hutchison, *Ultramicroscopy* **17** (1985) 203

44. M. Lunn and P. Dobson, Proceedings of the II-VI Interaction Meeting - III, R.S.R.E., Malvern, Jan. 1986

45. N.G. Chew and A.G. Cullis, *Inst. Phys. Conf. Ser.* **No. 78** (1985) 143

46. N.G. Chew, private communication

47. D.J. Barber, *Proceedings of the 5th European Congress on Electron Microscopy* (1972) 293

48. D.L. Flamm, V.M. Donnelly and D.E. Ibbotson, *J. Vacuum Sci. Technol.* **B1** (1983) 23

49. G.R. Booker, *Inst. Phys. Conf. Ser.* **No. 76** (1985) 201

50. N.G. Chew and A.G. Cullis, *Appl. Phys. Lett.* **44** (1984) 142

51. P.B. Hirsch, A. Howie, R.B. Nicholson, D.W. Pashley and M.J. Whelan, *Electron Microscopy of Thin Crystals*, pub. Butterworths, London, 1965

52. M.H. Loretto and R.E. Smallman, *Defect Analysis in Electron Microscopy*, pub. Chapman and Hall, London, 1975

53. M.H. Loretto, *Electron Beam Analysis of Materials*, pub. Chapman and Hall, London, 1984

54. Techniques for Electron Microscopy, ed. D.H. Kay, pub. Blackwell, 1965

55. International symposium on dislocations in tetrahedrally coordinated semiconductors, Hunfeld, FRG, *Journal de Physique* **C6** (1979)

56. S. Takeuchi, K. Suzuki, K. Maeda and H. Iwanaga, *Phil. Mag.* **A50** (1984) 171

57. P.B. Hirsch, P. Pirouz, S.G. Roberts and P.D. Warren, *Phil. Mag.* **52** (1985) 759

58. A. Howie and U. Valdrè, *Phil. Mag.* **8** (1963) 1981

59. G.P. Carey, S. Cole, T. Yamashita, J.A. Silberman, W.E. Spicer and J.A. Wilson, *J. Vacuum Sci. Technol.* **A3** (1985) 255

60. M.A. Lunn and P.S. Dobson, *J. Crystal Growth* **73** (1985) 379

61. H. Ryssal, G. Lang, J.P. Biersack, K. Muller and W. Kruger, *IEEE Trans. on Electron Devices* **Vol. ED-27 No. 1** (1980) 58

62. T. Yoshiie, H. Iwanaga, N. Shibata, K. Suzuki, M. Ichihara and S. Takeuchi, *Phil. Mag.* **47** (1983) 315

63. A.M. Gue and A. Mazel, *J. Crystal Growth* **72** (1985) 210

64. H.F. Schaake, *J. Vacuum Sci. Technol.* **A4** (1986) 2174

65. A.-B. Chen, A. Sher and W.E. Spicer, *J. Vacuum Sci. Technol.* **A1** (1983) 1674

66. D.W. Pashley and M.J. Stowell, *Phil. Mag.* **8** (1963) 1605

3. Polarity and the Sphalerite Structure

The polarity determination of CdTe: Warekois vs Fewster

3.1 Introduction

Non-centrosymmetric (polar) materials often exhibit macroscopic features, such as etch figures or surface facets, which reflect the anisotropy of the material microstructure (see the review by D.B. Holt[1]). Indeed, the non-equivalence of orthogonal $< 110 >$ directions in bulk sphalerite materials is illustrated, for example, by differences in specimen cleaving ,[2] dislocation formation[3] and by the differential motion of α and β dislocations.[4] Hence, there may be consequences for the epitaxial growth of sphalerite materials as evidenced by the orthogonal cracking of thin films of InGaP/$\{100\}$GaAs[5] and by problems with device fabrication.[6-8] It is therefore apparent that a reliable technique for the precise determination of crystal orientation is required in order to fully characterise bulk and epitaxial thin films of sphalerite materials. The purpose of this chapter is to present a precise, structural description of sphalerite and to show how the polarity of bulk and thin film material can be unambiguously determined using the combined techniques of etching and microdiffraction.

In section 3.2, the sphalerite structure is described in terms of its conventional space lattice and the reciprocal lattice. A description of the microdiffraction experimental technique and the procedure for microscope image rotation calibration are presented in sections 3.3 and 3.4 respectively. Sections 3.5 and 3.6 are concerned with the chemical etching and polarity determination of GaAs and CdTe and a review of the conflicting results for the polarity determination of CdTe is given in section 3.7. Finally, microdiffraction is used to determine CdTe crystal polarity in section 3.8, and the discrepancies in the literature are resolved.

3.2 The Sphalerite Structure

There are a number of models which are commonly employed to describe the sphalerite system. However, the opposite indexing systems proposed by Gatos[9] and Dewald[10] have led to considerable confusion over polarity in the literature.[1] All the models presented here are indexed in accordance with the more commonly used convention of Gatos.

Adamantine (diamond-like) semiconducting compounds are of the form of the characteristic space lattice shown in figure 3.1a. The 2-d projection of this model and the lattice unit cell are shown in figures 3.1b and 3.1c respectively. Following the polar sign convention,[1] 'AB' atom pairs are sited at points in the space lattice, with the lower valence 'A' element (open circles) located at the origin and the 'B' atom placed on the $(\frac{1}{4}\frac{1}{4}\frac{1}{4})$ position of the unit cell, for example (figure 3.1c). The $[111]_a$ direction taken from A to B is in the direction of a (111)A surface of triply bonded A-type atoms as indicated in figure 3.1b.

The two sets of four non-equivalent $\{111\}$ planes associated with the sphalerite structure may be illustrated by two Thompson tetrahedra (figures 3.2a and 3.2b). The A-planes are indexed as (111), $(\bar{1}1\bar{1})$, $(\bar{1}\bar{1}1)$ and $(1\bar{1}\bar{1})$, and the B-planes as $(\bar{1}\bar{1}\bar{1})$, $(\bar{1}11)$, $(1\bar{1}1)$ and $(11\bar{1})$. Each $\{111\}$ plane is in the sense of the corresponding $< 111 >$ direction drawn from the origin through each plane. Consideration of the Thompson tetrahedra in relation to the (001) growth plane indicates that there is a difference in the crystallography of the sphalerite structure when observed along the two orthogonal [110] and $[1\bar{1}0]$ directions.[5] [11] These are characterised by 'advancing' $\{\bar{1}\bar{1}\bar{1}\}$B and $\{111\}$A planes respectively. 'Advancing' in this case refers to those $\{111\}$ planes having a component of growth in the [001] direction. In figure 3.2b, these are the $(\bar{1}11)$B and $(1\bar{1}1)$B planes, and in figure 3.2a they are (111)A and $(\bar{1}\bar{1}1)$A. These figures show that only one type of advancing $\{111\}$ plane may be observed for each $< 110 >$ direction in the plane of the (001) layer.

Confirmation of this indexing system was obtained by Brongersma and Mul[12] using Ion Scattering Spectroscopy. These workers indexed the opposite polar faces of sphalerite ZnS by use of the anomalous absorption of X-rays and these measurements were correlated with chemical etching.[13,14] The polar faces were then mass analysed by the determination of the incident ion energy loss following backscattering at an atomically clean surface in ultra-high vacuum. The $\{111\}$A face of ZnS was found to be composed mainly of zinc, and an excess of sulphur was found on the $\{\bar{1}\bar{1}\bar{1}\}$B face, thereby giving credence to the indexing system used.

The reciprocal lattice

The reciprocal lattice shown in figure 3.3 is geometrically related to the face centred cubic space lattice. The origin of the two models (figures 3.1c and 3.3) is coincident, and the right handed set of axes x,y,z map to x',y',z'. The reciprocal lattice may be

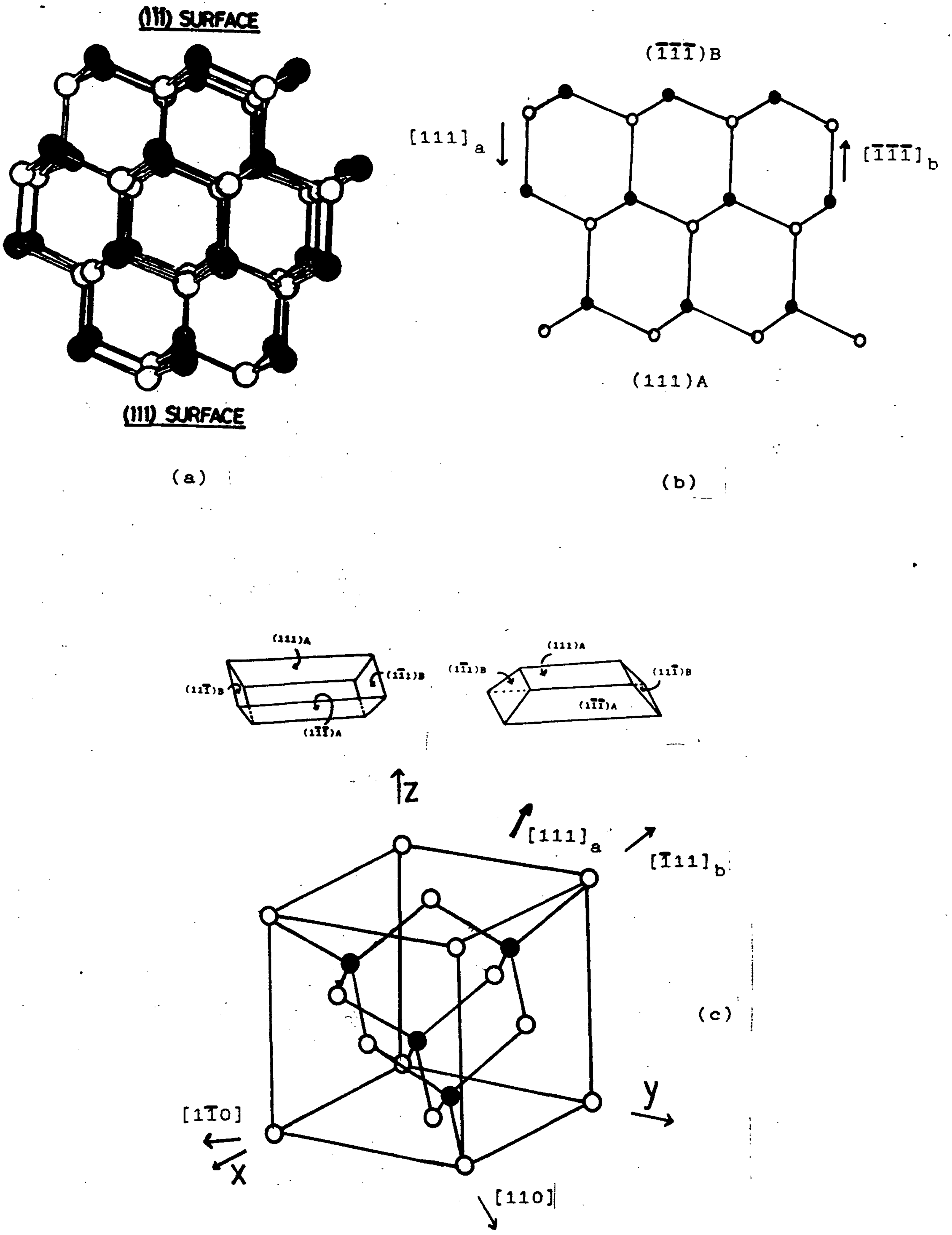

(a)

(b)

(c)

Figure 3.1 The sphalerite structure: a) 3-dimensions, b) 2-dimensions, showing a <110> projection and c) the unit cell.

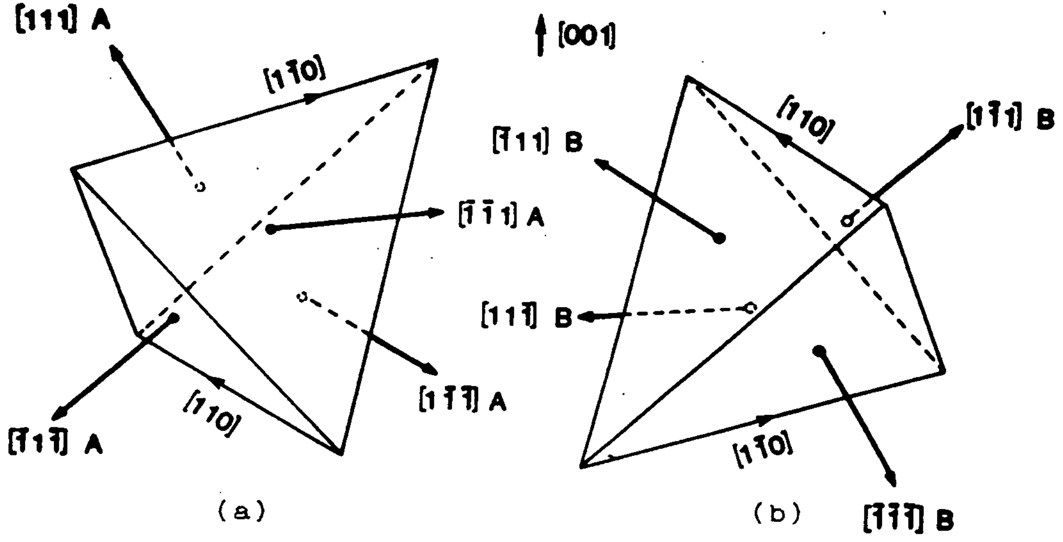

(a) (b)

Figure 3.2 Thompson tetrahedra bounded by a) {111}A planes b) $\{\bar{1}\bar{1}\bar{1}\}$B planes.

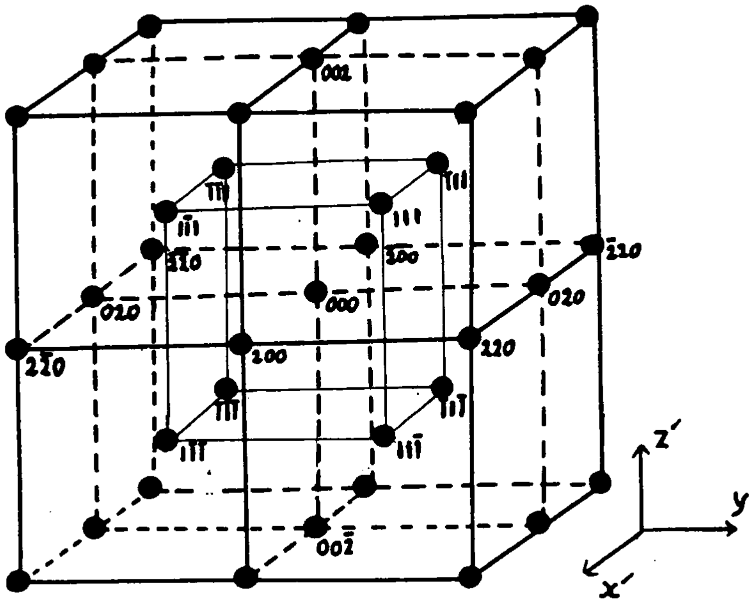

Figure 3.3 fcc reciprocal lattice.

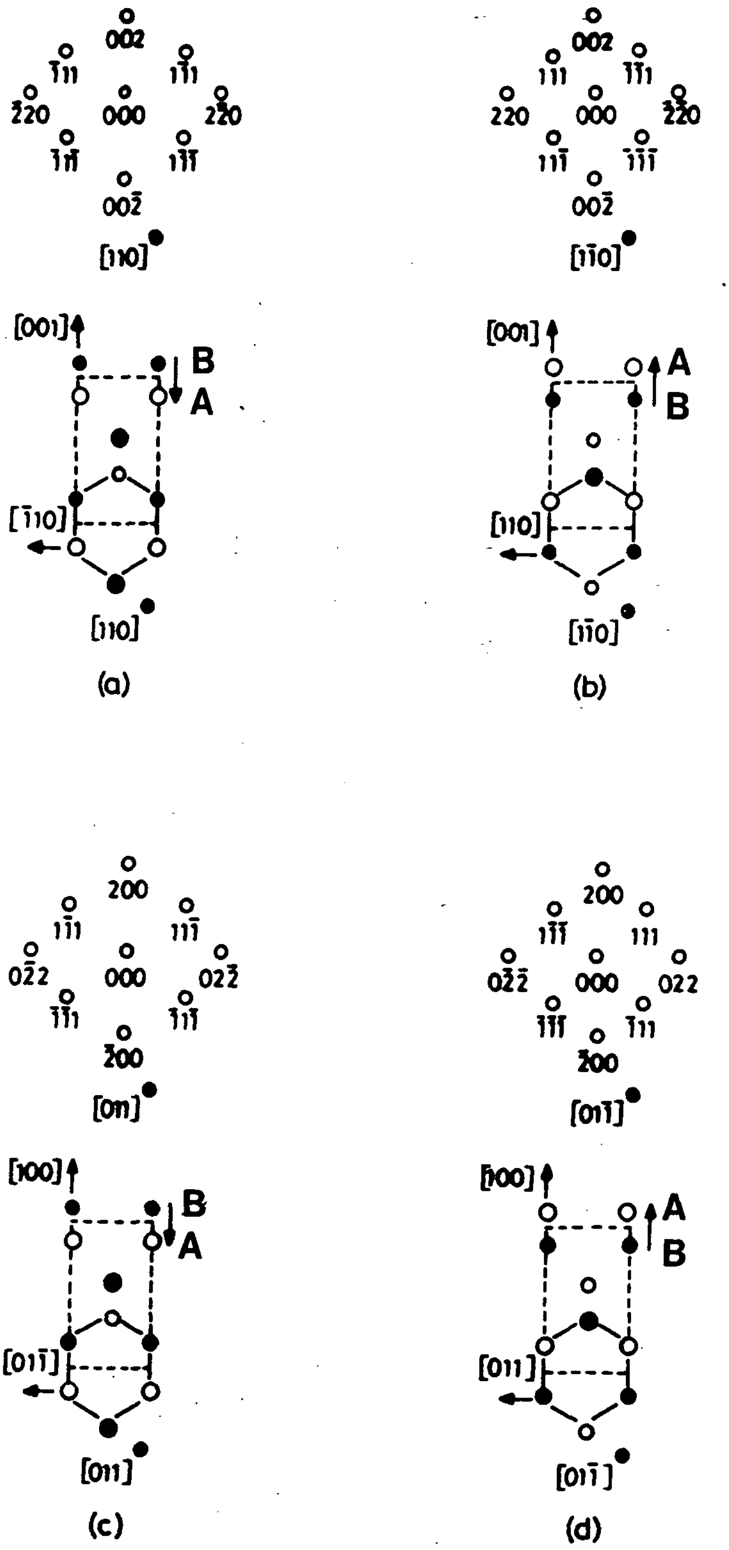

<u>Figure 3.4</u> Sphalerite space lattice and reciprocal lattice projections a) [110] b) [1$\bar{1}$0] c) [011] and d) [01$\bar{1}$]
The figures are indexed for an electron beam direction down into the page.

constructed by drawing points at a distance $\frac{1}{d}$ from the origin in a direction perpendicular to crystal planes of spacing d and each diffracting vector is in the same sense as its associated set of diffracting planes. The resultant array of points forms a body centred cubic structure of edge $\frac{2}{a_o}$ in the case of a face centred unit cell of lattice parameter a_o.

Several $< 110 >$ projections of this reciprocal lattice which correspond to the diffraction patterns commonly imaged on the microscope screen are compared with their respective space lattice projections in figures 3.4a to 3.4d. Reference to these diagrams will be made later when interpreting the data obtained using the microdiffraction technique.

The structure factor

The kinematical structure factor for a crystal is given by;

$$\Phi(hkl) = \sum_n f_n(\theta) e^{2\pi i(hu_n + kv_n + lw_n)} \qquad (3.1)$$

This expression represents the relative intensities of the reciprocal lattice points and may be used to predict the relative intensities of diffracted beams at the exact Bragg position. '$f(\theta)$' represents the atomic scattering amplitudes, while u_n, v_n, w_n are atom fractional coordinates. For certain reciprocal lattice points the structure factor will be zero, due to crystal symmetry, and no Bragg reflection will occur. For the face centred cubic structure it can be shown that the *hkl* indices must be all odd or all even, otherwise the structure factor is zero and the reflection is absent. From simple kinematical considerations, the amplitudes of the diffraction points are determined by the crystal structure, while their positions are determined by lattice geometry. This situation is, however, complicated for the more general case where dynamical effects and double diffraction lead to the appearance of weak spots in the positions of forbidden reflections.

The Ewald sphere construction

The diffraction pattern produced by a crystal may be predicted using the Ewald sphere construction. A sphere, centre C, of radius $\frac{1}{\lambda}$ (along the direction of the incident electron beam) is drawn through the origin of the reciprocal lattice (figure 3.5a). A diffracted beam will occur whenever the Bragg condition is satisfied, corresponding to the intersection of the reciprocal lattice point, P, by the sphere surface. The reflection

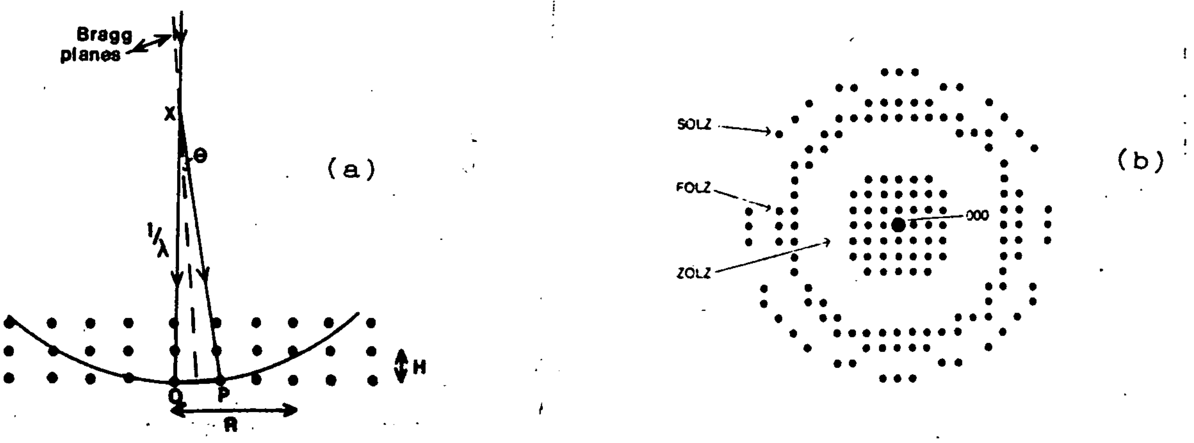

Figure 3.5 a) The Ewald sphere construction. Chapter 2, ref [53]. b) High Order Laue Zones.

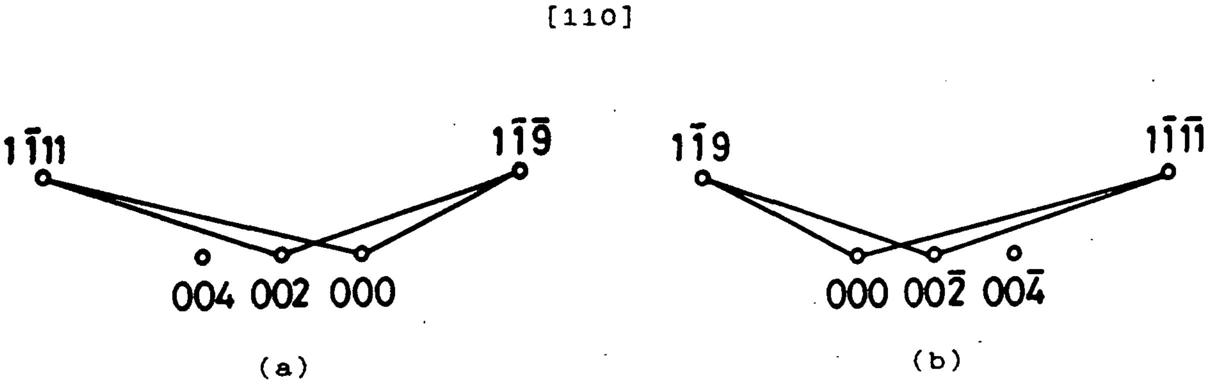

Figure 3.6 The interaction of doubly diffracted {9 1 1} and {11 1 1} reflections with directly scattered {200} beams. For a [110] projection; a) the (002) reflection exhibits constructive interference and b) the $(00\bar{2})$ reflection exhibits destructive interference.

sphere has a typical radius of about 25Å^{-1} (for 100kV electrons) as compared with a value of 1 to 2 Å^{-1} for the separation between reciprocal lattice points. Also, reciprocal lattice points are elongated into spikes for a thin crystal due to a relaxation of one of the Laue equations. Hence, the diffraction pattern produced for a low index zone axis is usually of the form as shown in figure 3.5b. The diffraction spots lie within circular bands, termed HOLZ (higher order Laue zones) lines.

3.3 Microdiffraction

For most cases of electron diffraction there is no difference in the intensities of beams scattered by hkl and $\bar{h}\bar{k}\bar{l}$ planes. This indeterminancy is known as Friedel's law. It is possible, however, to use the technique of microdiffraction (or Convergent Beam Electron Diffraction (CBED)), coupled with a breakdown in Friedel's law to determine sphalerite crystal polarity.[15,16] The interaction of the doubly diffracted high order, odd index $\{9\ 1\ 1\}$ and $\{11\ 1\ 1\}$ beams with a directly scattered $\{200\}$ reflection,[17] gives rise to either constructive or destructive interference through the $\{200\}$ disc,[17] when all the reflections are close to the Bragg position (figures 3.6a and 3.6b). The microdiffraction technique is fairly independent of foil thickness and allows the qualitative interpretation of results to determine crystal polarity. Structure factor phase relationships, polarity and the ionicity of GaAs,[15] [16] [17] [18] ZnSe,[15] ZnS[15] and CdTe[19] have been determined using this technique. Although, G. Lu and Cockayne[19] note that the technique is only appropriate for use with compounds containing elements of similar scattering amplitudes.

It becomes necessary to consider the dynamical equations of electron diffraction to predict which $\{200\}$ reflections exhibit these constructive and destructive interference effects. This then allows the unambiguous determination of sphalerite crystal polarity to be made without reference to any other experimental technique. A complete description of the interaction of an electron beam with a crystal lattice is a complex mathematical problem and so it is not proposed to consider this at length. It is, however, appropriate to introduce some of the basic principles of the dynamical theory of electron diffraction in order to illustrate how the microdiffraction technique can be used to determine sphalerite crystal polarity.

Electron scattering by a thin crystal

In general terms, the description of electron scattering by a thin crystal has been approached in two fundamentally different ways. The Schroedinger equation may be solved using either Bloch functions[20] or perturbation theory.[21] Alternatively there are integral equation formulations such as the 'physical optics' theory of Cowley and Moodie,[22] which assumes that a wavelength may be associated with a monoenergetic electron beam and then applies Huygens principle to the (scattered) electron waves. Both approaches to this problem give consistent results.[22]

The many beam dynamical theory of electron diffraction by a thin crystal may be used to predict the intensities of electron diffraction patterns and the contrast in conventional images. Simplification of this theory leads to the kinematic description of two beam interactions, where just one diffracted beam is at the exact Bragg position.

The n-beam polynomial predicted by the integral equation treatment may be represented by the very generalised equation:-

$$U(h) = \sum_{n=1}^{\infty} E_n(h) Z_n(h) \tag{3.2}$$

where $U(h)$ is the complex amplitude of a reflection (h), $E_n(h)$ is an operator which represents all summations and multiplications by all the complex structure factors $F_n(hkl)$, and $Z_n(h)$ is a function involving only geometric factors (including excitation errors). Taftø and Spence[15] suggested that this n-beam scattering polynomial can be interpreted using quasi-kinematical concepts if all the excitation errors are set to zero. A more detailed representation of equation 3.2, suggested by Ishizuka and Taftø,[16] is given in the Appendix. Expressions for the dynamical diffraction amplitudes of (200) and ($\bar{2}$00) reflections, for the [011] zone axis, are obtained and the kinematical structure factors of the contributing {9 1 1}, {11 1 1} and {200} reflections determined, indexed in accordance with the Gatos convention.[15] Inspection of the diffraction amplitudes demonstrates that the ($\bar{2}$00) reflection is π out of phase with the doubly diffracted beams, giving rise to destructive interference through this reflection. In contrast the (200) reflection is in phase with the doubly diffracted beams, thereby resulting in constructive interference.

Similarly, it may be demonstrated for the [110] zone axis that constructive and destructive interference occurs through the (002) and (00$\bar{2}$) reflections respectively. While for the orthogonal [1$\bar{1}$0] projection the interference effect is reversed such that the (00$\bar{2}$) and (002) reflections exhibit constructive and destructive interference. In more general terms, for a < 110 > projection, the deficiency black cross through a {200} reflection is always in the sense of the cation to anion, as shown in figures 3.4a to 3.4d (corresponding to the dumbells seen in high resolution lattice images[17]), and is always associated with the sense of advancing {111}A planes. Once the sense (*i.e.* polarity) of advancing planes in bulk or epitaxial material has been established, it then becomes possible to assign the zone axis as either [110] or [1$\bar{1}$0] given a free choice of the growth surface (*e.g.* an (001) epitaxial growth plane).

Microdiffraction:- experimental procedure

The microdiffraction technique has the advantage that only small ($\lesssim 1\mu$m diameter) areas of the specimen foil are sampled. Using a conventional electron microscope, a small electron beam size is selected and focussed using the condensor lens. A thin, fairly uniform region of material can then be brought into the field of view and preferably should be defined using a field limiting aperture. The diffraction mode is then selected and the camera length reduced to its minimum value (20cm for the case of a JEOL 100CX). The required experimental conditions of just {200}, {9 1 1} and {11 1 1} reflections in bright contrast are obtained by tilting the crystal roughly 10^o off the [110] zone axis along the (002) Kikuchi band, for example. Both constructive (bright) lines and destructive (dark) lines through {200} reflections can routinely be seen on the microscope screen and optimum conditions may be obtained by using a freshly prepared sample. The diffraction contrast effect is dependent to a certain extent on sample thickness.[16] Movement of the sample wedge, however, combined with specimen tilting usually enables representative patterns to be obtained. The microdiffraction technique is equally applicable to substrate as well as epitaxial material, provided sufficiently uniform foils are obtained and hence, may be readily used to determine the polarity of the substrate surface used for epitaxial growth, for example.

Although the condition of constructive interference was relatively easy to demonstrate on the microscope screen, considerable difficulty was encountered while trying to obtain micrographs illustrating this effect. An alternative approach to this problem is to consider the interaction of different high order reflections with the same {200} type reflections. Starting with the {9 1 1} and {11 1 1} reflections at the Bragg position, a very small tilt of the sample along the {200} Kikuchi band either towards or away from the $< 110 >$ zone axis, brings the {9 3 1}, {7 3 1} or {9 5 1}, {7 5 1} pairs of reflections into bright contrast respectively (see the Appendix). It can be shown that the {9 5 1}, {7 5 1} pair of reflections give rise to destructive interference through the {200} reflection which exhibits constructive interference for the {9 1 1}, {11 1 1} situation.

These microdiffraction patterns are absolute in their nature, *i.e.* they exhibit interference effects which are directly sensitive to crystal polarity. However, before these patterns can be applied to a particular crystal system, it is first necessary to correct for the effects of image rotation introduced by the electron microscope.

3.4 Image Rotation Calibration

To correct for the effects of image rotation it is first necessary to consider the image forming system of the microscope. In a JEOL 100CX electron microscope this consists of an objective lens, two intermediate lenses and a projector lens which are used to focus on the lower surface of a specimen, thereby producing a conventional image (figure 3.7a), or to focus on the back focal plane of the objective lens where the sample diffraction pattern is formed (figure 3.7b). The difference in lens currents for the two imaging conditions leads to a rotation between an image and its associated diffraction pattern when viewed on the microscope phosphor screen. This rotation, which varies with lens strength and hence lens current, results in an increase in relative rotation with image magnification. In addition, there is a further rotation of 180^o between the image and diffraction pattern caused by the objective lens. As shown in figure 3.7c, the objective lens produces an inversion between a specimen and the first intermediate image, while the diffraction pattern formed is such that each diffracting vector is in the same sense as the diffracting planes (figures 3.7b and 3.7d). It is therefore necessary to calibrate this rotational relationship between image and diffraction pattern for specimen polarity to be unambiguously determined. This may conveniently be done using pseudo-orthorhombic platelets of MoO_3 which grow with a long straight edge perpendicular to the [100] direction.[23]

Crystals of MoO_3 were obtained by heating $(NH_4)_6Mo_7O_{24}.4H_2O$ crystals in a boiling tube with a strong bunsen flame. The initial evolution of ammonia and water vapour

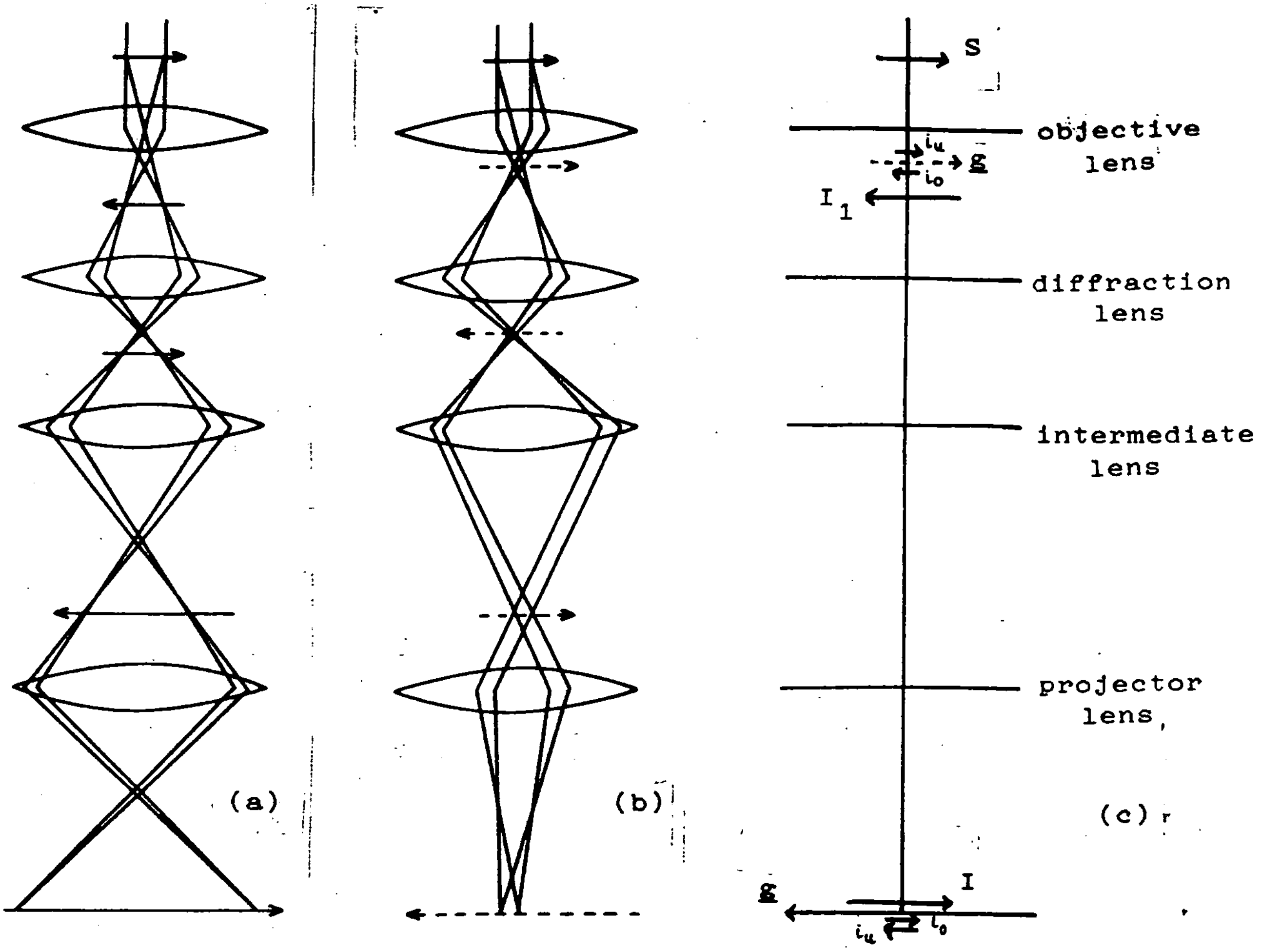

Figure 3.7 Schematic ray diagram to illustrate the formation of a) an image and b) a diffraction pattern in an electron microscope. c) Underfocussing the diffraction pattern allows the observation of the image i_u on the microscope screen. (The figure assumes all the image forming lens are in operation.)

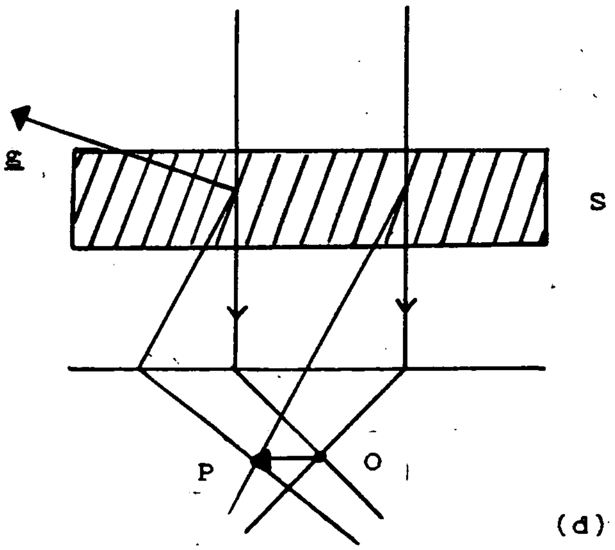

Figure 3.7d The diffraction vector **g** is in the same sense as the diffracting planes and hence, there is no inversion of first diffraction pattern with respect to the specimen.

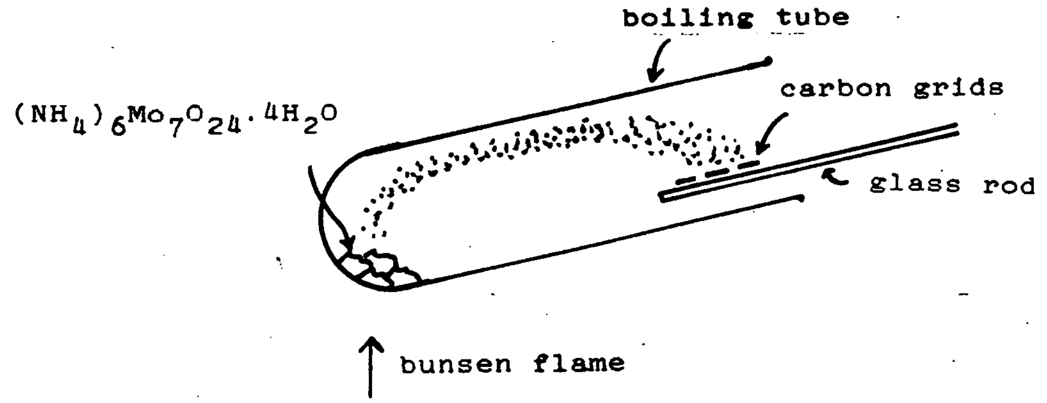

Figure 3.8 Preparation of MoO_3 crystals

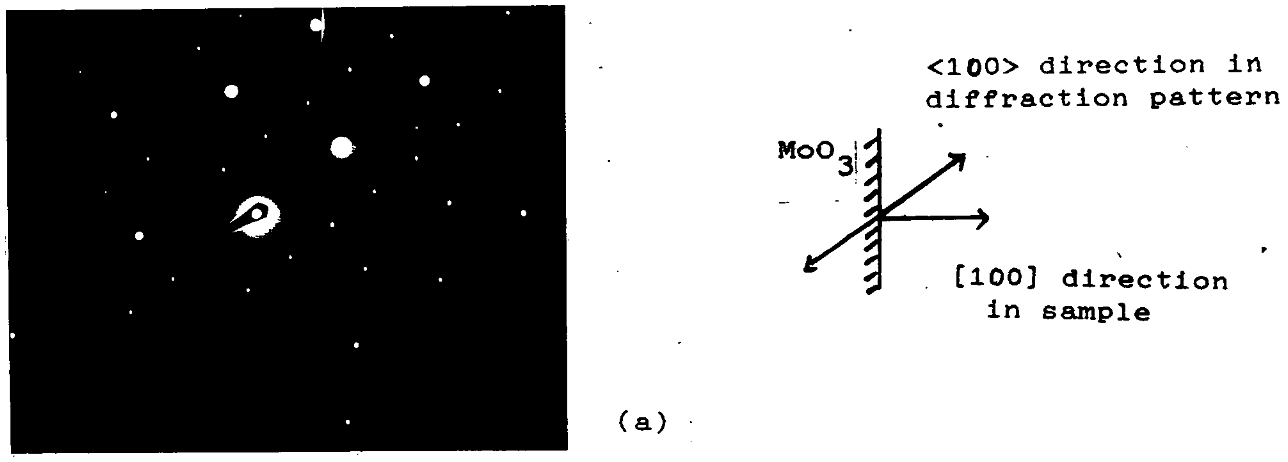

Figure 3.9a Image rotation calibration:- Micrographs of a MoO_3 crystal, with increasing magnification, are superimposed on its associated SAD pattern.

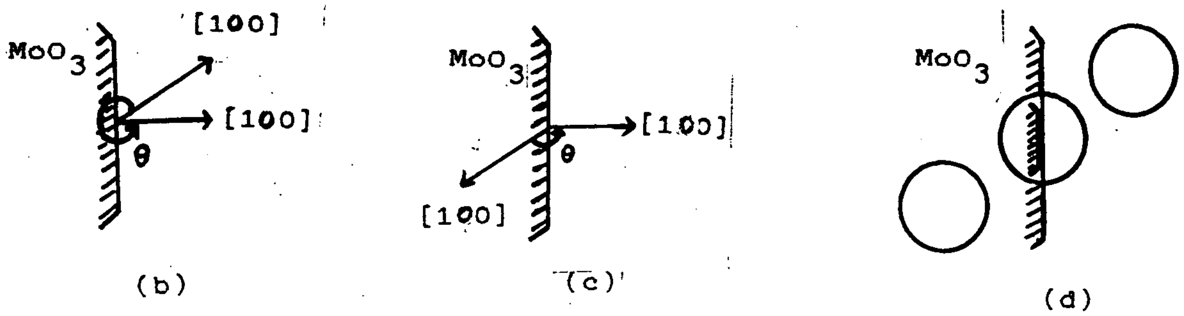

Figure 3.9b,c Due to the centro-symmetric nature of MoO_3 there is an uncertainty of 180° in the value of θ necessary to correct for image rotation. d) It is possible to precisely correct for the effects of image rotation by observation of the underfocussed diffraction pattern (see text).

was followed by the sublimation of MoO_3, particles of which were deposited onto carbon grids resting on a glass rod (figure 3.8). Observation in the electron microscope revealed the characteristic elongated MoO_3 platelets. A series of double exposure micrographs was taken for increasing magnification showing a long straight edge of a MoO_3 crystal superimposed on its diffraction pattern (figure 3.9a). All the negatives were printed with their emulsion facing upwards, which corresponds to the observation of the image on the microscope screen. The [100] direction in the electron diffraction pattern is that for the shorter spot separation.[23] The angle θ is defined as being the anticlockwise rotation of the diffraction pattern necessary to correct for image rotation (figures 3.9b and 3.9c), and this was tabulated against magnification.

Due to the centrosymmetric nature of MoO_3, there is an uncertainty when indexing the [100] and [$\bar{1}$00] directions. In addition, there is the initial 180^o rotation between the image and the diffraction pattern introduced by the objective lens. However, both these effects may be compensated for by the observation of out-of-focus diffraction patterns, using the procedure described by Loretto.[24] This experimental procedure indicates whether or not the initial 180^o rotation introduced by the objective lens is still present on the microscope screen for a given magnification. For example, comparison of the underfocussed diffraction pattern (obtained by decreasing the diffraction lens current), for which there is no inversion with respect to the first diffraction pattern formed (figure 3.7c), with the corresponding image formed at a magnification of 33,000 clearly indicates that there is no additional 180^o rotation on the microscope screen for these lens settings (figure 3.9d). Further, in view of the small angular rotation between image and diffraction pattern for this magnification setting, the [100] direction in the diffraction pattern must be in the same direction as the image normal (figure 3.9b), otherwise a 180^o rotation would have been seen on the microscope screen in the underfocussed diffraction pattern. Once the [100] direction in the MoO_3 crystal is ascertained, it then becomes possible to precisely calibrate the entire magnification range of the microscope for the effects of image rotation.

3.5 Etching and Polarity Determination:- GaAs

It is often possible to distinguish between the opposite polar faces of sphalerite materials by use of various chemical etches. This in isolation is insufficient for the absolute determination of polarity and it is necessary to correlate these etches with some independent polarity determination technique. The anomalous absorption of x-rays (XRD), first suggested by Coster et al[25] in 1930, was used by White and Roth[26] in 1959 to determine the absolute polarity of GaAs. Wavelengths just below the Ga and As absorption edges undergo an anomalous phase change when scattered by the Ga and As atoms respectively. This arises from the absorption of X-rays by the inner more closely bound electrons leading to a modification of the structure factor, which in turn leads to changes in the relative intensities of the diffracted beams from opposite polar faces. Care must be exercised, however, when using this technique, since the difference in integrated intensities is only of the order of 3% for GaAs.[27] White and Roth used an etchant consisting of 2:1:2 $HCl:HNO_3:H_2O$ and this was found to produce etch pits only on the $\{111\}$ Ga face, while the $\{\bar{1}\bar{1}\bar{1}\}$As face showed dark patches which are believed to be reaction products adhering to the sample surface.[28] This discriminatory etchant was later shown by Abrahams and Ekstrom[29] to be a dislocation etchant.

There are a number of reviews concerned with the chemical polishing[30] and etching[28] [31,32] of GaAs. Chemical polishing refers to the uniform bulk removal of surface material to leave a flat, shiny surface suitable for device fabrication, subsequent epitaxial growth or for the assessment of material defect content by chemical etching. Polishing procedures are usually used to remove work damaged material arising from cutting or mechanical polishing.

Chemical etching is simply the preferential removal of surface material and depends on the chemical activity of different crystallographic planes and hence sample orientation, and on the nature of the chemical etchant used. Chemical etching involves the transfer of electrons between the material surface and the chemical components of the etch. A common process is that of material oxidation by one component of the etch followed by oxide dissolution by a different chemical species, or complex formation. HNO_3, H_2O_2 and Br_2 are oxidising agents, for example, while HF is a complexing agent. The dissolution rate is usually a diffusion controlled process (*i.e.* is dependent on the arrival rate of the various chemical species at the sample surface). At low temperatures, chemical etching may become a reaction rate controlled process.[33] Etch pits usually initiate at surface heterogeneities and hence, chemical etches may be used to reveal imperfections in semiconducting materials, such as dislocations, precipitates, twin boundaries and grain boundaries. If a feature etches faster than the surrounding matrix, then an etch pit appears. Similarly, if a feature etches more slowly than the surrounding matrix, then an etch hillock is produced.[34] These processes result from strain fields introduced into the material by the imperfections concerned, or by surface oxides and poisoning effects which inhibit the localised action of an etchant. Hence, correct surface treatment is often required before the application of certain defect etchants for their successful operation. Not all defect etchants are sensitive to work damage and the Schell etch,[35] for example, may be used directly for the assessment of grown in material defect content.

Mention should be given to the chemical action of bromine in methanol[36] on GaAs. Highly polished surfaces are obtained on the $\{\bar{1}\bar{1}\bar{1}\}$As face using 0.05% Br_2/MeOH solution, while the $\{111\}$ Ga face is preferentially polished (*i.e.* produces an undulating surface[37]). The discriminatory action of this reagent was correlated with the XRD technique[26] by Sullivan and Kolb.[38] These workers[38] also reported that the $\{\bar{1}\bar{1}\bar{1}\}$As face etches about 30% faster than the $\{111\}$ Ga face.

A brief summary of etchants which can be used to differentiate between the opposite polar faces of GaAs is presented in Table 3.1. There is a common theme throughout the early etching studies of III-V semiconductors which is that the $\{111\}$A faces can be made to exhibit etch pits, while the $\{\bar{1}\bar{1}\bar{1}\}$B faces are chemically polished (see Table 3.1 and the references therein). This in turn led to the investigation of inhibitors which act to slow down the chemical polishing action and so reveal etch patterns on the $\{\bar{1}\bar{1}\bar{1}\}$B faces. It was found that the $\{111\}$ A faces tended to form shallow bottomed pits which with time resembled that of a polished face. See, for example, the work by Gatos and Lavine on InSb.[9] Also, Richards and Crocker[39] demonstrated that the action of Ag^+ ions in a solution of 1:3:0-4 HF:HNO_3:H_2O upon GaAs caused etch pits to appear on the $\{\bar{1}\bar{1}\bar{1}\}$As face while the $\{111\}$ Ga face was polished. Hence, it is apparent that care must be exercised when using chemical etchants to determine polarity in these materials.

As far as the author is aware, there are no other commonly recognised references in the international literature concerning the polarity determination of GaAs using some other independent, 'absolute' polarity determination technique. There are, however, a few discriminatory experimental techniques which are routinely used to monitor the (MBE) growth of GaAs. MacRae,[46] for example, demonstrated how Low Energy Elec-

reference	chemical etch	action of etchants	
		{111}Ga	$\{\bar{1}\bar{1}\bar{1}\}$As
Schell[35]	1:2 $HNO_3:H_2O$	Δ etch pyramids	terraced pattern
Grabmaier[43]	1:1.5 $HNO_3:H_2O$		
Richards[39]	1:3 $HNO_3:H_2O$		
Kyser[40]	conc. HNO_3	etch pits	patches of As_2O_3
White[26]	2:1:2 $HCl:HNO_3:H_2O$	etch pits	dark patches
Richards[41]	1:2:5 $HF:H_2O_2:H_2O$	etch pits	terraced pattern
Richards[39]	1:1 to 2 $HF:H_2O_2$	polish	etch pits
Richards[39]	1:3:0 to 4 $HF:HNO_3:H_2O$ (+1% $AgNO_3$)		
Sirtl[49]	$HF:CrO_3:H_2O$	Δ etch pits	
Abrahams[42]	2ml H_2O:8mg $AgNO_3$: 1g CrO_3:1ml HF	Δ etch pits	circular pits
Sullivan[38]	0.05% Br_2:MeOH	preferential polish	polish
Iida[44]	3:1:1 $H_2SO_4:H_2O_2:H_2O$	etch pits	polish

Table 3.1 Polarity Sensitive Etches:- GaAs.

tron Diffraction (LEED) is sensitive to the different surface reconstructions which occur on the opposite polar faces of GaAs. Patterns characteristic of a (2×2) surface structure were obtained from the $\{111\}$ Ga face, while the $\{\bar{1}\bar{1}\bar{1}\}$As face exhibited a (3×3) structure. Also, Pretzer and Hagstrum[47] used the phenomenon of Auger neutralisation of slow noble gas ions to investigate the polar surfaces of GaAs. Measurements of the electron yield and kinetic energy distribution were again found to be sensitive to differences in the electron energy distributions on the opposite polar faces of this compound. In both cases, these workers[46] [47] rely on the use of chemical etchants, correlated in turn with some 'absolute' technique, to determine the crystal polarity.

When the (001) face of GaAs is etched in 0.25% Br$_2$/MeOH, etch pits elongated along the $[1\bar{1}0]$ direction are produced[48] (see figure 3.1c). Whereas, rectangular etch hillocks, also elongated along the $[1\bar{1}0]$ direction are produced by the Sirtl etch[49] [5] (see figure 3.1c). Olsen[5] etched the opposite $\{100\}$ faces of a GaAs wafer using the Sirtl etch and demonstrated that the rectangular etch hillocks were rotated by 90^o. It is argued that the longer exposed faces of these features are the more slowly etched $\{111\}$Ga planes. Gatos and Lavine[9][33] suggested that the $\{\bar{1}\bar{1}\bar{1}\}$As face will be more chemically reactive than the $\{111\}$ Ga face due to an extra pair of unshared electrons at each surface As atom. While this explanation has been invoked many times throughout the literature it only provides a qualitative explanation for these etch figures and is certainly not adequate for the absolute determination of crystal polarity. Holt[50] noted that this model ignores the effects of resonance where sharing of unpaired electrons with neighbouring bonds occurs. More recently it has been suggested that chemical activity is more strongly dependent on the method of surface preparation, rather than on the degree of saturation of dangling bonds.[51] Nevertheless, the reproducibility of such rectangular etch features provides a way of distinguishing between [110] and $[1\bar{1}0]$ directions in the (001) plane.

3.6 Etching and polarity determination:- CdTe*

It is now intended to present a review of the different experimental techniques which have been used to identify the opposite polar faces of CdTe, and to correlate them with the various etches capable of distinguishing facedness in this material. Throughout this discussion, a close packed layer terminating in Cd atoms will be referred to as the $\{111\}$ Cd face (A-face) and that terminated by Te atoms as the $\{\bar{1}\bar{1}\bar{1}\}$Te face (B-face), in accordance with the more commonly used convention of Gatos.[9]

Polarity sensitive experimental techniques are regarded as being either 'absolute' or 'discriminatory'. 'Absolute' techniques are capable of the unambiguous determination of crystal polarity without reference to any other experimental technique. Whereas 'discriminatory' techniques are sensitive to differences arising from the polar nature of sphalerite materials but need to be correlated with some other absolute technique for the purpose of polarity determination. The absolute experimental techniques used for the polarity determination of CdTe include XRD,[26] [13] [52] microdiffraction or CBED,[15] [16] [19] electron diffraction,[53,54] High Resolution Electron Microscopy (HREM),[55] Rutherford Back Scattering (RBS),[56] Auger Electron Spectroscopy (AES)[57,58] and X-ray Photoelectron Spectroscopy (XPS).[59] The category of discriminatory techniques includes wet chemical etching, LEED[60] and RHEED.[59] The absolute techniques suffer from the main disadvantage of generally being time consuming and difficult to set up. For the purpose of quick, routine polarity determination it is, therefore, necessary to correlate the action of reliable discriminatory chemical etchants with some absolute polarity determination technique.

The physical difference between the opposite polar faces of CdTe has long been recognised. In 1963, Teramoto and Inoue compared the growth rates of sublimated CdTe on the opposite polar faces of a CdTe crystal. Layers grown on the $\{111\}$ plane exhibited many ($\approx 10^5\mathrm{cm}^2$) triangular pyramids, while irregular growth hillocks terminated by flat plateaus were formed less frequently on the $\{\bar{1}\bar{1}\bar{1}\}$ plane. Crystal growth rates were higher in the $< 111 >$ direction than in the $< \bar{1}\bar{1}\bar{1} >$ direction, although it is noted that no statement was given to qualify their assignment of polarity.

⋆ The author would like to thank Dr. K. Durose, now at B. T. and D., Ipswich, for many useful discussions concerning the chemical etching of CdTe

Unlike GaAs, for which there is no uncertainty when distinguishing between the opposite polar faces, considerable confusion exists in the literature concerning the polarity determination of CdTe. The non-equivalence of opposite {111} planes in CdTe has been well documented[63] and it is commonly recognised that only one {111} face of CdTe is suitable for epitaxial growth.[53] [56] Homoepitaxial growth on one {111} face leads to the formation of smooth, shiny surface layers with a lamellae twin defect content lying parallel to the epilayer/substrate interface[64] (see section 5.3), while growth on the opposite polar face results in the formation of layers with a matt surface and a highly faulted defect structure.[65] Similarly, the heteroepitaxial growth of MCT results in a twinned grain structure on the former {111} face, while growth on the latter {111} face produces a faceted surface[65] (see section 5.4).

The first identification of the {111} Cd and $\{\bar{1}\bar{1}\bar{1}\}$Te faces of CdTe was made by Warekois et al[13] in 1962 using the XRD technique described by White and Roth[26] for GaAs. This result was correlated with the action of the discriminating etchant, 3:2:1 HF:H_2O_2:H_2O which, the authors concluded, produced pits on the $\{\bar{1}\bar{1}\bar{1}\}$Te face and nearly polished the {111} Cd face. This X-ray experiment was repeated in 1983 by Fewster and Whiffin[52] and correlated with the action of a similar etchant, 3:2:2 HF:H_2O_2:H_2O (after Nakagawa et al[66]), and the opposite result was obtained (*i.e.* that the {111} Cd face became pitted, while the $\{\bar{1}\bar{1}\bar{1}\}$Te face was polished). Consequently, there are two opposite conventions for the polarity determination of CdTe and this has led to considerable confusion in the international literature. Papers which do not cite the convention used for the discrimination of crystal polarity are commonly encountered, and there has only recently been a general consensus regarding which convention to use. The two etchants based on HF:H_2O_2:H_2O are dependable in their action and so the finding that the pitted face is $\{\bar{1}\bar{1}\bar{1}\}$Te and {111} Cd by Warekois and Fewster respectively must be due to a genuine difference in the X-ray results and not due to some curious property of the reagents in question. (Warekois also cites a 1:1 mixture of HF:HNO_3 as being capable of distinguishing the opposite polar faces of CdTe. Whereas Fewster reports that this etchant is ineffective.) Since the work of Fewster and Whiffin[52] there have been a number of publications, using a variety of absolute experimental techniques, which report conflicting polarity conventions for CdTe (see Table 3.2). While it is generally acknowledged that favourable epitaxial growth can only occur on one polar face of CdTe, there is still uncertainty in the international literature as to which {111} face this is and so, in order to fully characterise the defect microstructure formed in

reference	technique	reference	technique
Warekois[13] convention (1962)	XRD	Fewster[52] convention (1983)	XRD
G. Lu[19] (1986)	microdiffraction	Hsu[59] (1987)	XPS, RHEED
Kolodziejski[55] (1986)	HREM	Y.C. Lu[57,58] (1987)	AES
Di Cioccio[53] (1987)	electron diffraction, HREM	Chami[56] (1988)	RBS
		Hewat[54] (1988)	electron diffraction

Table 3.2 Absolute Techniques for the Polarity Determination of CdTe.

bulk and thin films of this compound, it is necessary to resolve this discrepancy.

Chemical etching of CdTe

The opposite polar faces of CdTe can be distinguished by the various chemical etchants listed in Table 3.3. It should be noted that the stated action of these reagents is that given by the respective authors of the references concerned.

The composition of the Nakagawa etch[66] is very similar to that reported by Warekois.[13] However, no mention is made in the Nakagawa reference as to how the discriminatory action of this etchant was determined, and it is therefore assumed that the designation was simply based on the original work of Warekois. This etchant has been shown to produce rounded triangular pits on one {111} face and to leave the opposite polar face unaffected.[66]

The Inoue reagents E-Ag1 and E-Ag2 are the most commonly cited etchants used with CdTe and are based on the the action of a solution of potassium dichromate acidified with nitric acid (E-solution) with varying Ag^+ content.[67,68] The attraction of the E-Ag1 reagent is that all surface orientations yield pit shapes which are clearly related to the orientation of the face investigated. In the first Inoue paper[67] it was shown how the pit shapes were governed by the intersection of tetrahedrons of {111} planes with the {111}, {110} and {100} surfaces and this result has been analysed in detail for the low index planes of CdTe by Y.-C. Lu[69] and Iwanaga[70] [71] and also for higher index (twin related) orientations by Durose[72] and Iwanaga.[73]

Inoue[67] states that the polarity discriminatory action of these etchants can be determined using the XRD technique described by White and Roth.[26] However, no data was presented to justify the assignment of their action upon the opposite {111} polar faces. In the second paper Inoue[68] demonstrated the ability of the two etchants to discriminate between α and β type dislocations and in the same work the pitting behaviour is correlated with Warekois' x-ray results via a private communication. Inoue's two papers indicate that, according to the Warekois convention, E-Ag1 develops small pyramidal pits on the {111} Cd surface and large flat bottomed pits on the $\{\bar{1}\bar{1}\bar{1}\}$Te surface. Y.-C. Lu et al,[69] Durose,[72] and Hewat et al[54] showed independently that the face pitted by $HF:H_2O_2:H_2O$ is the one which develops small pyramidal pits with E-Ag1. (Both Y.-C. Lu and Durose rely on the Fewster convention for their polarity assignment.) These papers serve to illustrate an important discrepancy in the literature;

reference	chemical etch	action of etchants (according to author) {111}Cd	 $\{\bar{1}\bar{1}\bar{1}\}$Te
Warekois[13] (1962)	3:2:1 $HF:H_2O_2:H_2O$	nearly polished	Δ pits
	1:1 $HCl:HNO_3$	Δ pits in a background of flat Δ etch features	film plus random distribution of etch features
Nakagawa$ (1979)* [66]	3:2:2 $HF:H_2O_2:H_2O$	polished	pitted
Bagai[74] (1984)£	4:0.5:2 $HF:H_2O_2:H_2O$	-	etch pits -deep pyramidal pits and shallow Δ pits
Inoue[67] (1962)*,$	E-Ag1	small Δ pyramidal pits	large Δ flat bottomed pits
	E-Ag2	no pits	shallow Δ pyramidal pits
Meyers[75] (1983)X	1:1:1 $HF:HNO_3$:Lactic	shiny pitted surface	dull black coating
Durose[72] (1986)£	1:1:1 $HF:HNO_3$:Acetic	matt black	shiny
Fewster[52] (1983)&	Nakagawa	pits	no pits
Y.C. Lu[69] (1984)£	E-Ag1	small Δ pyramidal pits	large Δ flat bottomed pits
Hewat[54] (1988)x	E-Ag2	small Δ flat bottomed pits	large pyramidal pits
Durose[72] (1986)£	Nakagawa	roughly Δ pits	no pits
Iwanaga[70,71] (1983)y	E-Ag1	Δ etch pits	flat bottomed Δ pits

* Assumes Warekois convention

£ Assumes Fewster convention

$ Etch patterns indexed according to the convention later adpted by Fewster

X No justification for polarity assignment given

& correlates etching with XRD

x correlates etching with electron diffraction

y Correlates etching with G. Mandel and F.F. Moorhead, Appl. Phys. Lett. 4 (1964). Iwanaga reports Δ etch pits on the $\{\bar{1}\bar{1}\bar{1}\}$B surface (and not on {111}A), when etched with 3:2:1 $HNO_3:HF:H_2O$. However, this does not agree with the reference quoted, which is concerned with the etch patterns produced across an angle lapped p-n junction.

Table 3.3 Polarity Sensitive Etches:- CdTe.

i.e. that the patterns in Inoue's papers are indexed in accordance with the convention later adopted by Fewster (even though Inoue claims to be working with the Warekois convention).

In 1987, Bagai et al[74] reported a new preferential etchant of composition 4:0.5:2 HF:H_2O_2:H_2O. By assuming the Fewster convention for CdTe crystal polarity, these workers correlated this reagent with the Nakagawa etch and demonstrated that the $\{\bar{1}\bar{1}\bar{1}\}$Te face becomes pitted (*i.e.* the opposite polar face to that which is pitted by the Nakagawa etch).

The 'black-white' etch reported by Meyers et al[75] is a good reliable discriminatory etchant. However, these workers do not explain how the action of this etchant was ascertained. A similar 'black-white' etch based on acetic rather than lactic acid has been shown by Durose[72] to discriminate between the opposite polar faces of CdTe in the same manner. These reagents produce a uniform dull black coating on one $\{111\}$ face and a shiny, pitted surface on the opposite polar face of CdTe.

3.7 Absolute Experimental Techniques

X-ray diffraction:-

As mentioned earlier, Warekois et al[13] used the principle of the anomalous absorption of x-rays to distinguish between the opposite polar faces of CdTe and concluded that etching in a 3:2:1 mixture of HF:H_2O_2:H_2O for 2min left the $\{\bar{1}\bar{1}\bar{1}\}$Te face pitted while the $\{111\}$ Cd face was polished. The accuracy of this result was brought into question by Fewster and Whiffin[52] who initially identified the polar faces of MCT using XRD and these results were correlated with several discriminatory etchants, each of which produced pits on the metal face and left the non-metal face unpitted.[76] Examination of both CdTe substrates and epitaxial MCT indicated that a polarity reversal must occur if both the results of Warekois[13] (for CdTe) and Fewster[76] (for MCT) were correct. In view of this unlikely finding, Fewster and Whiffin[52] repeated the original XRD experiment of Warekois and concluded the opposite result, *i.e.* that the Nakagawa reagent produced pits on the $\{111\}$ Cd face and not on the $\{\bar{1}\bar{1}\bar{1}\}$Te face, thereby making their results for CdTe and MCT self consistent.

Mention should be made, however, of the nature of the x-ray data presented by Fewster. Even though the XRD technique can clearly distinguish between the opposite polar faces of sphalerite materials, the deviation of the diffracted intensities from those predicted by Friedel's law is still quite small. A difference of only 3 to 4% is predicted for GaAs, for example.[27] Fewster, however, records a large variation in the diffracted intensities from opposite polar faces and does not account for the reported large difference in readings obtained by rotating the sample through 90°. In addition, the intensities used are small compared to the standard deviations quoted and the author also questions the reliability of the weak {222}-type reflection which is used to normalise the diffracted x-ray intensities. In spite of these discrepancies, there are a number of alternative absolute experimental techniques which are in agreement with the polarity convention for CdTe as proposed by Fewster.

References in agreement with the Warekois convention

Microdiffraction:-

In order to determine whether a dislocation is of the α or β -type, crystal polarity and the sign of the dislocation Burgers vector must first be determined. Subsequent investigation of the dissociation of α and β dislocations using the technique of weak beam electron microscopy then allows a value for the material stacking fault energy to be determined.[77] Prior to TEM specimen preparation, G.Lu and Cockayne[19] etched CdTe samples for 10sec using one of Inoue's E-Ag reagents (not specified) and the opposite polar faces were identified using the convention proposed by Warekois[13] and Inoue.[68] Microdiffraction patterns obtained from the CdTe samples in the electron microscope were found to be consistent with this polarity designation. It is noted that these workers[19] reference the second Inoue[68] paper in which the E-Ag reagents are correlated with the Warekois convention, even though Inoue indexes these etch patterns in accordance with the convention later adopted by Fewster.

Electron Diffraction and HREM:-

Di Cioccio et al[53] reported an investigation of CdTe/HgTe superlattices on {111} CdTe substrates using HREM. Assuming good epitaxial growth occurred on the $\{\bar{1}\bar{1}\bar{1}\}$Te face, in accordance with the Fewster convention, it was found that the models for interfacial dislocation structures, as proposed by Bourret,[78] did not agree with the experimental observations.[53] Hence, these workers determined the orientation of the CdTe substrate from selected area diffraction (SAD) patterns in order to ascertain the epilayer growth direction.

Multiple (or dynamic) electron scattering from a non-centrosymmetric material reflects the lack of crystal symmetry and so, for a zone axis orientation, the intensities of the g^{th} and $-g^{th}$ beams are not in general identical. Consequently, $I_{\mathrm{g}}(t) \neq I_{\bar{\mathrm{g}}}(t)$ for a crystal of thickness t. Di Cioccio et al[53] used this phenomenon to determine crystal polarity by comparing experimental microdensitometer readings with calculated SAD patterns taken from a CdTe wedge in the $< 110 >$ orientation. Computer simulation of the diffracted intensities integrated over crystal thickness was based on the multislice theory of Cowley and Moodie. The difference in the diffracted beam intensities is readily apparent in higher order $\{113\}$, $\{331\}$ and $\{333\}$ type reflections using this technique. Ten SAD patterns were analysed to eliminate the effects of spherical aberrations and crystal inhomogeneities and all of the diffraction patterns were consistent with the use of a $\{111\}$ Cd face for epitaxy. This $\{111\}$ face was found to correspond to the unpitted face following etching with the Nakagawa reagent and so agrees with the Warekois convention for crystal polarity. It is noted, however, that this 'zone axis' experimental technique is very sensitive to crystal thickness.[15]

The problem of crystal polarity determination in CdTe is closely associated with the epitaxial growth of $\{111\}$ CdTe on $\{100\}$GaAs (see chapter 5). Investigation of the $\{111\}$ CdTe/$\{100\}$GaAs interface by Kolodziejski et al[55] using a 1MeV electron microscope demonstrated that the $\{111\}$ CdTe film had a $\{\bar{1}\bar{1}\bar{1}\}$Te face directed towards the GaAs substrate. Computer simulation using basic diffraction theory confirmed the interpretation of the HREM images.[55] The authors considered that this epitaxial relationship would give rise to a $\{111\}$ Cd face at the free surface, *i.e.* the growth face for subsequent epitaxy. It is shown in section 5.4, that satisfactory epitaxial growth of MCT occurs on $\{111\}$CdTe/$\{111\}$B GaAs hybrid substrates. Comparison of the defect content of $\{111\}$ CdTe epitaxial layers on both $\{111\}$B and $\{100\}$GaAs illustrates the same lamellae twin defect content lying parallel to the epilayer/substrate interface. Hence, the $\{111\}$ CdTe surface will be the same for both of these epitaxial systems and by inference with the observations of Kolodziejski,[55] this will be a $\{111\}$ Cd surface. Even though Kolodziejski et al do not correlate their findings with a chemical etchant one is able to infer that these HREM polarity observations are in agreement with the Warekois convention.

References in agreement with the Fewster convention

X-ray Photoelectron Spectroscopy and Auger Electron Spectroscopy

The Atomic number Z of a surface atom can be ascertained from the energy required to create a vacancy in the inner electron shell, or from the energies of the electron transitions involved in the decay of the vacancy. These are the two fundamental processes of the XPS and AES experimental techniques which are usually performed in the same experimental environment. The surface preparation of samples prior to investigation is critical and the low escape depths of x-ray photoelectrons and Auger electrons (typically 10 to 20Å) necessitates the use of ultra- high vacuum conditions (typically 10^{-11}torr).

XPS

The excitation of core electrons into high energy electron states by a monochromatic beam of x-rays provides the basis of the XPS experimental technique, in which the kinetic energies of the photoelectrons (with energies exceeding the sample work function) are measured. The XPS technique has been used by Hsu[59] to determine the growth face of $\{111\}$ CdTe on $\{100\}$GaAs. Calibrated amounts of CdTe were deposited onto the $\{100\}$GaAs substrate and the normalised photoelectron intensities of the 3d $\frac{5}{2}$ core levels of Cd and Te determined. The intensity ratio $\frac{I_{Cd}}{I_{Te}}$ was found to be $<< 1$ for CdTe layers less than 40Å. It is known that Te is the first deposited layer during the growth of CdTe and GaAs[79] and so, this observation could only be explained by the presence of an extra atomic layer of Te, which implies that the epilayer growth face is also a $\{\bar{1}\bar{1}\bar{1}\}$Te plane. The as-grown $\{111\}$ CdTe/$\{100\}$GaAs layers were found to be only slightly pitted using the Nakagawa reagent and these observations correspond to the polarity convention of Fewster. Hsu[59] also noted that it was possible to discriminate between the opposite polar surfaces of CdTe using RHEED. The $[1\bar{1}0]$ projection of the $\{\bar{1}\bar{1}\bar{1}\}$Te face was characterised by a $\frac{1}{6}$-integer order superstructure, while the corresponding direction on the $\{111\}$ Cd face exhibited a $\frac{1}{2}$-integer order superstructure. The RHEED technique is only discriminatory in its action, however, and needs to be correlated with chemical etching for the absolute determination of crystal polarity.

AES

AES has principally been used to investigate the surface compositions that result from the various surface treatments,[80] such as ion beam sputtering and chemical etching,[81] which are used during device processing. Unlike the x-ray and electron diffraction based techniques where comparatively large volumes of material are sampled in order to determine crystal polarity, the AES technique is extremely sensitive to the top few crystal atomic layers. Sample surfaces probed by a rastered electron beam undergo a series of electron transitions which result in the emission of Auger electrons. The Te(*MNN*) transition, for example, (where *MNN* refers successively to the energy level from which an electron is initially ejected, the energy level from which an electron falls to fill this vacancy, and the original energy level from which the Auger electron is emitted), is sensitive to a depth of about 15Å for CdTe, while the Te(*NOO*) peak is only sensitve to the top 5Å, or three atomic layers. Consequently, the normalised value of $\frac{Te(NOO)}{Te(MNN)}$ taken from opposite polar faces of CdTe is sensitive to the top atomic layer being either Cd or Te and hence, provides the basis of this experimental technique to determine crystal polarity.[57] [58]

Y.-C. Lu[57] prepared different CdTe samples for AES analysis by etching with Inoue's E-Agl and Nakagawa's reagent, and by sputtering with a Ne^+ ion beam. In a second paper[58] the surfaces of a hydrogen heat-treated sample, which is the only surface treatment found to retain a stoichiometric CdTe surface, were investigated. Samples were placed in an ultra-high vacuum chamber ($\approx 10^{-9}$torr background pressure) and probed by a rastered electron beam (3kV, 0.4mA cm^{-2}) at roughly 30^o to the sample normal. The emitted Auger electrons were measured in the differential mode ($\frac{dN(E)}{dE}$) using a single pass cylindrical mirror analyser. The experimental conditions were set so as to enhance the low energy Te(*NOO*) peak and this was normalised using the higher energy Te(*MNN*) peaks obtained from both polar $\{111\}$ faces. The normalised ratio from the $\{\bar{1}\bar{1}\bar{1}\}$Te surface was consistently found to be about 1.3 times that from the $\{111\}$ Cd surface and the Te rich surface was taken to be the $\{\bar{1}\bar{1}\bar{1}\}$Te crystal face. This Te rich surface exhibited flat bottomed pits with the Inoue E-Agl etchant but remained unpitted when etched with the Nakagawa reagent and hence, this polarity determination technique was found to be in agreement with the Fewster convention.

RBS

Chami[56] investigated the $\{111\}$ CdTe/$\{100\}$GaAs system using the RBS technique to determine the best $\{111\}$ CdTe face for epitaxy. It is noted that this paper is indexed in accordance with the Dewald convention. The advantage of the RBS technique over the XPS and AES surface sensitive techniques is that no special sample preparation processes are required. The mass of a surface atom can be ascertained from the recoil momentum given to an incident ion, and at sufficiently high energies the ion may penetrate many atomic layers (≈ few 100Å) before being backscattered. The stopping power is a characteristic of the material being investigated. This phenomenon may be extended for the purpose of polarity determination by the observation of asymmetries in the channeling patterns arising from the polar nature of the zincblende structure. Measurement of the backscattered yield at the critical angle for channeling along the {111} planes inclined to the surface indicates the nature of the Cd or Te steering ('advancing') planes and so permits polarity determination. It was found that the {111}Te face was the best growth face for epitaxy, which is in accordance with the polarity convention of Fewster.

Electron diffraction

The technique of electron diffraction was used by Di Cioccio et al[53] to determine the crystal polarity of CdTe and it was concluded that their assignment was in accordance with the Warekois convention. In a more recent paper (May, 1988), these same workers[54] reported the opposite assignment for CdTe crystal polarity (*i.e.* Fewster convention), which was also determined by means of the electron diffraction technique. It was considered the the original reference[53] was in error because of a 180^o inversion introduced by the computer program used to calculate the intensities of the diffracted electron beams.

3.8 Experimental Determination of CdTe Polarity using Microdiffraction

As demonstrated by section 3.7, there is genuine confusion over which polarity convention to use for CdTe. In order to try and resolve this issue the technique of microdiffraction has been used to determine the best polar face for the epitaxial growth of MCT.

For the purpose of this determination, two epitaxial systems were considered. A {111} CdTe/{111} B GaAs sample was used as a polarity standard to confirm the image rotation calibration of the electron microscope and epitaxial MCT/{111} CdTe layers which gave good MCT growth (*i.e.* twin grain formation[65]) provided the CdTe substrate material for investigation. As illustrated in section 3.5, there is no confusion over the polarity determination of GaAs, and the $\{\bar{1}\bar{1}\bar{1}\}$B (or $\{\bar{1}\bar{1}\bar{1}\}$As) substrate face is that which gives a flat, mirror finish when polished with Br_2/MeOH.[38]

For samples imaged in the JEOL 100CX electron microscope at a magnification of 20,000 (camera length (C.L.) = 76cm), the defocussed diffraction pattern technique (section 3.4) predicts that a value of θ=321^o (*i.e.* a 39^o clockwise rotation of the diifraction pattern (C.L.=76cm)) is necessary to correct for the effects of image rotation.

Microdiffraction patterns (C.L.=20cm) were obtained from $< 110 >$ orientations of the GaAs and CdTe substrates. Figure 3.10a, taken from the GaAs substrate, shows the deficiency black cross through a $\{200\}$ reflection arising from the interaction of doubly diffracted $\{9\ 1\ 1\}$ and $\{11\ 1\ 1\}$ beams with a directly scattered $\{200\}$ reflection, which in turn corresponds to the sense of advancing $\{111\}$ A planes (see figures 3.4 and 3.6). A 39^o clockwise rotation of the associated diffraction pattern (C.L.=76cm) taken from the GaAs substrate oriented a $\{\bar{1}\bar{1}\bar{1}\}$B diffraction spot ($< \bar{1}\bar{1}\bar{1} >_b$ direction) towards the $\{111\}$ CdTe/$\{\bar{1}\bar{1}\bar{1}\}$B GaAs growth interface as expected (see figures 3.10b and 3.10c). This procedure using a polarity calibrated sample confirmed that the electron microscope was precisely corrected for the effects of image rotation.

Microdiffraction patterns were similarly obtained from the substrates of four samples of MCT/$\{111\}$ CdTe. A similar dark cross (figure 3.10d) was found for the interaction of a pair of $\{9\ 1\ 1\}$, $\{11\ 1\ 1\}$ doubly diffracted beams with one of the $\{200\}$ reflections, while a doubly diffracted $\{9\ 5\ 1\}$, $\{7\ 5\ 1\}$ pair of beams were found to produce a dark cross through the opposite $\{\bar{2}00\}$ reflection, as shown in figure 3.10e. These observations are in accordance with the theoretical predictions of the microdiffraction experimental technique (section 3.3). Rotation of the diffraction pattern (C.L.=76cm) through a clockwise angle of 39^o for the sample at a magnification of 20,000 demonstrated that the MCT epilayer growth direction was $< \bar{1}\bar{1}\bar{1} >_b$ (figures 3.10f and 3.10g) and hence, that the best CdTe substrate surface for epitaxy was the $\{\bar{1}\bar{1}\bar{1}\}$B (or $\{\bar{1}\bar{1}\bar{1}\}$Te) plane. Consistent results were obtained using this procedure with all four MCT/CdTe samples. The $\{\bar{1}\bar{1}\bar{1}\}$Te polar surface becomes shiny when etched in a 1:1:1 mixture of HF:Nitric:Acetic and hence, this result is in agreement with the Fewster convention for CdTe crystal polarity.

A summary of the different chemical etchants used to distinguish facedness in CdTe is presented in Table 3.4 and their action is now recorded with respect to the Fewster convention.

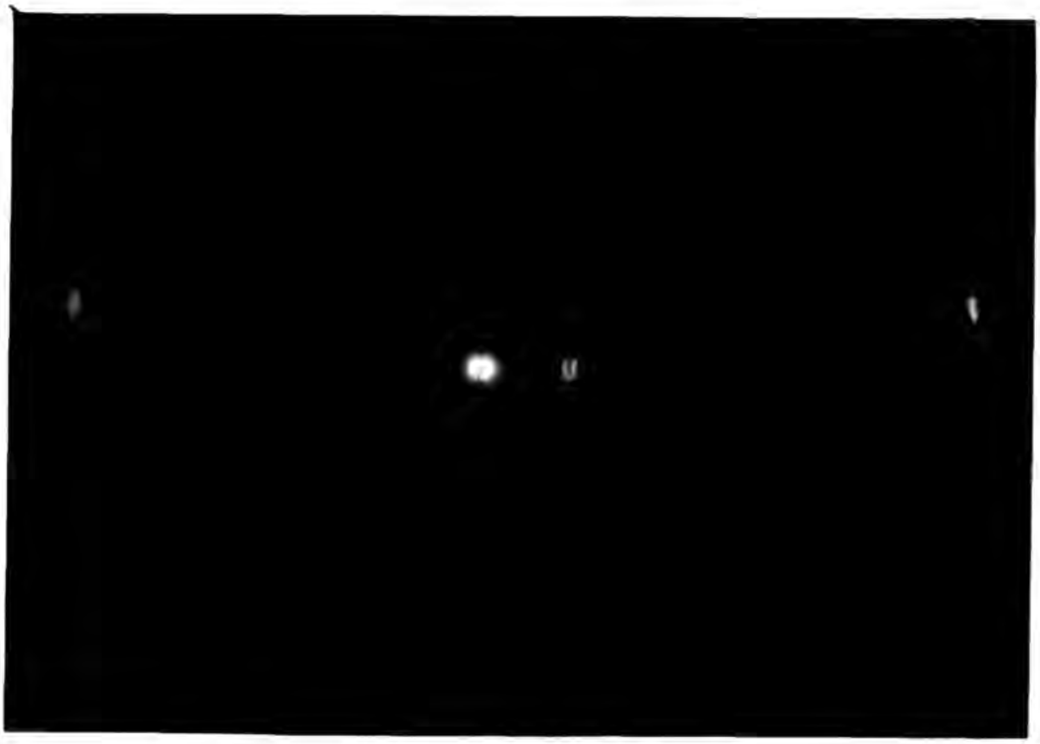

Figure 3.10a Microdiffraction pattern (CL=20cm) showing destructive interference from the interaction of a pair of doubly diffracted {9 1 1} and {11 1 1} reflections with a directly scattered {200} beam:- taken from the GaAs substrate of a CdTe/{$\bar{1}\bar{1}\bar{1}$}B GaAs polarity calibrated sample.

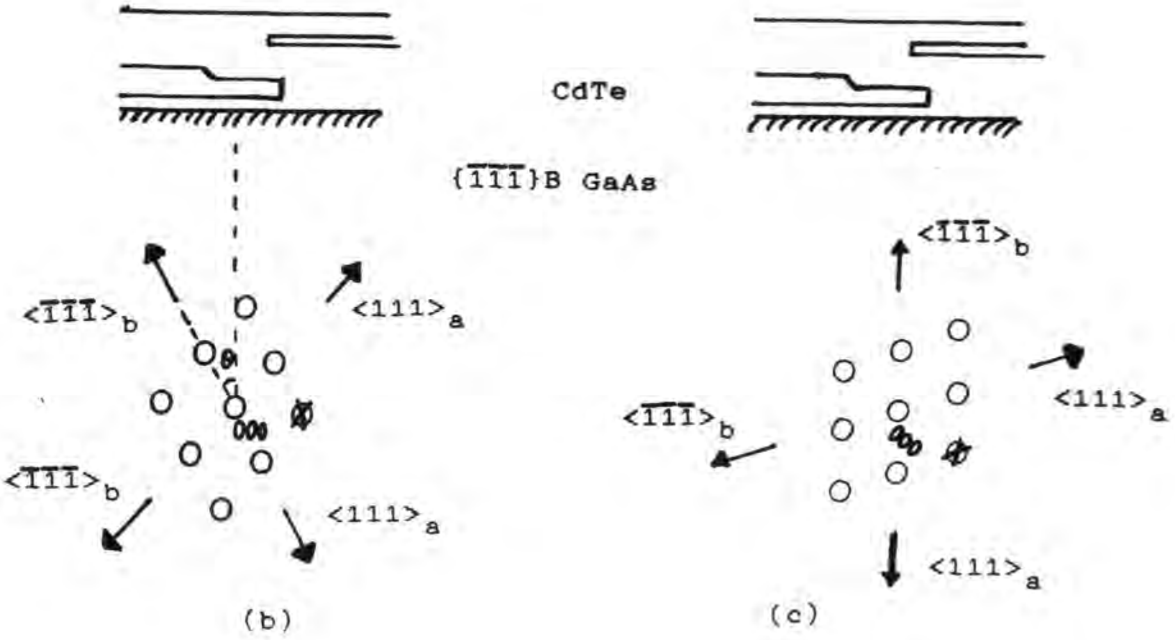

Figure 3.10b,c Correction for image rotation orients a <$\bar{1}\bar{1}\bar{1}$>$_b$ direction in the diffraction pattern (CL=76cm) towards the growth interface. Thereby confirming the image rotation calibration of the electron microscope as determined by the 'defocussed diffraction pattern' technique.

Figure 3.10d Microdiffraction pattern (CL=20cm) showing destructive interference through a {200} disc due to interaction with a pair of doubly diffracted {9 1 1}, {11 1 1} reflections:- taken from the CdTe substrate of an MCT/{111}CdTe sample which gave good MCT growth.

Figure 3.10e Microdiffraction pattern showing destructive interference through a $\{\bar{2}00\}$ disc due to interaction with a pair of doubly diffracted {9 5 1}, {7 5 1} reflections:- taken from the CdTe substrate of the same MCT/{111}CdTe sample.

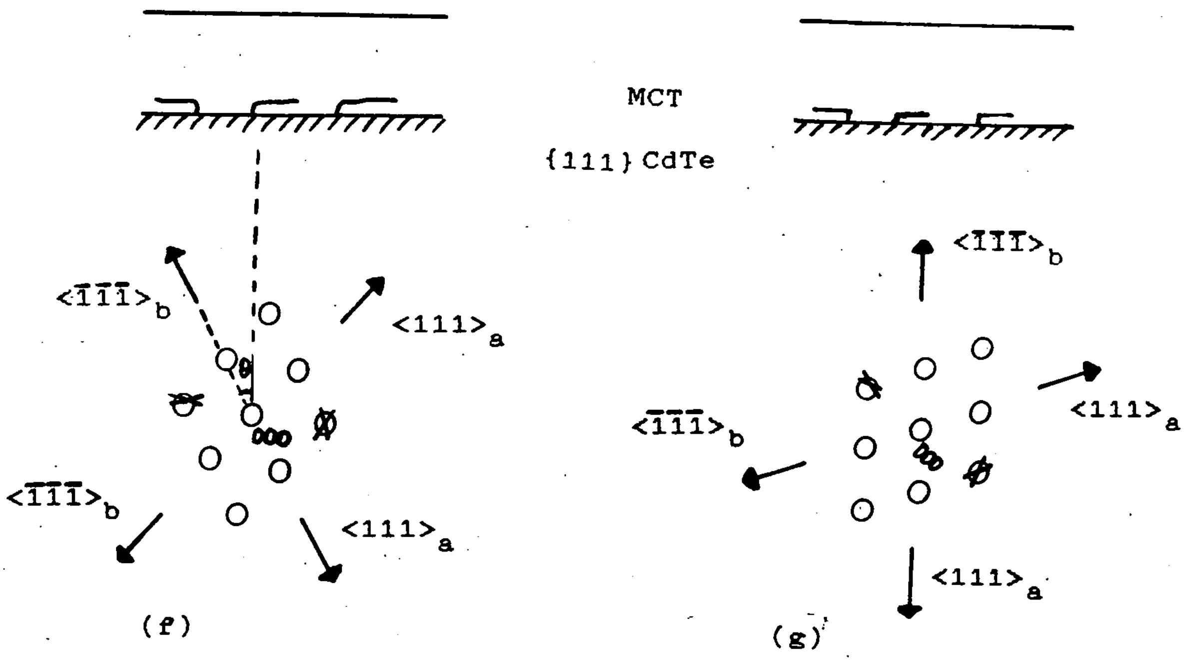

<u>Figure 3.10f,g</u> Correction of the diffraction pattern (CL=76cm) for image rotation orients a <$\bar{1}\bar{1}\bar{1}$>$_b$ direction towards the MCT/{111}CdTe growth interface, thereby confirming that the {$\bar{1}\bar{1}\bar{1}$}B CdTe face is the best polar face for MCT epitaxy.

reference	chemical etch	action of etchants (after the Fewster convention) {111}Cd	 {$\bar{1}\bar{1}\bar{1}$}Te
Warekois[13] (1962)	3:2:1 $HF:H_2O_2:H_2O$	Δ pits	nearly polished
	1:1 $HCl:HNO_3$	film plus random distribution of etch features	Δ pits in a background of flat Δ etch features
Nakagawa[66] (1979)	3:2:2 $HF:H_2O_2:H_2O$	pitted	polished
Bagai[74] (1984)	4:0.5:2 $HF:H_2O_2:H_2O$	-	etch pits -deep pyramidal pits and shallow Δ pits
Inoue[67] (1962)	E-Ag1	small Δ pyramidal pits	large Δ flat bottomed pits
	E-Ag2	no pits	shallow Δ pyramidal pits
Meyers[75] (1983)	1:1:1 $HF:HNO_3$:Lactic	dull black coating	shiny pitted surface
Durose[72] (1986)	1:1:1 $HF:HNO_3$:Acetic	matt black	shiny

Table 3.4 Polarity Sensitive Etches:- CdTe.

It has been shown that the microdiffraction technique produces a result which is contrary to that reported by G. Lu and Cockayne.[19] It is noted, however, that these workers correlate their microdiffraction patterns with the action of one of the Inoue E-Ag reagents, and that a very short etching time (5sec) was used. It has been suggested that the action of the Inoue E-Ag reagents is time dependent,[82] *i.e.* that a reversal of the etch pit shapes occurs with time and so, the unreliable action of this etchant is probably responsible for this discrepancy.

Regarding the HREM observations of Kolodziejski et al[55] it is generally accepted that the $\{111\}$ CdTe/$\{100\}$GaAs epitaxial system has a $\{\bar{1}\bar{1}\bar{1}\}$Te face directed towards the substrate. However, the XPS investigation reported by Hsu et al[59] suggests that there is also a $\{\bar{1}\bar{1}\bar{1}\}$Te growth surface, which indicates that a single monotomic layer of Te is inserted at the epilayer/substrate interface. In view of the complex computer simulation necessary for the interpretation of HREM images, it is possible that misinterpretation of these images was responsible for this conficting report.

3.9 Summary

The discriminatory action of chemical etchants on the opposite polar faces of sphalerite materials can be assigned by reference to some other absolute polarity calibration technique. In particular, the opposite polar faces of CdTe have been delineated by use of the anomalous absorption of x-rays and correlated with the action of discriminatory etchants based on HF:H_2O_2:H_2O. The two opposite conventions for the assignment of CdTe polarity suggested by Warekois[13] and Fewster,[52] as determined by use of the XRD technique, have led to considerable confusion in the recent international literature and so, the technique of microdiffraction has been used to resolve this discrepancy.

In section 3.3, the suitability of the microdiffraction experimental procedure for the absolute determination of sphalerite crystal polarity has been demonstrated. The interaction of high order, odd index doubly diffracted beams with the directly scattered $\{200\}$ reflections gives rise to interference effects which can be qualitatively interpreted, following correction for the effects of image rotation introduced by the electron microscope, to determine crystal polarity.

For the purpose of this study, a precise description of the sphalerite structure has been given in terms of the more commonly used convention of Gatos. Comparison of the

$< 110 >$ space lattice and associated reciprocal lattice projections have demonstrated that the $\{200\}$ reflection which exhibits destructive interference following interaction with a pair of doubly diffracted $\{9\ 1\ 1\}$ and $\{11\ 1\ 1\}$ reflections, corresponds to the sense of advancing $\{111\}$ A planes.

Correction for image rotation has been achieved firstly by use of crystals of MoO_3 and the defocussed diffraction pattern technique as descibed by Loretto, and secondly by means of a polarity calibrated sample comprised of $\{111\}$ CdTe/$\{\bar{1}\bar{1}\bar{1}\}$B GaAs. The brief review of the chemical etching of GaAs given in section 3.5 was included to demonstrate that there is no confusion concerning the determination of facedness in this compound. Both these rotation calibration procedures gave consistent results.

The reviews of the discriminatory chemical etchants and the absolute polarity determination techniques reported in connection with CdTe, presented in sections 3.6 and 3.7 respectively, clearly demonstrate that there is genuine confusion concerning this issue.

Samples of MCT/$\{111\}$ CdTe provided the source material for the microdiffraction polarity calibration of CdTe. The MCT layers were grown on the best CdTe face for epitaxy, and this polar face becomes shiny when etched in a 1:1:1 mixture of HF:Nitric:Acetic and is unpitted by the Nakagawa etch. Correction of the microdiffraction patterns obtained from the CdTe substrate material for the effects of image rotation oriented a $< \bar{1}\bar{1}\bar{1} >_b$ direction towards the epilayer/substrate interface, which conclusively demonstrates that the epitaxial growth face is the $\{\bar{1}\bar{1}\bar{1}\}$Te plane. This result is in agreement with the Fewster convention and with the workers using the AES,[57] [58] XPS,[59] RBS[56] and electron diffraction[54] techniques, and contradicts the Warekois convention and the reports based on the microdiffraction,[19] HREM[55] and electron diffraction[53] procedures.

REFERENCES

1. D.B. Holt, *J. Mater. Sci.* **23** (1988) 1131
2. H.Nagai, *J. Appl. Phys.* **43** (1972) 4254
3. H.Booyens, J.S. Vermaak and G.R. Proto, *J. Appl. Phys.* **49** (1978) 5435
4. P.B. Hirsch, P. Pirouz, S.G. Roberts and P.D. Warren, *Phil. Mag.* **B52** (1985) 759
5. G.H. Olsen, M.S. Abrahams and T.J. Zamerowski, *J. Electrochem. Soc.* **121** (1974) 1650
6. P.D. Brown, A.P.C. Jones, G.J. Russell, J. Woods, B. Cockayne and P.J. Wright, *Inst. Phys. Conf. Ser.* **No.87** (1987) 123
7. C.P. Lee, R. Zucca and B.M. Welch, *Appl. Phys. Lett.* **37** (1980) 311
8. N.Yokayama, H. Onodera, T. Ohnishi and A. Shibatomi, *Appl. Phys. Lett.* **42** (1983) 270
9. H.C. Gatos and M.C. Lavine, *J. Electrochem. Soc.* **107** (1960) 427
10. J.F. Dewald, *J. Electrochem. Soc.* **104** (1957) 244
11. W. Stutius and F.A. Ponce, *J. Appl. Phys.* **58** (1985) 1548
12. H.H. Brongersma and P.M. Mul, *Chem. Phys. Lett.* **19** (1973) 217
13. E.P. Warekois, M.C. Lavine, A.N. Mariano, and H.C. Gatos, *J. Appl. Phys.* **33** (1962) 690
14. idem, *erratum J. Appl. Phys.* **37** (1966) 2203
15. J. Taftø and J.C.H. Spence, *J. Appl. Cryst.* **15** (1982) 60
16. K. Ishizuka and J. Taftø, *Acta Cryst.* **B40** (1984) 332
17. B.C. De Cooman and C.B. Carter, *Appl. Phys. Lett.* **50** (1987) 40
18. Z. Liliental-Weber and L. Parechanian-Allen, *Appl. Phys. Lett.* **49** (1986) 1190
19. G. Lu and D.J.H. Cockayne, *Phil. Mag.* **A53** (1986) 307
20. H. Bethe, *Ann. Phys.* **87** (1928) 55
21. R.D. Heidenreich, *Phys. Rev.* **77** (1949) 271

22. J.M. Cowley and A.F. Moodie, Proceedings of the International Conference on Magnetism and Crystallography, *J. Phys. Soc. of Jpn.* **17 BII** (1962) 86

23. R.H. Alderson and J.S. Halliday, Ch15, Electron Diffraction, from *Techniques for Electron Microscopy*, ed. D.H. Kay, pub. Blackwell, 1965

24. M.H. Loretto, *Electron Beam Analysis of Materials*, p42, pub. Chapman and Hall, 1984

25. Coster, Knol and Prins, *Z. Physik* **63** (1930) 345

26. J.G. White and W.C. Roth, *J. Appl. Phys.* **30** (1959) 946

27. E.P. Warekois and P.H. Metzger, *J. Appl. Phys.* **30** (1959) 960

28. D.J. Stirland and B.W. Straughan, *Thin Solid Films* **31** (1976) 139

29. M.S. Abrahams and L. Ekstrom, Etch Pits, Deformation and Dislocations in GaAs, from *Properties of Elemental and Compound Semiconductors*, ed. H.C. Gatos, *Metallurgical Society Conferences* **5** (1960) 225

30. B. Tuck, *J. Mater. Sci.* **10** (1975) 321

31. B.A. Irving, Ch6 Chemical Etching of Semiconductors, in *The Electrochemistry of Semiconductors*, ed. P.J. Holmes, Academic Press, 1962

32. W. Kern, *RCA Review* **39** (1978) 278

33. H.C. Gatos and M.C. Lavine, *J. Phys. Chem. Solids* **14** (1960) 169

34. B.W. Batterman, *J. Appl. Phys.* **28** (1957) 1236

35. H.A. Schell, *Z. Metallk.* **48** (1957) 158

36. C.S. Fuller and W.H. Allison, *J. Electrochem. Soc.* **109** (1962) 880

37. J.C. Dyment and G.A. Rozgonyi, *J. Electrochem. Soc.* **118** (1971) 1346

38. M.V. Sullivan and G.A Kolb, *J. Electrochem. Soc.* **110** (1963) 585

39. J.L. Richards and A.J. Crocker, *J. Appl. Phys.* **31** (1960) 611

40. D.F. Kyser and M.F. Millea, *J. Electrochem. Soc.* **111** (1964) 1102

41. J.L. Richards, *J. Appl. Phys.* **31** (1960) 600

42. M.S. Abrahams and C.J. Buiocchi, *J. Appl. Phys.* **36** (1965) 2855

43. J.G. Grabmaier and C.B. Watson, *phys. stat. sol.* **32** (1962) K13

44. S. Iida and K. Ito, *J. Electrochem. Soc.* **118** (1971) 768

45. Y. Tarui, Y. Komiya and Y. Harada, *J. Electrochem. Soc.* **118** (1971) 118

46. A.U. MacRae, *Surface Science* **4** (1966) 247

47. D.D. Pretzer and H.D. Hagstrum, *Surface Science* **4** (1966) 265

48. A. Rudra, J.C. Grenet, P. Gibart, H. Heral and A. Rocher, *J. Crystal Growth* **87** (1988) 535

49. E. Sirtl and A. Adler, *Z. Metallk.* **52** (1961) 529

50. D.B. Holt, *J. Appl. Phys* **31** (1960) 2231

51. M. Alonso, F. Soria and J.L. Sacedon, *J. Vacuum Sci. Technol.* **A3** (1985) 1598

52. P.F. Fewster and P.A.C. Whiffin, *J. Appl. Phys.* **54** (1983) 4668

53. L. Di Cioccio, E.A. Hewat, A. Million, J.P. Gailliard and M. Dupuy, *Inst. Phys. Conf. Ser.* **No.87** (1987) 243

54. E.A. Hewat, L. Di Cioccio, A. Million, M. Dupuy and J.P Gailliard, *J. Appl. Phys.* **63** (1988) 4929

55. L.A. Kolodziejski, R.L. Gunshor, N. Otsuka and C. Choi, *J.Vacuum Sci.Technol.* **A4** (1986) 2150

56. A.C. Chami, E. Ligeon, R. Danielou and J. Fontenille, *Appl.Phys.Lett.* **52** (1988) 1502

57. Y.-C. Lu, C.M. Stahle, J. Morimoto, R.H. Bube and R.S. Feigelson, *J.Appl.Phys.* **61** (1987) 924

58. Y.-C. Lu, C.M. Stahle, R.S. Feigelson and J. Morimoto, *J.Appl.Phys.* **62** (1987) 4453

59. C. Hsu, S. Sivananthan, X. Chu and J.P. Faurie, *Appl. Phys. Lett.* **48** (1986) 908

60. A.J. Van Bommel and J.E. Crombeen, *Surface Science* **57** (1976) 437

61. I. Teramoto and M. Inoue, *Phil. Mag.* **8** (1963) 1593

62. I. Teramoto, *ibid.* 357

63. K.Zanio, Chapter 2, 'Physics' in *Semiconductors and Semimetals*, Volume 13 (Cadmium Telluride), ed. Willardson and Beer, pub. Academic Press, 1978.

64. P.D. Brown, G.J. Russell, J.E. Hails and J. Woods, *Appl. Phys. Lett.* **50** (1987) 1144

65. J.E. Hails, G.J. Russell, P.D. Brown, A.W. Brinkman and J. Woods, *J. Crystal Growth* **86** (1988) 516

66. K. Nakagawa, K. Maeda and S. Takeuchi, *Appl. Phys. Lett.* **34** (1979) 574

67. M. Inoue, I. Teramoto and S. Takayanagi, *J. Appl. Phys.* **33** (1962) 2578

68. *idem, ibid.* **34** (1963) 404

69. Y.-C. Lu, R.K. Route, D. Elwell and R.S. Feigelson, *J. Vacuum Sci. Technol.* **A3** (1985) 264

70. H. Iwanaga, T. Yoshiie, S. Takeuchi and K. Mochizuki, *J. Crystal Growth* **61** (1983) 691

71. H. Iwanaga, A. Tomizuka, N. Shibata and K. Mochizuki, *J. Crystal Growth* **74** (1986) 113

72. K. Durose, *Structural Defects in CdTe*, Ph.D. thesis, Dunelm, 1986

73. H. Iwanaga, N. Shibata A. Tanaka and Y. Masa, *J. Crystal Growth* **84** (1987) 345

74. R.K. Bagai, G. Mohan, G.L. Seth and W.N. Borle, *J. Crystal Growth* **85** (1987) 386

75. T.H. Meyers, J.F. Schetzina, T.J. Magee and R.D. Ormond, *J. Vacuum Sci. Technol* **A3** (1983) 1598

76. P.F. Fewster, S. Cole, A.F.W. Willoughby and M. Brown, *J. Appl. Phys.* **52** (1981) 4568

77. S. Takeuchi, K. Suzuki, K. Maeda and H. Iwanaga, *Phil. Mag.* **A50** (1984) 171

78. A. Bourret, J. Desseaux and A. Renault, *Phil. Mag.* **A45** (1982) 1

79. H.A. Mar, N. Salansky and K.T. Chee, *Appl. Phys. Lett.* **44** (1984) 898

80. R.D. Feldman, R.L. Opila and P.M. Bridenbaugh, *J. Vacuum Sci. Technol.* **A3** (1985) 1988

81. P. Gaugash and A.G.Milnes, *J. Electrochem. Soc.* **128** (1981) 924

82. Dr. K. Durose, private communication

APPENDIX

A1 Microdiffraction:- background theory

The polynomial expression

$$\Psi(h,k) = \sum_{l}\sum_{n}\sum_{h_1}\cdots\sum_{h_{n-1}}(-i\sigma)^n\Phi(h_1)\ldots\Phi(h_{n-1})\Phi(h_n)Z_n(\xi_1\ldots\xi_{n-1}\xi_n) \qquad \text{(A1)}$$

which is derived from the integral equation formulation (or 'physical optics' theory) developed by Cowley and Moodie[1] may be used to express the dynamical diffraction amplitude for h,k reflection from a parallel plate crystal. Where

1. h_j represents the 3-d indices $h_jk_jl_j$ of each scattering vector,
2. n defines the number of interactions,
3. Φ is a kinematical structure factor,
4. ξ is an excitation error,
5. the function Z_n depends on specimen thickness,
6. $\sum_{l}$ is a summation over the index l, the reciprocal axis normal to the crystal surface, and
7. $\sigma = \frac{2\pi me\lambda}{h^2}$

Strictly speaking, $\{hkl\}$ is not correct to specify the dynamical diffraction amplitude, but $\{hkl\}$ may be used to specify reflections near the Ewald sphere.[2]

For the experimental conditions illustrated by figure A1.a, there will be one direct scattering ($000 \mapsto 200$) and two double scattering ($000 \mapsto \bar{9}\ 1\ \bar{1} \mapsto 200$ and $000 \mapsto 11\ 1\ \bar{1} \mapsto 200$) processes. When the Bragg condition is satisfied, $Z \propto H$ and $Z \propto \frac{H^2}{2}$ for direct and double scattering respectively, where H represents specimen thickness.

The 20 and $\bar{2}0$ dynamical diffraction amplitudes (*i.e.* 200 and $\bar{2}00$ reflections) may be approximated by the following expressions[2]

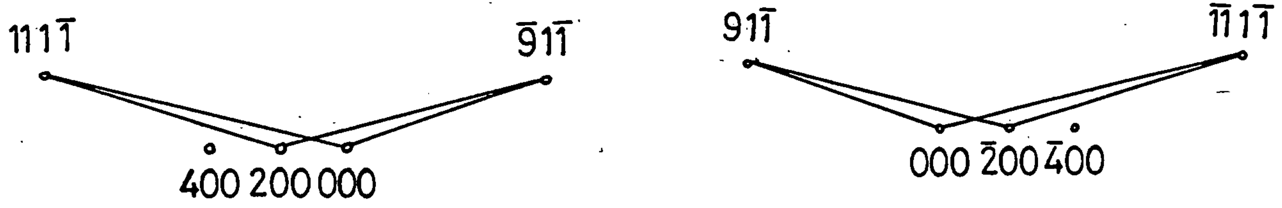

(a)

Figure A.1 Schematic ray diagram to illustrate the conditions for interference in microdiffraction patterns. For a [011] crystal projection:- a) The interaction of a pair of {9 1 1}, {11 1 1} doubly diffracted beams with the directly scattered 200 and 200 reflection gives rise to constructive and destructive interference respectively.

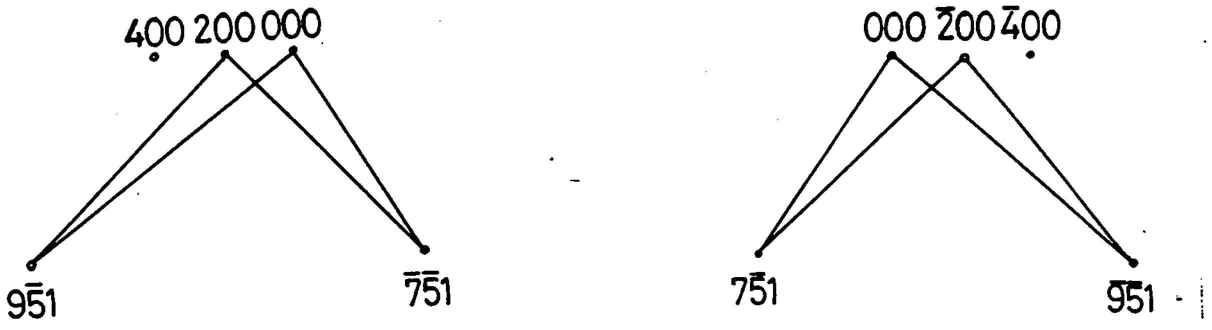

(b)

b) The interaction of a pair of doubly diffracted {9 5 1}, {7 5 1} beams with the same 200 and 200 reflections gives rise to destructive and constructive interference respectively.

$$\Psi(20) \approx -i\sigma H\Phi(200) + \frac{(-i\sigma H)^2}{2}[\Phi(\bar{9}\ \bar{1}\ 1)\Phi(11\ 1\ \bar{1}) + \Phi(11\ \bar{1}\ 1)\Phi(\bar{9}\ 1\ \bar{1})] \qquad \text{(A2)}$$

$$\Psi(\bar{2}0) \approx -i\sigma H\Phi(\bar{2}00) + \frac{(-i\sigma H)^2}{2}[\Phi(\bar{1}\bar{1}\ \bar{1}\ 1)\Phi(9\ 1\ \bar{1}) + \Phi(9\ \bar{1}\ 1)\Phi(\bar{1}\bar{1}\ 1\ \bar{1})] \qquad \text{(A3)}$$

For a sphalerite binary crystal of the form AB, with the origin such that nearest atoms are positioned at $^-\frac{1}{8}{}^-\frac{1}{8}{}^-\frac{1}{8}$ and $\frac{1}{8}\frac{1}{8}\frac{1}{8}$ respectively, the kinematical structure factor is given by;

$$\Phi(hkl) = [f_{A_{hkl}} e^{2\pi i(-\frac{1}{8}h-\frac{1}{8}k-\frac{1}{8}l)} + f_{B_{hkl}} e^{2\pi i(\frac{1}{8}h+\frac{1}{8}k+\frac{1}{8}l)}]G(hkl) \qquad \text{(A4)}$$

where $G(hkl)$ is a geometrical factor for the fcc system and is equal to 4, when h, k, l are all even or all odd (otherwise $G(hkl)$ is equal to zero).

Consider $\Phi(200)$, for example;

$$\Phi(200) = 4[f_{A_{(200)}} e^{-\frac{\pi i}{2}} + f_{B_{(200)}} e^{\frac{\pi i}{2}}] \qquad \text{(A5)}$$

Putting $f_A = \bar{\text{f}}\text{-}\Delta$ and $f_B = \bar{\text{f}}+\Delta$ (Δ is positive), where $\bar{\text{f}}$ is a mean value of the atomic scattering factors and Δ is some small deviation from this,

$$\Phi(200) = 4[(\bar{\text{f}}_{200} - \Delta)e^{-\frac{\pi i}{2}} + (\bar{\text{f}}_{200} + \Delta)e^{\frac{\pi i}{2}}] \qquad \text{(A6)}$$

$$= 4\Delta[-e^{-\frac{\pi i}{2}} + e^{\frac{\pi i}{2}}] \qquad \text{(A7)}$$

$$= 8\Delta i \qquad \text{(A8)}$$

Similarly,

$$\Phi(\bar{2}00) = -8\Delta i \tag{A9}$$

Also,

$$\Phi(\bar{9}\ 1\ \bar{1}) = 4[(\bar{\mathrm{f}}_{9\ 1\ 1} - \Delta)e^{\frac{9\pi i}{4}} + (\bar{\mathrm{f}}_{9\ 1\ 1} + \Delta)e^{-\frac{9\pi i}{4}}] \tag{A10}$$

$$= 4\sqrt{2}[\bar{\mathrm{f}}_{9\ 1\ 1} - \Delta i] \tag{A11}$$

$$\approx 4\sqrt{2}\bar{\mathrm{f}}_{9\ 1\ 1} \qquad (\ = \Phi(\bar{9}\ \bar{1}\ 1)\ ) \tag{A12}$$

It can be shown that

$$\Phi(9\ 1\ \bar{1}) = \Phi(9\ \bar{1}\ 1) = 4\sqrt{2}[\bar{\mathrm{f}}_{9\ 1\ 1} + \Delta i] \approx 4\sqrt{2}\bar{\mathrm{f}}_{9\ 1\ 1}$$

$$\Phi(\bar{1}\bar{1}\ 1\ \bar{1}) = \Phi(\bar{1}\bar{1}\ \bar{1}\ 1) = -4\sqrt{2}[\bar{\mathrm{f}}_{11\ 1\ 1} + \Delta i] \approx -4\sqrt{2}\bar{\mathrm{f}}_{11\ 1\ 1}$$

$$\Phi(11\ 1\ \bar{1}) = \Phi(11\ \bar{1}\ 1) = -4\sqrt{2}[\bar{\mathrm{f}}_{11\ 1\ 1} - \Delta i] \approx -4\sqrt{2}\bar{\mathrm{f}}_{11\ 1\ 1}$$

Substituting these values back into the general expression for the dynamical diffraction amplitudes,

$$\Psi(20) \approx -i\sigma H 8\Delta i + \frac{(-i\sigma H)^2}{2}[4\sqrt{2}\bar{\mathrm{f}}_{9\ 1\ 1}(-4\sqrt{2})\,\bar{\mathrm{f}}_{11\ 1\ 1} + 4\sqrt{2}\bar{\mathrm{f}}_{9\ 1\ 1}(-4\sqrt{2})\bar{\mathrm{f}}_{11\ 1\ 1}]$$

$$\Psi(20) = 8\sigma H\Delta + 32\sigma^2 H^2 \bar{\mathrm{f}}_{11\ 1\ 1}\bar{\mathrm{f}}_{9\ 1\ 1} \tag{A13}$$

and

$$\Psi(\bar{2}0) \approx -i\sigma H(-8\Delta i) + \frac{(-\sigma H)^2}{2}[(-4\sqrt{2})\bar{\mathrm{f}}_{11\ 1\ 1}4\sqrt{2}\bar{\mathrm{f}}_{9\ 1\ 1} + 4\sqrt{2}\bar{\mathrm{f}}_{9\ 1\ 1}(-4\sqrt{2})\bar{\mathrm{f}}_{11\ 1\ 1}]$$

$$\Psi(\bar{2}0) = -8\sigma H\Delta + 32\sigma^2 H^2\bar{\mathrm{f}}_{11\ 1\ 1}\bar{\mathrm{f}}_{9\ 1\ 1} \qquad \text{(A14)}$$

It is apparent by inspection of equations A13 and A14 that the term in $\bar{2}00$ is π out of phase with the doubly diffracted beams, and that the 200 term is in phase with the doubly diffracted beams. This explains the experimental observation of constructive and destructive interference through 200 and $\bar{2}00$ diffracted beams respectively (for a [011] sample projection).

Alternative diffraction conditions

This microdiffraction experimental technique can now be extended to investigate the effects of different pairs of high order, odd indexed reflections through {200} type reflections. For example, it is relatively simple to observe the interaction of {931} and {731}, and {951} and {751} reflections through {200} type reflections, since only a very small sample tilt is away from the {9 1 1}, {11 1 1} situation is required to set up either of these diffraction condition.

Consideration of the structure factors for the $(\bar{9}\bar{5}1)$, $(7\bar{5}1)$ case, for a [011] sample projection, demonstrates that

$$\Phi(7\bar{5}1) = \Phi(75\bar{1}) = -4\sqrt{2}[\bar{\mathrm{f}}_{751} - \Delta i] \approx -4\sqrt{2}\bar{\mathrm{f}}_{751}$$

and

$$\Phi(\bar{9}\bar{5}1) = \Phi(\bar{9}5\bar{1}) = -4\sqrt{2}[\bar{\mathrm{f}}_{951} - \Delta i] \approx -4\sqrt{2}\bar{\mathrm{f}}_{951}$$

which gives

$$\Psi(\bar{2}0) = -8\sigma H\Delta - 32\sigma^2 H^2 \bar{\mathrm{f}}_{951}\bar{\mathrm{f}}_{751}$$

Similarly, it can be shown that

$$\Psi(20) = +8\sigma H\Delta - 32\sigma^2 H^2 \bar{\mathrm{f}}_{951}\bar{\mathrm{f}}_{751}$$

It is therefore predicted that the interaction of a pair of doubly diffracted {951} and {751} beams, and a pair of doubly diffracted {9 1 1}, {11 1 1} beams would give rise to destructive and constructive interference respectively, following interaction with the *same* {200} reflection (see section 3.8).

REFERENCES

1. J.M. Cowley and A.F. Moodie, Proceedings of the International Conference on Magnetism and Crystallography,, *J. Phys. Soc. of Jpn.* **17 BII** (1962) 86
2. K. Ishizuka and J. Taftø, *Acta Cryst.* **B40** (1984) 332
3. J. Taftø and J.C.H. Spence, *J. Appl. Cryst.* **15** (1982) 60

4. Wide Band-Gap II-VI Compounds

Anisotropic Defect Distribution in (001) Oriented Sphalerite Epitaxial Layers

4.1 Introduction

The commercial demand for visible light emitting materials for flat panel displays and signal applications has promoted the development of electroluminescent (EL) device structures in which light is generated by the application of an electric field. ZnSe and ZnS, with band-gaps of 2.6eV and 3.6eV respectively, are consequently of interest, and have potential application in optoelectronic devices operating in the yellow/blue regions of the spectrum. However, there are a number of problems associated with the crystal growth of these wide band-gap II-VI compounds. Controlled melt growth, for example, is hindered by the effects of sublimation and decomposition at temperatures well below the compound melting points (1830°C and 1520°C for ZnS and ZnSe respectively). Similarly, crystals of the same composition grown at lower temperatures (800-1300°C) by vapour phase techniques are characterised by high defect concentrations and exhibit behaviour nearer to that of insulators than semiconductors (see the review by Cockayne and Wright, 1984).[1] Consequently, low temperature growth ($< 500°C$) by MOVPE is of interest for the production of these materials.

This chapter presents a study of the microstructural defect distribution in epitaxial layers of ZnSe, ZnS and ZnSe/ZnS grown on $\{100\}$ oriented GaAs substrates. Brief details of the MOVPE growth of these epilayers is given in section 4.2, and the anisotropic macroscopic features which hinder the fabrication of d.c. electroluminescent (DCEL) devices from the as-grown ZnSe/ZnS/GaAs layers are introduced in section 4.3. Section 4.4 is concerned with various structural aspects of $\{100\}$ oriented sphalerite crystals. The remainder of this study (section 4.5 to 4.7) describes the anisotropy of the defect microstructure of these epilayers, and these observations are discussed in terms of the differential motion of α and β dislocations. In section 4.8, a short study of sputtered ZnS films on glass substrates is presented, and a comparison is made between growth on transparent conducting oxide buffer layers of cadmium stannate and zinc oxide, which are used as front electrical contacts in EL devices.

4.2 MOVPE growth of ZnSe/ZnS/GaAs

Details of the conditions used for the MOVPE growth of the ZnSe and ZnSe/ZnS layers examined in this work may be found elsewhere.[2,3] (Also, see Table 2.1.) Briefly, however, radio frequency induction was used to heat a SiC coated graphite susceptor while pure hydrogen carried dimethylzinc (Me_2Zn) and either H_2S or H_2Se to a horizontal reaction chamber where the following reactions occurred :

$$(CH_3)_2Zn + H_2S \mapsto ZnS + 2CH_4 \tag{4.1}$$

$$(CH_3)_2Zn + H_2Se \mapsto ZnSe + 2CH_4 \tag{4.2}$$

The high defect content of bulk grown II-VI crystals necessitates the use of better quality III-V compounds as substrates for epitaxial growth and GaAs is the most suitable candidate due to its relatively low cost and wide availability. Before being loaded into the reactor, GaAs substrates were polished to a mirror finish, degreased with boiling propan-2-ol and blown dry with filtered nitrogen, and then etched for 20 minutes in a 5:1:1 solution of H_2SO_4:H_2O_2:H_2O, rinsed with deionised water and blown dry from boiling propan-2-ol. Substrates were then flushed with purified hydrogen for 15 minutes and given a 10 minute bake-out at 500°C. The temperature was then reduced to around 275°C for epitaxial growth. The growth of a ZnS I-layer of thickness 0.2μm took about 2 to 3 minutes for a H_2S flow rate of 80cm^{3}min^{-1}. The reaction chamber was then flushed with hydrogen for a further 2 minutes to expel residual H_2S. During the subsequent growth of ZnSe, low reactant concentrations of typically $2 \times 10^{-4} H_2Se$ and 5×10^{-5} Me_2Zn mole fractions and high flow rates of approximately 4.5lmin^{-1} were established to minimise the effects of premature reaction.

4.3 ZnSe/ZnS MIS Electroluminescent Devices*

MOVPE grown ZnSe/ZnS epitaxial layers on (001) oriented GaAs have been used in this laboratory to fabricate a novel DCEL device, the geometry of which was designed to investigate the electrical and optical properties of II-VI epitaxial layers in the absence of influence from the substrate material.[4] Also, use of the MOVPE technique facilitates the deposition of high quality, single crystal films which are free of the impurities commonly associated with devices formed from sputter deposited material (see section 4.8). A number of (001) ZnSe/ZnS/GaAs samples were investigated, with ZnSe layers roughly 3μm in thickness and a range of ZnS I-layer thicknesses (0.2 to 0.9μm). Devices were fabricated as shown in figures 4.1a and 4.1b. The ZnS I-layer acted as an etch stop during the chemical removal of the GaAs substrate using an etch of composition 95% H_2O_2 (100vol) to 5% NH_3 (35% solution). The main advantage of the MOVPE grown single crystal material employed in this device configuration is the greater uniformity in spatial distribution of the electroluminescence obtained as compared with the equivalent polycrystalline devices for which the electroluminescence is localised at a few scattered bright spots[5] (see section 4.9).

Cracking of thick ($\gtrsim$ 1μm) ZnS layers in just one < 110 > direction following substrate removal was a common problem encountered during the device fabrication process. The as-grown ZnSe/ZnS/GaAs layers also exhibited surface faceting with ridges oriented predominantly along only one < 110 > direction (see section 4.6). The observation of these macroscopic features prompted a microstructural study of the defect distribution in the as-grown ZnSe/GaAs, ZnS/GaAs and ZnSe/ZnS/GaAs epitaxial layers. This investigation was made using the combined techniques of Scanning Electron Microscopy (SEM), Reflection High Energy Electron Diffraction (RHEED), Transmission Electron Microscopy (CTEM) and microdiffraction.

⋆ The DCEL devices descibed here were fabricated by Dr. A.P.C. Jones, now at B.T. and D., Ipswich

4.4 Structural Aspects of Wide Band-Gap II-VI Heteroepitaxial Layers

It is known that band-gap luminescence in semiconducting compounds is readily quenched by dislocations and stacking faults.[6] These defects act as scattering centres for the charge carriers[7] and hence, lead to a reduction in device efficiency. Consequently, there is a need to gain structural information on the type and nature of defects which are formed during heteroepitaxial growth. In view of the macroscopic effects of polarity in sphalerite materials it might also be expected that the differences in growth rates of $\{111\}$ A and $\{\bar{1}\bar{1}\bar{1}\}$B planes, coupled with the differences in the velocities of α and β dislocations, would be manifested in the form of some anisotropic distribution of the defect content of sphalerite materials. Indeed, recent TEM studies of micro-indentation deformed (001)GaAs surfaces revealed the formation of perfect α-dislocations along the [110] rosette arm, while the orthogonal $[1\bar{1}0]$ direction corresponding to the projection of partial β-dislocations, was characterised by the formation of mechanical microtwins.[8] The dependence of the relative velocity of dislocations on material doping is also recognised (see section 4.7). In addition, De Cooman and Carter[9] note the influence of dislocation polarity in ion implanted epitaxial layers of GaAs and (Al,Ga)As to explain the observation that stacking fault tetrahedra imaged in the [110] direction pointed more often in the [001] growth direction than the $[00\bar{1}]$ direction.

Most of the structural studies of wide band-gap II-VI epitaxial layers in the literature report High Resolution Electron Microscope (HREM) observations. Epitaxial layers of the $\{100\}$ orientation grown by MOVPE which have been investigated include ZnSe on GaAs[6] [7] [10] and Ge,[11,12] along with $ZnSe_yS_{1-y}$ on GaAs, GaP and Ge.[13] In addition, there have been a number of CTEM studies of MBE grown layers of ZnSe/GaAs[14,15] and of MOVPE grown ZnSe/ZnS/GaAs.[16,17] Several of these studies[6] [7] [10] [12] [13] describe defects which are now thought to be artefacts of the sample preparation process.[18] Stutius and Ponce[7] report the dependence of ZnSe photoluminescence (PL) on substrate orientation. Growth in the $< 100 >$ direction produced defects which were similar to isolated compensating centres, while epilayers grown on $\{110\}$ and $\{111\}$ substrate orientations exhibited extended defects and grain boundaries. Twinning parallel to the epilayer/substrate for the $\{111\}$ epitaxial orientation heavily reduced the material PL efficiency. No microtwins were found in the $\{100\}$ layers while growth on the $\{110\}$ oriented substrate led to the production of a high density of microtwins on just one of the inclined $\{111\}$ planes.

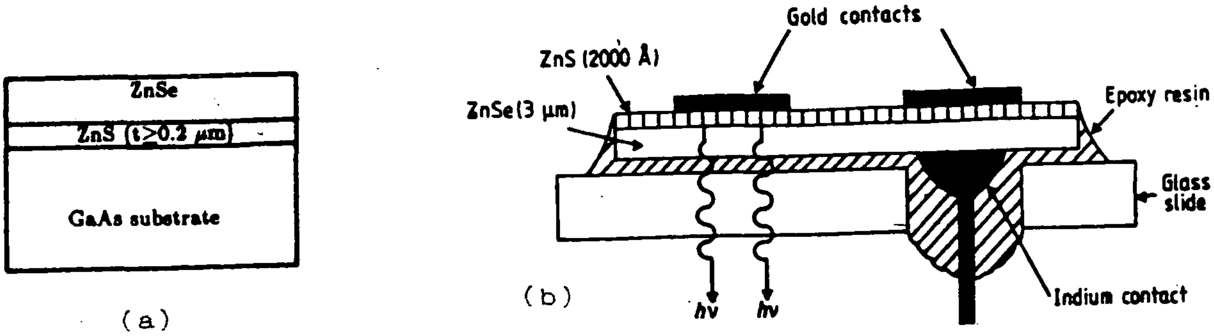

Figure 4.1 a) MOVPE grown ZnSe/ZnS heterostructure on (001)GaAs
b) DCEL device ref [22]

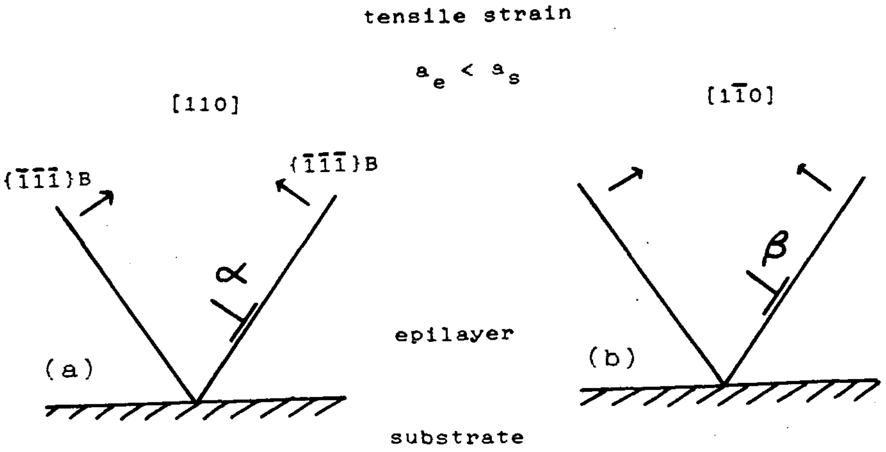

Figure 4.2 For the condition $a_e < a_s$, extra planes of atoms lie in the epilayer which is under tensile strain:- a) For the [110] layer projection, α dislocations are associated with advancing $\{\bar{1}\bar{1}\bar{1}\}$B epilayer planes, while b) β dislocations are associated with advancing {111}A planes in the orthogonal $[1\bar{1}0]$ layer projection.

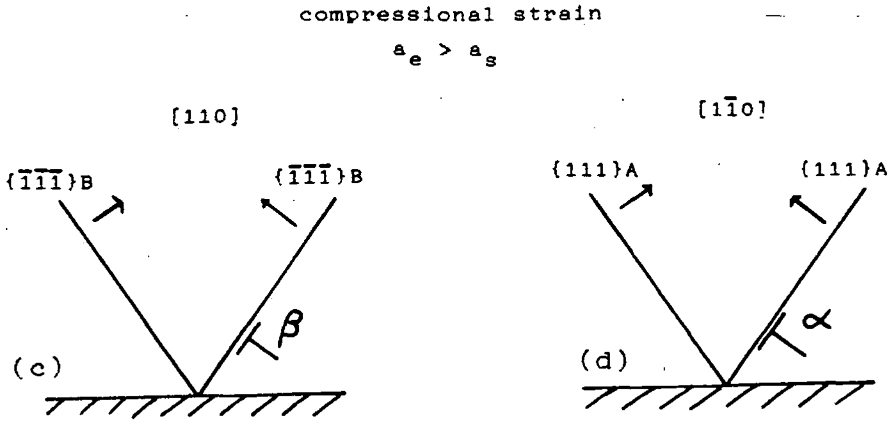

For the condition $a_e > a_s$, extra planes of atoms lie in the substrate and so, the epilayer is under compressional strain. c) For the [110] layer projection, β dislocations are associated with advancing $\{\bar{1}\bar{1}\bar{1}\}$B planes, while d) α dislocations are associated with advancing {111}A planes in the orthogonal $[1\bar{1}0]$ layer projection.

Only three investigations[7] [16] [17] have been concerned with the in-plane anisotropy of the defect distribution of these wide band-gap epitaxial layers. It is proposed to address this problem further and indicate factors which might influence this phenomenon in {100} oriented sphalerite epitaxial layers (see section 4.7).

Consideration must also be given to the influence of tension and compression on heteroepitaxial layers. The associated lattice parameter, a_o, of the cubic materials under investigation are 5.6535Å, 5.4093Å and 5.6686Å* for GaAs, ZnS and ZnSe respectively. Hence, epitaxial ZnS on (001) GaAs is characterised by a lattice mismatch of -4.3% and is in biaxial tensile strain. In contrast, ZnSe on (001) GaAs has a small +0.27% lattice mismatch and is in a state of biaxial compressional strain. Further, epitaxial ZnSe on ZnS has a mismatch of +4.8% and is under compressional strain. The components of tension and compression in heteroepitaxial layers influence the type of dislocations that are generated to relieve interfacial strain.[9] This in turn might affect the orientation and nature of larger crystallographic defects which are subsequently formed.

In particular, for the [110] projection of an (001) epilayer under tensile strain ($a_e < a_s$) extra planes of atoms lie in the epilayer and so correspond to α dislocations lying on advancing $\{\bar{1}\bar{1}\bar{1}\}$B planes (figure 4.2a). Whereas, β dislocations are associated with advancing {111} A planes in the orthogonal $[1\bar{1}0]$ direction (figure 4.2b). Conversely, for an epilayer under compressional strain ($a_e > a_s$), extra planes of atoms are introduced into the epilayer from the substrate and these correspond to β and α dislocations for the [110] and $[1\bar{1}0]$ sample orientations respectively (figures 4.2c and 4.2d). In view of the differences in velocities of these α and β dislocations (see section 4.7) the geometry of any defect anisotropy will depend on whether or not the epilayer is under tension or compression.

4.5 Experimental

Several epitaxial layers of ZnSe, ZnS and ZnSe/ZnS on (001) oriented GaAs have been investigated. The techniques of RHEED and SEM were used to monitor the surface properties of the as-grown layers. The former was performed in a JEM-120 electron microscope operated at 100kV and observations of as-grown surfaces were made along orthogonal < 110 > directions. The GaAs substrates were subsequently etched for the purpose of uniquely identifying the [110] and $[1\bar{1}0]$ directions.[19] Degreased substrates

---

* room temperature

were chemically polished and immersed in the Sirtl etch for approximately 4 minutes at room temperature. This process produced rectangular etch hillocks whose long axis lay along [110][19] on the GaAs $(00\bar{1})$ surface and these directions were correlated with the RHEED observations.

TEM samples were prepared in cross-section using the technique of Chew and Cullis[18] with a minor, but significant, modification. Throughout this study, the first process in the preparation of specimens for TEM investigation was to cleave the samples along orthogonal {110} planes lying mutually perpendicular to the surface (figure 4.3) By virtue of this novel specimen preparation technique, regions of electron transparent material across the glue line correspond to the projection of two orthogonal < 110 > zone axes. This allows a direct comparison of the defect structure of (110) and $(1\bar{1}0)$ slices to be made for the same epilayer using a single TEM sample.

Crystal polarity was independently determined in the electron microscope using the technique of microdiffraction as described in section 3.3. Once determined, it is then possible to assign either a [110] or $[1\bar{1}0]$ projection to each layer orientation assuming an [001] growth direction.

4.6 Results

ZnSe/GaAs

The SEM micrograph shown in figure 4.4, taken from a ZnSe epilayer grown on a {100} oriented GaAs substrate, illustrates the formation of surface facets which are found to give rise to ridges that lie predominantly along one < 110 > direction. This observation is similar to that previously reported for MOVPE grown of ZnSe.[20]

A more detailed investigation of the ZnSe/GaAs epitaxial system was performed using the technique of cross-sectional TEM. Figure 4.5a illustrates the presence of a large number of linear defects lying on two sets of {111} planes at roughly 55^o to the epilayer/substrate interface. These defects give rise to extra spots at $\frac{1}{3}a_o < 110 >$ positions in their associated SAD patterns (figure 4.5b) and these extra spots show slight streaking along the < 111 > directions which is indicative of the very thin nature of the defects concerned. Dark field imaging using the two types of additional spots (aligned along two different < 111 > directions) produced the micrographs shown in figures 4.5c

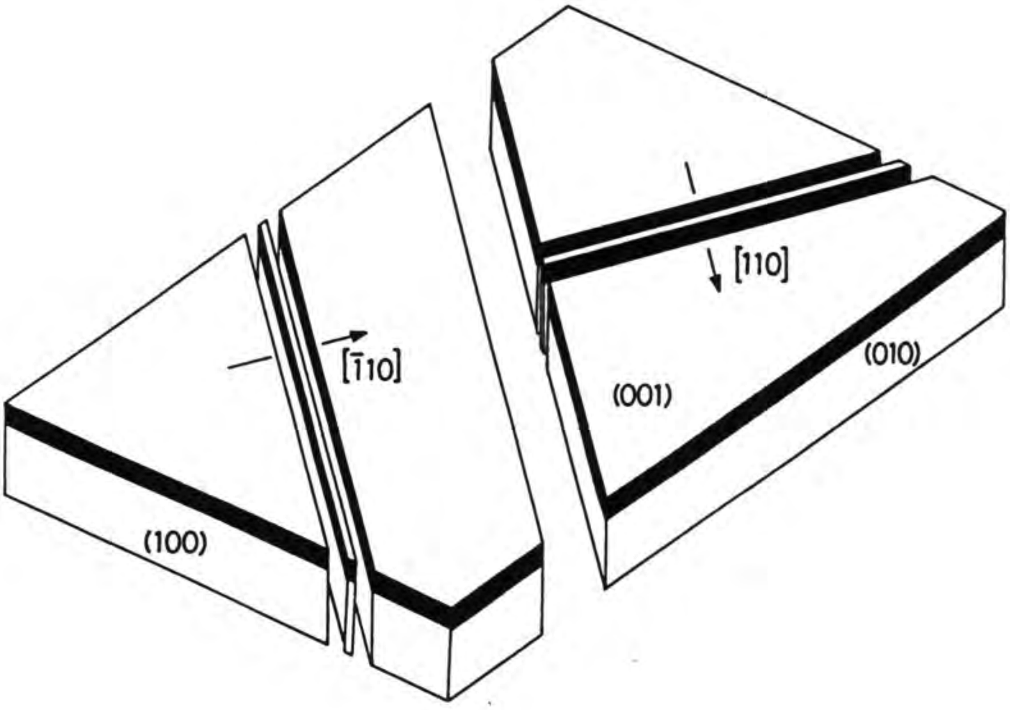

Figure 4.3 Two strips of material are cleaved along orthogonal <110> directions prior to TEM sample preparation. This facilitates the observation of two orthogonal <110> projections of the epilayer across the glue line for the same TEM sample.

Figure 4.4 SEM micrograph showing the surface of a ZnSe/(001)GaAs sample. The facets lie predominantly along one <110> direction. (Figure provided by Dr. A.P.C. Jones (APCJ))

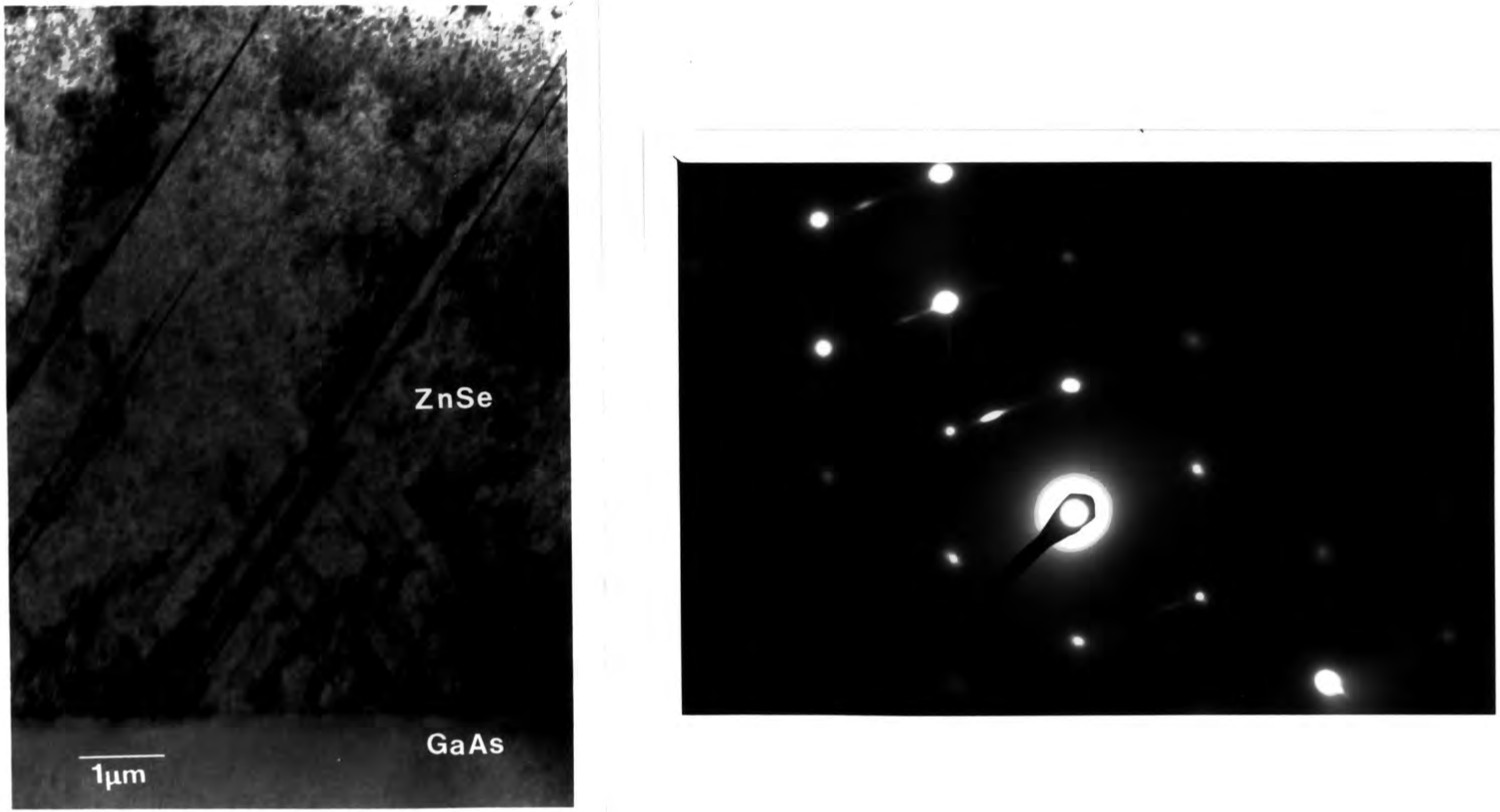

(a)

(b)

Figure 4.5 a) Bright field TEM micrograph of ZnSe/(001)GaAs
b) SAD pattern showing the presence of additional spots in $1/3\ a_o\langle 111\rangle$ positions.

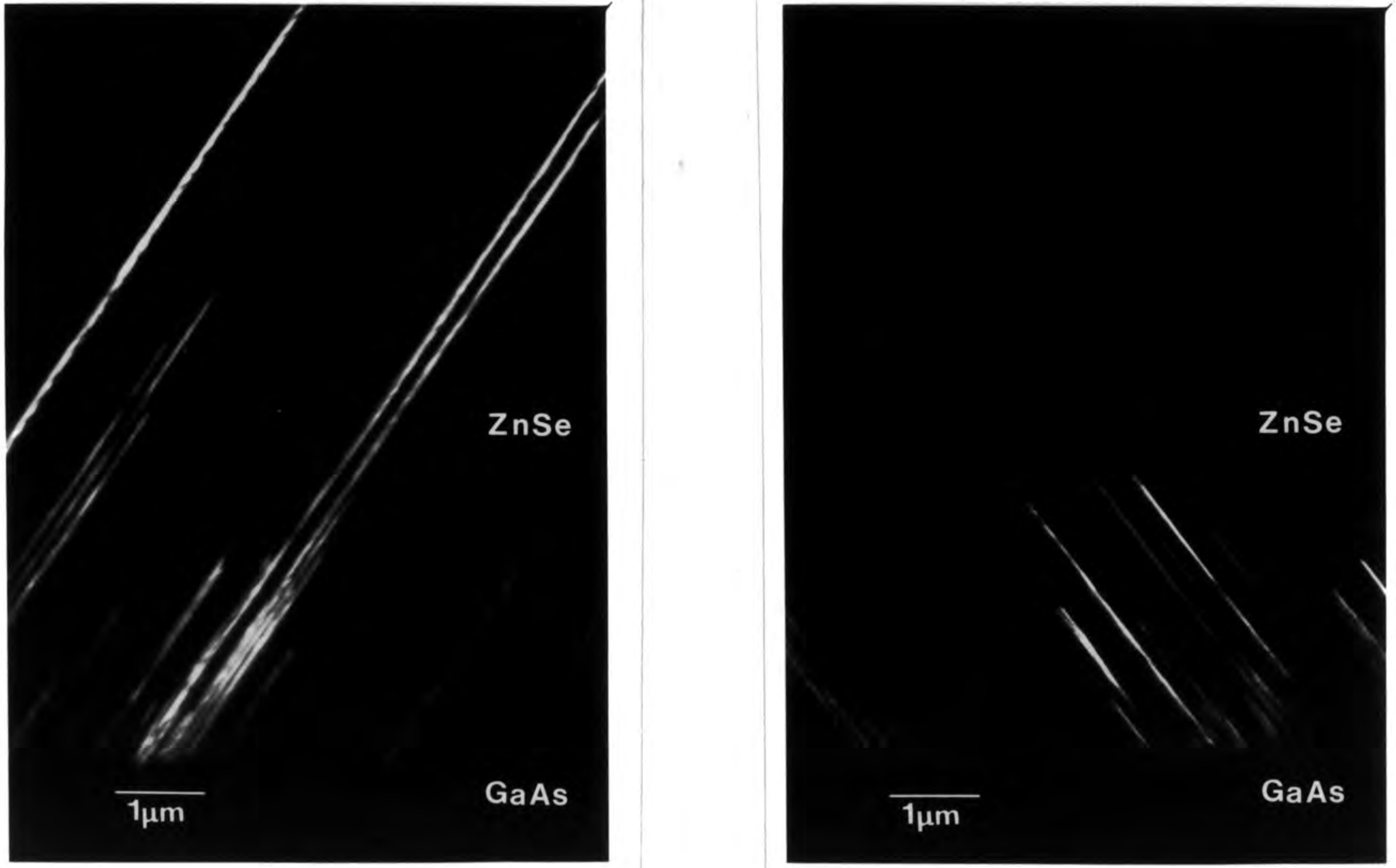

(c)

(d)

Figures 4.5c and d Dark field micrographs, obtained using the additional spots in the SAD pattern, taken from the same sample region as figure 4.5a. Bright contrast delineates the linear features which confirms that the defects are microtwins.

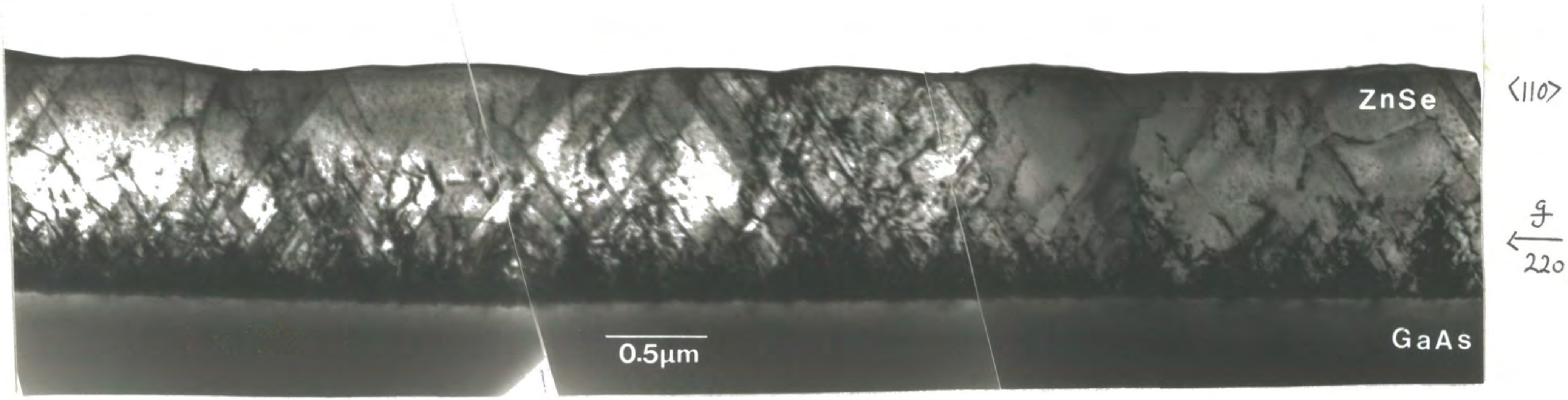

<u>Figure 4.5e</u> ZnSe/(001)GaAs

and 4.5d respectively. These micrographs clearly illustrate that the linear defects are responsible for the presence of these extra spots in the diffraction pattern and confirm that the defects are microtwins.[21] In addition, there is a network of misfit dislocations, most of which grow out within $0.2\mu m$ of the interface. It should be mentioned that there is a greater number of defects present (roughly $\times 10$) than can be accounted for by just misfit (0.26%) alone.* This implies that these substrates were not completely desorbed prior to epitaxial growth (see section 4.7). Also, the relatively large number of additional dislocations initiated during layer growth (figure 4.5e) suggests the disruption of the crystal lattice by impurities or unwanted reaction products during the MOVPE growth of this material.** Observation of these ZnSe/GaAs epitaxial layers along two orthogonal $< 110 >$ directions revealed a comparable number of microtwins for each layer projection.

ZnS/GaAs

Similar investigations were also made of a $0.2\mu m$ ZnS layer grown on (001)GaAs. The layer surface morphology was fairly uniform[22] with a slight orange peel type texture. However, observation in the TEM revealed a major difference in the defect content along the two orthogonal $< 110 >$ directions. As shown in figures 4.6b and 4.6a respectively, the $[1\bar{1}0]$ projection contains a large number of inclined microtwins, while there is a distinct absence of these defects from the $[110]$ layer projection. In addition, it is noted that the microtwins had a strong tendency to lie just on one of the two sets of advancing $\{111\}$ planes.

ZnSe/ZnS/GaAs

The ZnS I-layers of the ZnSe/ZnS/GaAs heterostructures used to fabricate DCEL devices were doped with $\approx 0.1\%$ Mn (see section 4.7), which is favoured for these EL devices because of its large impact ionization cross-section and its associated high radiative lifetimes. However, the ZnSe/ZnS/GaAs samples used for the following TEM investigation were nominally undoped. During the device fabrication process (section 4.3), the GaAs substrate was chemically removed to permit contacts to be made directly to the ZnS I-layer. For samples with an I-layer thickness $\gtrsim 1\mu m$, cracking was found to occur in one of the $< 110 >$ directions (figure 4.7). Further, when substrates of samples with an I-layer thickness less than $0.2\mu m$ were etched, areas of the ZnS layer became exposed to the etchant in a non-uniform fashion, and so some regions of the

---

* Unfounded speculative statement. In order to determine the extent to which a heteroepitaxial layer has relaxed, detailed knowledge of the Burgers vector of each type of defect accommodating this relaxation is required.

** While it is recognised that additional dislocations may be generated during the process of epilayer growth, it is also noted that the observation of isolated dislocations away from the interface may also correspond to the intersection of interfacial dislocations (nucleated outside the sample foil) with the sample foil.

(a)

Figure 4.6 ZnS on (001)GaAs observed along a) [110] and b) [11̄0].

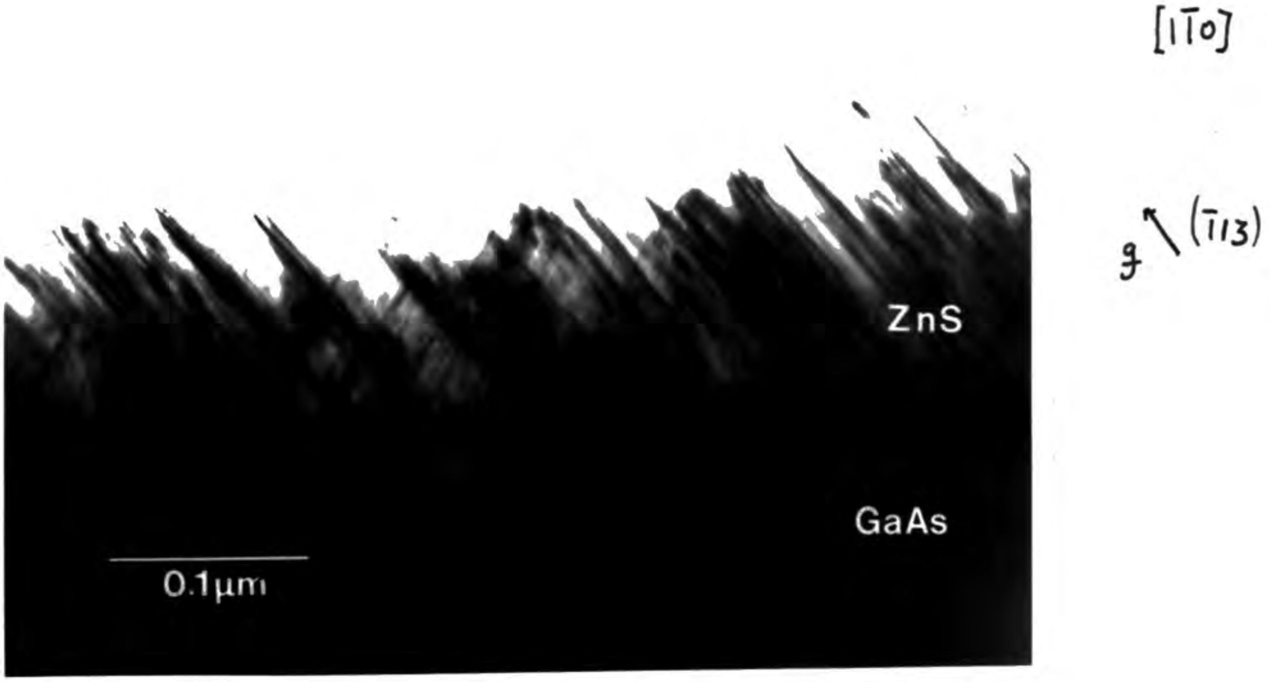

(b)

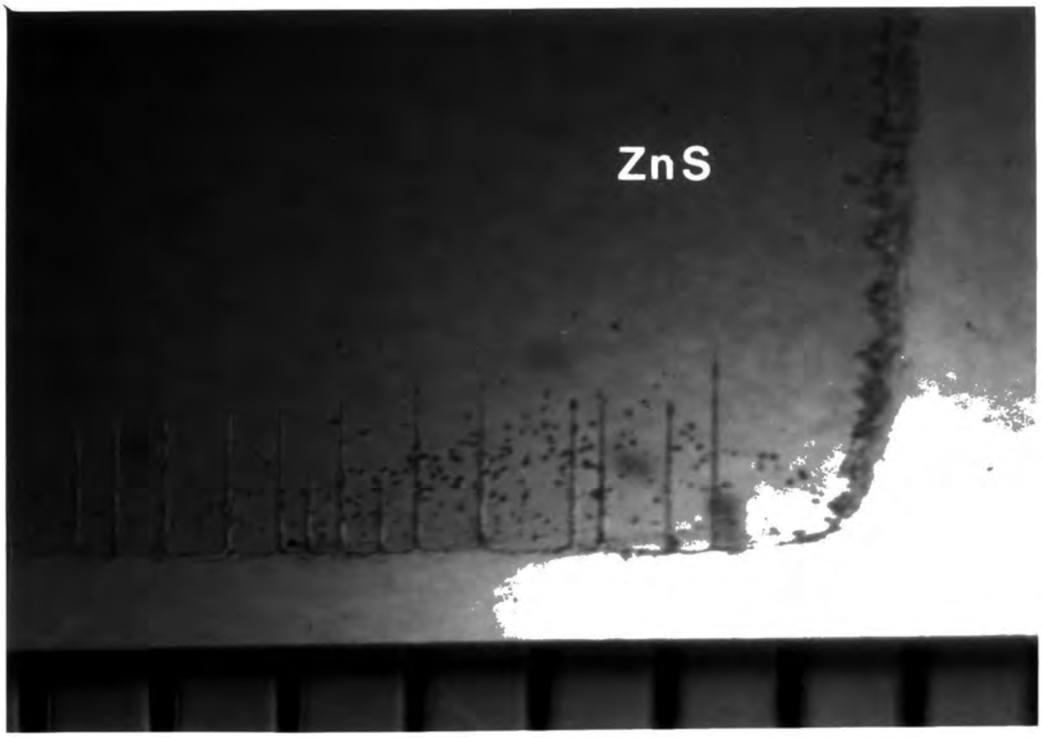

Figure 4.7 Optical photograph showing the uniaxial cracking of the ZnS I-layer along one <110> direction. (Figure provided by APCJ.)

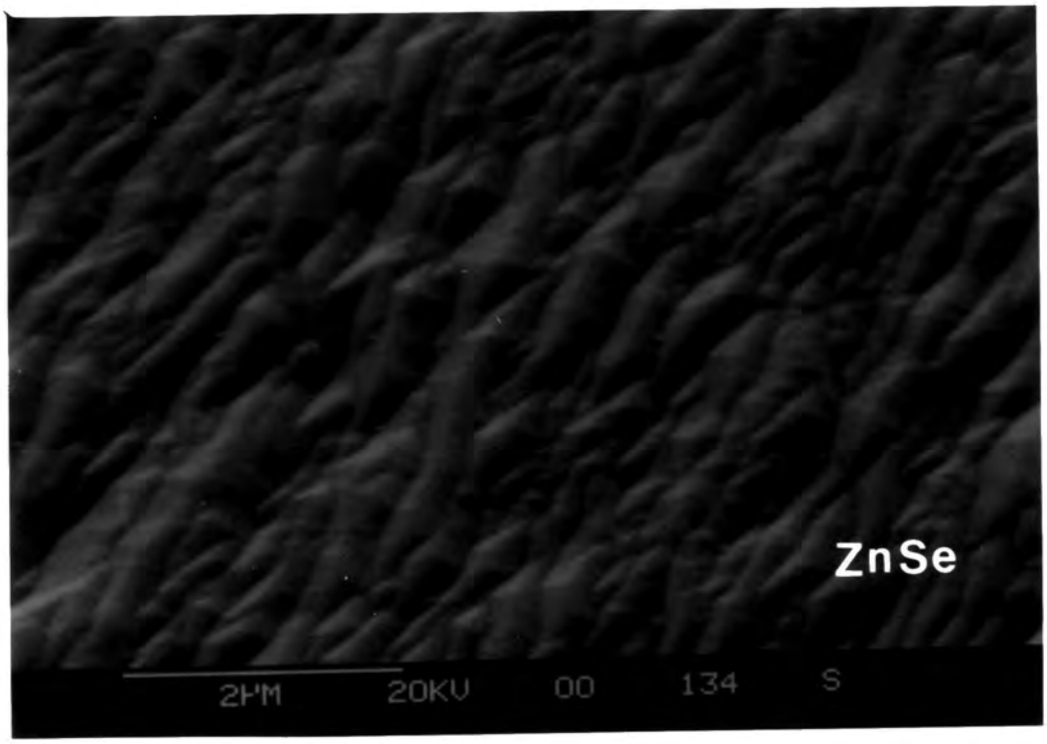

Figure 4.8 SEM micrograph of the surface of a ZnSe/ZnS/GaAs sample showing ridge shaped growth features oriented preferentially along one <110> direction.

ZnS film received prolonged exposure to the etchant which caused layer perforation followed by rapid chemical attack of the ZnSe underneath. The ZnSe was observed to be etched in an anisotropic manner and the films were rendered useless for device fabrication.[22] SEM observations also revealed surface faceting of these as-grown heterostructures (figure 4.8). Devices fabricated from ZnSe/ZnS/GaAs samples were shown to exhibit an increasingly improved spatial distribution of electroluminescence as the ZnS I-layer thickness was increased from 0.2μm to 1μm.[22] This finding was in contradiction to theoretical predictions for these DCEL devices which suggested that the optimum ZnS:Mn thickness for luminescence was around 0.2μm.[22] This coupled with the macroscopic phenomenon which hindered the formation of devices instigated a microstructural study of four ZnSe/ZnS/GaAs samples for a range of I-layer thicknesses (0.2 to 0.9μm).

A pair of RHEED patterns taken from an (001) ZnSe surface of a ZnSe/ZnS heterostructure along orthogonal [110] and $[1\bar{1}0]$ projections is shown in figures 4.9a and 4.9b. The sample orientations corresponding to these patterns were uniquely determined with reference to the rectangular etch features produced on the reverse side of the GaAs substrate (figure 4.10).[19] Both RHEED patterns contain distinct spots which are indicative of the excellent crystallinity of these layers. However, it can be clearly seen that the $[1\bar{1}0]$ pattern, which corresponds to advancing {111}A planes in the (001) sphalerite layer, contains extra spots at $\frac{1}{3}a_o < 111 >$ positions. These extra spots indicate the presence of microtwins lying on {111} planes inclined at 54^o 44' to the epilayer/substrate interface. The relatively strong intensity of these extra spots suggests that these defects are present in large numbers. No such twin spots are contained in the orthogonal [110] pattern, and hence, these RHEED observations alone indicate that there is strong anisotropy in the distribution of defects in these ZnSe/ZnS epitaxial layers.

A more detailed study of this system was undertaken using cross-sectional TEM. Figures 4.11a and 4.11b illustrate the interfacial defect content for a sample in the [110] and $[1\bar{1}0]$ projections respectively for a ZnS I-layer thickness of 0.9μm. The difference between the two micrographs is quite apparent. The $[1\bar{1}0]$ orientation (figure 4.11b) is characterised by a large number of linear defects viewed edge on lying at $\approx 55^o$ to the interface. The associated diffraction pattern, which was similar to that obtained by RHEED with extra spots in $\frac{1}{3}a_o < 111 >$ positions, establishes the defects as being microtwins. Most of the defects appear to be generated at the ZnS/GaAs interface along with a number of misfit dislocations. The majority of the microtwins continue through

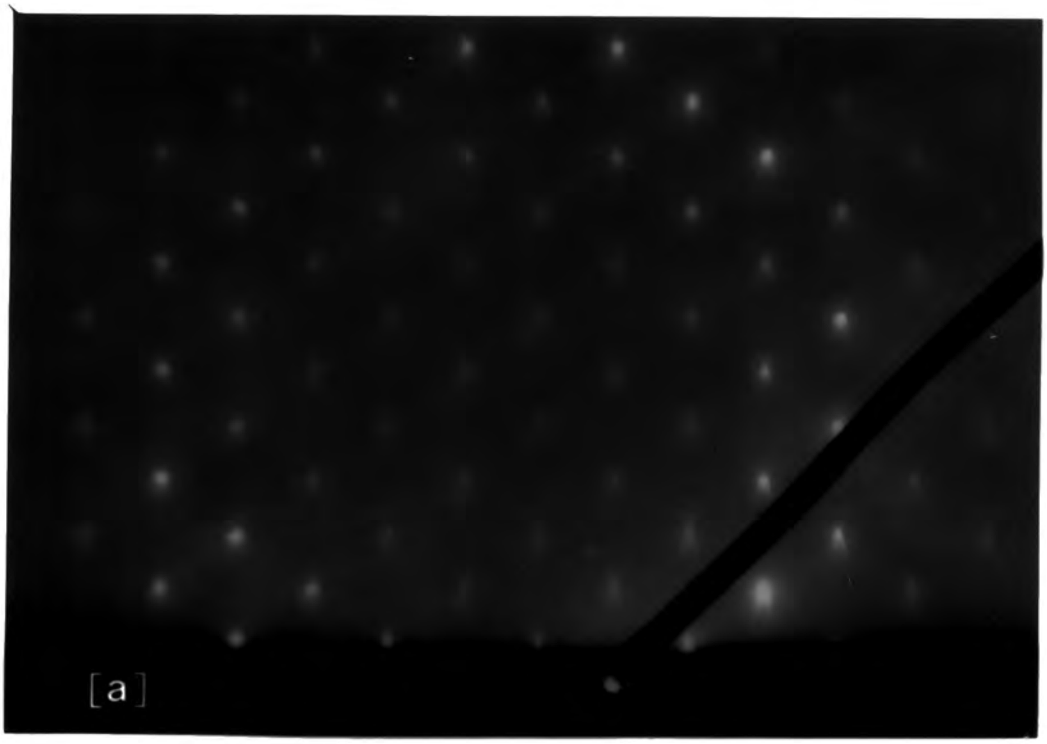

(a)

Figure 4.9 RHEED patterns taken from the surface of a ZnSe/ZnS heterostructure on (001)GaAs showing the a) [110] and b) [$1\bar{1}0$] projections.

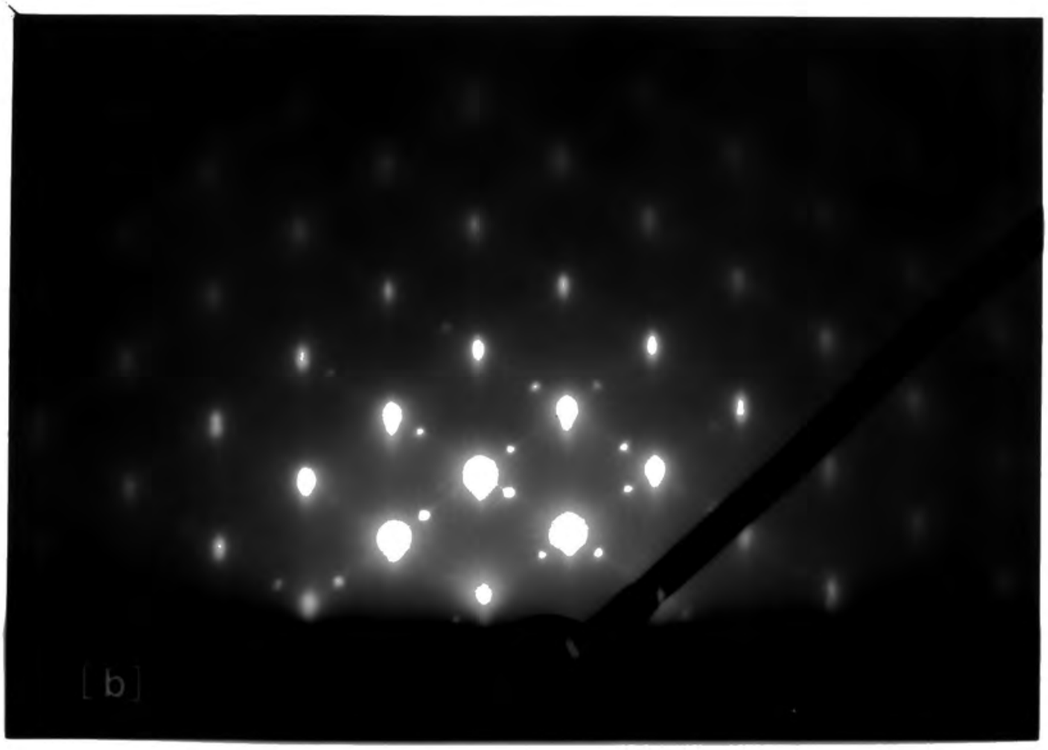

(b)

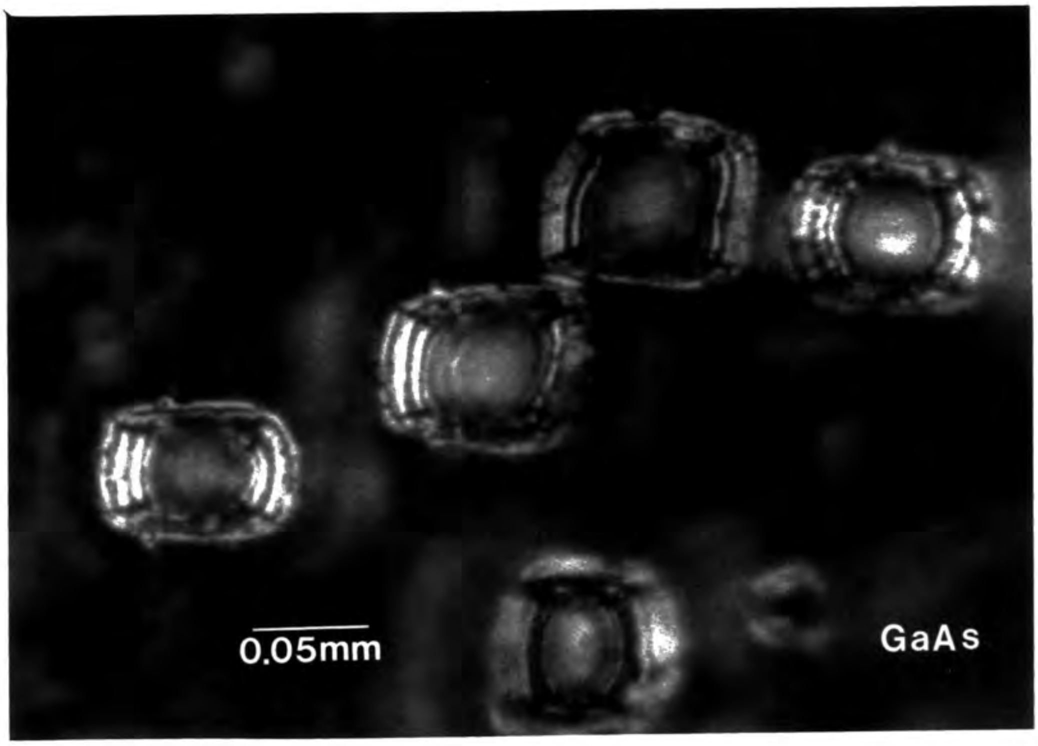

Figure 4.10 Optical micrograph showing the rectangular etch hillocks produced by the Sirtl etch on the $(00\bar{1})$GaAs surface.

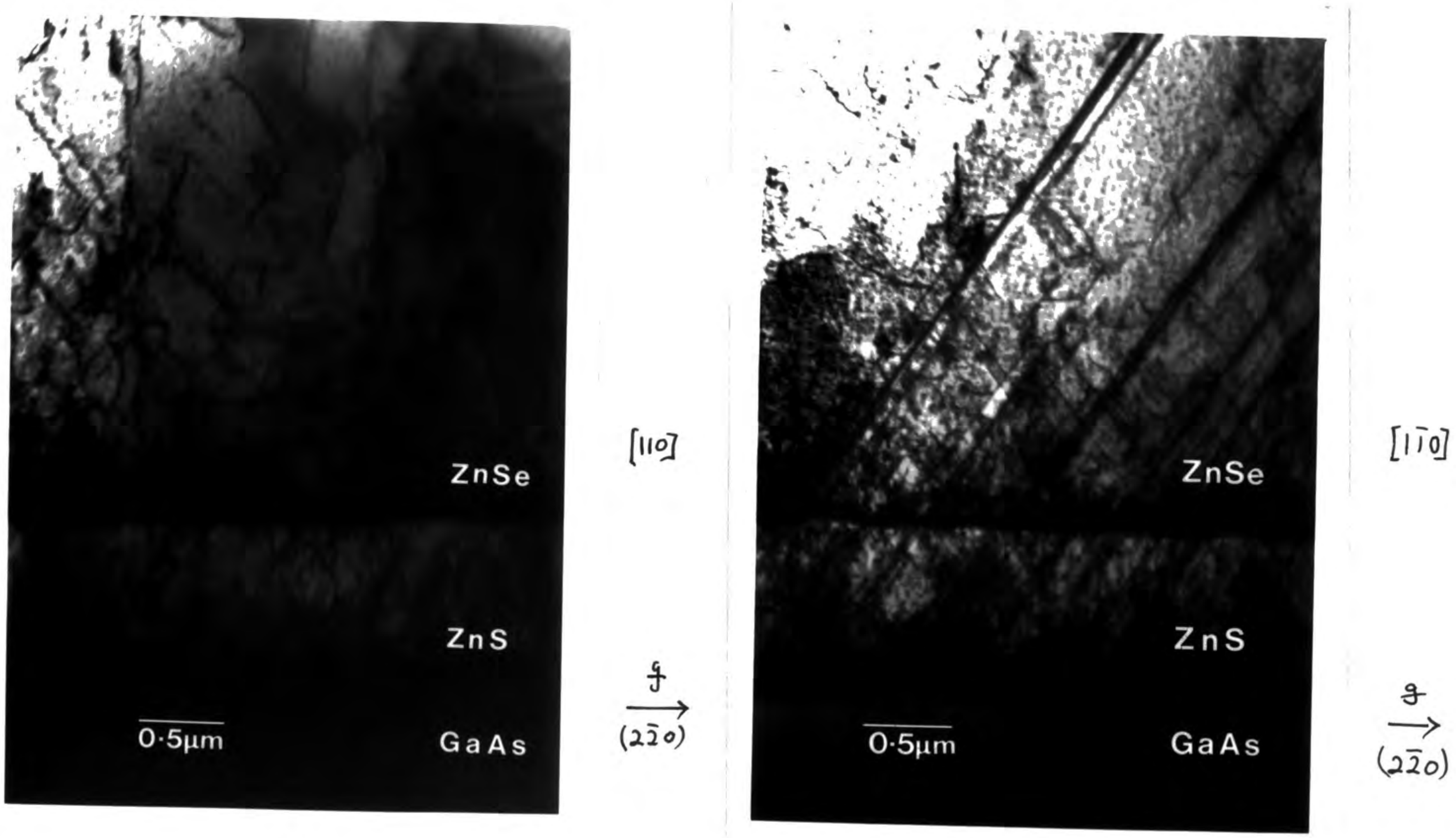

(a)

(b)

Figure 4.11 ZnSe/ZnS heteroepitaxial layers on (001)GaAs viewed along a) [110] and b) [1$\bar{1}$0].

the ZnSe/ZnS interface, where a network of misfit dislocations is also generated, and many are propagated through the entire epilayer. A small number of the microtwins are found to terminate at the ZnSe/ZnS interface. In complete contrast, there is a notable absence of microtwins in the [110] projection (figure 4.11a). Instead, misfit dislocations initiate at both the ZnS/GaAs and ZnSe/ZnS interfaces. Epitaxial layers in the [110] orientation also contain several features which exhibit fringe contrast parallel to the epilayer/substrate interface (figure 4.12). These arise due to the observation of microtwins lying on {111} planes inclined to the electron beam (*i.e.* the linear defects which are seen edge on for the $[1\bar{1}0]$ projection). The background speckle effect in these micrographs is probably due to the presence of small dislocation loops which are artefacts of the sample preparation process.[18] This anisotropic defect distribution was found in all of the layers investigated, irrespective of the ZnS I-layer thickness, and so is unrelated to variations in the spatial distribution of electroluminescence in the devices. In addition, for some samples there was a strong suggestion that the microtwins lay preferentially on just one of the two advancing {111}A planes.

This anisotropic defect distribution is illustrated more clearly by the low magnification micrograph shown in figure 4.13. It shows regions of the ZnSe surface for the [110] and $[1\bar{1}0]$ projections on opposite sides of the glue line. The top area of this micrograph which contains dislocations only, corresponds to the section for which the beam is parallel to [110] and exhibits a straight, linear surface. In contrast, the lower region in which the beam is parallel to $[1\bar{1}0]$, clearly shows microtwins running through to the sample surface and demonstrates that these defects are seen edge on in the same projection as that in which the surface facets are observed. The angles of intersection of the surface facets were measured using the microtwin defects as a reference and the surface facets were found to be advancing {411}A and {511}A type planes.

Microdiffraction patterns were obtained from the GaAs substrate and from regions of the ZnSe epilayer for both $< 110 >$ projections. Figures 3.6a and 3.6b illustrate schematically the diffraction conditions used to observe constructive and destructive interference effects through the (002) and $(00\bar{2})$ reflections, respectively, for a [110] layer projection. Examples of these patterns for this layer orientation taken from the ZnSe and GaAs regions of a sample are shown in figures 4.14a and 4.14b. Correction for the effects of image rotation introducd by the microscope (section 3.4), allowed the sense of the advancing {111} planes for each $< 110 >$ sample projection to be unambiguously

Figure 4.12 Region of the ZnSe epilayer for the [110] projection, showing features exhibiting fringe contrast, arising from the intersection of inclined microtwins with the sample foil.

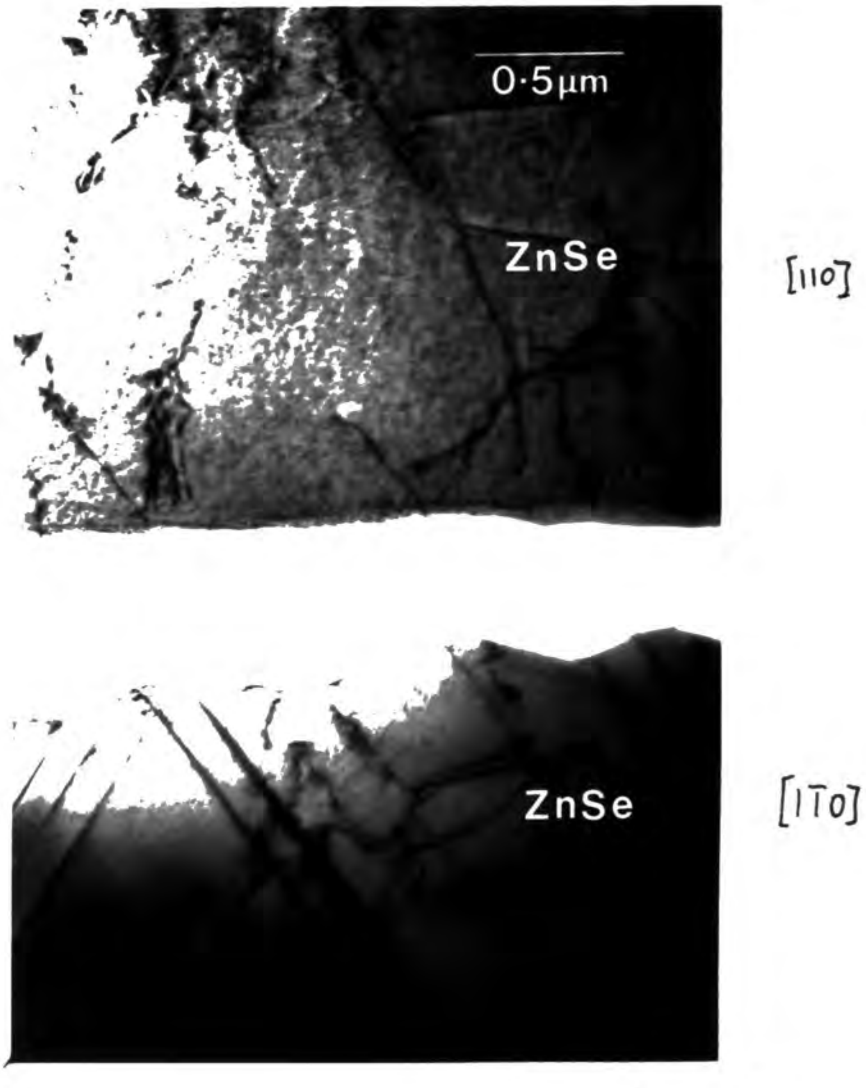

Figure 4.13 ZnSe observed across the glue line showing both [110] and [$1\bar{1}0$] epilayer projections

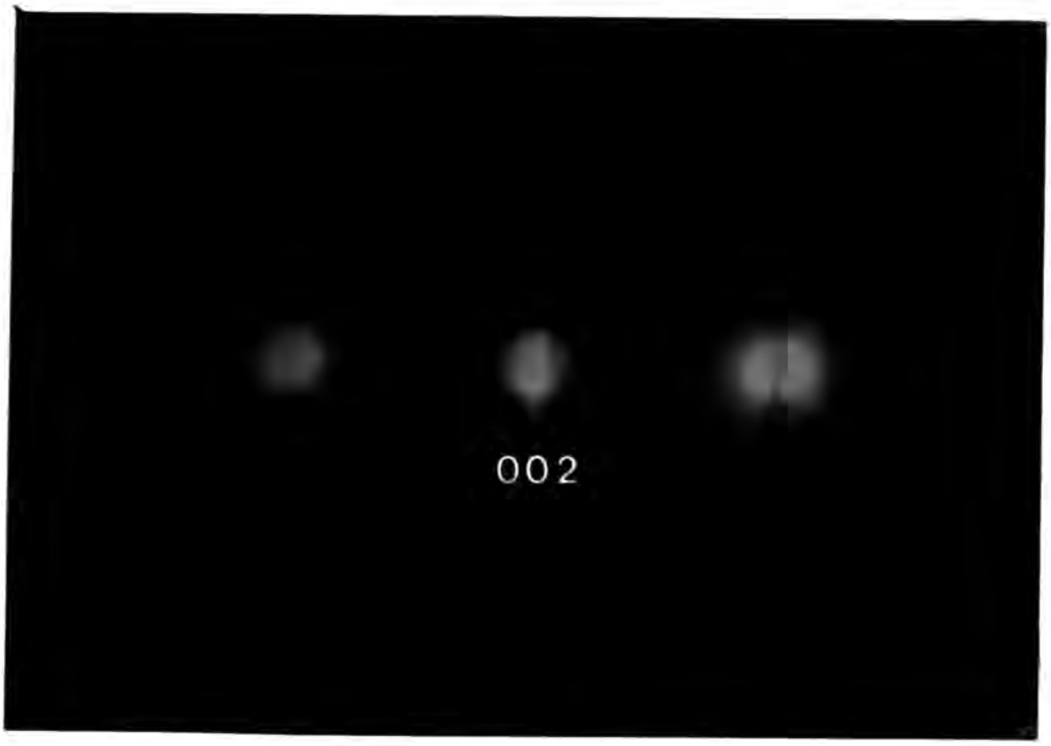

(a)

Figure 4.14 Microdiffraction patterns taken from a) the ZnSe epilayer showing constructive interference through an (002) reflection and b) the GaAs substrate showing destructive interference through an (00$\bar{2}$) reflection.

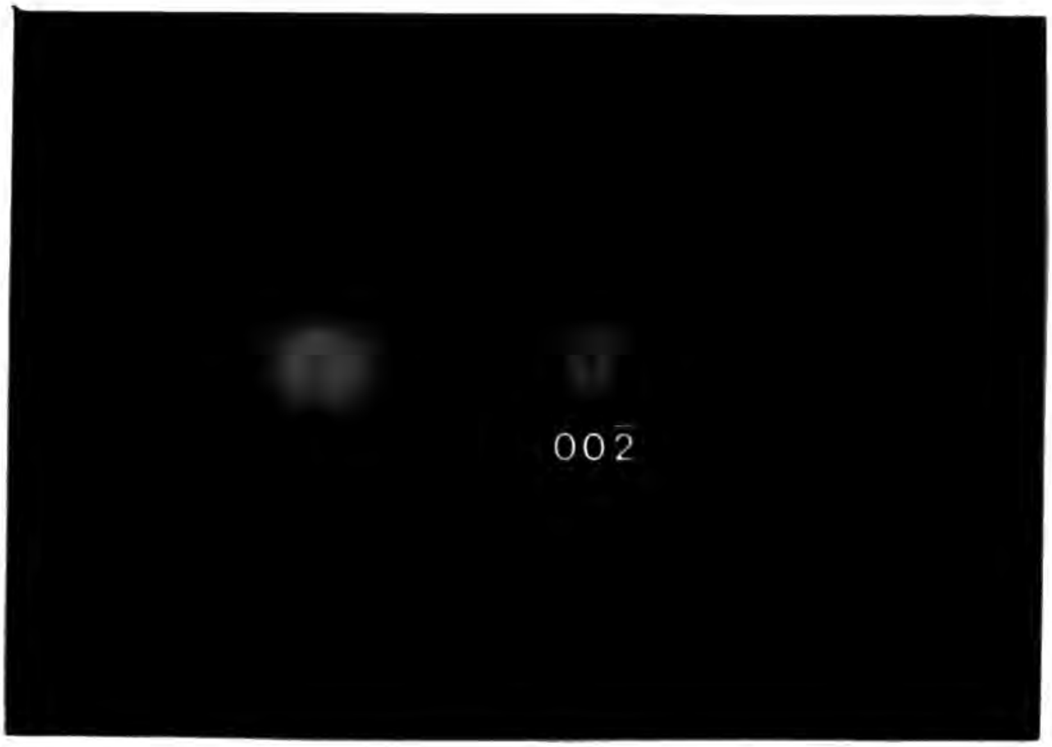

(b)

determined. It was found that the microtwins seen in figure 4.11b lay on advancing {111}A planes which is consistent with their independently determined orientation from substrate etching (figure 4.10). Also, identical microdiffraction patterns were obtained from the GaAs substrate and ZnSe epilayer material for the same diffraction conditions which indicates that this ZnSe/ZnS/GaAs crystal system undergoes parallel epitaxy (*i.e.* that the $< 110 >$ direction in the substrate corresponds to the same $< 110 >$ direction in the epilayer material (see section 5.5)). Investigation of the ZnS sample regions led to the production of indistinct microdiffraction patterns, which is consistent with the prediction that the technique is only suitable for use with compounds where the ions exhibit comparable atomic scattering factors (see section 3.3).

4.7 Discussion

The schematic diagram shown in figure 4.15 is included to summarize the results of this study. Specimen polarity was determined independently by substrate etching and microdiffraction techniques, the results of which were correlated with RHEED and TEM observations respectively. These studies demonstrate that the microtwins in ZnSe/ZnS epitaxial layers on (001) oriented GaAs lie exclusively on advancing {111}A planes. This result is in contradiction with previously reported observations.[16] [7] It is noted that a similar anisotropic distribution of microtwins, lying only on advancing {111} A planes, has very recently been reported for MBE grown epitaxial MCT/CdTe on {100}(Cd,Zn)Te substrates[23]

Microtwins are likely to form due to a number of different causes. Stutius and Ponce[7] demonstrated that microtwins in ZnSe on GaAs usually originate at contaminants or imperfections at the epilayer/substrate interface. These nucleation sources are likely to arise from substrate roughness or from incomplete desorption of the GaAs surface oxide layer prior to epitaxial growth. However, studies of the initial growth stages of ZnSe on {100} GaAs using TEM[15] and X-ray[24] techniques indicate that plastic deformation of the epitaxial layers occurs only when they exceed a certain critical thickness (0.2 to 0.5μm). Layer relaxation, followed by misfit dislocation and microtwin formation[15] are subsequently found to occur. Hence, there is evidence to suggest that microtwins also originate in epitaxial layers due to deformation processes. The observation of a highly faulted defect structure in a 0.2μm ZnS epitaxial layer on GaAs[16]

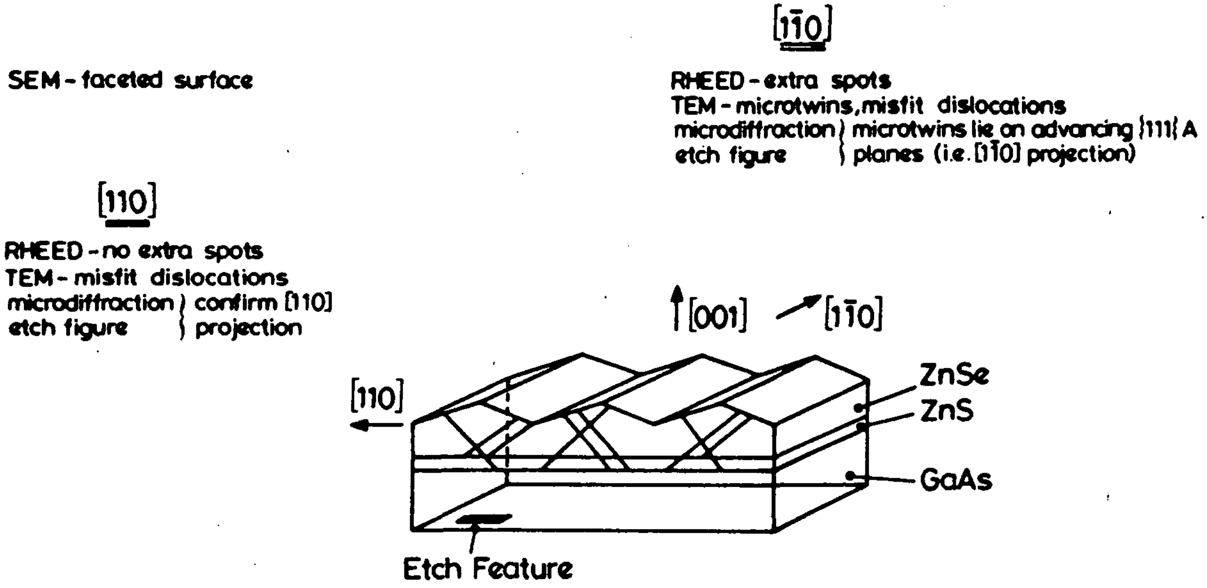

Figure 4.15 Summary of results

(figure 4.6b) implies that the onset of plastic deformation occurs at a much lower critical thickness, and that this is a consequence of the higher lattice mismatch (4.3%) associated with the ZnS/GaAs system. The presence of such a large number of microtwins in the ZnSe/ZnS/GaAs layers examined (*i.e.* greater than could be accounted for by just lattice mismatch alone) suggests that the interfacial dislocation network is unable to relieve the strain at the interface and that microtwins are formed from a combination of stress induced deformation and nucleation processes.

Microtwins are thought to be produced by the propagation of partial dislocations with trailing stacking faults on adjacent {111} planes,[8] while thicker twins arise from the successive passage of partials across adjacent double atomic {111} planes or from the interaction of twinning dislocations with other dislocations.[25]

It has been suggested that the observed defect anisotropy in these materials is depedent on a number of factors, including the relative ionic radii of the anion and cation, the ionicity and degree of covalent bonding, the stacking fault energy (SFE) and the type of doping and its concentration.[16] In addition, consideration must be given to the geometrical factors arising from the components of tension and compression in the epitaxial layers concerned (see section 4.4). It is necessary to consider the effects of these parameters in greater detail, with particular reference to their effects on the relative motion of α and β dislocations, in order to identify which parameters are primarily responsible for the observed defect anisotropy.

For sphalerite material, the SFE is linearly related to ionicity for III-V compounds, while the charge redistribution index, which in turn is related to the difference in electrostatic energy between the zincblende and wurtzite material phases, is the relevent parameter for II-VI materials.[26] ZnSe and ZnS both have very low SFEs, *i.e.* 13mJm^{-2} and $\lesssim$ 6mJm^{-2} respectively,[26] and like many II-VI compounds, dislocations in these materials are found in their dissociated form.[27,28] G. Lu[29] has demonstrated that α and β dislocations in CdTe exhibit comparable SFEs. By inference, while the low SFEs explain the ease of formation of a large number of microtwins for ZnSe and ZnS, it is unlikely to be the controlling parameter for the defect anisotropy in these ZnSe/ZnS epitaxial layers.

Emphasis should, therefore, be placed on the parameters which strongly influence the differential motion of α and β dislocations. In this context, the relative atomic radii of the anion and cation, and the compound doping concentrations are likely to be particularly important in controlling the defect anisotropy for the polarity described.

The differential motion of α and β dislocations in the sphalerite structure is known to be heavily dependent on doping, due to the interaction of dislocations with kink sites.[30] Twinning dislocations in indentation deformed n-type GaAs (Se doped $10^{18}cm^{-3}$),[8] (Te doped $10^{18}cm^{-3}$)[31] and S.I. GaAs,[32] for example, are found to be of the $30^o\beta$ type, which is the least mobile partial dislocation in this material. (The velocity of α dislocations is found to be $\approx$ 100 times greater than that of β type dislocations in n-type GaAs.[31]) In contrast, p-type GaAs (Zn doped $10^{18}cm^{-3}$)[31] [32] leads to a reversal in the magnitude of the relative velocities of α and β dislocations. (The velocity of β dislocations is found to be about twice that of α dislocations in this material.) Similarly, α dislocations are found to be highly mobile in n-type ZnSe. (The velocity of α dislocations is found to be of the order of 100 times that of β dislocations for n-type material.[33])

The ZnS I-layers of the samples used to fabricate the DCEL devices were doped with 0.1% Mn. Electron paramagnetic studies have demonstrated that Mn^{2+} ions substitute on metal sites in the ZnS lattice.[34] Interaction with the host lattice crystal field and exchange with neighbouring ions, gives the Mn^{2+} 3d orbitals (which are half filled, unlike the full Zn 3d orbitals) some p-like characteristics, for which optical transitions are allowed, and devices fabricated from this material exhibit yellow luminescence.[22] It should be noted, however, that autocompensation effects in ZnS still result in the formation of material exhibiting n-type behaviour. Reliable data for dislocation mobilities in ZnS is not readily available, but by inference from the sign of the currents induced by the motion of dislocations in this material, it is suggested that α dislocations are the most mobile dislocation in n-type ZnS.[35] Also, the degree of dislocation asymmetry is greater in crystals with high flow stress,[33] and this in turn increases with free carrier concentration (*i.e.* doping). In view of the large difference in ionic radii of Zn^{2+} and S^{2-}, it is likely that this mobility asymmetry is further accentuated.

Epitaxial layers of ZnS on GaAs are in tensile strain, with extra half planes lying in the ZnS epilayer. For a [110] sample projection, 60^o dislocations of the α type would lie on advancing {111}B planes in the (001) ZnS layer (figure 4.2a). Since α dislocations are expected to be more mobile in ZnS, these dislocations are probably swept through the entire epilayer leaving perfect crystal behind them. Whereas, splitting of the slowly moving β dislocations in the $[1\bar{1}0]$ sample projection, with the leading partial dislocations[9] being swept through to the ZnSe/ZnS interface, gives rise to the formation of microtwins. Once initiated in the ZnS I-layer, the defect distribution is maintained across the ZnSe/ZnS interface and is propagated throughout the entire ZnSe layer. This model explains the anisotropic defect distribution for the polarity described for these ZnSe/ZnS/GaAs epitaxial layers.

Further, support for this dislocation model is given by the observation that the microtwins lie in the same sense as the advancing surface facets (figure 4.11). Facet planes tend to be the planes of slowest growth and these have been shown to be of the {111}A type for most zincblende systems.[19] [36] It is known, however, that crystal plane growth rates are not simply related to the surface free energies. While there is a correlation that the faces of lowest surface energy tend to be the faces of lowest growth rate, which in turn naturally correspond to the faces of low index orientation, it is not possible to strengthen this correlation into a law of proportionality.[37] Hence, for crystal growth on a macroscopic scale, anisotropy of the crystal surface free energy coupled with thermodynamic, surface kinetic and supersaturation effects at the growth interface will cause inhomogeneous layer growth and facet plane formation, contrary to that predicted from perfectly homogeneous equilibrium growth conditions. This helps to explain why the surface facet planes were of the {411}A and {511}A type and this observation is similar to reports of facet plane formation in GaAs following MOVPE growth on {111} groves in a {100} growth plane .[38] It is also noted that Koestner[23] attributes the formation of facet planes in MBE grown MCT epitaxial layers to HgTe desorption from the growth surface, which would lead to the preferential exposure of the low energy {111} planes.

Hirsch[31] suggests that the dependence of hardness on polarity in the sphalerite structure is likely to be related to the anisotropy of the dislocation velocity through the slip system operating in the stress field. Hence, the anisotropy in the defect distribution of these epilayers, arising from differences in the formation and motion of α and β partial dislocations in the sphalerite structure, gives rise to some anisotropic stress distribution in the layers. Asymmetric relaxation of the ZnSe/ZnS epilayer, following substrate removal due to the etching process therefore explains the observation of the uniaxial cracking in the ZnS I-layer (figure 4.7).

It has been reported that epitaxial layers of ZnSe (n-type $10^{16} cm^{-3}$) on (001)GaAs contain a comparable number of microtwins for the two orthogonal [110] and [$1\bar{1}0$] layer projections[16] (see section 4.6). This implies that the doping concentration, in this case, is insufficient to be reflected in an anisotropic distribution of defects in these epitaxial layers, irrespective of the differential motion of α and β dislocations. It is noted that doping concentrations of the order of $10^{18}cm^{-3}$ are necessary for the appearance of some anisotropic behaviour in GaAs.[31] Alternatively, or in addition, the less different sizes of the anion and cation may be responsible for the absence of anisotropy of the defect distribution in {100} ZnSe layers.

The TEM observation of an anisotropic defect distribution in nominally undoped ZnSe/ZnS/GaAs samples demonstrates that the large difference in the ionic radii of the Zn^{2+} and S^{2-} ions is primarily responsible for the anisotropic defect distribution in these epitaxial layers. It is likely that the high Mn^{2+} doping concentration in the ZnS layers of samples used to fabricate devices (which, in turn, is expected to have a large effect on the differential motion of α and β dislocations) would additionally promote the macroscopic cracking phenomenon exhibited by these layers.

No attempts were made to correlate the observations reported here with substrate misorientation. GaAs substrates oriented 2^o off {100} in a < 110 > direction are commonly favoured for epitaxial growth and hence, it is likely that such misorientations might explain the observation of microtwins lying preferentially on just one of the two advancing {111}A planes. The substrate misorientation is likely to promote the initial formation of these defects on one of the {111} planes, the effect of which is maintained throughout the subsequent layer growth.

Consideration is now given to the origin of the interfacial dislocation network. It has been suggested that several dislocation sources may be operative during this formative process[39] including;

1. substrate dislocations threading through into the epilayer;
2. island agglomeration during the initial epilayer growth (*i.e.* dislocations are expected to form between the growth islands to accommodate any translational or rotational displacements) and
3. plastic deformation of the film during growth and subsequent cooling.

In addition, Matthews[40,41] also suggests that surface sources may be responsible for dislocation formation, followed by glide along inclined {111} planes to the interfacial region. A substrate dislocation density of $\approx 10^5cm^{-2}$ is unlikely to be the main defect source, along with island agglomeration which is similarly expected to introduce a relatively small dislocation content. Hence, it is possible that epilayer strain coupled with some surface source mechanism is primarily responsible for the formation of defects at the epilayer/substrate interface. Petruzzello et al[42] have recently demonstrated that the misfit dislocation density in MBE grown ZnSe/GaAs increases with epitaxial layer thickness. TEM studies of samples with thicknesses ranging between 0.05μm and 4.9μm have illustrated the mechanism by which the interfacial dislocation network is formed. Below a critical thickness of approximately 150nm, for which the epilayer undergoes pseudomorphic growth (*i.e.* the epilayer is strained and lattice matched to the substrate), pairs of stacking faults close to the interface are formed. Beyond the critical thickness, 60^o perfect dislocations are formed to relieve the epilayer strain. Their presence is consistent with the operation of surface sources and their subsequent glide along $\{111\}$ planes to the interfacial region. The Frank partial dislocations associated with the stacking faults are predicted to undergo the reaction

$$\frac{1}{3}a < 111 > \quad \mapsto \quad \frac{1}{2}a < 110 > + \frac{1}{6}a < 112 >$$

with the formation of a perfect misfit dislocation and a Shockley partial which glides out via the epilayer surface. As the epilayer thickness increases, this dislocation content also increases and is accompanied by the interaction of pairs of 60^o dislocations to form Lomer dislocations.[43] These latter dislocations are of the pure edge type and are characterised by Burgers vectors which lie in the plane of the epilayer and hence, are efficient at strain relief. In contrast, 60^o dislocations only provide a component of their Burgers vector for strain relief and so are relatively inefficient. As the epilayer thickness increases still further, the Lomer dislocations promote work hardening effects and so inhibit the introduction and interaction of additional dislocations, and so explain why the final interfacial dislocation content is composed mainly of inefficient* 60^o dislocations.[44] This model, which is supported by TEM observations of epitaxial GaAsP/GaAs,[44] predicts the formation of a large number of dislocations which are relatively inefficient at strain relief, and so is consistent with the observation of a larger defect content in these ZnSe/ZnS/GaAs heterostructures than would be expected from just lattice mismatch considerations alone.

---

* i.e. 50%

4.8 Sputter Deposited ZnS

The use of MOVPE for the deposition of thin film ZnS:Mn for EL device applications has been a relatively recent initiative.[45] Previously, both a.c. and d.c. EL devices employed either powder or sputter deposited polycrystalline thin films.[46] Development of the polycrystalline devices was stimulated by improvements in sputter technology which allowed the deposition of semiconductors and insulators in thin film form with good homogeneity over a large area. Although a.c. thin film devices presently offer the best brightness and 'turn on voltage' characteristics,[46] their DCEL counterparts are still of interest because of the lower voltages needed for their operation and the lower cost of the driving circuitry. However, avalanche breakdown at high electric fields, which causes localised destructive breakdown of the thin film EL elements, is still the major problem associated with these devices and necessitates their operation in 'short-pulse' mode.

Blackmore et al[47] have illustrated the large number of processing and operational parameters that influence the stability of sputter deposited ZnS:Mn DCEL devices. As shown in figure 4.16 these devices may be formed by the sequential sputter deposition onto a glass substrate of a transparent conducting oxide (TCO), an active ZnS:Mn layer and a current distributing anode. Cadmium stannate (CdSt)⋆⋆ has attracted most interest as the TCO and when produced by sputtering in an oxygen ambient onto a water cooled substrate followed by heating to 450^oC in a 10% H_2/N_2 atmosphere and immediate cooling to room temperature produces material with a sheet resistance of 5Ω/square and 85% transmission.[47]

The sputter deposition of the ZnS:Mn layer is a very complex process and resultant DCEL devices have been shown to be chamber dependent.[47] The following deposition procedures have been shown to produce devices which exhibit yellow luminescence.[47] Sintered ZnS targets containing approximately 0.5 at.% Mn are sputter deposited in a 10%H_2/N_2 ambient onto a substrate held at 200^oC. Prior to layer deposition the substrate is heated to 350^oC in vacuum (10^{-7}torr) before cooling to the growth temperature. Layers of 7000Å are grown at a rate of 10Åsec^{-1} and then cooled to room

---

⋆ The samples used in this study were supplied by Jenny Blackmore, R.S.R.E., Malvern.

⋆⋆Cd_2SnO_4

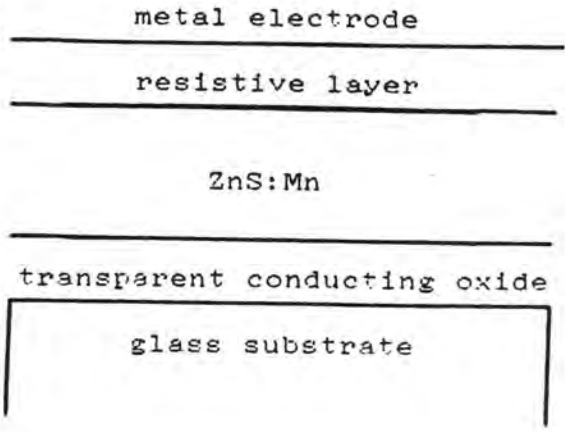

Figure 4.16 Sputter deposited ZnS:Mn DCEL device

Figure 4.17 SAD pattern taken from ZnS/glass

temperature over a period of a few hours. This process is followed by a brief anneal at 450°C in a flowing argon ambient. The deposition of a capping layer of 20%Ni/Si or amorphous silicon is then required to facilitate device operation in the high current pulse mode. Electrical connection is made to the device via a 2000Å evaporated aluminium contact, and it is necessary to encapsulate these devices because of their strong humidity dependence.

Device stability has been shown to depend critically on the ambient gas mixture used during layer deposition.[47] Also, in view of the high instability of devices fabricated from high quality MOVPE grown ZnS onto CdSt/glass substrates,[48] it is probable that the structural defects associated with the sputter deposited polycrystalline thin films may act to improve device stability.[48]

The procedure of cross-sectional TEM has been used to compare sputtered ZnS layers deposited onto CdSt/glass and ZnO/glass substrates. Samples were prepared in the usual manner for observation in the electron microscope with the exception that the supporting silicon blocks used to form the sandwich structure were replaced by glass to facilitate more uniform mechanical polishing. Charging of the glass substrate in the electron microscope severely hindered sample observation. Specimen drift was a constant problem and frequent realignment of the microscope was necessary to retain focussed images.

A preliminary study of ZnS deposited directly onto a glass substrate revealed a slight degree of preferential orientation of the epitaxial polycrystalline grains, as demonstrated by the SAD pattern shown in figure 4.17. Investigation of the ZnS/CdSt/glass and ZnS/ZnO/glass samples revealed a similar and greater degree of ordering of the polycrystalline grains respectively. The micrograph shown in figure 4.18a was taken from the former sample and gives faint indication of columnar growth, and the polycrystalline nature of the ZnS/CdSt epilayer and its slight preferential orientation is illustrated by its associated SAD pattern shown in figure 4.18b. The diffraction pattern taken from the ZnO buffer layer of the latter sample was similar to that shown in figure 4.17, again indicating slight preferential orientation, while the overlying ZnS layer exhibited strong columnar growth as shown in figure 4.19. In particular, feature *a* in the micrograph indicates the formation of platelets within the columnar structure.

This preliminary comparative study of sputtered ZnS films on TCO/glass substrates indicates that ZnS forms a more pronounced columnar growth structure on ZnO rather

Figure 4.18a TEM micrograph of ZnS/CdSt/glass showing faint indications of columnar growth.

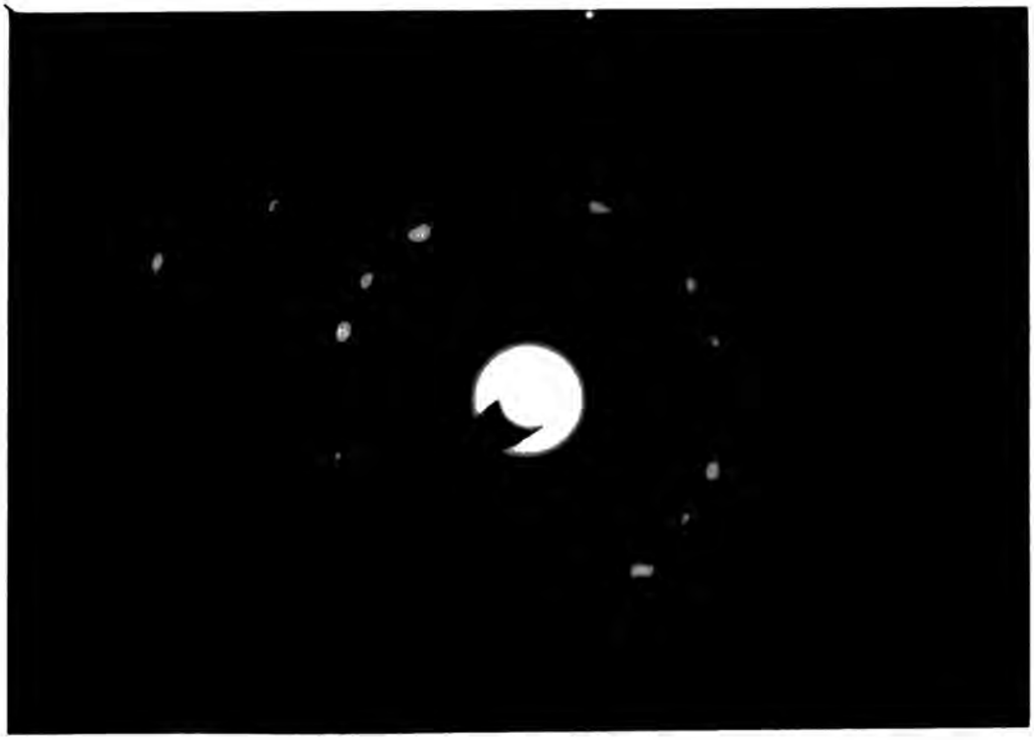

Figure 4.18b Associated SAD pattern demonstrating the polycrystalline nature of the epilayer and indicating a slight amount of preferential orientation.

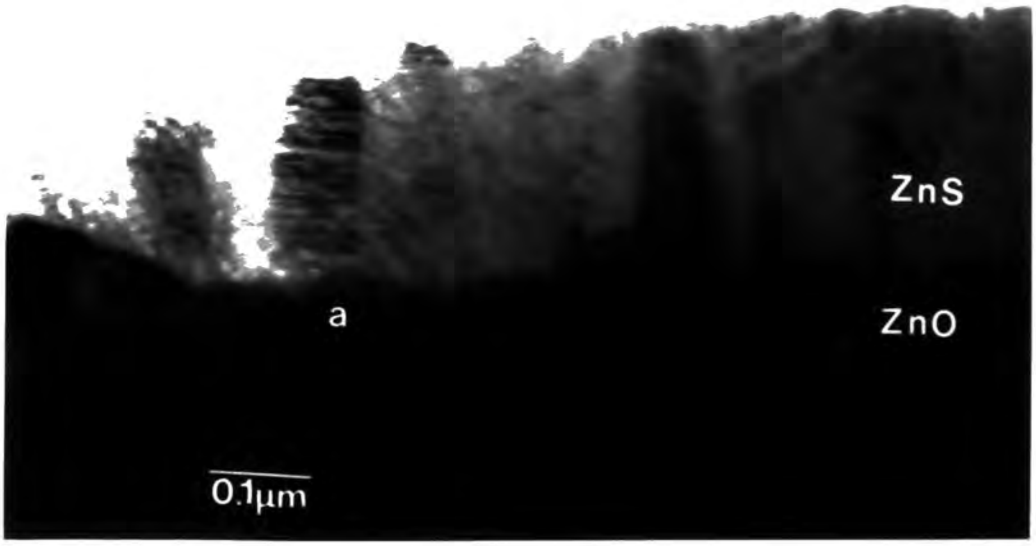

Figure 4.19 ZnS/ZnO/glass showing the formation of platelets within the columnar structure.

than CdSt. While it is appreciated that the deposition of these films is a highly complex process, with many parameters influencing the resultant device properties, it is recognised that the complex defect structure within the polycrystalline layers act to improve device stability. Hence, it would seem appropriate to make the tentative suggestion that ZnO would be the more suitable TCO material for use with this DCEL device structure.

4.9 Summary

ZnSe/ZnS heterostructures grown by MOVPE on (001) oriented GaAs have been used to form a novel DCEL device. The chemical removal of the GaAs substrate during the process of device fabrication, however, was accompanied by uniaxial cracking of the exposed ZnS when the thickness of this I-layer exceeded 1μm. The as-grown ZnSe/ZnS/GaAs layers also exhibited surface faceting which was characterized by ridges lying predominantly along one $< 110 >$ direction. Investigation of the microstructure of several ZnS/GaAs and ZnSe/ZnS/GaAs samples demonstrated that strong anisotropy exists in the defect distribution of the (001) oriented sphalerite epitaxial layers. Specimen orientations were uniquely determined by means of substrate etching correlated with RHEED observations and also by microdiffraction. Microtwins were found exclusively in the $[1\bar{1}0]$ sample projection lying on advancing $\{111\}$ A planes, while the two orthogonal $< 110 >$ layer orientations contained a network of interfacial dislocations. In contrast, the ZnSe/GaAs system exhibited a comparable defect distribution for both $< 110 >$ layer projections.

Consideration has been given to the formation of microtwins and interfacial dislocations, and to the parameters which influence their anisotropic distribution in (001) ZnSe/ZnS epitaxial layers. It is likely that microtwins are formed due to a combination of nucleation and stress induced deformation processes, while the relief of epilayer strain and the generation of interfacial dislocations is regarded as being mainly due to the action of surface sources.

The large difference in the ionic radii of Zn^{2+} and S^{2-}, and the high Mn^{2+} doping concentration of the ZnS I-layers are expected to greatly influence the motion of α and β dislocations in this material. The expectation that α dislocations are more mobile than β dislocations in ZnS allows the construction of a simple dislocation model for an epilayer in tensile strain which explains the formation of microtwins for the polarity described. It is considered that material stacking fault energies (and hence ionicities) do not directly influence the anisotropic defect distribution in these ZnSe/ZnS/GaAs samples. The asymmetric relaxation of the II-VI epilayer following the chemical removal of the GaAs substrates explains the observation of uniaxial cracking, while the anisotropy of the crystal surface free energy coupled with thermodynamic, surface kinetic and supersaturation effects at the growth interface are believed to be responsible for the formation of uniaxial growth facets. These observations may have consequences for all (001) oriented sphalerite epitaxial layers.

DCEL devices formed from MOVPE grown ZnS exhibit a high spatial distribution of electroluminescence, whereas sputtered ZnS layers on TCO/glass substrates allow the formation of devices with improved stability, arising from the polycrystalline nature of these layers. A preliminary comparative assessment of sputtered ZnS layers on CdSt/glass and ZnO/glass substrates has demonstrated that these layers adopt a preferred orientation. While it is appreciated that the sputtering process is a very complex technique, the evidence for stronger columnar growth in ZnS/ZnO/glass layers suggests that this system may be preferable for the fabrication of these DCEL devices.

REFERENCES

1. B. Cockayne and P.J. Wright, *J. Crystal Growth* **68** (1984) 223
2. P.J. Wright and B Cockayne, *J. Crystal Growth* **59** (1982) 148
3. A.P.C. Jones, A.W. Brinkman, G.J. Russell, J. Woods, P.J. Wright and B. Cockayne, *J. Crystal Growth* **79** (1986) 729
4. A.P.C. Jones, P.J. Wright, A.W. Brinkman, G.J. Russell, J. Woods and B. Cockayne, *I.E.E.E. Trans. on Electron Devices* **Ed-34** (1987) 937
5. A.P.C. Jones, A.W. Brinkman, G.J. Russell, J. Woods, P.J. Wright and B. Cockayne, *Semicond. Sci. Technol.* **1** (1986) 41
6. F.A. Ponce, W. Stutius and J.G. Werthen, *Thin Solid Films* **104** (1983) 133
7. W. Stutius and F.A. Ponce, *J. Appl. Phys.* **58** (1985) 1548
8. A. Lefebvre, Y. Androussi and G. Vanderschaeve, *phys. stat. sol.(a)* **99** (1987) 405
9. B.C. De Cooman and C.B. Carter, *Inst. Phys. Conf. Ser.* **No. 87** (1987) 259
10. J.O. Williams, E.S. Crawford, J.L.L. Jenkins, T.L. Ng, A.M. Patterson, M.D. Scott, B. Cockayne and P.J. Wright, *J. Mater. Sci. Lett.* **3** (1984) 189
11. J.O. Williams and A.C. Wright, *Phil. Mag.* **A 55** (1987) 99
12. J.G. Werthen, W. Stutius and F.A. Ponce, *J. Vacuum Sci. Technol.* **B1** (1983) 656
13. J.O. Williams, T.L. Ng, A.C. Wright, B. Cockayne and P.J. Wright, *J. Crystal Growth* **68** (1984) 237
14. J.O. Williams, A.C. Wright and T. Yao, *Phil. Mag.* **A54** (1986) 553
15. J. Kleiman, R.M. Park and S.B. Qadri, *J. Appl. Phys.* **61** (1987) 2067
16. P.D. Brown, A.P.C. Jones, G.J. Russell, J. Woods, B. Cockayne and P.J. Wright, *Inst. Phys. Conf. Ser.* **No. 87** (1987) 123
17. P.D. Brown, G.J. Russell and J. Woods, to be published in the Journal of Applied Physics.
18. N.G. Chew and A.G. Cullis, *Ultramicroscopy* **23** (1987) 175

19. Y. Tarui, Y. Komiya and Y. Harada, *J. Electrochem. Soc.* **118** (1971) 118

20. W. Stutius, *J. Electron. Mater.* **10** (1981) 95

21. D.W. Pashley and M.J. Stowell, *Phil. Mag.* **8** (1963) 1605

22. A.P.C. Jones, *Electroluminescence in Epitaxial thin Films of ZnS and ZnSe*, Ph.D. thesis, Dunelm, 1987

23. R.J. Koestner and H.F. Schaake, *J. Vacuum Sci. Technol.* **A6** (1988) 2834

24. H. Mitsuhashi, I. Mitsuishi, M. Mizuta and H. Kukimoto, *Jpn. J. Appl. Phys.* **24** (1987) L578

25. E.O. Hall *Twinning and Diffusionless Transformations in Metals*, pub. Butterworths, 1954, p116

26. S. Takeuchi, K. Suzuki, K. Maeda and H. Iwanaga, *Phil Mag* **A50** (1984) 171

27. G. Rivaud, M.F. Denanot, H. Garem and J.C. Desoyer, *phys. stat. sol. (a)* **73** (1982) 401

28. A.V. Zaretskii, Y.A. Osip'yan, V.F. Petrenko, G.K. Strukova and I.I. Khodos, *Phil. Mag.* **A48** (1983) 279

29. G. Lu and D.J.H. Cockayne, *Phil. Mag.* **A53** (1986) 307

30. P.B. Hirsch, *Journal de Physique* **C6** (1979) 117

31. P.B. Hirsch, P. Pirouz, S.G. Roberts and P.D. Warren, *Phil. Mag.* **B52** (1985) 759

32. Y. Androussi, G. Vanderschaeve and A. Lefebvre, *Inst. Phys. Conf. Ser.* **No. 87** (1987) 291

33. Yu.A. Osip'yan, V.F. Petrenko, A.V. Zaretskiǐ and R.W. Whitworth, *Adv. in Phys.* **35** (1986) 115

34. R.S.Title in *Physics and Chemistry of II-VI Compounds*, ed. Aven and Prener, pub. North Holland, 1967, p267

35. V.F. Petrenko and R.W. Whitworth, *Phil. Mag.* **A 41** (1980) 681

36. H.C. Gatos and M.C. Lavine, *J. Phys. Chem. Solids* **14** (1960) 169

37. F.C. Frank *The Growth and Perfection of Crystals*, Proceedings of an International Conference on Crystal Growth, Cooperstown, New York, ed. Doremus, Roberts and Turnbull, 1958

38. S.D. Hersee, E. Barbier and R. Blondeau, *J. Crystal Growth* **77** (1986) 310

39. M.J. Stowell, *Defects in Epitaxial Deposits*, in Epitaxial Growth, part B, ed. J.W. Matthews, Academic Press, New York, 1975

40. J.W. Matthews, *Coherent Interfaces and Misfit Dislocations*, in Epitaxial Growth, part B, ed. J.W. Matthews, Academic Press, 1975

41. J.W. Matthews, S. Mader and T.B. Light, *J. Appl. Phys.* **41** (1970) 3800

42. J. Petruzzello, B.L. Greenberg, D.A. Cammack and R. Dalby, *J. Appl. Phys.* **63** (1988) 2299

43. S. Mader, A.E. Blakeslee and J. Angilello, *J. Appl. Phys.* **45** (1974) 4730

44. J.S. Ahearn and C. Laird, *J. Mater. Sci.* **12** (1977) 699

45. A.F. Cattell, B. Cockayne, K. Dexter, J. Kirton and P.J. Wright, *IEEE Trans. on Electron Devices* **Vol. Ed.30** (1983) 471

46. H. Hartmann, R. Mach and B. Selle, 3.2.1.2., Electroluminesecent Polycrystalline Displays, p216, *Wide Gap II-VI Compounds as Electronic Materials*, in Current Topics in Materials Science, Vol. 9, ed. E. Kaldis, pub. North Holland, 1982

47. J.M. Blackmore, A.F. Cattell, K.F. Dexter, J. Kirton and P. Lloyd, *J. Appl. Phys.* **61** (1987) 714

48. A.P.C. Jones, D.Y. Watts, A.W. Brinkman, G.J. Russell and J. Woods, *J. Crystal Growth* **86** (1988) 880

5. Narrow Band-Gap II-VI Compounds

Hybrid Substrates for the Epitaxial Growth of (Hg,Cd)Te

5.1 Introduction

There is a commercial demand for the production of focal plane infra-red detector arrays, based on large areas ($\gtrsim 1cm^2$) of high quality (Hg,Cd)Te (MCT), for thermal imaging applications. In view of the high defect content associated with bulk grown MCT, greater emphasis has been given in recent years to the production of epitaxial layers of this alloy. This introduces the problem of finding a suitable substrate (and substrate orientation) for the subsequent epitaxial growth of MCT. Lattice matching and metallurgical considerations suggest that CdTe should form an ideal substrate, but bulk grown crystals of this binary compound also suffer from an unacceptably large defect concentration, such as sub-grain boundaries, precipitates, dislocations and twins,[1] that results in epitaxial films of poor structural quality.[2] There is also the additional disadvantage that single-crystal CdTe is mechanically *very* soft.[3] The demand for high structural quality CdTe has instigated the investigation of hybrid substrates, consisting of buffer layers of CdTe on foreign substrates.

The purpose of this chapter is to illustrate how the defect content of MOVPE layers of CdTe grown on CdTe and GaAs substrates is dependent primarily on substrate orientation (sections 5.2 and 5.3). This study is then extended in section 5.4 to the comparison of epitaxial layers of MCT grown by MOVPE on both bulk $\{\bar{1}\bar{1}\bar{1}\}$B CdTe and hybrid CdTe/$\{\bar{1}\bar{1}\bar{1}\}$B GaAs substrates. This work is complemented by section 5.5 which presents a study of MBE grown CdTe/(Cd,Zn)Te strained layer superlattices, produced with the aim of obtaining high quality lattice matched substrates for the epitaxial growth of $Hg_{0.8}Cd_{0.2}Te$. To conclude, section 5.6 presents a preliminary investigation of epitaxial layers of ZnTe and CdTe/ZnTe superlattices grown by MOVPE on {100} oriented GaAs.

5.2 The Epitaxial Growth of CdTe

homoepitaxy

The homoepitaxial growth of CdTe has been reported by MBE,[4] MOVPE,[5-10] closed-tube chemical vapour deposition[11] and Atomic Layer Epitaxy(ALE),[12] and this work has been prompted by a need to gain further understanding of the nature of this binary compound. Early studies of the MBE[4] homoepitaxial growth of CdTe on hydroplane polished substrates demonstrated that an entirely different film growth morphology occurred on the opposite substrate polar faces. Myers et al[4] reported the growth of smooth featureless layers on the $\{111\}$ A face, and a textured facetted surface on the $\{\bar{1}\bar{1}\bar{1}\}$B face. The assignment of polarity in this work presumably followed the Warekois convention (see chapter 3), although no statement concerning the method of polarity determination was given. More recently, Oron et al[13] have used X-ray rocking curves to show that favourable CdTe homoepitaxy also occurs on just one of the substrate polar faces for MOVPE grown layers. These workers[13] show that the rocking curve full width half maxima for $\{\bar{1}\bar{1}\bar{1}\}$B CdTe layers are typically of the order of 400 to 800arcsec, while the $\{111\}$ A layers exhibit much narrower rocking curves. These observations also indicate that better quality layers may be grown on the $\{111\}$A face, but again no explanation was given as to how the CdTe crystal polarity was determined. In Chapter 3 it is shown that better homoepitaxial growth of CdTe occurs on the $\{\bar{1}\bar{1}\bar{1}\}$B face, in accordance with the polarity convention proposed by Fewster. Hence, these references[4] [13] also serve to illustrate the confusion which exists in the international literature concerning the polarity determination of CdTe.

heteroepitaxy

The main attraction of III-V compounds as foreign substrates over bulk grown single crystal II-VI's is their superior structural quality. In addition, they offer the possibility of lower production costs and improved mechanical properties. The ideal foreign substrate should:[3]

1. be transparent over the 3 to 12μm range;
2. have a thermal expansion coefficient comparable to that of CdTe in order to limit the formation of stress induced defects;
3. have a thermal conductivity higher than CdTe for adequate heat sinking;

4. have a melting point considerably greater than the CdTe epilayer growth temperature and
5. be insoluble in water.

Schmit[3] suggests that InP and GaAs are most appropriate for use as foreign substrates, mainly due to their attractive mechanical and thermal properties. GaAs can be produced in high quality over the required dimensions relatively cheaply and so is commercially more viable, in spite of its large lattice mismatch (14.6%) with CdTe. InSb has also attracted considerable interest because of its close lattice match (0.07%) to CdTe.

The heteroepitaxial growth of CdTe on a {100}GaAs substrate is unique because the controlled growth of either a {100} or a {111} oriented epilayer is possible. This curious phenomenon, which arises from the large lattice mismatch between these two compounds (see section 5.4), has been demonstrated by MBE,[14-18] MOVPE,[16] [19] Hot Wall Epitaxy[20,21] and laser assisted deposition (LADA).[22] In addition, both MBE[23-26] and MOVPE[10] have been used for the growth of epitaxial layers of CdTe on InSb, and there have also been several reports of the MOVPE and MBE growth of CdTe on Silicon,[27,28] Sapphire,[29,30] and hybrid GaAs/Si[31] substrates.

The heteroepitaxial growth of any crystal inevitably introduces some strain into the epitaxial layer. Beyond a certain critical thickness this usually leads to the formation of a network of misfit dislocations (see section 4.7). The structural defect content of the CdTe/GaAs heteroepitaxial system is largely dependent on the orientation of the GaAs substrate; *i.e.* epitaxial layers of {100}CdTe grown on {100}GaAs are found to contain misfit dislocations and microtwins inclined to the substrate/epilayer surface when grown by MBE[32-34] and MOVPE.[35-38] Whereas {111} CdTe layers grown by MBE on {100}GaAs[32] [33] [34] [39] and by MOVPE on {100}GaAs,[36] [37] [38] $\{\bar{1}\bar{1}\bar{1}\}$B GaAs,[37] [38] and $\{\bar{1}\bar{1}\bar{1}\}$B CdTe[37] [40] are characterised by the presence of lamella twins lying parallel to the substrate plane. Misfit dislocations and inclined microtwins have also been observed in layers of CdTe grown on {100}InSb.[35] [41-45]

The MOVPE growth of CdTe *

The main problem with the growth of CdTe epitaxial layers on CdTe substrates cut 2^o off $\{100\}$ in a $< 110 >$ direction is the inevitability that any substrate twin lying on one of the four $\{111\}$ planes will intersect the growth interface. It is well established that defects at the substrate surface are likely to propagate through into the epitaxial layer, and the presence of twins results in extensive linear regions of the epitaxial material being unsuitable for device fabrication. Homoepitaxial $\{100\}$CdTe grown by MOVPE also suffers from poor surface morphology. Hence, it would seem logical to grow layers on slices which are cut such that their large area faces are parallel to the specific $\{111\}$ plane on which the twinning predominantly occurs.[46]

The polarity of the faces of the CdTe slices was established by etching the as-sawn substrates for approximately 15sec in a 1:1:1 mixture of HF:HNO_3:CH_3COOH. The face which remained shiny after etching was denoted as $\{\bar{1}\bar{1}\bar{1}\}$B, after the convention of Fewster (see Chapter 3).

Prior to epitaxial growth, the CdTe substrates were hydroplane polished in 2% Br_2/MeOH solution for 45min and then thoroughly washed in methanol. After loading into the reaction chamber they were heat treated with a hydrogen gas stream at 400^oC for 30min immediately before growth. Layers of CdTe were then grown on the opposite $\{111\}$ polar faces of CdTe at a growth temperature between 390^o and 400^oC, using the alkyls Me_2Cd and Et_2Te, where the following reaction occurred;

$$Cd(CH_3)_2 + (C_2H_5)_2Te \ \mapsto \ CdTe + hydrocarbon\ products$$

Similarly, the epitaxial growth of CdTe was performed on $\{100\}$, $\{111\}$ A and $\{\bar{1}\bar{1}\bar{1}\}$B GaAs substrates, with the exception that $\{100\}$GaAs substrates were hydrogen heat treated at 580^oC in order to obtain $\{111\}$ oriented CdTe epitaxial layers.

---

* All the epitaxial layers studied were grown by Dr. J.E. Hails, now at R.S.R.E., Malvern.

5.3 Structural Studies of CdTe Epitaxial Layers

Samples were prepared in cross-section for examination in the electron microscope in the usual way (see section 2.4).

The micrograph shown in figure 5.1a, obtained from the interfacial region of the {111} CdTe/$\{\bar{1}\bar{1}\bar{1}\}$B GaAs epitaxial system, clearly illustrates the presence of a number of twin lamellae lying parallel to the substrate/epilayer interface. The twin widths are typically of the order of 100Å to 1000Å and the twinning frequency was found to be fairly consistent throughout the entire ($\approx 3\mu$m) epilayer. P.-Y. Lu,[36] however, notes that these defects in MOVPE grown {111} CdTe epilayers become broader and finally grow out after 4 to 5μm. The identification of the defects as twin lamellae was confirmed by the presence of extra spots in $\frac{1}{3}a_o < 111 >$ positions in $< 110 >$ selected area diffraction (SAD) patterns taken from the epilayer (figure 5.1b). In addition, the displacement of these extra spots from the matrix reflections in only one $< 111 >$ direction indicates that twinning occurred on just one {111} plane. The outer $< 110 >$ pattern in figure 5.1b arises from the GaAs substrate, and it should be noted that that no extra spots were present in the SAD patterns taken from the substrate material, the excellent crystallinity of which was confirmed by the complete absence of any defects in the vicinity of the fringe contrast in the GaAs (figure 5.1a). A similar density and distribution of these twin lamellae was found in epitaxial layers of {111} CdTe on {100}GaAs (figure 5.2) and $\{\bar{1}\bar{1}\bar{1}\}$B CdTe (figure 5.3) substrates. Indeed, the formation of {111} oriented CdTe epilayers has previously been reported for growth on cleaved alkali halides,[47] which present a {100} face for epitaxy, in addition to basal plane CdS[48] and sapphire[30] The epitaxial growth of CdTe on the opposite {111} A polar faces of CdTe and GaAs resulted in the formation of highly faulted layers which were unsuitable for the subsequent epitaxial growth of MCT.

These lamella twins are commonly observed to terminate at lateral twin boundaries, as shown in figure 5.4. The coincidence-site lattice model predicts the occurrence of four types of these boundaries for the sphalerite structure.[49] Indexing with respect to matrix and twin orientations, feature *a* (figure 5.4) corresponds to a {115}-{111} type boundary, feature *b* is a {112} – {112} type boundary, and *c* is either a {112} – {112} or a {110} – {114} type boundary. In this third case the angle between the intersection of the lateral twin boundary with the $< 112 >$ direction in the {110} plane does not

Figure 5.1a TEM micrograph showing lamella twins in a {111}CdTe epitaxial layer grown on $\{\bar{1}\bar{1}\bar{1}\}$B GaAs.

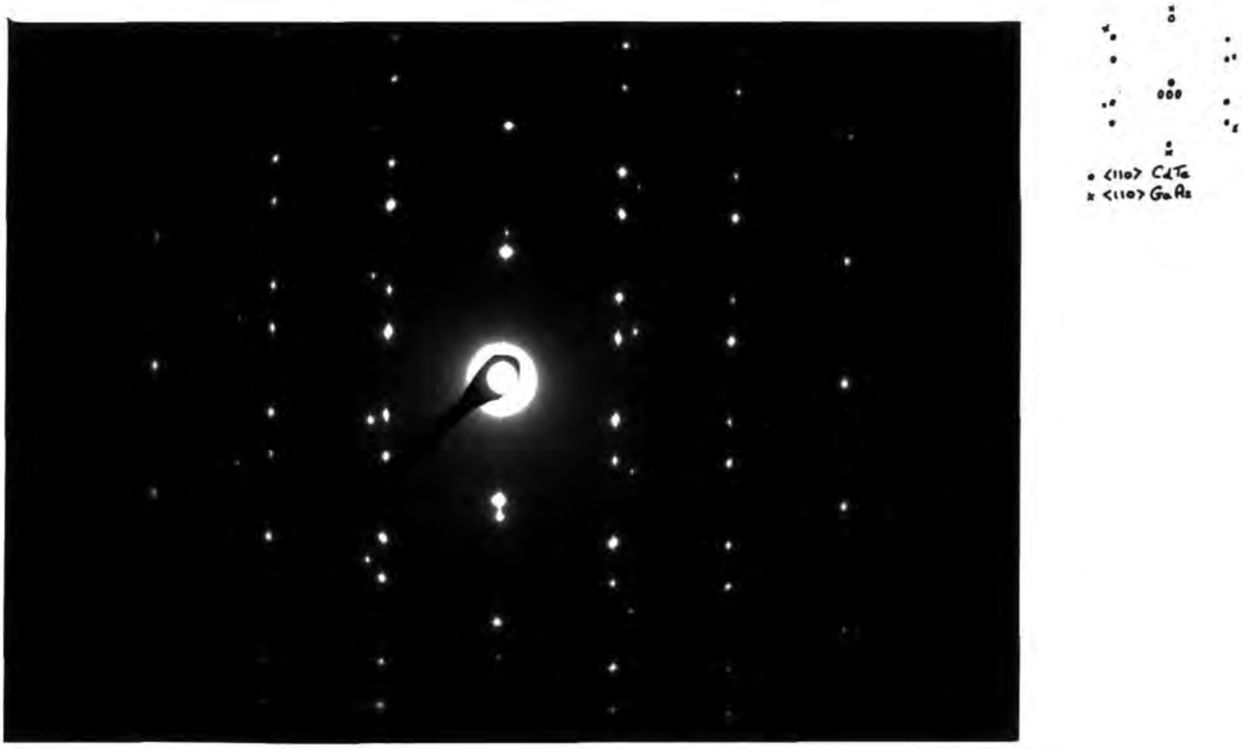

igure 5.1b SAD pattern showing a <110> sample projection. The inner <110> pattern from the CdTe epilayer contains twin spots. The outer <110> pattern is from the GaAs substrate material.

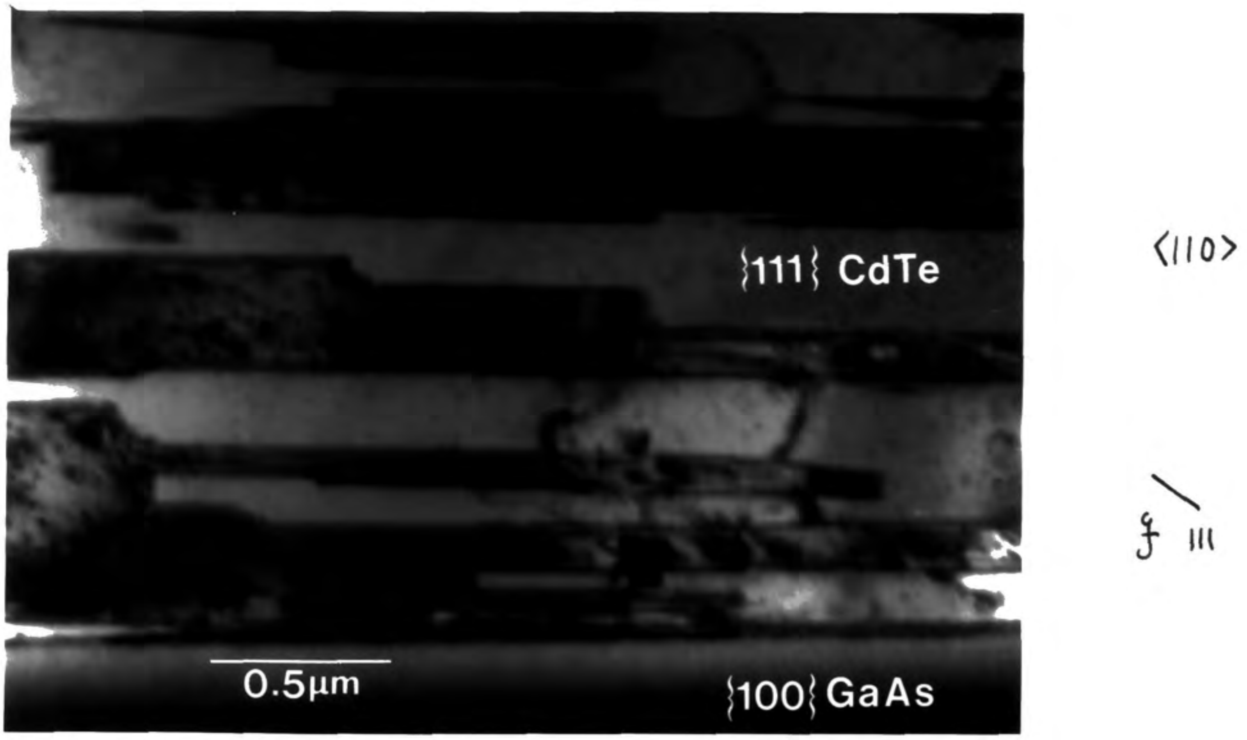

Figure 5.2 {111}CdTe/{100}GaAs

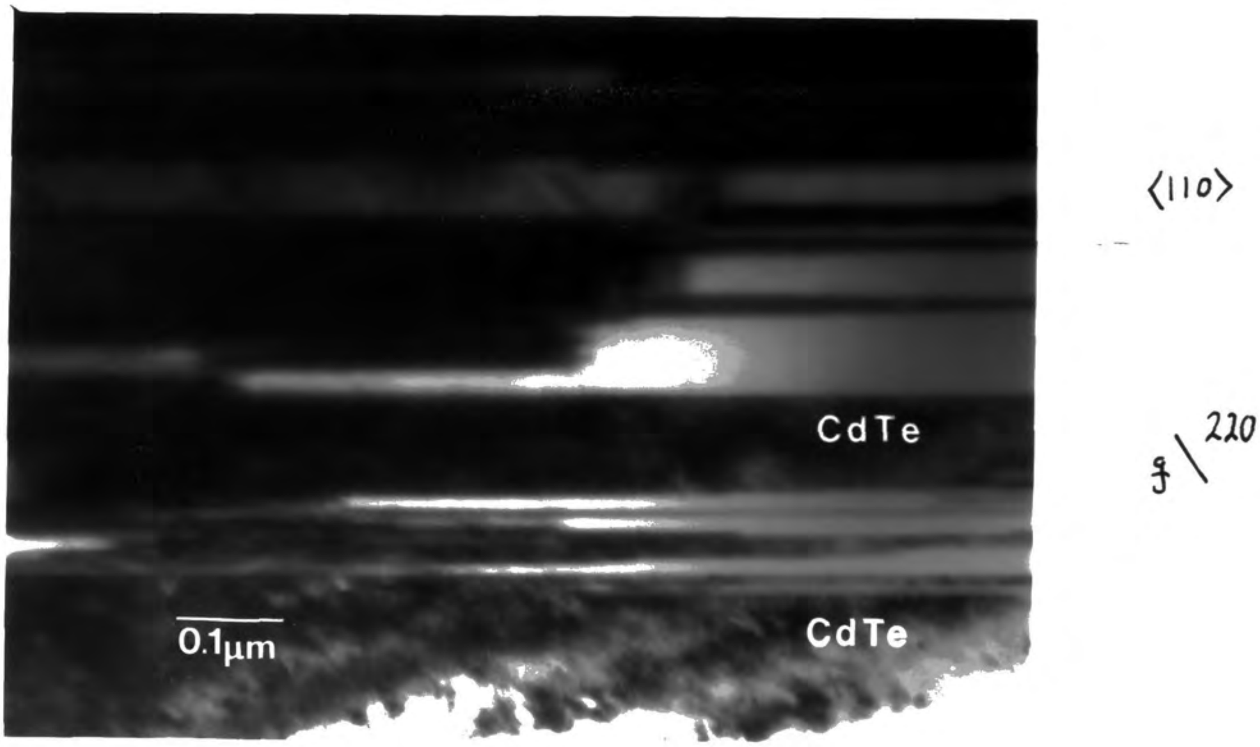

Figure 5.3 {111}CdTe/{$\bar{1}\bar{1}\bar{1}$}B CdTe

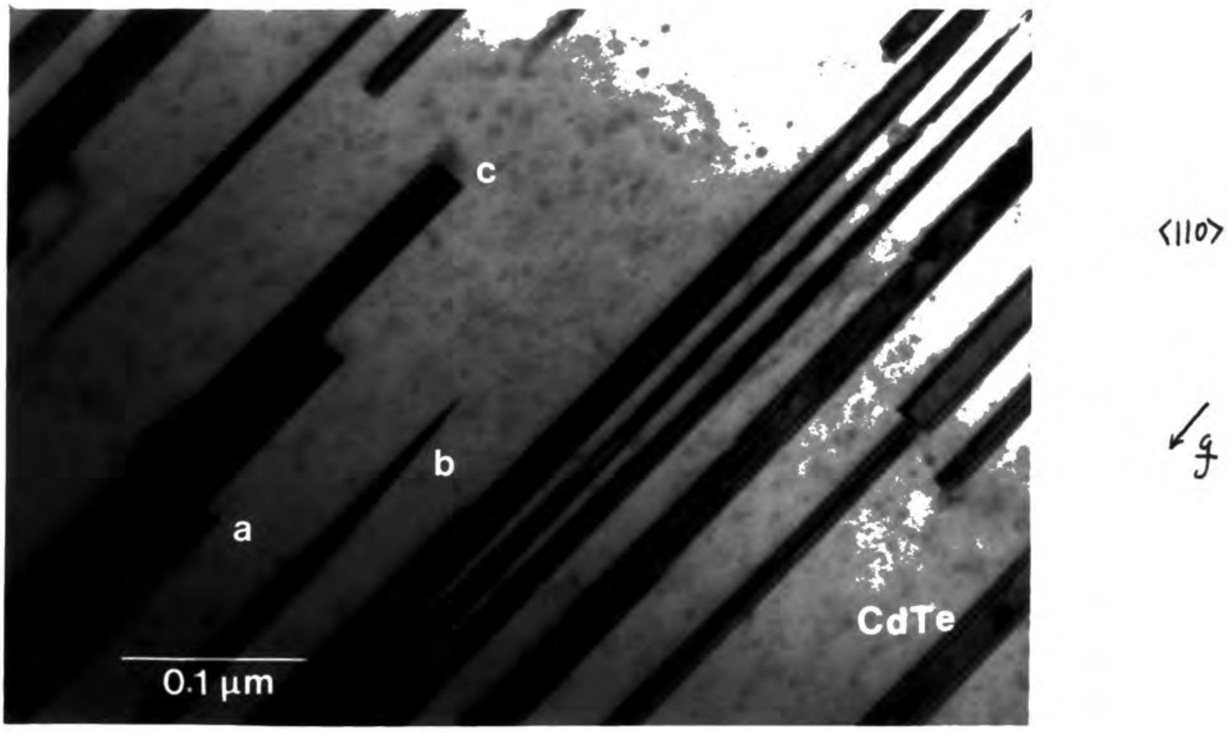

Figure 5.4 Lateral twin boundaries in a {111} CdTe epilayer.

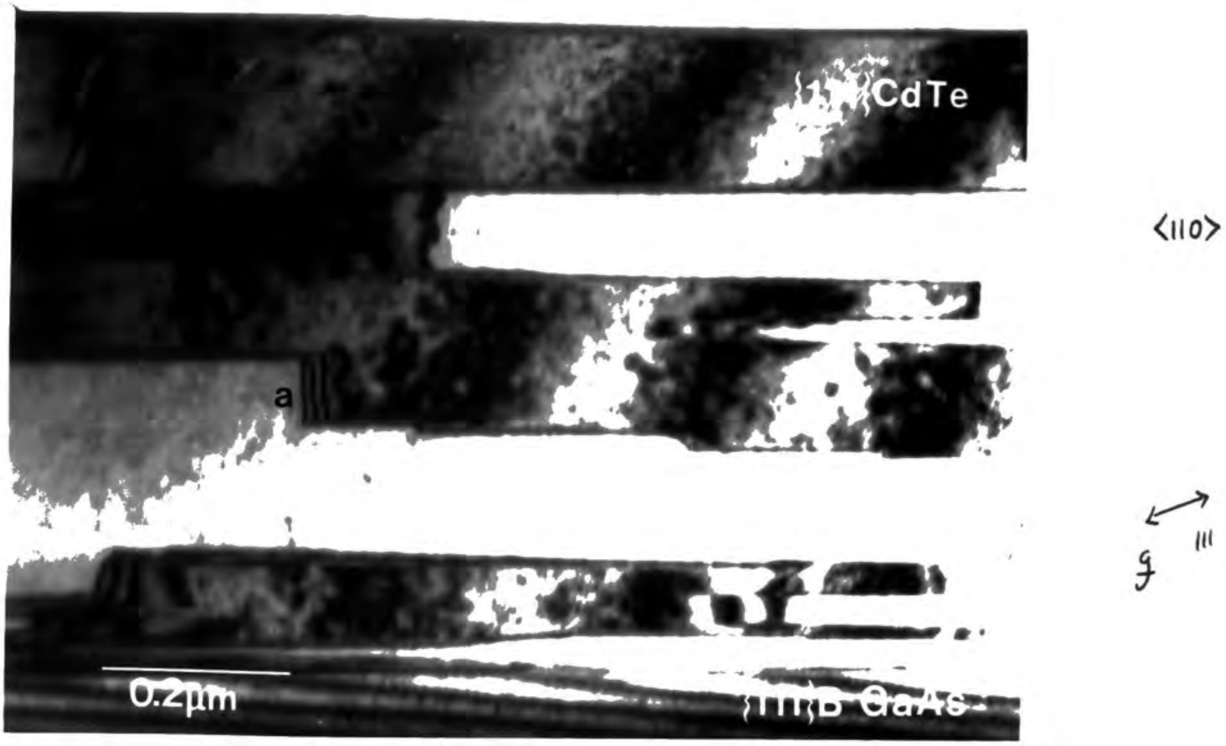

Figure 5.5 {111}CdTe/{$\bar{1}\bar{1}\bar{1}$}B GaAs, showing fringe contrast at a lateral twin boundary (feature 'a').

permit a definitive identification. These boundaries are consistent with those observed in bulk CdTe grown from the vapour phase.[50]

Under certain conditions, these lateral twin boundaries exhibit strong fringe contrast, as shown in figure 5.5 (feature *a*), and this provides information on the 'relaxed' structure of the boundary. Vlachavas and Pond[51] have analysed similar boundaries in silicon using computer simulation.

The crystallographic relationship of the {111} CdTe/{100}GaAs epitaxial system was determined by comparing SAD patterns taken from the substrate and epilayer. The absolute orientation of the GaAs substrate was also determined using the microdiffraction technique (as described in chapter 3). It was not possible to use this procedure with the CdTe epilayer because of the high concentration of lamellae twins. The SAD pattern shown in figure 5.6 demonstrates that a $< 211 >$ direction in the epilayer is parallel to a $< 110 >$ zone axis in the GaAs substrate. Microdiffraction patterns demonstrated that this corresponded to the [110] substrate direction. Conversely, a $< 110 >$ epilayer was found to be parallel to the $[1\bar{1}0]$ substrate orientation.

To demonstrate the importance of substrate orientation, figure 5.7 shows the interfacial region of a {100}CdTe layer grown on a {100} oriented GaAs substrate. The 14.6% lattice mismatch associated with this crystal system results in the production of a large number of misfit dislocations. The dislocation tangles were found to extend a distance of $\approx 0.5\mu$m into the epitaxial layer from a highly dense layer of defects ($\approx 0.1\mu$m wide) near the interface. Also, microtwins inclined at $\approx 55^o$ to the interface, in a $< 110 >$ projection, were occasionally observed in this system. It is noted, however, that other workers have found that these defects can propagate up to 1.5μm into the epilayer before growing out.[52]

Figures 5.8a and 5.8b are included to illustrate defect content of a {111} CdTe layer (grown on a $\{\bar{1}\bar{1}\bar{1}\}$B GaAs substrate) when the sample is tilted such that the twins are out of contrast. It can be seen that many of the dislocations in the layer are associated with the lateral twin boundaries. Also, dislocations that propagate through the epilayer tend to be bent into the plain of the lamellae twins. A more severe example of this effect is shown by figure 5.9, taken from a {111} CdTe layer on a {100}GaAs substrate. The large number of dislocations in this epilayer were found to lie almost entirely parallel to the twin lamellae.

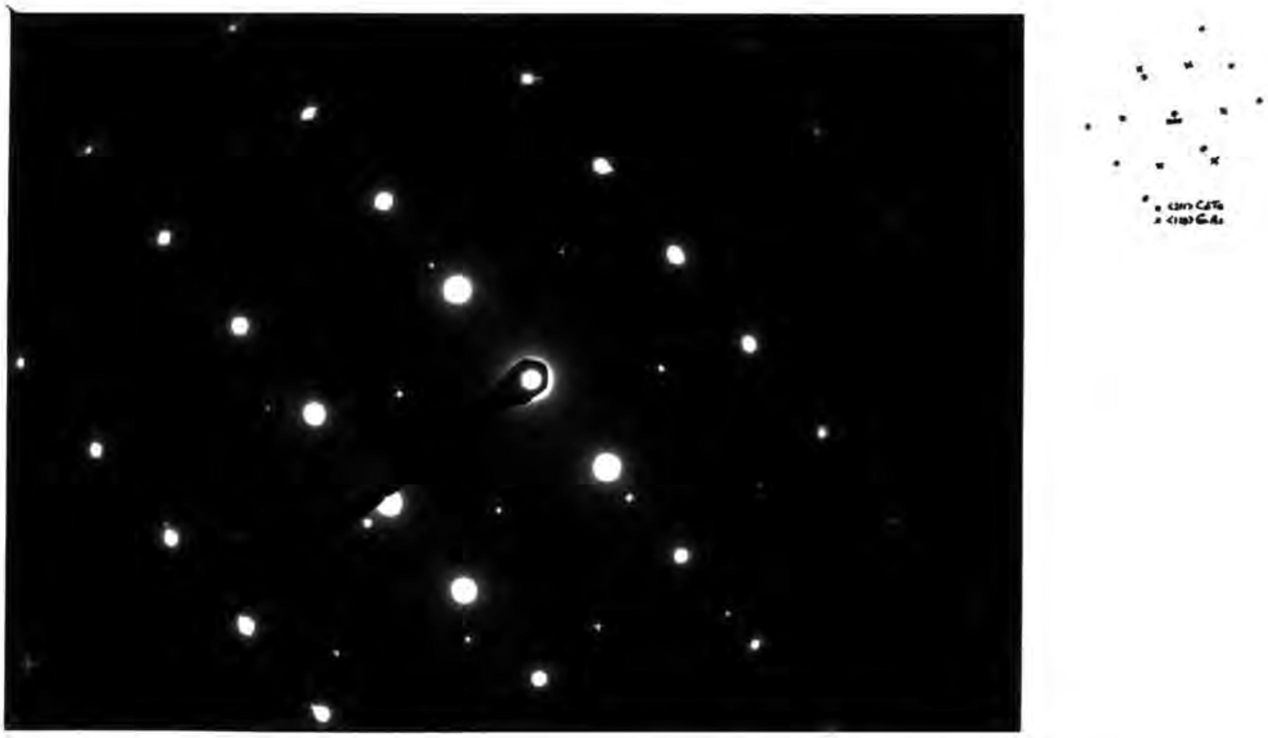

Figure 5.6a SAD pattern taken from {111}CdTe/{100}GaAs demonstrating that the <211> epilayer projection is parallel to a <110> direction in the substrate.

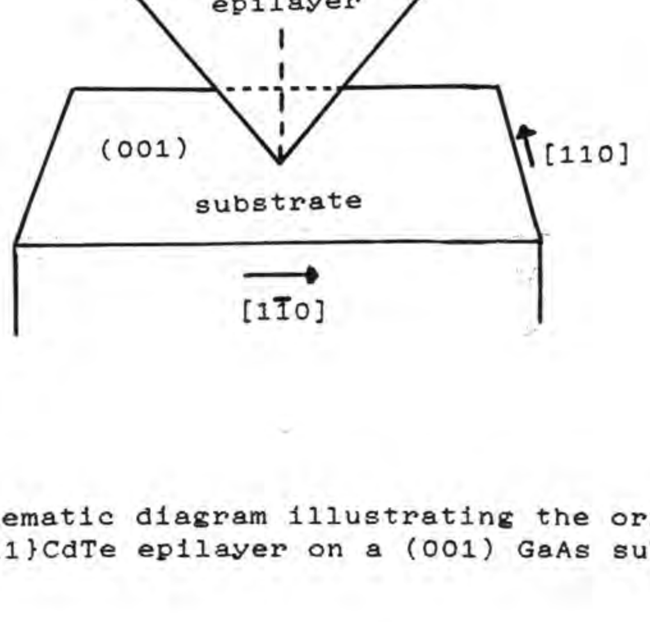

Figure 5.6b Schematic diagram illustrating the orientation of a {111}CdTe epilayer on a (001) GaAs substrate.

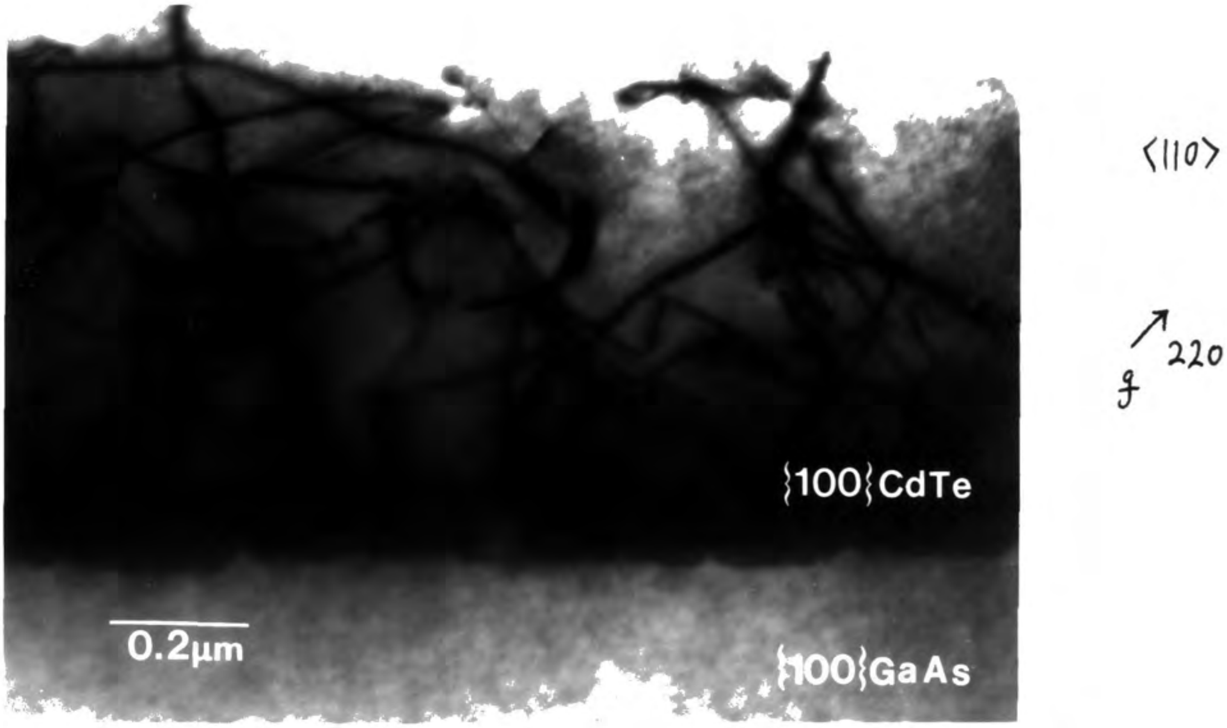

Figure 5.7 {100}CdTe/{100}GaAs

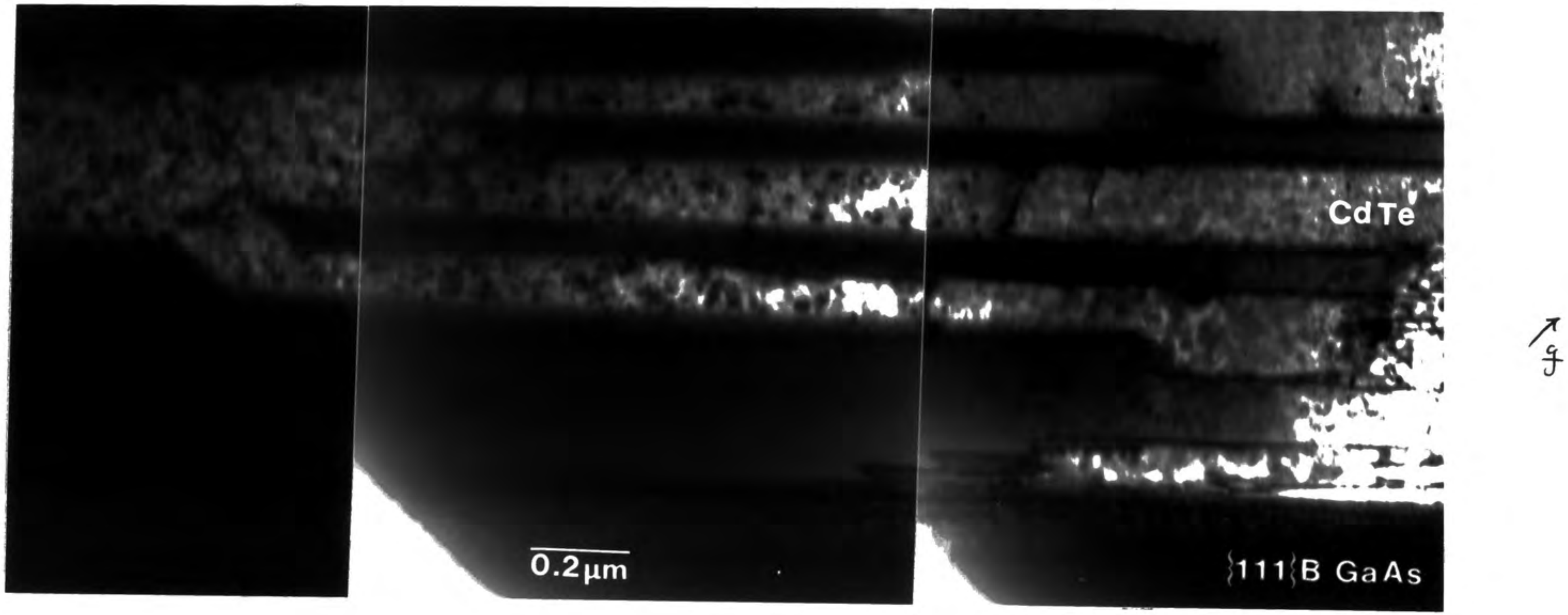

Figure 5.8a {111}CdTe/{$\bar{1}\bar{1}\bar{1}$}B GaAs

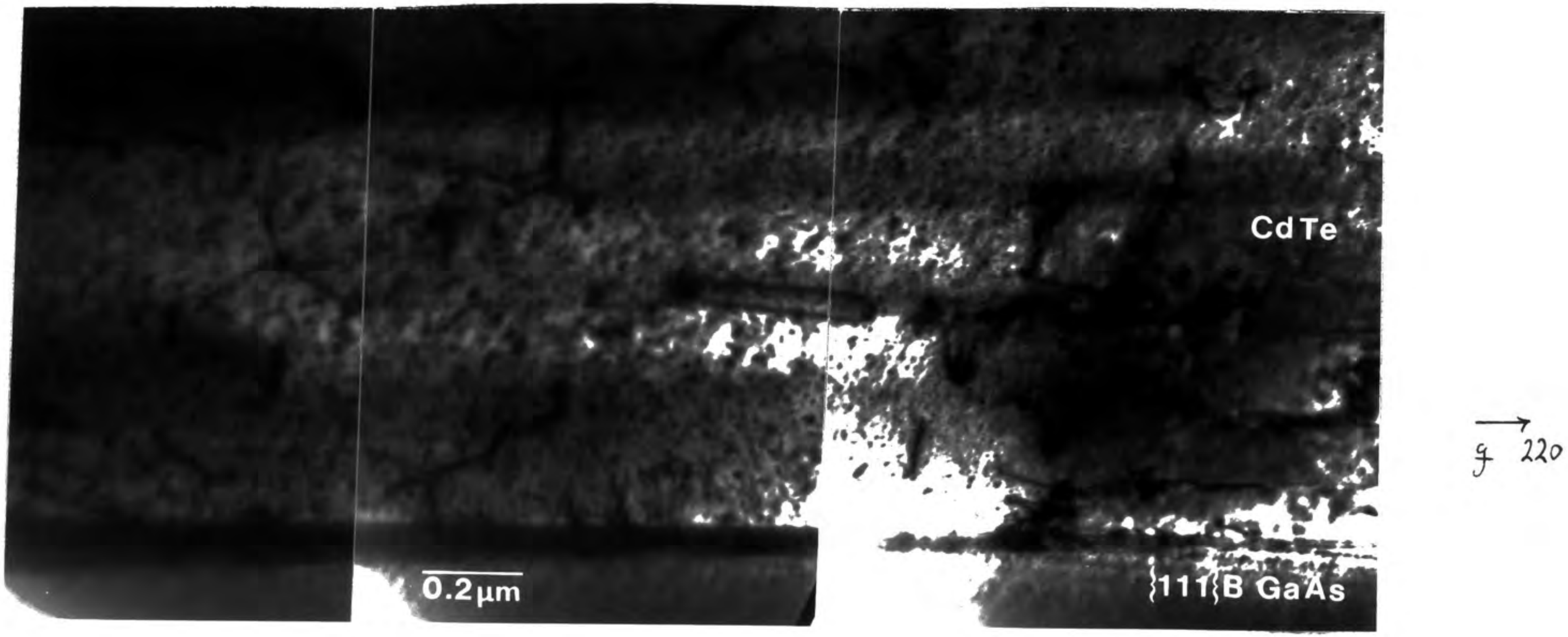

Figure 5.8b {111}CdTe/{$\bar{1}\bar{1}\bar{1}$}B GaAs, taken from the same region as Figure 5.8a, but with the sample tilted such that the twins are out of contrast.

Figure 5.9 The dislocation content in a {111}CdTe epilayer grown on {100}GaAs, tilted such that the twin lamellae are out of contrast.

Discussion

Attention is drawn to the following points;

1. Favourable epitaxial growth of CdTe only occurs on the CdTe and GaAs $\{\bar{1}\bar{1}\bar{1}\}$B substrate faces.
2. Twin lamellae lying parallel to the epilayer/substrate interface are formed in $\{\bar{1}\bar{1}\bar{1}\}$B CdTe layers grown on $\{100\}$ and a $\{\bar{1}\bar{1}\bar{1}\}$B GaAs substrates. A similar defect distribution is found in homoepitaxially grown CdTe, for which there is no lattice mismatch.
3. It is possible to obtain both $\{111\}$ and $\{100\}$ oriented CdTe epitaxial layers on a $\{100\}$GaAs substrate.

The different surface morphologies of epitaxial CdTe grown on the opposite polar faces of CdTe and GaAs may be explained in terms of the difference in vapour pressure of the various components and their dependence on polarity.[53] The process of epitaxial growth of CdTe by MBE, for example, is determined by the following competative growth processes:

$$Cd_{(v)} \mapsto Cd_{(s)} \qquad Te_{2(v)} \mapsto Te_{2(s)}$$

$$Cd_{(s)} + \frac{1}{2}Te_{2(s)} \mapsto CdTe_{(s)}$$

For homoepitaxial growth on the $\{111\}$ A face, the dominant process competing with the formation of CdTe is the re-evaporation of Cd, since its vapour pressure is much higher than tellurium. Since the re-evaporation of Cd from the $\{111\}$ A face is much greater than from the $\{\bar{1}\bar{1}\bar{1}\}$B face, the growth rate of the $\{111\}$ A face is much slower. Consequently, the fast Cd evaporation leads to the formation of Te-Te stacking faults and eventually a heavily facetted morphology.[53] These ideas may be extended to explain the same observations for MOVPE grown homoepitaxial CdTe, except that the situation is further complicated by the presence of additional reaction products from the source alkyls.

It has recently been shown that improved MBE growth can occur on a $\{111\}$ A face of CdTe by changing the species at the growth interface. Sivananthan et al[54] obtained layers with a better surface morphology by growing under conditions of excess Cd (by using a second Cd effusive cell). Also, Cheung[53] achieved a similar effect using a modified MBE system, in which a laser induced tellurium evaporation source was used in place of the conventional Te_2 effusive cell. The complete photo- dissociation of Te_2 to form the more reactive atomic Te led to an enhancement of the growth rate of CdTe on the {111} A surface and so led to an improvement in the epilayer surface morphology.

The formation of twin lamellae lying parallel to the epilayer/substrate interface for the case of homoepitaxial growth on the $\{\bar{1}\bar{1}\bar{1}\}$B surface clearly demonstrates that this process is an inherent property of CdTe on the {111} growth plane,[37] and is probably associated with the high ionicity[55] and low stacking fault energy ($\approx$10mJm^{-2}) of this material,[56] which favour twin formation.

Vere et al[55] have demonstrated that twinning in CdTe occurs following 'accidents' at the growth interface. Once initiated, the formation of these defects into lamella platelets may be explained in terms of the re-entrant corner mechanism, as described by Ming and Sunagawa.[57] The 'rough' atomic configurations associated with the sides of a lamella twin act as self perpetuating step sources that result in the preferential lateral (*i.e.* sideways) growth of the twin lamellae to form platelets.

There have been several investigations of the conditions necessary to control the epitaxial growth of {100} and {111} CdTe on GaAs, using a variety of different growth techniques. Most of these fundamental studies have been performed using MBE. However, this work has more recently been reproduced by workers using the MOVPE growth technique. The early MBE studies of the CdTe/{100}GaAs epitaxial system report either the formation of a {100} CdTe[58,59] or a {111} CdTe[60–62] layer. More recently, there have been a number of reports of the controlled MBE growth of {100} and {111} oriented CdTe on GaAs.[14] [15] [16] [18] Similarly, it has been reported that MOVPE grown epitaxial layers of CdTe form the {100} orientation,[59] [63] or alternatively, can be controlled to form both {100} and {111} epitaxial orientations.[16] [19] [36]

In general, the substrate preparation process is critical when controlling the orientation of the CdTe epilayer on {100} oriented GaAs. Early HREM studies of MBE grown material suggested that an oxide layer at the CdTe/GaAs interface was responsible for the formation of {100} CdTe,[32] whereas growth on a perfectly desorbed substrate led to the epitaxial growth of {111} CdTe. Ballingall et al,[14] for example, noted that it was possible to reproducibly grow the two different CdTe orientations by altering the substrate temperature during pretreatment. Heat treatment at 580°C for 5 to 10min resulted in the growth of a {111} CdTe epilayer. Epitaxial growth on a substrate with an oxide at the surface, formed due to the pregrowth chemical polishing processes required to remove surface damage arising from the mechanical cutting of these substrates, always resulted in the formation of a {100} CdTe epilayer. These workers,[14] however, noted that better quality {100} CdTe layers could be grown on substrates which had been desorbed for a short time prior to epitaxial growth. Faurie et al[15] also reported that the epilayer orientation could be controlled by the substrate preheating process, but concluded that oxygen does not play a key role in determining which epilayer orientation is formed. This was based on the observation that it was possible to obtain a {100} oriented CdTe layer on an almost completely desorbed (< 1 monolayer of O_2) GaAs substrate.[15] It is therefore suggested that oxygen plays a mechanical role rather than a chemical role in the determination of the CdTe epilayer orientation.

It is known from the AES assessment of the initial stages of CdTe heteroepitaxial growth that Te is initially adsorbed rather than Cd for any GaAs substrate orientation.[62] Feldman et al[16] have noted that different amounts of Te acted to change the orientation of the CdTe epilayer. A relatively small Te concentration (< 1 monolayer) on the substrate surface led to the formation of a {111} CdTe orientation, while higher concentrations always produced the {100}CdTe orientation, even for the case of a GaAs substrate completely desorbed prior to epitaxial growth. It was shown that growth on a prebaked oxygen desorbed GaAs substrate led to the formation of a {111} CdTe layer, while the introduction of a Te flux prior to epilayer growth on a prebaked substrate led to the formation of a {100}CdTe epilayer. In general, however, the reproducible controlled growth of each epilayer orientation is quite difficult, and HREM observations have shown that for {111} CdTe growth, a small percentage of the {100}oriented material is also present.[39]

Most recently, Srinivasa et al[18] have shown that the CdTe epilayer orientation may also be predetermined by the GaAs precursor surface reconstruction. During MBE growth this may be achieved by variation of the GaAs effusion oven temperature, which determines the ratio of the As_2 to Ga flux in the molecular beam, during the growth of a GaAs buffer layer prior to CdTe epilayer growth, and altering the temperature of the GaAs substrate, typically between 500°C and 620°C. The optimum growth temperature for CdTe lies between 275°C and 300°C. A Ga-stabilised surface leads to the formation of a {111} CdTe layer, while an As-stabilised surface produces a {100} oriented CdTe epilayer.

The controlled growth of {100} and {111} oriented CdTe epitaxial layers on {100} GaAs by MOVPE may be achieved by variation of the surface kinetic processes. The nature of the GaAs substrate surface reconstructions prior to epitaxial growth are not readily observable in MOVPE growth system, but comparisons can be made since the MOVPE deposition process is closely related to the physical vapour deposition process of MBE. Anderson[19] has shown that CdTe forms coarse polycrystalline material through to high quality specular single crystal films when grown at temperatures ranging from 220°C to 440°C, and that the epilayer surface morphologies are dependent on variations in the alkyl concentrations. Epitaxial growth on a {100}GaAs substrate baked in H_2 at 600°C for 20min, with a Cd:Te ratio of 1.25:4 and flow rates designed to generate low alkyl mole fractions and a slow growth rate of $2\mu mhr^{-1}$, led to the formation of a {100}CdTe layer. Whereas, alteration of the mole fractions to give a growth rate of $4\mu mhr^{-1}$ produced a {111} oriented CdTe epilayer. These results seemed to demonstrate that the interfacial oxide model for the control of the CdTe orientation was also inappropriate for MOVPE. Growth initiated under Cd rich conditions was always found to give {100} oriented CdTe epilayers, while all other growth conditions produced a {111} CdTe epitaxial layer.

The crystallography of the CdTe/GaAs epitaxial system

It is appropriate at this stage to consider some crystallographic aspects of the CdTe/GaAs system. It is apparent from the epitaxial growth of this epilayer that the {111} CdTe orientation is favoured over the {100}CdTe orientation for growth on a GaAs substrate heat treated in a hydrogen ambient at ≈ 600°C prior to epitaxial growth. This observation is consistent with theoretical predictions for the heteroepitaxy of this system. It has been shown by SAD and microdiffraction studies of the {111} CdTe/{100}GaAs system that the epilayer is oriented such that a $< 211 >$ direction is parallel to the absolute [110] direction in the substrate (see figure 5.6b). Even though there is a lattice mismatch of 14.6% from consideration of the lattice parameters of CdTe and GaAs, the difference in interplanar spacing between atoms for the $< 211 >$/[110] sample projection is only 0.7%.

By minimising the CdTe unit cell area at the growth interface, Zur and McGill[64] have shown that the {111} CdTe epitaxial orientation is favoured for growth on a

{100}GaAs substrate. In addition, Cohen-Solal et al[65] have developed models for the CdTe/{100}GaAs system by considering the chemical interactions at the interface following the adsorption of different amounts of Te onto the substrate surface, coupled with the different surface reconstruction states exhibited by the GaAs substrate. It was shown that a {111} CdTe orientation is expected for the case of an As deficient substrate surface, with a $\{\bar{1}\bar{1}\bar{1}\}$B CdTe face at the epilayer surface. This prediction is consistent with the experimental conditions for the controlled epitaxial growth of CdTe as described by Feldman[16] and Srinivasa[18] and also with the XPS polarity determination experiment reported by Hsu et al[66] (see section 3.7), which predicts that a Te surface results from the epitaxial growth of {111} CdTe on {100}GaAs and that the Fewster convention should be used for the purpose of CdTe polarity determination. The models of Cohen-Solal also predict the formation of a {100}CdTe layer following growth on a {100} GaAs substrate under Ga-stabilised conditions. Perhaps more importantly, it is predicted that the CdTe $[0\bar{1}1]$ direction is parallel to the [011] direction in the GaAs substrate for both {111} and {100} CdTe orientations on {100} GaAs. Hence, it is noted that a rotation of 90^o of the epilayer with respect to the substrate is predicted for the {100}CdTe/{100}GaAs system (see section 5.5).

5.4 Comparison of (Hg,Cd)Te Epitaxial Layers Grown on Bulk CdTe and Hybrid CdTe/GaAs Substrates

There have been several reports of the TEM investigation of MCT layers grown by MOVPE or MBE on {100}GaAs,[35] [38] [43] [44] [67] and by LPE on {111} A CdTe[68] and (Cd,Zn)Te[69] substrates. Observations of low-angle wedges of LPE-grown MCT on {111} oriented CdTe and (Cd,Zn)Te have revealed the blocking of threading dislocations at these interfaces.[70] In addition, the epitaxial growth of MCT on CdTe/GaAs hybrid substrates has been reported for both the {100} and {111} CdTe buffer layer orientations. A faceted structure invariably results for the {100} orientation,[71] while a twinned grain structure is formed for the {111} orientation.[9] [71] Both of these structural features act to the detriment of devices fabricated from these MCT layers. The MCT layers examined in this study were grown using the IMP process, and the relevent growth parameters are given in Table 2.1.

The micrograph shown in figure 5.10 was obtained from an epitaxial layer of MCT deposited onto a CdTe/$\{\bar{1}\bar{1}\bar{1}\}$B GaAs hybrid substrate. In spite of the twin lamellae

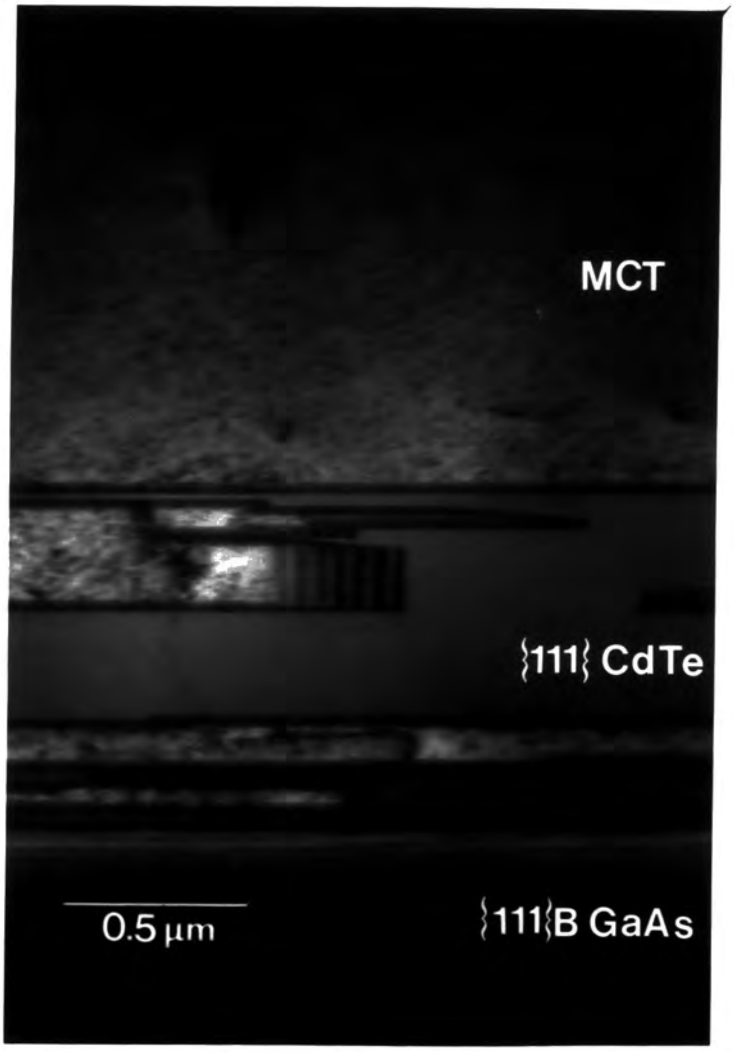

⟨110⟩

g 111

Figure 5.10 MCT/$\{\bar{1}\bar{1}\bar{1}\}$B GaAs

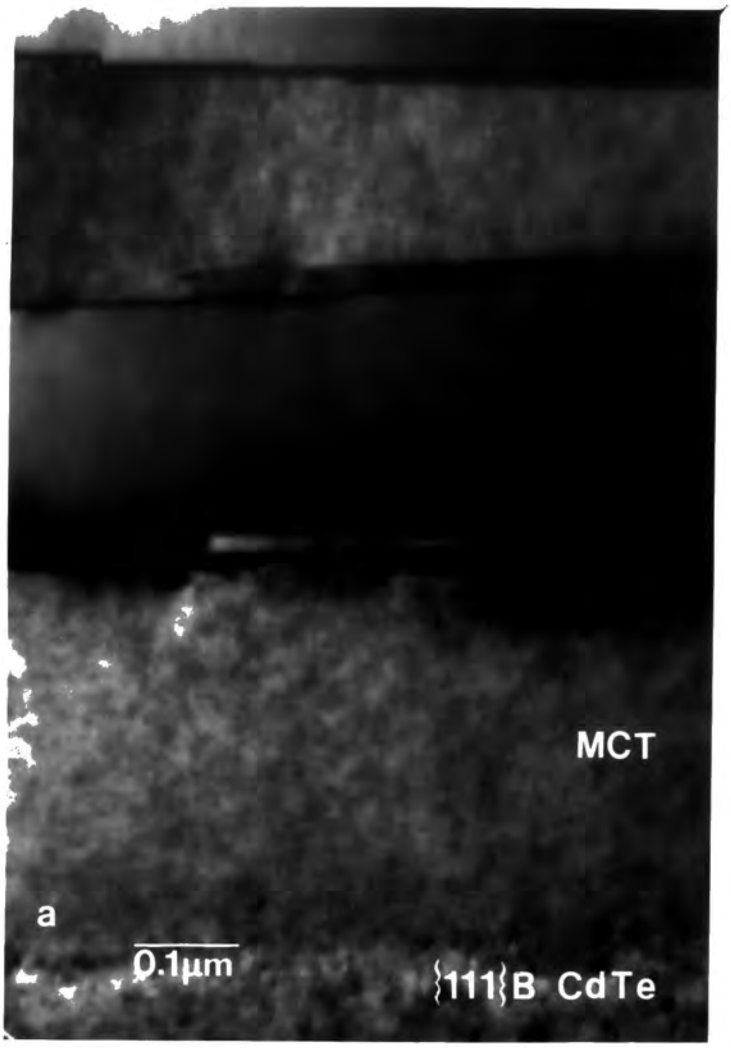

Figure 5.11a MCT/{$\bar{1}\bar{1}\bar{1}$}B CdTe, showing broad lamella twins in the epilayer. Feature 'a' denotes the interfacial region.

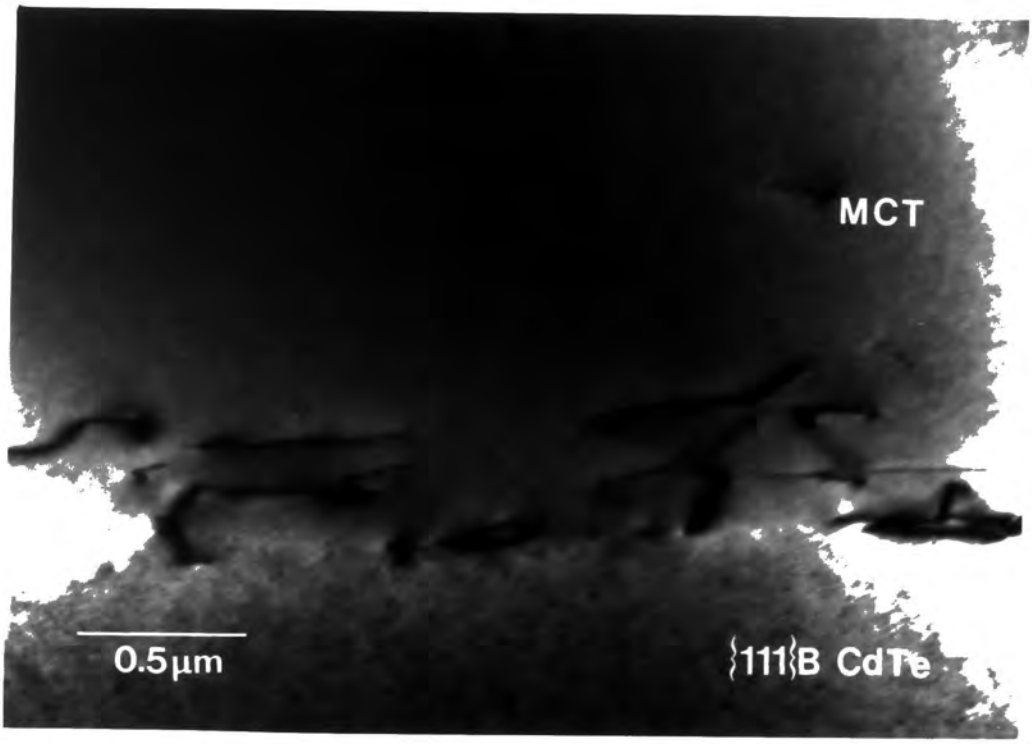

Figure 5.11b MCT/{$\bar{1}\bar{1}\bar{1}$}B CdTe, showing the blocking of interfacial misfit dislocations.

lying parallel to the substrate in the CdTe buffer layer, it can clearly be seen that good quality epitaxial MCT may be grown on such hybrid substrates.[72]

For comparison, micrographs of MCT grown on bulk $\{\bar{1}\bar{1}\bar{1}\}$B CdTe substrates are shown in figures 5.11a and 5.11b. These layers typically exhibit either broad twins ($> 0.5\mu$m wide) lying parallel to the interface (figure 5.11a) or none at all (figure 5.11b). The MCT/CdTe interface in figure 5.11a is identified by the slight change in 'speckle' damage across feature *a* that arises from a difference in the milling behaviour of these two materials.[73] The interface shown in figure 5.11b shows the same effect and further reveals the blocking of misfit dislocations propagating into the MCT epilayer. The observation of these blocked dislocations near the interface in IMP-grown layers provides evidence of a residual layered structure and implies that for the first few IMP layers interdiffusion is incomplete. The dislocations typically propagate $\approx 0.1\mu$m into the layer before being bent into the plane of the layer, and this distance corresponds to the thickness of the first binary layer deposited.[74]

SEM observations of the MCT layers deposited onto either hybrid or bulk CdTe substrates indicate that MCT often grows in the form of twin related grains.[9] Such features have been observed in cross-section and take the form of irregular boundaries lying approximately prependicular to the interface. It is likely that these boundaries are similar to the lateral twin boundaries characterised for the CdTe buffer layers. The dislocation content of layers grown on hybrid substrates (typically 10^5cm^{-2}) was in general significantly lower than those grown on $\{111\}$ CdTe wafers. Regions varying in dislocation content from 10^5 to 10^8cm^{-2} were observed in the latter case.

The observation that epitaxial MCT contains broad lamella twins or is untwinned may be related to the Hg content of these layers. Hails[75] has shown that epitaxial HgTe grown by MOVPE on $\{\bar{1}\bar{1}\bar{1}\}$B CdTe is untwinned. In contrast, homoepitaxially grown CdTe has been shown to contain a high density of twin lamellae. Twinning in CdTe is regarded as being inherent to the chemical bond structure of this compound[55] and is related to its high value of ionicity (0.717). HgTe has a lower ionicity (0.65) which suggests that the incorporation of Hg into CdTe to form MCT acts to lower the alloy ionicity and thereby reduce the probability of (lamella) twin formation.

In spite of the excellent surface morphology of $\{111\}$ MCT epitaxial layers,[8] a high incidence of twin islands are formed. Their associated lateral twin boundaries are expected to contain a periodic array of broken bonds which would make them electrically active[49] and hence, would act to the detriment of devices formed from such layers. This has led very recently to the investigation of the epitaxial growth of MCT by MBE on higher order index planes. Koestner and Schaake[76] have demonstrated that twin free MCT may be obtained on the {211} surfaces of CdTe. Also, Million et al[77] similarly report the production of twin free MCT on the non polar {310} surface of $Cd_{0.96}Zn_{0.04}Te$, following the growth of a graded step (Cd,Zn)Te/GaAs hybrid substrate to block the propagation of misfit dislocations and establish a $Cd_{0.96}Zn_{0.04}Te$ growth surface. The resultant MCT epilayers exhibited fewer surface facets as compared with the {100} oriented epilayers and contained a lower dislocation content.

5.5 (Cd,Zn)Te/CdTe Strained Layer Superlattices*

Introduction

The accurate lattice matching of (Cd,Zn)Te (CZT) or Cd(Te,Se) to (Hg,Cd)Te should act to improve the quality of MCT epitaxial layers and hence, improve device properties.[78] The ternary alloy of composition $Hg_{0.795}Cd_{0.205}Te$, is of great interest since its band-gap of 0.1eV coincides with the atmopheric window positioned at 12.4μm, and very recently there have been reports of the growth of MCT on $Cd_{0.96}Zn_{0.04}Te$ by MBE[77] and on $CdTe_{0.96}Se_{0.04}$ by MOVPE.[79] The incorporation of Zn into the CdTe lattice acts to strengthen the mechanical properties of the alloy, but this in turn leads to the formation of arrays of subgrain boundaries. In view of the potential of epitaxial growth techniques to produce high quality material, as compared with bulk growth techniques, there has been recent interest in the production of hybrid substrates, incorporating buffer layers of CZT,[80] which can be lattice matched to MCT. In addition, the incorporation of a strained layer superlattice (SLS) into the buffer layer should inhibit the propagation of misfit dislocations and hence, lead to the formation of a low defect density CZT surface at the MCT growth interface.[81]

In order to investigate the feasability of such a structure for use as a hybrid substrate, it was proposed to grow by MBE the $CdTe/Cd_{0.92}Zn_{0.08}Te$ SLS system as shown in figure

---

⋆ These MBE epilayers were grown by T.D. Golding† and J.H. Dinan, U.S. Army Center for Night Vision and Electro-Optics, Fort Belvoir, Virginia 22060 5677.

†On leave from the Cavendish Laboratory, University of Cambridge, Cambridge, United Kingdom.

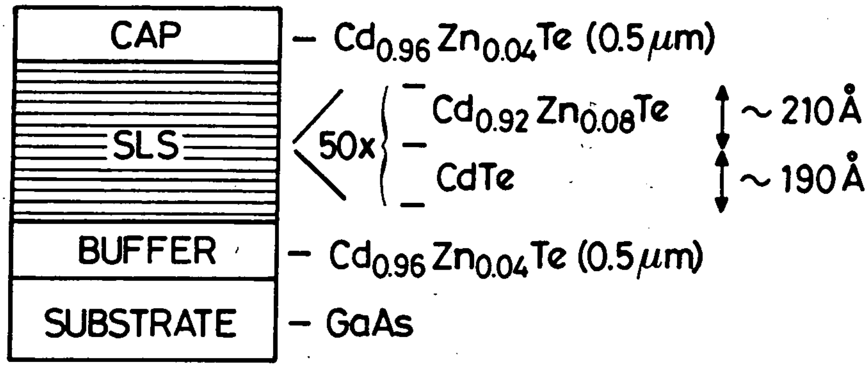

Figure 5.12 Schematic diagram showing the proposed CZT/CdTe superlattice structure.

5.12. The structure consists of a 50 period superlattice sandwiched between two 0.5μm $Cd_{0.96}Zn_{0.04}Te$ buffer and capping layers. The CZT composition was chosen to ensure an exact lattice match with $Hg_{0.8}Cd_{0.2}Te$. Also, in order to avoid the generation of misfit dislocations between the superlattice, cap and buffer layers, the thickness ratio between the $Cd_{0.92}Zn_{0.08}Te$ and CdTe strained layers was tailored to allow the superlattice free standing lattice parameter to match that of $Cd_{0.96}Zn_{0.04}Te$. In addition, it was proposed to investigate the effect of a higher Zn concentration in the superlattice by growing a 50 period structure of the form $Cd_{0.84}Zn_{0.16}Te$/CdTe, again sandwiched between a buffer and capping layer of $Cd_{0.96}Zn_{0.04}Te$.

Experimental

The samples were grown in a Varian 360 MBE system equipped with quadrapole mass analyser and in situ RHEED and flux monitoring facilities. The base pressure during growth was below 5×10^{-10}torr. A single effusion cell containing high purity CdTe was used to provide a stoichiometric beam of Cd and Te_2[23] for the growth of CdTe and was supplemented by an effusion cell containing Zn for the growth of CZT. Calibration of the Zn cell setting against Zn content for the growth of CZT layers was determined by growing a series of CZT layers with various Zn cell settings and determining their Zn content by Energy Dispersive x-ray Analysis and Double Crystal (DC) x-ray analysis. Prior to epitaxial growth (001) GaAs polished substrates were cleaned in a 4:1:1 solution of H_2O:H_2O_2:H_2SO_4 and mounted onto molybdenum support blocks using indium.

The substrates were heated to 610°C and held at this temperature until the native oxide had been desorbed, as indicated by RHEED. To ensure the growth of a (001) oriented $Cd_{0.96}Zn_{0.04}Te$ buffer layer, the technique described by Kolodziejski et al[82] was employed where the Zn and CdTe cells were opened whilst the substrate was at the elevated temperature of 610°C. The substrate temperature was then dropped to the desired growth temperature of 250°C which was maintained constant throughout the subsequent growth process. Confirmation of (001) oriented epitaxy was obtained by RHEED. Following the growth of the 0.5μm $Cd_{0.96}Zn_{0.04}Te$ buffer layer a 50 period $Cd_{0.92}Zn_{0.08}Te$ /CdTe superlattice was grown. DC X-ray analysis of the superlattice yielded a 330Å period, calculated from the separation between the resulting satellite peaks, indicating individual layer thicknesses of 165Å in this instance.[81] Finally a 0.5μm $Cd_{0.96}Zn_{0.04}Te$ capping layer was grown on the SLS.

Similarly, a second superlattice structure was grown with a 50 period $Cd_{0.84}Zn_{0.16}Te$ /CdTe structure between buffer and capping layers of $Cd_{0.96}Zn_{0.04}Te$. DC X-ray analysis in this case indicated individual layer thicknesses of 85Å and 245Å for the $Cd_{0.84}Zn_{0.16}Te$ and CdTe layers respectively.

Samples were prepared in cross-section for structural examination in the usual way (section 2.4), but with the as-grown samples being cleaved along orthogonal $< 110 >$ directions before bonding them face to face between polycrystalline silicon blocks. This procedure allowed the observation of both [110] and $[1\bar{1}0]$ epilayer orientations on opposite sides of the glue line for the same TEM sample. The exact polar orientation of the GaAs substrate (assuming an [001] growth direction) was determined using the technique of microdiffraction (section 3.3).

Results

The micrograph shown in figure 5.13a corresponds to a [110] projection of the GaAs substrate and clearly illustrates the entire superlattice structure. At the $Cd_{0.96}Zn_{0.04}Te$/ GaAs interface, a large number of misfit dislocations are seen to be introduced as might be expected from the large lattice mismatch between these two structures. At a distance of about 0.5μm into the epilayer a series of striations lying parallel to the epilayer/substrate interface can be seen and these correspond to the SLS. Above this structure is the $Cd_{0.96}Zn_{0.04}Te$ capping layer. It is also immediately apparent that the epilayer contains a large number of microtwins lying on $\{111\}$ planes, inclined at approximately 55^o to the interface. These defects tend to propagate through the entire thickness of the epitaxial layer. In addition, a large number of dislocations are generated during the process of epilayer growth.[*]

By tilting the sample so as to eliminate the fringe contrast arising from the superlattice, it is possible to see the underlying defect content for this specimen orientation more clearly (figure 5.13b). It is apparent that the superlattice structure in this case is ineffective at blocking the interfacial defect content.

The superlattice is also out of contrast in the micrograph shown in figure 5.14, which was taken on the opposite side of the glue line and hence, correponds to the $[1\bar{1}0]$ orientation of the GaAs substrate. It is clearly obvious that there is a complete absence of microtwins seen edge on for this sample projection. The epilayer simply contains an array of misfit dislocations generated at the epilayer/substrate interface, along with

---

[*] see ref p66

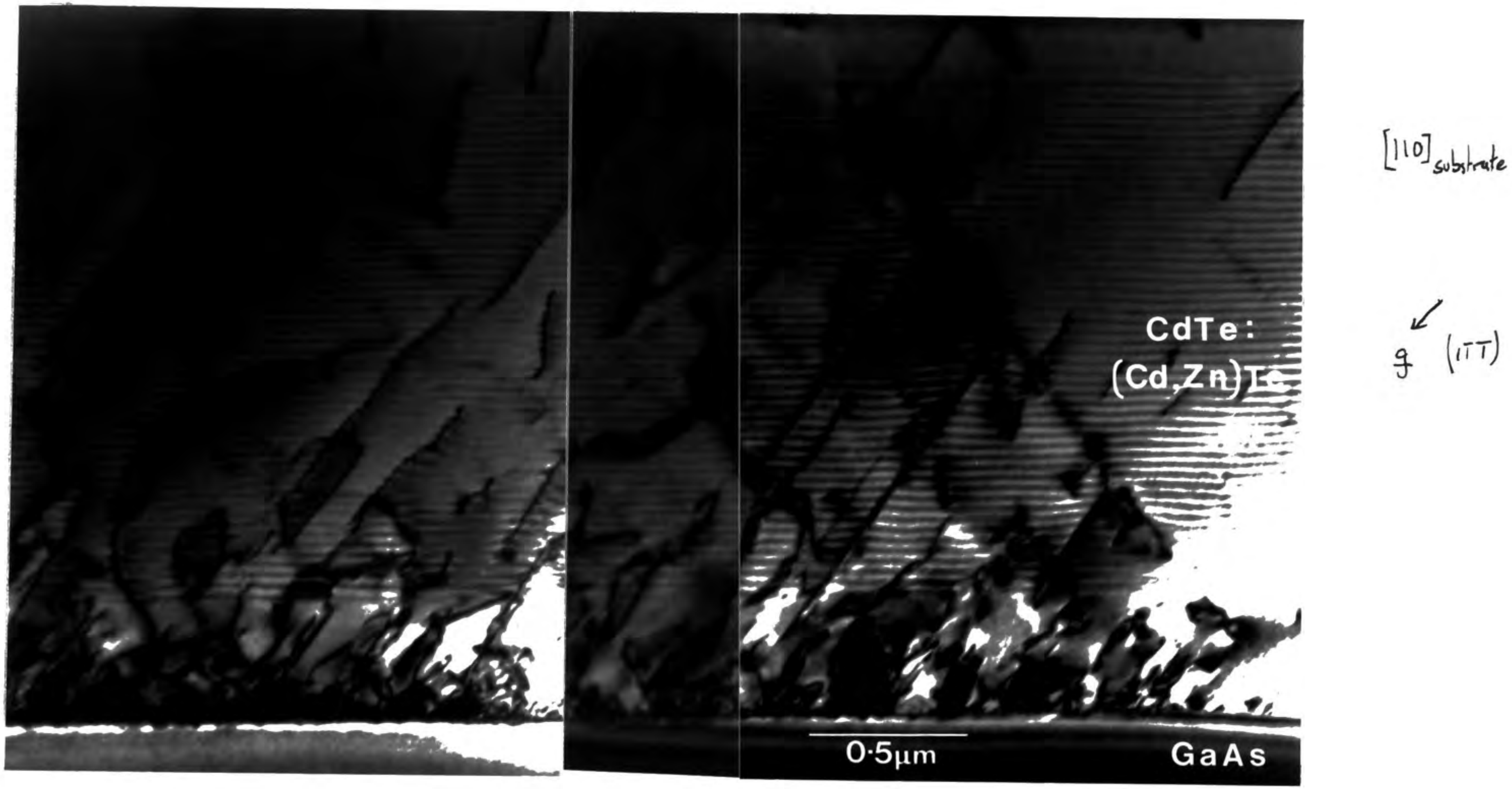

Figure 5.13a CdTe/$Cd_{0.92}Zn_{0.08}Te$ strained layer superlattice on a (001) oriented GaAs substrate ([110] substrate projection).

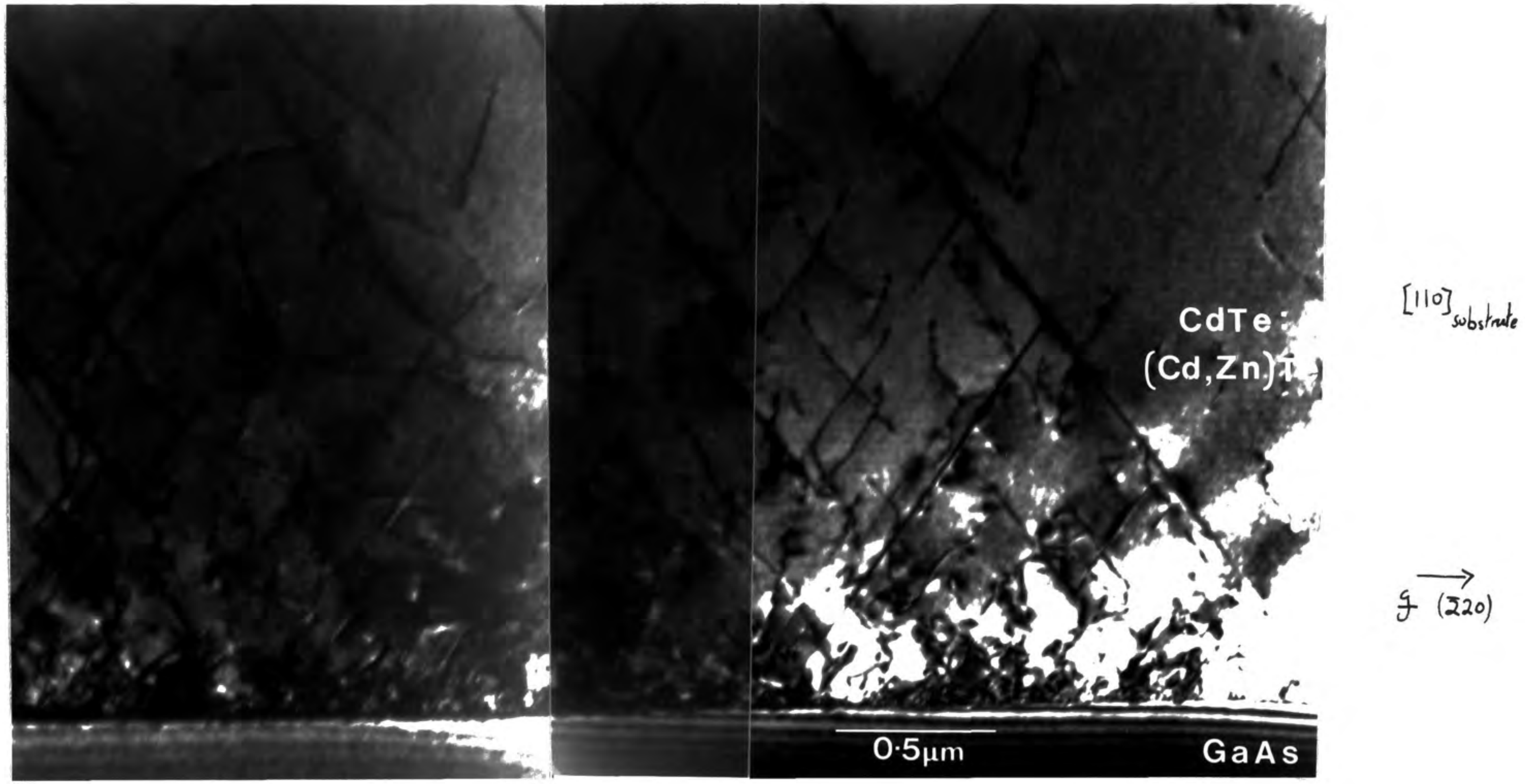

Figure 5.13b CdTe/$Cd_{0.92}Zn_{0.08}Te$ superlattice, showing the same region as Figure 5.13a, but with the sample tilted such that the fringes are out of contrast.

$[1\bar{1}0]_{substrate}$

←

g $(\bar{2}\bar{2}0)$

Figure 5.14 CdTe/$Cd_{0.92}Zn_{0.08}Te$ superlattice on a (001) GaAs ($[1\bar{1}0]$ substrate projection).

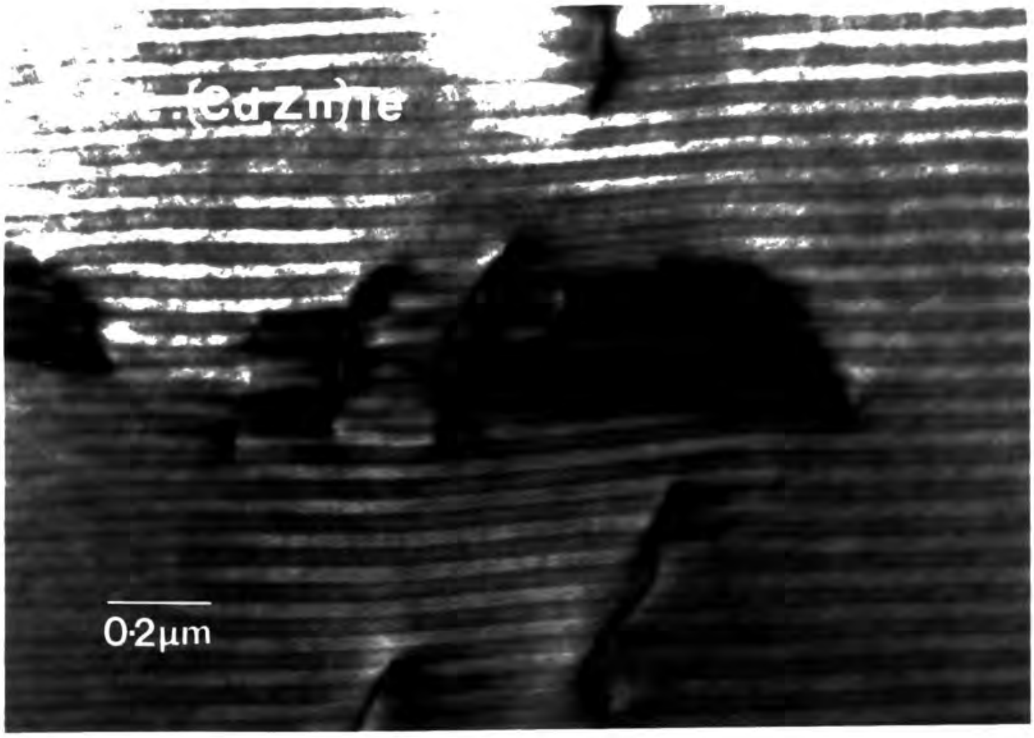

$[1\bar{1}0]_{substrate}$

↗

g (111)

igure 5.15 CdTe/$Cd_{0.92}Zn_{0.08}Te$ superlattice on (001) GaAs, ($[1\bar{1}0]$ substrate projection), showing features with strong fringe contrast (see text).

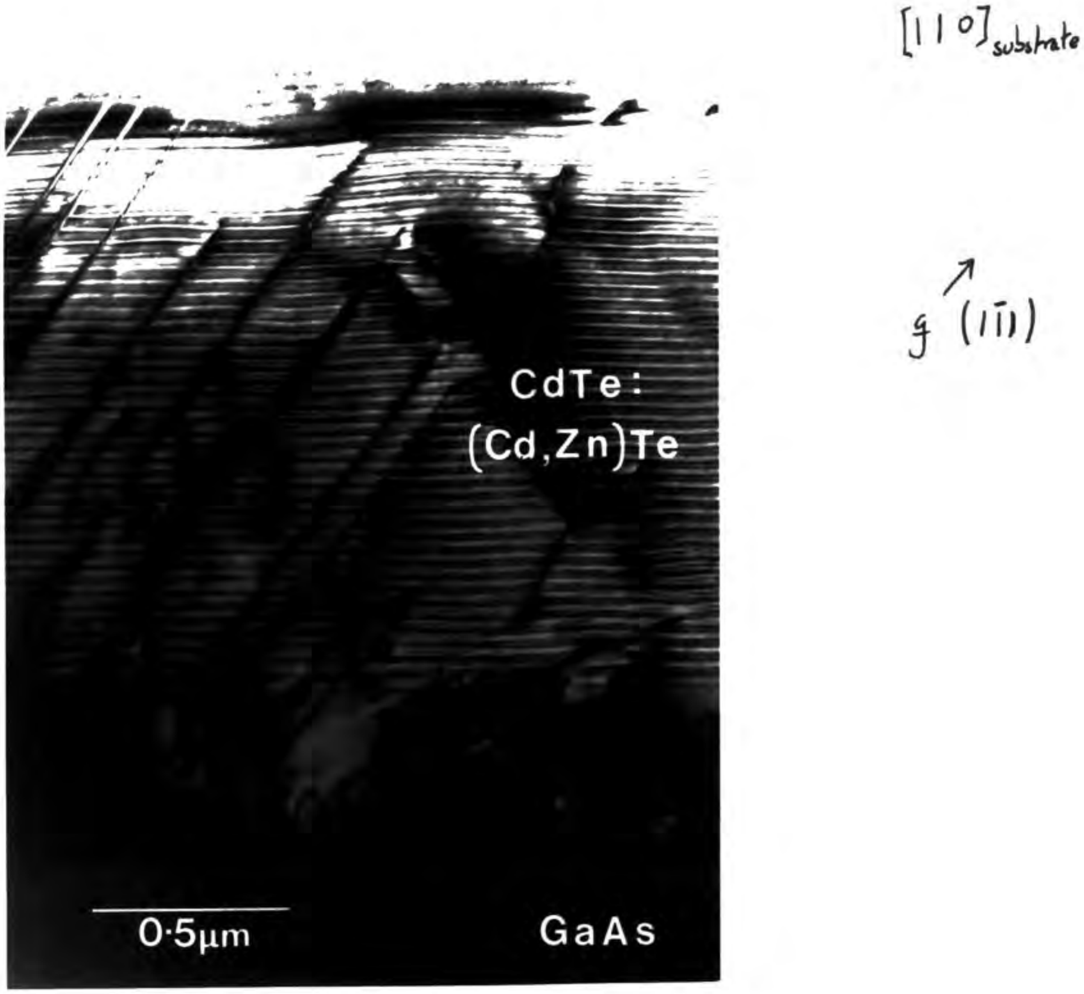

Figure 5.16 CdTe/Cd$_{0.84}$Zn$_{0.16}$Te superlattice ([110] substrate projection).

additional dislocations formed during the subsequent growth of the superlattice. When the crystal is tilted such that the alternate layers of the superlattice exhibit strong contrast (figure 5.15), a large number of features exhibiting even stronger fringe contrast lying parallel to the superlattice can be seen. These are believed to be due to the observation of the same microtwins as were observed edge on in the orthogonal $< 110 >$ epilayer projection but in this $[1\bar{1}0]$ (substrate) orientation they lie on $\{111\}$ planes inclined to the direction of the incident electron beam, intersecting the sample foil.

An identical anisotropic defect distribution of the epilayer defect content was also found in the $Cd_{0.84}Zn_{0.16}Te$ /CdTe superlattice structure, with the microtwins being observed edge on for one $< 110 >$ epilayer zone axis (figure 5.16) and the same defects giving rise to fringe contrast (similar to that shown in figure 5.15) in the orthogonal $< 110 >$ sample projection. TEM specimens with this increased Zn content were prone to extensive cracking parallel to the superlattice layers during sample preparation and prolonged irradiation with a focussed electron beam.

Discussion

It has previously been shown in Chapter 4 that a similar anisotropic defect distribution exists in epitaxial layers of ZnSe/ZnS/$\{100\}$GaAs grown by MOVPE. Microdiffraction patterns taken from the GaAs substrate and the ZnSe regions of the epilayer for this epitaxial system demonstrated that the microtwins lay exclusively in the $[1\bar{1}0]$ epilayer projection, whereas there was a complete absence of microtwins in the $[110]$ sample projection. This epitaxial system was also shown to exhibit parallel epitaxy on the (001) growth plane with the $[110]$ direction in the GaAs substrate corresponding to the $[110]$ direction in the ZnSe region of the epilayer. This observation was explained in terms of the differential motion of α and β dislocations in the ZnS buffer layer arising from the large difference in the ionic radii of the Zn^{2+} and S^{2-} ions. For this material it was predicted that the more highly mobile α dislocations lying on advancing $\{\bar{1}1\bar{1}\}$B planes in the $[110]$ epilayer projection are swept through the crystal leaving perfect crystal behind them. Whereas, splitting of the slowly moving β dislocations for the $[1\bar{1}0]$ sample orientation led to the leading partial dislocation being swept through to the sample surface, resulting in the formation of a stacking fault. The interaction of successive dislocations on adjacent $\{111\}$ planes leads to the formation of microtwins.

For these MBE grown layers of CZT it is also expected that the α dislocation is the most highly mobile dislocation in this material. But this epitaxial system is under compressional strain and consequently, one would expect that the [110] epilayer projection would exhibit microtwins whereas the orthogonal $[1\bar{1}0]$ zone axis would not. Microdiffraction patterns taken from the GaAs substrate clearly illustrate that this is not the case (assuming parallel epitaxy). This discrepancy can, however, be resolved once it is realised that the {100}CdTe/{100}GaAs system is predicted to be rotated by 90^o at the epilayer/substrate interface, such that the [110] CdTe epilayer zone axis is parallel to the $[1\bar{1}0]$ direction in the GaAs substrate[65] (section 5.3). Hence, for these CZT/CdTe strained layers, the observation of microtwins for a $[1\bar{1}0]$ substrate projection in fact corresponds to a [110] epilayer projection, and this in turn is in agreement with the dislocation model used to explain the anisotropic formation of microtwins.

It is apparent that a number of problems must be overcome if superlattices of the structure described are to be of use as lattice matched hybrid substrates for the epitaxial growth of $Hg_{0.8}Cd_{0.2}Te$.[83] It is necessary to improve the substrate desorption process (possibly by heating in a hydrogen ambient) in order to eliminate the contaminants which are considered to be responsible for formation of microtwins in epitaxial layers.[84] In addition, it is necessary to find a superlattice structure which blocks the misfit dislocations generated at the buffer/GaAs interface more effectively, without introducing so much strain that cracking of the superlattice structure is too easily promoted. There is also the problem of the relatively large number of dislocations which are formed during the process of epilayer growth. While it is possible that these defects might arise due to impurities in the effusion cell source material, there is also the possibility of alloy segregation effects in CZT to form small regions of the associated binary compounds which act to disrupt the lattice structure and initiate the formation of dislocations. Golding et al,[81] however, suggest that this high defect content is mainly related to the large lattice mismatch between the epilayer and the GaAs substrate, and is independent of the superlattice period. High quality CZT/CdTe superlattices of the type described here have been reported for growth on {100}InSb and {100}CdTe substrates, as indicated by x-ray diffraction data, while identical layers grown on {100}GaAs were of a much poorer quality.[81]

5.6 Intermediate Band-Gap II-VI Compounds

In view of the increasing level of control over epitaxial growth (*i.e.* stoichiometry, uniformity and doping) offered by modern techniques such as MBE and MOVPE, there has been renewed interest in the last couple of years in the intermediate band-gap ternary alloys, based principally on ZnTe, for optoelectronic applications. (Hg,Zn)Te (MZT), for example, is recognised as being a potential replacement for MCT as an infra-red detector because the presence of Zn acts to strengthen the weak Hg-Te bond.[85] Although, use of this ternary alloy is presently limited because of high segregation coefficients at elevated temperatures.[86] The variation of the alloy composition of CZT allows its band-gap to be tuned between 1.5 and 2.2eV and this material may be used both as an optical source and as a detector operating in the green/blue regions of the spectrum.[87] Similarly, variation of the CZT composition also allows this material to be used as a lattice matched substrate for the epitaxial growth of MCT or MZT.[78] [88] Alternatively, it is suggested that CdTe/ZnTe multilayer structures may be used to form optoelectronic devices with even higher efficiencies. By control of the relative thickness of the superlattice component layers it is possible to modify both the epilayer lattice parameter and the effective band-gap of the material.[89] The latter phenomenon arises from the large (6.5%) lattice mismatch, and hence strain, associated with the CdTe/ZnTe superlattice system. Recent studies of MBE[90] and MOVPE[91] grown CdTe/ZnTe superlattices report sharper, more intense photoluminescence spectra as compared with those obtained from the ternary alloy, and these findings reflect the improved crystallinity of the superlattice over the mixed crystal system. As a prerequisite to the study of CdTe/ZnTe superlattices, it is first necessary to ascertain the optimum growth conditions for the ZnTe binary.

ZnTe/GaAs

Epitaxial layers of ZnTe were deposited in Durham onto {100}GaAs substrates at a temperature of 410°C using the precursors Me_2Zn and Et_2Te (see Table 2.1). As for the case of CdTe, it was found that high flow rates were necessary to avoid polycrystalline deposition from gas phase reactions,[92] and growth rates of 550Åmin^{-1} were achieved. RHEED investigations highlighted the high crystallinity of the as-grown layers, while SEM observations demonstrated that anisotropic faceting of the surface[92] occurred in a manner similar to that previously reported for ZnSe and ZnSe/ZnS heterostructures (see Chapter 4).

As shown in figure 5.17, MOVPE grown layers of ZnTe on {100}GaAs contain a large number of dislocations along with a few inclined microtwins. A large dislocation content is expected to form at the interface because of the large lattice mismatch of the ZnTe/GaAs system ($\approx$ 7%), but unlike CdTe for which the dislocation content grows out within 1.5μm,[52] a relatively large number of dislocations are found to propagate through the entire 2μm thickness of this epilayer. These observations are in contrast to those reported for MBE grown ZnTe/GaAs,[93] where the interfacial defect content grows out within 0.3μm of the epilayer/substrate interface. These workers[93] note that the epilayer dislocation content increases again beyond a thickness of 1.3μm with the additional appearance of Te precipitates. While this occurrence cannot be related to the relaxation of the strain in the epilayer, this reproducible observation[93] remains unexplained. It is probable that the higher dislocation content found in MOVPE grown ZnTe/GaAs arises from the higher growth temperature associated with this technique (410°C) as compared with MBE (300°C).[92]

ZnTe/CdTe multilayer structures

This study presents the results of the first attempt in Durham to grow a CdTe/ZnTe strained layer superlattice by MOVPE.[92] Alternate layers of CdTe and ZnTe were sequentially deposited onto a {100}GaAs substrate, using growth times of 2 and 30sec respectively. In order to allow for gas phase dispersion within the reactor and to minimise the mixing of the alkyl precursors, the reactor was purged for 15sec with H_2 prior to the growth of each layer. SEM observation of the as-grown epilayer demonstrated good surface morphology with an anisotropic network of striations, which Shtrikman[94] attributed to slip traces.

TEM observations of this sample in cross section revealed the uniform $\approx$50nm period of this multilayer structure (figure 5.18), and SAD patterns demonstrated that the thicker layers corresponded to ZnTe. Estimates of the relative thicknesses of the alternate layers were 12nm and 38nm for CdTe and ZnTe respectively. These thicknesses are far in excess of that required for this structure to be a strained layer superlattice. Miles[95] predicts a value of only 50Å for the CdTe/ZnTe system, while Kisker[91] suggests that this value may be even lower for MOVPE grown superlattices. TEM observations also revealed cracks lying perpendicular to the epilayer/substrate interface running through the entire $\approx$ 2μm thickness of the epilayer. These are probably formed because of the inability of the multilayer structure to fully relax. The formation of microcracks has

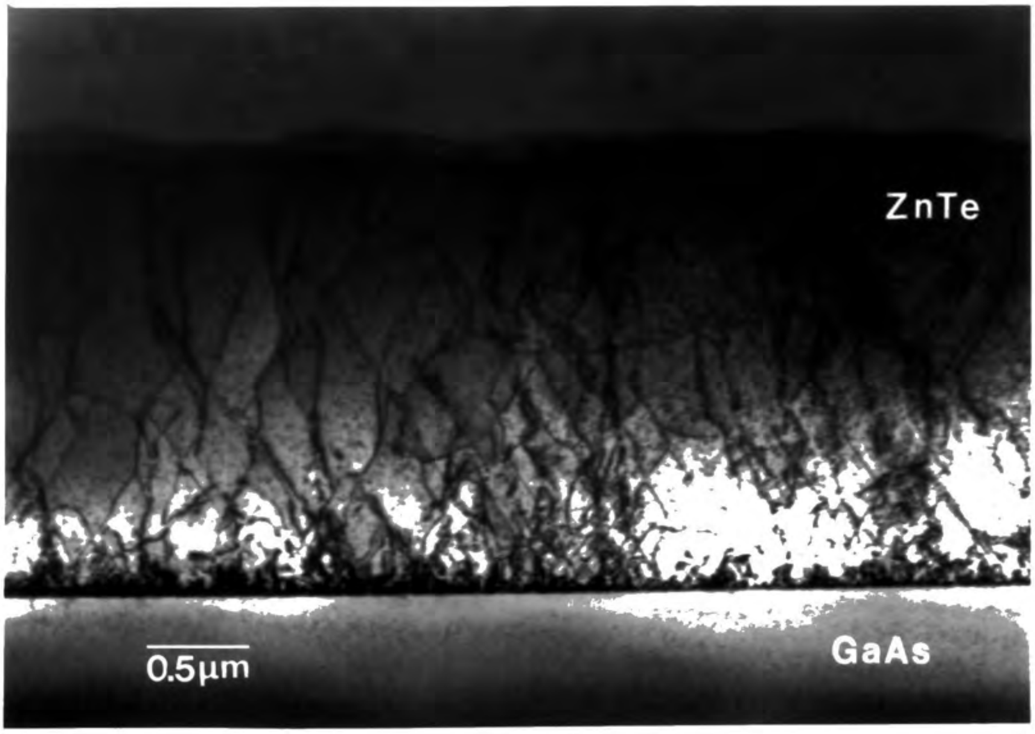

Figure 5.17   ZnTe/{100}GaAs

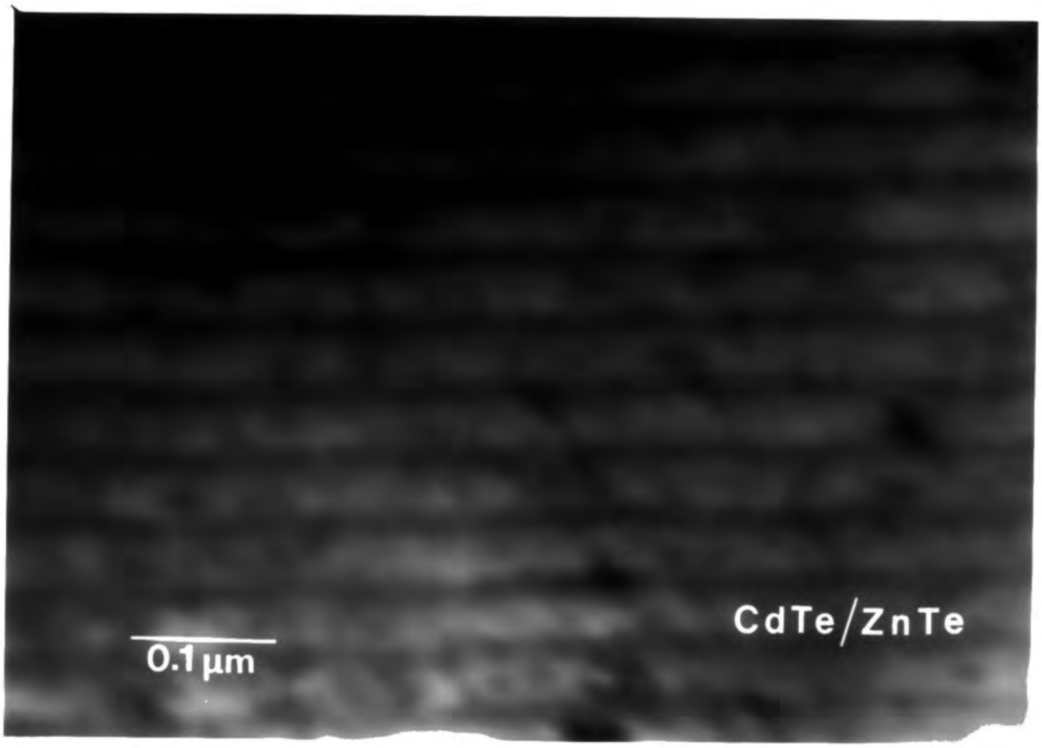

Figure 5.18   CdTe/ZnTe multilayer structure.

similarly been noted as a mechanism of strain relief in samples of $In_{0.48}Ga_{0.52}As/InP$[96] which are similarly under tensile strain. This brief study does, however, demonstrate the ability of the MOVPE technique to produce multilayer CdTe/ZnTe epitaxial structures, although it is apparent that much thinner layers must be grown if a true superlattice is to be formed.

5.7 Summary

There is a demand for very high quality MCT for far infra-red optoelectronic applications. Bulk grown MCT cannot meet this stringent requirement, and the high defect content similarly associated with bulk grown CdTe obviates the use of this binary compound as a substrate for MCT epitaxy. Consequently, hybrid substrates comprised of buffer layers of CdTe on high structural quality III-V compounds, have attracted a great deal of interest in the last five years, in addition to lattice matched CZT substrates.

The cross-sectional TEM characterisation of epitaxial CdTe on GaAs has demonstrated the complex microstructure of these hybrid substrates. The nature of the defect distribution, arising from the large lattice mismatch between the two compounds, is shown to be dependent on the GaAs substrate orientation and surface pre-treatment prior to epitaxy. The deposition of $\{111\}$ oriented CdTe is possible on $\{100\}$ and $\{\bar{1}\bar{1}\bar{1}\}$B GaAs, and on $\{\bar{1}\bar{1}\bar{1}\}$B CdTe substrates. The defect microstructure of these $\{111\}$ CdTe epilayers consists of a large number of lamella twins lying parallel to the epilayer/substrate interface. The twin lamellae are found to terminate at one of four lateral twin boundaries, which correspond to those found in bulk CdTe grown from the vapour phase, and there is evidence to suggest that the twins act to block the passage of threading dislocations. In contrast, the $\{100\}$CdTe/$\{100\}$GaAs epitaxial system contains an array of interfacial misfit dislocations. The observation of lamella twins in homoepitaxially grown CdTe demonstrates that this phenomenon is not due to strain introduced by lattice mismatch, but is an inherent property of the growth of CdTe on the $\{\bar{1}\bar{1}\bar{1}\}$B plane and so, is related to the high value of CdTe ionicity and its low stacking fault energy. The epitaxial growth of $\{111\}$ CdTe with good surface morphology is only possible on the non-metal faces of CdTe and GaAs. Deposition on the opposite polar face of these substrates leads to the formation of highly faulted layers. This observation is attributed to the higher re-evaporation coefficient of Cd from the metal polar face. It is considered that the surface pretreatment of {100}GaAs substrates is critical for the controlled deposition of {111} and {100} oriented CdTe. The {111} epilayer orientation is favoured from simple crystallographic consideration, since the < 211 > epilayer projection has a close lattice match (0.7%) to < 110 > GaAs. MBE studies of the CdTe/{100}GaAs system have shown that a {100} epilayer is formed following growth on an undesorbed or an As-stabilized substrate surface, or for growth under conditions of excess Te. Whereas growth on an oxide desorbed or a Ga-stabilized substrate surface promotes {111} CdTe epitaxy.

Comparison of MOVPE grown MCT deposited using the IMP process on bulk $\{\bar{1}\bar{1}\bar{1}\}$B CdTe and hybrid CdTe/$\{\bar{1}\bar{1}\bar{1}\}$B GaAs substrates suggests that good epitaxial growth is possible on both of these substrates. MCT grown on bulk CdTe tends to form either a network of interfacial dislocations which are bent into the plane of the epilayer, or to form broad twin lamella. It is considered that the introduction of Hg into CdTe acts to reduce the alloy ionicity and so inhibit the formation of lamella twins. SEM observations, however, indicate that {111} MCT epitaxial layers form a twin-grained structure. The expected introduction of electrically active lateral twin boundaries into the epilayer would act to the detriment of devices formed from such layers. The requirement that twinning be completely eliminated from MCT epitaxial layers has instigated the investigation of alternative higher order index plane substrate orientations for the epitaxial growth of MCT over the last year or so.

MBE grown CZT/CdTe strained layer superlattices (SLS), tailored to match the free standing lattice parameter of $Cd_{0.96}Zn_{0.04}Te$, have potential as high quality lattice matched substrates for the growth of $Hg_{0.8}Cd_{0.2}Te$. The investigation of a $Cd_{0.92}Zn_{0.08}Te$ /CdTe SLS grown on $Cd_{0.96}Zn_{0.04}Te/(00\bar{1})$ GaAs, however, demonstrated the severe defect anisotropy associated with this epitaxial system. Microtwins were found exclusively in one < 110 > sample projection, while misfit dislocations and fringe contrast, arising from the intersection of microtwins with the sample foil, were found in the orthogonal < 110 > layer projection. Similar observations were reported in Chapter 4 for ZnSe/ZnS heterostructures grown on (001) oriented GaAs. A similar defect distribution was also found in a $Cd_{0.84}Zn_{0.16}Te$/CdTe SLS sample, where the additional Zn content promoted cracking in this superlattice parallel to the epilayer/substrate interface. The absolute orientation of the GaAs substrate was determined by microdiffraction. This technique, however, could not be used with the epilayer material because of the nature of the superlattice. The formation of an anisotropic defect distribution in these (001) epilayers, which are under compressional strain, may be explained in terms of the differential motion of α and β dislocations by introducing a 90^o rotation of the epilayer with respect to the substrate. This finding is in agreement with the model of Coten-Solal[65] for the {100}CdTe/{100}GaAs epitaxial system. The high defect content of these SLS samples is considered to be mainly due to the large lattice mismatch with the GaAs substrate, since identical superlattices with high structural quality have been reported for growth on {100}InSb and {100}CdTe substrates.

A preliminary investigation of MOVPE grown ZnTe/(001)GaAs has demonstrated that a large dislocation content is generated in this epilayer. These dislocations propagate considerably greater distances into the epilayer than those found in MBE grown samples, and this observation is attributed to the higher temperature associated with the MOVPE growth technique. Finally, investigation of a CdTe/ZnTe epitaxial structure grown in Durham by MOVPE has demonstrated the multilayer nature of this sample, and that the mechanism of strain relief in this epitaxial layer is the formation of microcracks.

REFERENCES

1. K. Durose, G.J. Russell and J. Woods, *Inst. Phys. Conf. Ser.* **No. 76** (1985) 233
2. R.F.C. Farrow, *J. Vacuum Sci. Technol.* **A3** (1985) 60
3. J.L. Schmit, *J. Vacuum Sci. Technol.* **A4** (1986) 2141
4. T.H. Myers, J.F. Schetzina, T.J. Magee and R.D. Ormond, *J. Vacuum Sci. Technol.* **A1** (1983) 1598
5. W.E. Hoke, P.J. Lemonias and R. Traczewski, *Appl. Phys. Lett.* **45** (1984) 1092
6. W.E. Hoke and P.J. Lemonias, *Appl. Phys. Lett.* **46** (1985) 398
7. J.E. Hails, G.J. Russell, A.W. Brinkman and J. Woods, *J. Appl. Phys.* **60** (1986) 2624
8. J.E. Hails, G.J. Russell, A.W. Brinkman and J.Woods, *J. Crystal Growth* **79** (1986) 940
9. J.E. Hails, G.J. Russell, P.D. Brown, A.W. Brinkman and J. Woods, *J. Crystal Growth* **86** (1988) 516
10. C.H. Wang, K.Y. Cheng, S.J. Yang and F.C. Hwang, *J. Appl. Phys.* **58** (1985) 757
11. A.M. Mancini, P. Pierini, A. Quirini, A. Rizzo and L. Vasanelli, *J. Crystal Growth* **62** (1983) 34
12. M.A. Herman, M. Vulli and M. Pessa, *J. Crystal Growth* **73** (1985) 403
13. M. Oron, A. Raizman, H. Shtrikman and G. Cinader, *Appl. Phys. Lett.* **52** (1988) 1059
14. J.M. Ballingall, M.L. Wroge and D.J. Leopold, *Appl. Phys. Lett.* **48** (1986) 1273
15. J.P. Faurie, C. Hsu, S. Sivananthan and X. Chu, *Surface Science* **168** (1986) 473
16. R.D. Feldman, R.F. Austin, D.W. Kisker, K.S. Jeffers and P.M. Bridenbaugh, *Appl. Phys Lett.* **48** (1986) 248

17. T. Siegrist, A. Segmuller, H. Mariette and F. Holzberg, *Appl. Phys. Lett.* **48** (1986) 1395

18. R. Srinivasa, M.B. Panish and H. Temkin, *Appl. Phys. Lett.* **50** (1987) 1441

19. P.L. Anderson, *J. Vacuum Sci. Technol.* **A4** (1986) 2162

20. D. Schikora, H. Sitter, J. Humenberger and K. Lischka, *Appl. Phys. Lett.* **48** (1986) 1276

21. R. Korenstein and B. MacLeod, *J. Crystal Growth* **86** (1988) 382

22. J.T. Cheung and T. Magee, *J. Vacuum Sci. Technol.* **A1** (1983) 1604

23. R.F.C. Farrow, G.R. Jones, G.M. Williams and I.M. Young, *Appl. Phys. Lett.* **39** (1981) 954

24. C. Fontaine, Y. Demay, J.P. Gailliard, A. Million and J. Piaguet, *Thin Solid Films* **130** (1985) 327

25. A.J. Noreika, R.F.C. Farrow, F.A. Shirland, W.J. Takei, J. Greggi Jr., S. Wood and W.J. Choyke, *J. Vacuum Sci. Technol.* **A4** (1986) 2081

26. C. Fontaine, J.P. Gailliard, S. Magli, A. Million and J. Piaguet, *Appl. Phys. Lett* **50** (1987) 903

27. Y. Lo, R.N. Bicknell, T.H. Myers, J.F. Schetzina and H.H. Stadelmaier, *J. Appl. Phys.* **54** (1983) 4238

28. R.-L. Chou, M.-S. Lin and K.-S. Chou, *Appl. Phys. Lett.* **48** (1986) 523

29. T.H. Myers, Y. Lo, R.N. Bicknell and J.F. Schetzina, *Appl. Phys. Lett.* **42** (1983) 247

30. J. Thompson, K.T. Woodhouse and C. Dineen, *J. Crystal Growth* **77** (1986) 452

31. R.C. Bean, K.R. Zanio, K.A. Hay, J.M. Wright, E.J. Saller, R. Fischer and H. Moro¸, *J. Vacuum Sci. Technol.* **A4** (1986) 2153

32. N. Otsuka, L.A. Kolodziejski, R.L. Gunshor, S. Datta, R.N. Bicknell and J.F. Schetzina, *Appl. Phys. Lett.* **46** (1985) 860

33. R.L. Gunshor, N. Otsuka, M. Yamanishi, L.A. Kolodziejski, T.C Bonsett, R.B. Bylsma, S. Datta, W.M. Becker and J.K. Furdyna, *J. Crystal Growth* **72** (1985) 294

34. L.A. Kolodziejski, R.L. Gunshor, N. Otsuka and C. Choi, *J. Vacuum Sci. Technol.* **A4** (1986) 2150

35. A.G. Cullis, N.G. Chew, J.L. Hutchison, S.J.C. Irvine and J. Giess, *Inst. Phys. Conf. Ser.* **No. 76** (1985) 29

36. P.-Y. Lu, L.M. Williams and S.N.G. Chu, *J. Vacuum Sci. Technol.* **A4** (1986) 2137

37. P.D. Brown, G.J. Russell, J.E. Hails and J. Woods, *Appl. Phys. Lett* **50** (1987) 1144

38. A.G. Cullis, N.G. Chew, S.J.C. Irvine and J. Giess, *Inst. Phys. Conf. Ser.* **No. 87** (1987) 141

39. F.A. Ponce, G.B. Anderson and J.M. Ballingall, *Surface Science* **168** (1986) 564

40. H.F. Schaake and R.J. Koestner, *J. Crystal Growth* **86** (1988) 452

41. N.G. Chew and A.G. Cullis, *Appl. Phys. Lett.* **44** (1984) 142

42. S. Wood, J. Greggi, Jr., R.F.C. Farrow, W.J. Takei, F.A. Shirland and A.J. Noreika, *J. Appl. Phys.* **55** (1984) 4225

43. J.L. Hutchison, *Ultramicroscopy* **18** (1985) 349

44. J.L. Hutchison, *Inst. Phys. Conf. Ser.* **No.87** (1987) 1

45. N.G. Chew, G.M. Williams and A.G. Cullis, *Inst. Phys. Conf. Ser.* **No.68** (1983) 437

46. K. Durose, G.J. Russell and J. Woods, *J. Crystal Growth* **72** (1985) 85

47. H.M. Manasevit, *J. Crystal Growth* **22** (1974) 125

48. Dr. Janet Hails and Paul Burgess, unpublished observations.

49. K. Durose and G.J. Russell, *Inst. Phys. Conf. Ser.* **No.87** (1987) 327

50. K. Durose, *Structural Defects in CdTe*, PhD thesis, Dunelm (1986).

51. D. Vlachavas and R.C. Pond, *Inst. Phys. Conf. Ser.* **60** (1981) 159

52. J. Petruzzello, D. Olego, S.K. Ghandhi, I. Bhat and N.R. Taskar, *Appl. Phys. Lett.* **50** (1987) 1423

53. J.T. Cheung, *Appl. Phys. Lett.* **51** (1987) 1940

54. S. Sivananthan, X. Chu, J. Reno and J.P. Faurie, *J. Appl. Phys.* **60** (1986) 1359

55. A.W. Vere, S. Cole and D.J. Williams, *J. Electron. Mater.* **12** (1983) 551

56. S. Takeuchi, K. Suzuki, K. Maeda and H. Iwanaga, *Phil. Mag.* **A 50** (1984) 171

57. N. Ming and I. Sunagawa, *J. Crystal Growth* **87** (1988) 13

58. R.N. Bicknell, R.W. Yanka, N.C. Giles, J.F. Schetzina, T.C. Magee, C. Leung and H. Kawayoshi, *Appl. Phys. Lett.* **44** (1984) 313

59. W.E. Hoke, P.J. Lemonias and R. Traczewski, *Appl. Phys. Lett.* **44** (1984) 1046

60. P. P. Chow, D.K. Greenlaw and D. Johnson, *J. Vacuum Sci. Technol.* **A1** (1983) 562

61. H.A. Mar, K.T. Chee and N. Salansky, *Appl. Phys. Lett.* **44** (1984) 237

62. H.A. Mar, N. Salansky and K.T. Chee, *Appl. Phys. Lett.* **44** (1984) 898

63. S.K. Ghandhi, N.R. Taskar and I.B. Bhat, *Appl. Phys. Lett.* **47** (1985) 742

64. A. Zur and T.C. McGill, *J. Appl. Phys.* **55** (1984) 378

65. G. Cohen-Solal, F. Bailly and M. Barbe, *Appl. Phys. Lett.* **49** (1986) 1519

66. C. Hsu, S. Sivananthan, X. Chu and J.P. Faurie, *Appl. Phys. Lett.* **48** (1986) 908

67. J. Giess, J.S. Gough, S.J.C. Irvine, G.W. Blackmore, J.B. Mullin and A. Royle, *J. Crystal Growth* **72** (1985) 120

68. S. Wood, J. Greggi, Jr. and W.J. Takei, *Appl. Phys. Lett* **46** (1985) 371

69. B. Pellicari, *J. Crystal Growth* **86** (1988) 146

70. T.W. James and R.E. Stoller, *Appl. Phys. Lett.* **44** (1984) 56

71. J. Giess, J.S. Gough, S.J.C. Irvine, J.B. Mullin and G.W. Blackmore, *Materials Research Society Symposium Proceedings* **90** (1987) 389

72. P.D. Brown, J.E. Hails, G.J. Russell and J. Woods, *J. Crystal Growth* **86** (1988) 511

73. G.P. Carey, S. Cole, T. Yamashita, J.A. Silberman, W.E. Spicer and J.A. Wilson, *J. Vacuum Sci. Technol.* **A3** (1985) 255

74. J. E. Hails, unpublished observations, 1987

75. J.E. Hails, II-VI Interaction Meeting-IV, Coventry, Sept. 1986

76. R.J. Koestner and H.F. Schaake, *J. Vacuum Sci. Technol.* **A6** (1988) 2834

77. A. Million, L. Di Cioccio, J.P. Gailliard and J. Piaguet, *J. Vacuum Sci. Technol.* **A6** (1988) 2813

78. H. Booyens and J.H. Basson, *phys. stat. sol. (a)* **85** (1984) 449

79. I.B. Bhat, H. Fardi and S.K. Ghandhi, *J. Vacuum Sci. Technol.* **A6** (1988) 2800

80. J.P. Faurie, J. Reno, S. Sivananthan, I.K. Sou, X. Chu, M. Boukerche and P.J. Wijewarnasuriya, *J. Vacuum Sci. Technol.* **B4** (1986) 585

81. T.D. Golding, S.B. Qadri and J.H. Dinan, *Molecular Beam Epitaxial Growth and X-ray Characterization of (Zn,Cd)Te/CdTe Strained Layer Superlattices*, to be published in J. Vacuum Sci. Technol.

82. L.A. Kolodziejski, R.L. Gunshor, N. Otsuka, X.C. Zhang, S.K. Chang and A.V. Nurmikko, *Appl. Phys. Lett.* **47** (1985) 882

83. P.D. Brown, G.J. Russell, J. Woods, T. Golding and J. Dinan *Anisotropic Distribution of Defects in CdTe/(Cd,Zn)Te Strained Layer Superlattices*, submitted to Applied Physics Letters.

84. W. Stutius and F.A. Ponce, *J. Appl. Phys.* **58** (1985) 1548

85. A. Sher, A.-B. Chen, W.E. Spicer and C.K. Shih, *J. Vacuum Sci. Technol.* **A3** (1985) 105

86. R. Triboulet, *J. Crystal Growth* **86** (1988) 79

87. B.K. Wagner, J.D. Oakes and C.J. Summers, *J. Crystal Growth* **86** (1988) 296

88. J.H. Dinan and S.B. Qadri, *Thin Solid Films* **131** (1985) 267

89. G. Monfroy, S. Sivananthan, X. Chu, J.P. Faurie, R.D. Knox and J.L. Staudermann, *Appl. Phys. Lett.* **49** (1986) 152

90. R.H. Miles, J.O. McCaldrin and T.C. McGill, *J. Crystal Growth* **85** (1987) 188

91. D.W. Kisker, P.H. Fuoss, J.J. Krajewski, P.M. Amirtharaj, S. Nakahara and J. Menendez, *J. Crystal Growth* **86** (1988) 210

92. P.A. Clifton, J.T. Mullins, P.D. Brown, G.J. Russell, A.W. Brinkman and J. Woods, *Growth and Characterisation of ZnTe and ZnTe/CdTe Superlattices on GaAs Substrates*, accepted for publication in J. Crystal Growth

93. J. Petruzzello, D.J. Olego, X. Chu and J.P. Faurie, *J. Appl. Phys.* **63** (1988) 1783

94. H. Shtrikman, A. Raizman, M. Oron and D. Eger, *Materials Letters* **5** (1987) 345

95. R.H. Miles, T.C. McGill, S. Sivananthan, X. Chu and J.P. Faurie, *J. Vacuum Sci. Technol.* **B5** (1900) 000

96. N.G. Chew, A.G. Cullis, S.J. Bass, L.L. Taylor, M.S. Skolnick and A.D. Pitt, *Inst. Phys. Conf. Ser.* **No.87** (1987) 231

6. Conclusions

This study has principally been concerned with the structural assessment of a range of II-VI epitaxial layers by cross-sectional TEM. Many of these II-VI compounds have potential application in optoelectronic device structures, ranging from detectors in the far infra-red through to light emitters operating in the blue region of the spectrum. Bulk grown II-VI crystals have an unacceptably high defect concentration and this has necessitated their production in thin film form, in particular by MOVPE, MBE and LPE. An essential part of this development process is the structural characterisation of these epitaxial thin films.

There are three main themes within the framework of this on-going research program which have been developed throughout this thesis. These are;

1. The absolute determination of sphalerite crystal polarity by microdiffraction.
2. The anisotropy of the sphalerite structure and its influence on the defect distribution in $\{100\}$ oriented epitaxial layers.
3. Hybrid substrates for the epitaxial growth of MCT.

TEM analysis in isolation is limited because very small regions of material are investigated, and it is uncertain whether or not the observations made reflect the nature of the whole sample. However, cross-sectioning facilitates the direct observation of epilayer/substrate interfaces and when used in conjunction with other techniques such as SEM and RHEED, becomes a powerful tool for materials characterisation.

The production of electron transparent material free from artefacts introduced by the sample preparation process is a non-trivial exercise! Conventional chemical polishing is found to be inappropriate for use with heteroepitaxial systems because of non-uniform attack of the epilayer and substrate material. This necessitates the use of some ion beam milling procedure for the final stage of sample preparation. Milling using argon ions introduces a large number of small dislocation loops into many II-VI compounds,[1] and these have been shown to interact under certain (severe) milling conditions to form dislocations, dislocation loops and stacking faults. Conversion to iodine reactive ion sputtering[1] enabled the careful production of sample foils with a significantly reduced artefactual defect content. A brief study of bulk CdTe grown from the vapour phase using the Durham technique demonstrated that the native defect content of this binary compound comprised dislocations, sub-grain boundaries and twins.

The confusion over the determination of CdTe crystal polarity has been resolved by use of the microdiffraction technique. This absolute polarity determination technique was used to identify the best $\{111\}$ CdTe face for the epitaxial growth of MCT. Correction of microdiffraction patterns for the effects of image rotation introduced by the electron microscope resulted in a $< \bar{1}\bar{1}\bar{1} >_b$ diffraction spot being directed towards the MCT/CdTe growth interface, thereby demonstrating that this was the $\{\bar{1}\bar{1}\bar{1}\}$Te surface. This polar surface becomes shiny when etched in a 1:1:1 mixture of HF:Nitric:Acetic and the observation is in agreement with the convention proposed by Fewster for the assignment of CdTe crystal polarity.

The investigation of wide band-gap ZnSe/ZnS heterostructures on (001)GaAs substrates developed into an academic study of the anisotropic defect distribution in these (001) oriented II-VI sphalerite epitaxial layers. It is considered that the findings reported here may have consequences for all $\{100\}$ oriented sphalerite epitaxial layers. A novel modification to the TEM sample preparation technique allowed the observation of orthogonal $< 110 >$ layer projections for the same TEM sample. This clearly demonstrated that microtwins were present only in the absolute $[1\bar{1}0]$ epilayer projection (as determined by microdiffraction) in addition to a misfit dislocation content, while the orthogonal $[110]$ epilayer orientation was characterised by a complete absence of these microtwin defects. A model based on the differential motion of α and β dislocations was introduced to explain the anisotropy of the defect distribution in these as-grown ZnSe/ZnS/GaAs samples for the polarity described. It was considered that large differences in the ionic radii of the Zn^{2+} and S^{2-} ions and material doping were primarily responsible for the defect anisotropy.

This study was complemented by a brief investigation of sputter deposited ZnS:Mn layers. Indeed, it is slightly ironic that these polycrystalline layers allow the formation of more stable DCEL device structures, as compared with devices fabricated from high quality MOVPE grown material. The comparison of thin film ZnS:Mn deposited onto two different TCO buffer layers indicated that stronger columnar growth occurred on ZnO than on CdSt, which suggests that ZnO may be more suitable for use in these DCEL devices structures.

The production of high quality MCT for far infra-red device applications has provided the impetus for research into the narrow band-gap II-VI compounds. An essential part of this research program has been the development of a suitable substrate for MCT epitaxial growth. The limitations of bulk grown II-VI compounds have stimulated interest in hybrid substrates comprised of CdTe on structurally superior III-V substrates. The study reported here has principally been concerned with the orientation effects of GaAs substrates on the epitaxial growth of CdTe. Lamella twins lying parallel to the interfacial plane were found in $\{111\}$ epitaxial layers of CdTe on $\{100\}$ and $\{\bar{1}\bar{1}\bar{1}\}$B GaAs, and on $\{\bar{1}\bar{1}\bar{1}\}$B CdTe substrates. Whereas, $\{100\}$ CdTe epilayers on $\{100\}$ oriented GaAs exhibited the misfit dislocation network more commonly associated with heteroepitaxial growth.

The formation of twin lamellae in CdTe was attributed to the low SFE and high ionicity of this compound. While the observation that $\{111\}$ CdTe may be formed on either $\{\bar{1}\bar{1}\bar{1}\}$B or $\{100\}$ GaAs was attributed to the large lattice mismatch of this epitaxial system and the surface pretreatment of the GaAs substrate. The differential re-evaporation of Cd from the opposite polar faces of CdTe and GaAs was considered to be responsible for the observation that good epitaxial growth of CdTe only occurred on the non-metal faces of these substrates.

A comparison of epitaxial MCT grown on $\{\bar{1}\bar{1}\bar{1}\}$B CdTe and CdTe/$\{\bar{1}\bar{1}\bar{1}\}$B GaAs hybrid substrates demonstrated that good epitaxial growth of MCT is possible for both of these systems. SEM observations illustrated the excellent surface morphology of these $\{111\}$ epitaxial layers, but also indicated the formation of twinned grains.[2] The twin lamellae in the $\{111\}$ oriented CdTe buffer layer of the hybrid substrate and the twin grains in the MCT epilayer are both expected to introduce electrically active defects which act to the detriment of devices formed from such layers. Twinning is considered to be an inherent property of CdTe. Hence, it is suggested that a different substrate orientation should be used for the epitaxial growth of MCT.

To complement this study, MBE grown CZT/CdTe superlattices on buffer layers of $Cd_{0.96}Zn_{0.04}Te$/$\{100\}$GaAs substrates were investigated. The free standing lattice parameters of these superlattices were tailored to match that of the $Cd_{0.96}Zn_{0.04}Te$ capping layer, which is lattice matched to $Hg_{0.8}Cd_{0.2}Te$. However, the superlattices were found to be highly faulted, with a similar anisotropic distribution of defects to that reported for ZnSe/ZnS heterostructures on $\{100\}$ GaAs. The geometry of this superlattice defect anisotropy could be explained, for an epilayer under compressional strain, in terms of the differential motion of α and β dislocations, only by the introduction of a 90^o rotation of the epilayer with respect to the substrate. This finding is in accordance with the predictions of Cohen-Solal[3] for the {100}CdTe/{100}GaAs epitaxial system. The potential application of these superlattice structures as high quality lattice matched substrates for the growth of MCT may be realised by the use of more closely lattice matched {100}InSb or {100}CdTe substrates.

Finally, a high dislocation content was found in epitaxial ZnTe grown on {100} oriented GaAs by MOVPE. The defects extended through the entire ≈2μm thickness of the epilayer, indicating that lower temperature growth is required for the production of this intermediate band-gap II-VI compound. The ability of the MOVPE growth technique to deposit multilayer structures of CdTe/ZnTe was also demonstrated, although it is apparent that much thinner layers of material must be deposited if a true superlattice is to be formed.

Future Prospects

There is a general trend in the recent literature towards more sophisticated growth techniques in order to produce these II-VI compounds with the high structural quality required. In particular, the production of MCT by pyrolytic MOVPE has seen the emergence of new alkyl precursors which facilitate deposition at lower temperatures. The development of photolytic decomposition techniques is also very topical, with the use of laser ultra-violet radiation to promote deposition at even lower temperatures. The commercial application of MBE to the production of MCT is presently limited because of high Hg consumption, but this growth technique will have increasing importance in the development of more esoteric devices structures. The commercial exploitation of many II-VI compounds necessitates improvements in material purity, uniformity and reproducibility. In addition, there is the difficult challenge of the p-type doping of these materials to high concentrations.

MCT may eventually be superseded by either MZT or by CdTe/HgTe superlattices.[4] The incorporation of Zn into the former acts to strengthen the weak Hg-Te bond. Whereas the latter is the more promising candidate because it becomes possible to select the detected radiation wavelength by control of the relative epilayer thicknesses, thereby allowing greater control at longer wavelengths than may be achieved by control of the bulk alloy composition. The incorporation of Mn into many of these II-VI materials to form dilute magnetic semiconductors is also of interest. This allows the production of materials which exhibit large Faraday rotations and have tunable band-gaps.

However, the development of superlattice structures must surely be the main prospect for the future of II-VI compounds in the future, with the possibility of fabricating novel device structures which are unique to this group of materials.

REFERENCES

1. N.G. Chew and A.G. Cullis, *Ultramicroscopy* **23** (1987) 175
2. J.E. Hails, G.J. Russell, P.D. Brown, A.W. Brinkman and J. Woods, *J. Crystal Growth* **86** (1988) 516
3. G. Cohen-Solal, F. Bailly and M. Barbe, *Appl. Phys. Lett.* **49** (1986) 1519
4. J.N. Schulmann and T.C. McGill, *Appl. Phys. Lett.* **34** (1985) 663